Findlay, Caroline Margaret (2012) *Image analysis tool for the characterisation of bone turnover in the appendicular skeleton.* PhD thesis.

http://theses.gla.ac.uk/3657/

IMAGE ANALYSIS TOOL FOR THE CHARACTERISATION OF BONE TURNOVER IN THE APPENDICULAR SKELETON

Caroline M. Findlay
MEng, Dipl-Ing (France), MSc

Submitted in fulfilment of the requirements for the degree of Doctor of Philosophy (PhD)

Department of Clinical Physics
College of Medical, Veterinary & Life Sciences
University of Glasgow
July 2012

Abstract

Introduction

Osteoporosis is a disease characterised by reduced bone mass and altered microarchitecture leading to an increased risk of fracture. The consequences of osteoporosis include reduced quality of life and pain, associated with fractures. Its financial burden on health services are significant. Characterisation of osteoporosis using imaging techniques is therefore important. Peripheral Quantitative Computed Tomography (pQCT) is a cross-sectional imaging method which is used to scan bones in the appendicular skeleton. pQCT imaging may be particularly useful in clinical groups where changes in bone mineral density (BMD) and structure are known to occur in the limbs. Two such groups are patients following spinal cord injury (SCI) or anterior cruciate ligament (ACL) injury.

Aims

This project aimed to develop analysis techniques to characterise bone in pQCT images. Their purpose was to describe localised changes within pQCT images of the bone, as opposed to the standard global measurements.

Methods

Fully automated segmentation and registration software was developed and tested followed by two independent processing algorithms. The first generates spatial maps to characterise local changes in BMD. This is achieved using both quadrant analysis software and a voxel-based approach, the latter comparing pairs of images and generating a voxel-by-voxel ΔBMD map of changes in BMD. The second processing algorithm uses morphological granulometries to investigate the bone microarchitecture.

Results

Evaluation of these image analysis methods was carried out using two clinical studies. The first investigates acute longitudinal changes in the distal tibia (DT) and distal femur (DF) post-motor-complete-SCI using pQCT. Images from 15 subjects (13M, 2F) with a mean age of 36y±19y, were acquired at 4-monthly intervals during the first year post-injury. The second comprises of ACL injury subjects, with imaging of the injured and contralateral proximal tibia (PT) and distal femur before (n=19, 18M 1F, 30y±9y of age) and after (n=8, 8M 0F, 31y±9y of age) surgical ACL reconstruction.

The software developed to automatically segment bone from surrounding structures was successful: 98% success rate for epiphyseal tibial regions, 67% success rate for the distal femur. Registration of images was then performed and the spatial analysis methods to automatically produce quadrants of trabecular bone were applied, displaying individual results graphically. The voxel based analysis method was developed, tested and applied to produce ΔBMD maps, utilising statistical inference and corrections for multiple comparisons using a false-discovery-rate technique. These maps characterised localised changes in BMD between pairs of both longitudinal and contralateral images. Software was also developed to apply morphological granulometries to pQCT images, calculating global and local pattern spectrum moments.

On application of the analysis methods to the longitudinal SCI images, the BMD and microarchitecture findings were observed to be disparate amongst subjects, with large variations in bone characteristics both globally and regionally. The quadrant and voxel based analysis methods provided information on longitudinal regional changes in each subject, indicating individual patterns of change. Structural analysis of bone microarchitecture using granulometries was demonstrated to have potential as a useful adjunct to BMD in identifying SCI subjects more susceptible to rapid bone loss.

The analysis methods were also successfully applied to the ACL injury subjects. Following segmentation and registration, the total and trabecular BMD in the injured knee was observed to be significantly lower than that of the contralateral control knee pre-operatively for both the PT and DF ($p < 0.05$). Post-operatively the total and trabecular BMD in the injured DF remained significantly low ($p < 0.05$), however the PT demonstrated significantly lower BMD in the injured leg for the trabecular bone only ($p < 0.05$). Reduced BMD in the PT post-operatively in humans is a novel observation, and indicates a benefit afforded by segmenting trabecular from cortical bone. Regional analysis using quadrants indicated some anatomical variation in bone loss within the injured limb, although it is acknowledged that these are preliminary findings which would require to be confirmed in larger studies. The voxel ΔBMD maps generally indicated global losses across the bones of the ACL injured leg both pre-operatively and post-operatively. No consistent patterns were obtained in the ΔBMD maps for these subjects, suggesting individual patterns of response to ACL injury. The structural information provided by granulometric analysis was limited for the ACL study.

Conclusions

Automated software has been developed to characterise bone in pQCT images of the appendicular skeleton. It has been successfully applied to two clinical studies, facilitating localised changes in bone density to be demonstrated and descriptions of microarchitecture to be provided. The SCI subjects appear to have individualistic responses to injury, with a wide range of changes in bone density and microarchitecture observed. ACL injury patients all lost bone mass, but patterns of change were variable. The analysis methods developed to permit characterisation of bones in individual subjects, are proposed to be of value in both clinical and research domains exploring bone mass and microarchitecture, with the ultimate goals being the prediction of fracture risk and tailoring therapy for the individual.

Dedicated to my dad,
Ian Alexander Findlay

Contents

List of Tables

List of Figures

Acknowledgments

There are many people who have helped me during this PhD over the last six and a half years, a list too lengthy for these acknowledgements. The following however are those who played a significant role in getting me across the finishing line.

Firstly, special thanks to Dr Alice Nicol for her supervision and guidance throughout the duration of the PhD. I am very grateful for all the time and effort she has invested in me. My second supervisor, Professor Dave Wyper, has also provided me with continued positive support and feedback, even after his retirement. Thanks to Professor Steve Marshall and Dr Paul Murray from the University of Strathclyde, for sharing their knowledge of morphological image processing and Dr Henrik Gollee from the Centre of Rehabilitation Engineering (CRE), University of Glasgow, for his Matlab and LaTeX advice.

Dr Sylvie Coupaud, CRE, has been a continuous source of guidance, support, encouragement and friendship. I couldn't have got here without your help. *Merci mille fois.*

Thanks to all the SCI and ACL volunteers who gave up their free time to participate in the clinical studies described in this thesis. To the Spinal Injuries Unit and CRE at the University of Glasgow, for enabling me to set up this collaboration, and welcoming me into your departments as one of your own. The PhD students and colleagues at CRE, past and present, were all great support and friends during this time.

I am very grateful to the Department of Clinical Physics and the Scottish Cochlear Implant Programme, for giving me time during my working week to dedicate to this research. Also to all of the staff in both of these departments, who supported me and worked around my PhD.

I am also thankful to the NHS Greater Glasgow & Clyde Bursary Scheme and well as Ian and Carla Findlay, who helped me fund these studies.

This thesis would not have come together if it were not for Dr Rowena Murray, University of Strathclyde, and her many writers retreats at Loch Lomond and Gartmore. Rowena taught me the skills and discipline I needed to write up whilst working full time. My fellow retreaters helped me out of writer's blocks and were enjoyable company during cake filled tea breaks.

I have a great group of very patient friends, who made sure I always had a good life balance during this PhD, even if it was just for a berry tea and a cupcake in Tinderbox. Mairéad, Gill, Lorna, Sinead, Ali and Carolyn - thanks for all your moral support and laughter. And to everyone in my Tukido family, especially Teh's angels, who kept my spirits high and made sure I had the bruises to show for it.

Finally, thank you to my own family, the Findlays at Camp Cottages, Claire, Carla and of course Dad. You have been my biggest supporters, and never once doubted that I would get there.

Author's declaration

I declare, except where explicit reference is made to the contribution of others, that this dissertation is the result of my own work and has not been submitted for any other degree at the University of Glasgow or any other institution.

All of the image processing in this thesis was carried out using software developed by the author.

The clinical studies were carried out by the Spinal Injuries Unit, SGH, Glasgow (*"Osteoporosis in acute SCI"*) and the department of Orthopaedics/Nuclear Medicine, SGH, Glasgow (*"Osteoporosis following ACL injury"*). The author does not claim ownership of these studies.

C.M. Findlay
July 2012

Publications

Manuscripts

Findlay C, Coupaud S, Nicol A, Marshall S, McLean AN, Allan DB, Wyper D
Mapping spatiotemporal changes in bone mineral density at the distal tibia after spinal cord injury, using peripheral Quantitative Computed Tomography scan series
Paper in preparation for Radiology (2012)

Abstracts

Findlay C, Jameson SS, Marshall S, Walker B, Walker C, Meek RD, Nicol A
Image analysis of bone density following anterior cruciate ligament injury
Journal of Bone & Joint Surgery, British Volume, 94-B(SUPP XVIII):31, 2012.
Presented at British Orthopaedic Research Society annual conference, Cardiff, 2010

Findlay C, Nicol A, Marshall S
Localised temporal and spatial image analysis of bone turnover using pqct
Bioengineering 10, IPEM, 2010
Presented at The Bioengineering Society (UK) annual conference, Nottingham University, 2010

Definitions/abbreviations

μ-CT	Micro-Computed Tomography
ACL	Anterior Cruciate Ligament
ACLX	Anterior Cruciate Ligament Transection
BMC	Bone Mineral Content
BMD	Bone Mineral Density
BMDtot	Total Bone Mineral Density
BMDtrab	Trabecular Bone Mineral Density
BMDTrab45	Trabecular BMD using 45% Concentric peel
BMDTrabTP	Trabecular BMD using Threshold peel
CI	Confidence Interval
COM	Centre of Mass
CRE	Centre of Rehabilitation Engineering
CSA	Cross-sectional Area
CSV	Comma Spaced Values
CT	Computed Tomography
DF	Distal Femur
DT	Distal Tibia
DXA	Dual-Energy X-ray Absorptiometry
FBP	Filtered Back Projection
FDR	False Discovery Rate
FES	Functional Electrical Stimulation
FIR	Finite Impulse Response
fMRI	functional Magnetic Resonance Imaging
FWE	Familywise Error
HA	Hydroxyapatite
HR-pQCT	High Resolution peripheral Quantitative Computed Tomogrpahy
HU	Hounsfield Units
MRI	Magnetic Resonance Imaging
PA	Posterior to Anterior projection
PET	Positron Emission Tomography

PI	Principal Investigator
pQCT	peripheral Quantitative Computed Tomography
PSD	Pattern Spectrum Distribution
PSM	Pattern Spectrum Mean
PSS	Pattern Spectrum Skewness
PSV	Pattern Spectrum Variance
PT	Proximal Tibia
PVE	Partial Volume Effect
QCT	Quantitative Computed Tomography
QUS	Quantitative Ultrasound
QENSIU	Queen Elizabeth National Spinal Injuries Unit
ROI	Region of Interest
SCI	Spinal Cord Injury
SD	Standard Deviation
SE	Structuring Element
SGH	Southern General Hospital
SoP	Sum of Products
SPECT	Single Photon Emission Computed Tomography
SPM	Statistical Parametric Mapping
WSR	Wilcoxon signed rank

Chapter 1

Introduction

1.1 Osteoporosis

Osteoporosis is a condition of the bone which is characterised by a loss of bone mass and micro-architecture. This results in bone fragility and an increased probability of low-impact fractures. Its financial burden on the health service in the UK is significant, with the annual cost of treating osteoporotic fractures in the elderly population estimated to be between £900 million to £1.8 billion [1, 2, 3].

Osteoporosis is not unique to the elderly population. Following periods of immobilisation for example, the skeleton or immobilised limbs will experience disuse osteoporosis, or disuse bone atrophy. This is hypothesised to be a consequence of the mechanostat mechanism which regulates bone mass such that it fits its day to day mechanical usage.

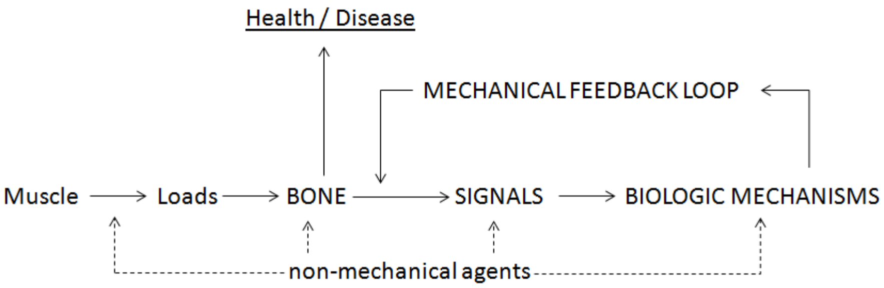

Figure 1.1: Simplified Mechanostat Feedback Mechanism

The feedback relationship described in Figure 1.1 is a simplified scheme of Harold Frost's Utah Paradigm of skeletal physiology [4] which proposes that mechanical factors dominate the mechanisms which control the bone mass, with nonmechanical influences such as hormones, calcium or Vitamin D, having only a secondary influence. The mechanostat theory states that muscle loading and mechanical stresses on the bone provide a feedback mechanism maintaining the bone's integrity. Removal of these forces consequently results in demineralisation of the affected bone(s), which in extreme cases can result in disuse osteoporosis [5, 6, 7, 8, 9]. This response to the removal of mechanical forces on the bone is evident in patient groups such as spinal cord injury and stroke, and even patients immobilised following a leg fracture.

The effect of even small changes in mechanical loading can result in rapid changes in bone mineral density as a result of changing forces on the bone. In knee injuries for example, the initial post-injury immobilisation and subsequent change in weight bearing on the affected knee as a result of impairment or to minimise pain from the injury can result in post-traumatic osteoporosis [10, 11, 12, 13]. Stress shielding of surgical implants such as hip or knee replacements can also induce osteoporosis in the surrounding bone as a result of the normal forces on the bone being removed or altered by the implant. This could ultimately result in the loosening of the prosthesis and potentially the requirement to revise the surgery. For all of these reasons, it is therefore evident why osteoporosis, its causes and its prevention have become widely researched in the scientific community, with the common goal of reducing the massive burden it is placing on our national health service and society as a whole.

1.2 Bone Densitometry

The adult human skeleton is made up of 206 major bones. The five main purposes of the skeleton are: support; storage of lipids and minerals; blood cell production; protection and leverage. Every bone contains two forms of osseous (bone) tissue: compact cortical bone (relatively solid) and spongy trabecular bone (cancellous, open network of struts and plates). The cortical bone forms the surface of bones, providing a dense protective layer around the spongy trabecular bone in the interior of the bone as demonstrated in Figure 1.2 (adapted from [14]).

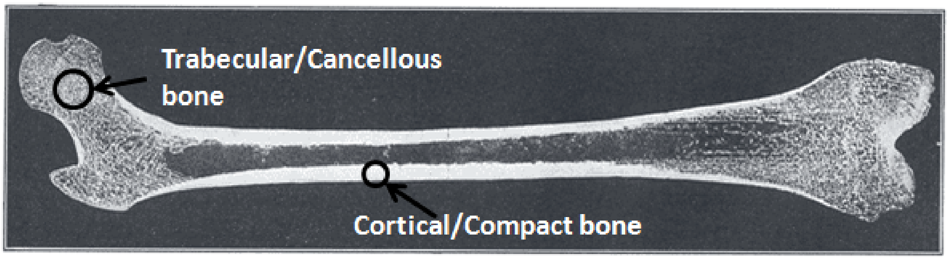

Figure 1.2: Trabecular and cortical bone in the femur, cadaveric sample

The trabecular cancellous bone is clearly visible in the epiphyses of the femur, whereas the cortical compact bone is more obvious in the shaft of the bone. This is due to the different functions required of each of these types of bone. Spongy bone is located where bones are not heavily stressed or where stresses arrive from many directions, whereas compact bone is thickest where stresses arrive from a limited range of directions. Bones are constantly changing to adapt to the demands placed on them, a process known as remodeling. Cells called osteoclasts and osteoblasts are constantly removing and replacing bone cells respectively, normally at equal rates. This turnover is quite high, for example in young adults as much as one fifth of the adult skeleton is recycled and replaced each year, occurring primarily in the trabecular regions due to its greater surface area [15]. By measuring the amount of trabecular and cortical bone present within a bone, it is possible to determine how strong or at risk of fracture the bone is. Peak bone mass is reached around the mid-twenties, after which gradual bone loss will occur. Osteoblast activity begins to decline whereas the osteoclast activity continues at previous levels. This results in the bones becoming weaker with time, with women losing roughly 8% of their skeletal mass every decade and men losing about 3% per decade. This decrease in Bone Mineral Density (BMD) is natural with age. However, when the reduction in BMD is so great that it becomes at least 2.5 standard deviations below peak bone mass (20 year old, sex-matched healthy person), the World Health Organization (WHO) defined this threshold as a condition known as Osteoporosis [16]. With osteoporosis, there is a higher risk of fracture therefore diagnosis is important in order to provide medical intervention or lifestyle advice.

As bone consists of Calcium, Phosphorus and other minerals, the only true method for measuring bone mineral density requires the bone to be incinerated. The resulting ash is then weighed to calculate the true bone mineral density. In vivo methods for measuring bone mineral density include:

- Bone Densitometry, which can be performed using electromagnetic radiation or ultrasound.
- Bone Biopsy taken after labeling it with a tracer.
- Biochemical markers of bone turnover which reflect either bone formation or bone resorption.

Of these methods, the non-invasive imaging techniques which measure attenuation of an energy source passing through the bone are the most widely used. This can be either using electromagnetic radiation or an ultrasound beam, the attenuation of which will vary depending on the density of the bone. If the degree of attenuation can be quantified, it would be possible to quantitatively assess the tissue density as well. This is the basis of photon absorptiometry and the measurement of bone density.

1.2.1 Dual-energy X-ray Absorptiometry

Dual-energy X-ray Absorptiometry, or DXA, is the most widely used method in the UK of measuring bone mineral density. The DXA scanner (Figure 1.3) calculates BMD by quantifying the reduction in X-ray photons incident on a detector after they have passed through a patient's bone. It compensates for the contribution of photon attenuation from the bone's surrounding soft tissue by passing two distinct photon energies through the patient, posteriorly to anteriorly (PA), to a detector. These photon energy peaks are specifically chosen to maximally attenuate photons from the two different tissue structures of bone and soft tissue e.g. 40keV and 80keV. The result is an areal image of the site of interest and using regions of interest the BMD can be calculated in g/cm^2 (Bone Mineral Content, BMC, per unit area). DXA BMD measurements are extremely fast, low dose (approximately 0.04mSv PA spine and proximal femur), low cost and can be applied to numerous skeletal sites. The most common of these sites are the hip, and spine due to their high fracture rate in the osteoporotic elderly population. Worldwide screening programmes therefore recommend the use of DXA in their osteoporosis screening and management guidelines for the general (aging) population [16, 17].

Figure 1.3: GE Lunar Prodigy$^{\text{TM}}$ (Image courtesy of Southern General Hospital, Glasgow)

There are however limitations to using an areal projection when calculating BMD. The measurement will be affected by the size, or area, of the bone and is only given as a bone mass per unit area (g/cm^2) as opposed to volumetric information. It is also not possible to distinguish between cortical and trabecular bone, the latter being of particular interest due to its high turnover. Any rapid changes in BMD will primarily be seen in the trabecular network. Quantitative Computed Tomography (QCT) is an alternative imaging technique of measuring BMD which addresses these issues.

1.2.2 Quantitative Computed Tomography

Quantitative Computed Tomography is a means by which 3D volumetric data can be acquired using a Computed Tomography (CT) scanner to determine BMD in g/cm^3. It also allows segmentation and quantification of cortical and trabecular components of the bone independently, without the superposition of overlaying tissues. In parallel to QCT's development by Genant and Boyd in 1977 [18], a smaller dedicated forearm peripheral QCT was also introduced by Rüegsegger *et al* in 1974 [19]. Peripheral Quantitative Computed Tomography or pQCT scanners, have much smaller, more compact gantries and are dedicated to measuring BMD at appendicular skeletal sites. They are relatively inexpensive in comparison to diagnostic CT scanners, with a significantly lower radiation exposure to the patient, however their scan times can be considerably longer. Typical scan parameters for QCT (Single Energy) and pQCT can be found in Table 1.1 [20, 21].

	QCT	pQCT
Voltage (kV)	80	60
Current (mA)	70-140	0.2
Slice Thickness (mm)	10	2.3
Scan Time (s)	2	90
Effective Dose per scan (μSv)	~300	<2

Table 1.1: QCT Versus pQCT parameters

These scanners calculate BMD using a calibration phantom containing known quantities of water-equivalent material representing soft-tissue and hydroxyapatite representing bone. This is used to convert the photon attenuation coefficients at each pixel location in the image to bone mineral concentration. Each pixel represents a volume xyz cm^3, where xy is the pixel size and z is the slice thickness. The combination of the attenuation coefficients within volume element xyz, also known as a voxel, with the calibration phantom produces a hydroxyapatite-equivalent bone mineral density image in mg/cm^3.

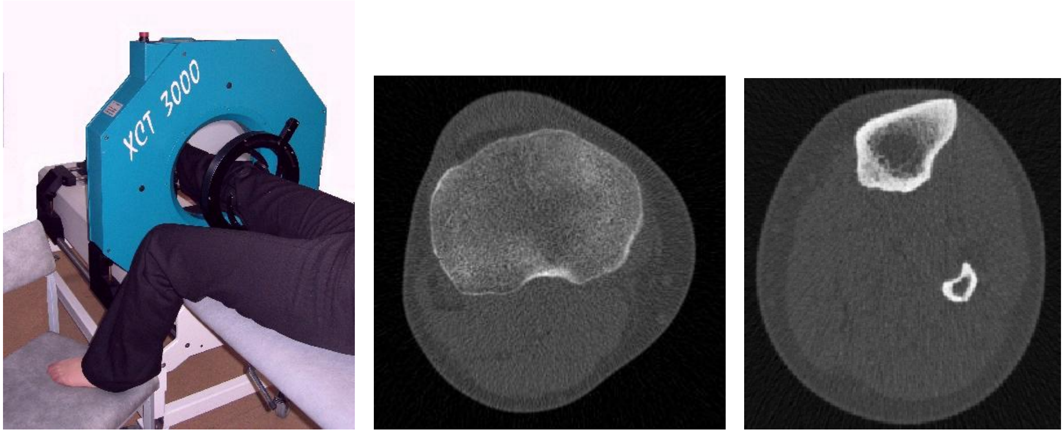

(a) Stratec$^{\text{TM}}$pQCT Scanner (b) 4% Proximal tibia image demonstrating trabecular bone (c) 66% Distal tibia image demonstrating cortical bone

Figure 1.4: pQCT scanner in use and a tomographical slices of tibia

It is possible to visualise and independently measure both the trabecular and cortical bone density of the bones contained within the slice, as well as measure cross-sectional area of the surrounding fat and muscle tissue. Using these densitometric images where each voxel represents an equivalent density of bone, volumetric BMD for that slice can be determined from regions of interest. These images are therefore very useful when monitoring bone turnover and the efficacy of treatment. This is because trabecular bone alone, which has a much higher turnover in comparison to cortical bone due to its greater surface area, can now be quantified.

The benefits of monitoring bone turnover using pQCT over DXA are even more evident in patient groups who will suffer from soft tissue changes, such as muscle atrophy, over the period they are being monitored. The assumptions made in DXA measurements of BMD are that the transmitted photons will only pass through two homogeneous tissue types, bone and soft-tissue. It does not take into consideration variations in tissue density within the soft tissue component such as the differences between muscle and fat. Consequently, DXA has been shown to introduce inaccuracies in BMD measurements from differences in surrounding soft-tissue composition [22, 23, 24]. pQCT linearly transforms voxel values into hydroxyapatite equivalents, using reconstructed projected data, reducing the effect of changes in overlaying soft-tissue densities on the BMD measurement. The drawbacks to pQCT are the requirement for precise patient positioning given the single slice acquisition, with the scanning time much slower than conventional CT. This can ultimately lead to a more lengthy appointment which can take up to an hour depending on the physical limitations of the patient under investigation.

1.2.3 Non-ionising Measures of Bone Densitometry

Two alternative methods of assessing bone densitometry using non-ionising radiation include ultrasound and MRI. Quantitative ultrasound (QUS) measurement is an alternative low-cost technique measuring the attenuation of an ultrasound beam through the calcaneus. The heel is placed in a water bath and both a transmitter and receiver are placed either side of the bone. The energy lost as the ultrasound beam traverses the bone is related to the material properties of the bone (and surrounding soft tissue). Evidence from a large number of studies suggest that QUS would be suitable for assessment of fracture risk in elderly women, having some prognostic value for future hip fracture prediction. However although it is a low cost rapid method of assessing bone structure (15 to 20 minutes), it currently cannot provide diagnostic criteria for osteoporosis [16].

MRI is commonly used to assess the musculoskeletal system and it's associated pathology. Unlike the previous methods discussed, MRI applies the principles of magnetism to create images from the lipids, marrow and water in the porous spaces within the bone matrix, producing a positive image of the interstitial space between trabeculae, and a negative image of the bone matrix [25]. Using the assumption that the bone tissue remains constant independent of gender or age, these images can be used to calculate the apparent bone density. Hong *et al* demonstrated a strong linear correlation between these calculated measures using MRI with those of ash density. Scan times using MRI can be variable depending on the imaging sequences used, however on average these can take 30 minutes. The benefits of MRI include good structural assessment of the trabecular bone without the influence of marrow and other fluids as well as it having no associated ionising radiation exposure. Limitations however include the high cost of the scanner and safety implications should the patient have any metal implants.

This thesis will focus on the assessment of BMD changes in two patient groups susceptible to osteoporosis and muscle atrophy in the appendicular skeleton, where pQCT is the optimal imaging modality for these investigations. This is due to its ability to separate and independently measure trabecular BMD without influence from it's surrounding structures and providing true volumetric data at peripheral sites of the skeleton. The first of these groups is the Spinal Cord Injury (SCI) population. Osteoporosis is a known consequence of SCI, where bone loss is predominately sub-lesional and in the long bones of the lower limbs making them at higher risk of low-impact fractures [26, 27, 28]. The second group are patients following injury and surgical repair of their anterior cruciate ligament (ACL). This group experience post-traumatic osteoporosis in the injured knee as a result of initial altered loading, post-surgical immobilisation and changes in mechanical forces within the knee [12, 29, 30].

1.3 Spinal Cord Injury

The spinal cord is the body's sensory, motor and nervous conduit which runs down the vertebral column of the spine. Damage to the spinal cord can result in partial or complete paralysis below the level of the injury. One of the many secondary complications as a result of immobilisation following SCI is disuse-related osteoporosis in the bones below the level of the injury. As the patient is no longer weight bearing, bone tissue is removed in response to the lack of mechanical forces exerted on them, supporting Frost's proposed mechanostat model (referred to as the "disuse window" of bone adaptation). Additional factors potentially contributing to bone loss in SCI include age and gender, level and extent of lesion, as well as disruption of normal neural, vascular and endocrine functionality. Consequently, SCI patients are at a higher risk of low impact fractures for example during transfers into their wheelchair with the overall lifetime risk being double that for the non-SCI population [28, 31, 32]. The complications as a result of fractures include associated health care costs and an increase in morbidity and mortality.

Eser *et al* [33] carried out a cross-sectional study looking at the relationship between paralysis duration and BMD using pQCT. Eighty-nine motor complete spinal-cord injured men with a paralysis duration between 2 months and 50 years were included (both tetraplegic and paraplegic subjects). The bone mineral density of the epiphyses of both tibia and femur was found to reach a new steady-state after 3-8 years having experienced a bone loss of 50% and 60% in the femur and tibia respectively. This was also confirmed for the Scottish chronic SCI population by Coupaud *et al* [34]. Similar studies have reported this steady state between bone resorption and formation to be between 16 months [27] to 2 years [35, 36], each with comparable bone loss percentages to Eser.

Further work by Eser *et al* [32] to define BMD fracture thresholds looked at cross-sectional data of ninety-nine motor complete SCI subjects. Twenty-one of these subjects had sustained a fracture of the tibia or femur, the most common fracture sites in SCI. The authors concluded that subjects with a trabecular BMD less than 114mg/cm^3 and 72mg/cm^3 for the femoral and tibial distal epiphysis respectively, had experienced fractures. Using these thresholds as a guide, approximately 50% of the subjects with chronic SCI (defined as 5 & 7 years post-injury for femur and tibia respectively) had trabecular BMD values below the fracture threshold in the femur and two-thirds below the fracture threshold for the tibia. These findings assist categorisation of SCI patients into those who are at either low or high risk of sustaining a fracture of the paralysed limbs with the use of pQCT imaging.

Many anti-osteoporosis interventional studies have been carried out in the SCI population aimed at slowing or reversing the bone loss experienced in the affected limbs. Interventions range from pharmacological and weight bearing to Functional Electrical Stimulation (FES). The future success of these methods is not clear, with results varying from no change in BMD to some preservative effects being observed. Leeds *et al* [37] performed 6 months of FES cycle ergometry on six SCI tetraplegic men (paralysis duration between 2-7 years) and measured no change in BMD in DXA measurements of the hip. Similarly Eser *et al* [38] performed an FES-cycling interventional study on 39 acute-SCI subjects (19 of these subjects were used as controls). pQCT scans of the right tibia diaphysis showed no attenuation of bone loss in the intervention group compared to the control group. Interestingly, a study carried out by Frotzler *et al* [39] of high volume FES in chronic SCI demonstrated significant increases in pQCT BMD measurements in the distal femoral epiphysis. However, in agrement with Eser's findings no significant changes were observed in any of the measured bone parameters in the tibia. Both studies by Eser and Frotzler calculated the total BMD of the entire slice. A recent study by Dudley-Javoroski *et al* [40] carried out uni-lateral soleus muscle training using FES on sub-acute, chronic and non-SCI subjects. In particular, this paper looked for any asymmetric changes in BMD within the bone itself following this intervention. Bi-lateral pQCT images of the distal tibial were acquired and subsequently partitioned into anterior and posterior sections of the bone. The bone-sparing effect of soleus stimulation occurred almost entirely in the posterior region of the tibia, demonstrated in the trained images in Figure 1.5 [40] (Permission to reproduce this image has been granted by Professor R.K. Shields, University of Iowa).

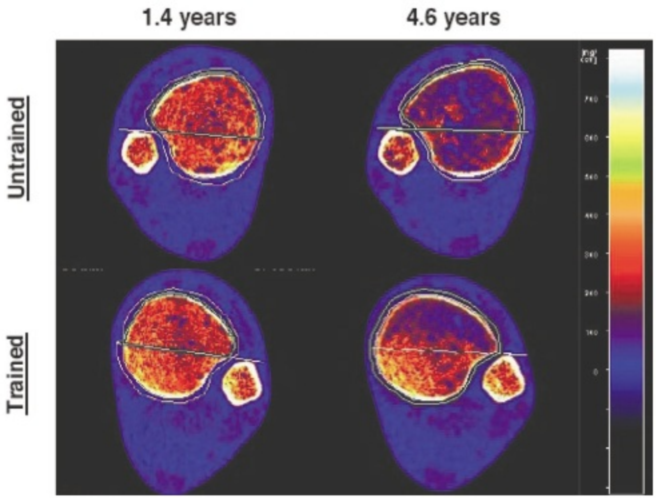

Figure 1.5: Asymmetric bone adaptations following FES soleus training

These findings raise the question as to whether previous FES studies which did not demonstrate any change in BMD could potentially have had some localised non-homogeneous adaptations within the bone. These preservative effects may not have been apparent due to the effect of regions within the same slice still experiencing loss, as both areas would have been contained within the global BMD measurements.

1.4 Post-Anterior Cruciate Ligament Injury

Cross-sectional studies of musculoskeletal injuries such as an anterior cruciate ligament tear, have been shown to cause reduction of BMD in the injured limb as a result of the immediate trauma and subsequent immobilisation, surgery and rehabilitation. However, full recovery of the bone to its pre-injury density following these types of injury has not been observed [41, 29, 42]. This has implications as to the long-term effect on the knee as a lack of bone density and subsequent ambulatory changes applying different loads to the cartilage may contribute to the progression of osteoarthritis in the joint [43, 44]. An ACL injury often occurs in the young and active population. The ACL is a ligament of considerable strength which inserts anteriorly in the proximal tibia crossing over to the lateral condyle of the distal femur (Figure 1.6, Edited from the 20th U.S. edition of Gray's Anatomy of the Human Body, 1918, copyright expired [14].)

The ACL can be ruptured following a sharp twisting motion or trauma to the knee such as a fall. Patients can experience acute swelling and pain, and in the longer term report knee locking and instability. This type of injury often leads to them having to withdraw from their previously active life or sporting activities. ACL injuries can be treated conservatively

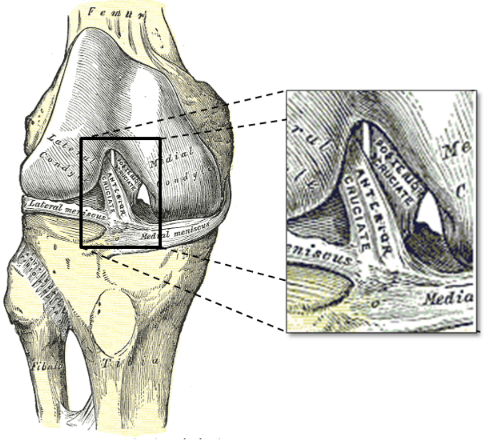

Figure 1.6: Left knee-joint from the front, with zoomed anterior cruciate ligament

with no surgical intervention if the patient is not experiencing any long term discomfort or problems with their knee. Surgery is however recommended if any knee locking, pain or instability is experienced or if they are unable to return to their pre-injury activities.

Leppälä *et al* [12] looked at the difference in bone density between conservative and surgical treatments of ACL using DXA in humans. BMD of the knee amongst other regions was determined at the time of the injury and after 4, 8, and 12 months. The surgically treated group demonstrated significant bone loss in the affected knee up to 12 months post-injury (distal femur 21%, patella 17%, proximal tibia 14%; $p < 0.001$ in each). The conservatively treated group did not experience as much loss, with a small but statistically significant bone loss at the patella (-3%; $p = 0.005$) and proximal tibia (-2%; $p = 0.022$) of the injured limb. Although these findings are quite contrasting, the authors noted that as the severity of the injuries of the latter group were not as severe as the former they are not comparable.

A pQCT study of the bone density in the canine knee by Boyd *et al* [13] in the first year following ACL transection (ACLX) demonstrated changes in BMD in both the femur and tibia as early as 3 weeks post-ACLX versus contralateral control knee. Similarly to the Dudley-Javorosky *et al* study [40], Boyd looked at compartmental BMD changes in the canine knee. The most significant region of bone loss at 3 weeks was observed in the postero-medial compartment of the femur, whereas by 12 weeks all regions in the tibia and femur had exhibited significant bone loss, the greatest in the postero-medial compartment of the femur (-142 ± 21 mg/cm^3).

A second study looking at regional analysis of BMD in the unreconstructed ACL-injured knee using DXA was assessed by Bayer *et al* [30]. Subjects' knees were scanned at a mean time post-injury of 24 months. BMD at nine Regions of Interest (ROI) within the knee laterally and PA were measured. The authors reported significant bone loss in the injured knee in specific regions, in particular at the patella, medial tibial plateau and lateral femoral condyle. The findings from these two studies may be of particular value to surgeons when considering localised bone strength requirements for the long term success of graft fixations.

What is becoming apparent is that, similarly to the spinal cord injury patient group, there seem to be localised bone losses occurring within the knee in response to the ACL injury and surgical repair. In addition to this, both of these injuries and consequently bone losses often occur in young people, which is unlike the traditional thinking of “osteoporosis” as being an old person’s disease. Localised analysis of pQCT images of the knee before and after ACLX reconstruction surgery may provide an insight into true BMD patterns of change across the bone in this population. It may also be possible to observe if these regions relate to areas of stress shielding as a result of the surgical implant.

1.5 Aims and Motivation

It seems therefore evident that an image analysis tool for the localised assessment of trabecular bone turnover may be of clinical benefit, not exclusively but specifically to these two groups. The outcomes of these analyses could inform research and development programmes and assist health care professionals perform more focussed interventional techniques as well as provide information on bone integrity prior to implant placement. Literature available on medical image analysis of bones and osteoporosis is extensive across many imaging fields, from plain film x-rays to complex Magnetic Resonance Imaging (MRI) sequences. As outlined previously, pQCT provides the user with an alternative, low dose means of assessing bone mineral density, but literature on pQCT image analysis appears to be much more limited. This is most probably a result of the fact that pQCT scanners are not currently used clinically, but primarily in the research domain.

An opportunity exists therefore to explore the use of medical image processing to assist the characterisation of bone mass and microarchitecture from pQCT images. Image analysis methods will be developed and applied to subjects who have experienced either SCI or ACL injury. The development of analysis techniques to facilitate comparisons between localised BMD values in pair of images at voxel level would therefore facilitate this evaluation. Ideally, this should produce additional information on both bone density and microarchitectural changes occurring within the bone. Data present within the pQCT images could provide users with a further insight into where specific patient groups experience the greatest magnitude of bone changes and whether these changes are across the entire bone or localised to specific compartments within the bone. This premise is explored in the following chapters of this thesis, which detail the development and assessment of image analysis tools in the assessment of BMD changes in SCI and ACL patient data.

1.6 Organisation of Thesis

This introductory chapter has briefly defined osteoporosis, explored existing methods in determining bone mineral density and identified the current limitations which exist in the localised assessment of bone turnover. In Chapter 2, a review of the existing image analysis techniques applied to pQCT will be presented, going on to discuss potential alternative image processing methods which could provide additional information.

In Chapter 3 the pQCT scanner used for the image acquisition is described in detail, including technical specifications. The pre-processing tools developed for the manipulation of the pQCT raw image data prior to analysis are outlined, including software validation.

Chapters 4 and 5 present two different image analysis tools developed for analysis of pQCT images. Chapter 4 outlines a technique which co-registers pairs of images and generates a spatial map of changes in bone density across the image. It then goes on to describe the registration of image pairs, which is a fundamental component to the image comparisons. This is done either through automated quadrant analysis or through the generation of a voxel-by-voxel map of changes in bone density across the image. Chapter 5 introduces the use of morphological granulometries as a means of assessing the global pattern of trabecular struts within the image.

The image analysis tools presented in these chapters are then applied to two independent subject groups in Chapters 6 and 7. The results from the SCI subject analysis is given in Chapter 6 with the ACL subject analysis in Chapter 7. Chapter 8 provides a critical appraisal of the image processing tools in the characterisation of bone within these two clinical studies and their potential for applicability beyond these studies. Conclusions are drawn, the findings from this research are summarised and finally avenues for further work are explored.

Chapter 2

Literature Review

Image processing of medical images to facilitate and improve diagnosis is widely researched across all radiological modalities including MRI, plain film radiography, CT, DXA, ultrasound and pQCT. Each of these modalities has its pros and cons with regard to their success in identifying and quantitatively assessing changes in BMD, with each having image processing techniques better suited to one in comparison to another. The review of literature in this thesis will outline various methods which have been applied to pQCT images in the assessment of osteoporosis. It will also introduce alternative modality publications which utilise methods which may also be applicable to pQCT. The overarching aim of this review chapter is to give a critical appraisal of image processing methods which could be applied to the study of global and localised changes in BMD from pQCT images of the appendicular skeleton. This may be carried out using and optimising the manufacturer's software supplied with the pQCT scanner, or through the development of novel image processing software.

This chapter can be broken down in to several sections:

1. Prior to performing any analysis of bone structure from pQCT images, a degree of image pre-processing is required. Segmentation of the bone of interest from the surrounding soft tissue is one of the most obvious first steps. There are many segmentation methods which have been investigated and applied to pQCT images, ranging from relatively straightforward thresholding to more computationally complex contour detection or region growing. This review will present and evaluate the suitability of some of these methods, with reference to their application to the SCI and ACL image data.

2. Additionally, as one of the aims of this study is to look at localised changes in bone pattern using comparisons to other images (either longitudinally or contralaterally), registration of images will be necessary. An assessment of methods applicable to registering pairs of images will therefore be made.

3. Finally, an appraisal of the post-processing methodologies applied to pQCT will be carried out in order to identify how these can be taken forward and developed for

the assessment of changes in BMD, in particular for the two clinical groups described previously. These methods are categorised into two groups: those methods which describe global changes and those describing local changes.

2.1 Image Pre-processing

The common aim in the pre-processing stage is to optimise the images acquired in order to assist further investigation. Despite pQCT enabling independent cortical and trabecular bone measurements where DEXA does not, low dose pQCT systems still the lack spatial resolution to separate individual trabeculae (which are only visible using μ-CT scanners). pQCT images are also susceptible to noise, arising from, but not exclusively, the back-projection reconstruction algorithm, non-uniformity of the X-ray beam and intrinsic detector characteristics. Most authors therefore include a degree of pre-processing in their analysis which primarily involves smoothing to reduce the effects of noise.

Cervinka *et al* [45] investigated whether pre-processing alone could enhance structural analysis of the bone within pQCT images, comparing two novel pre-processing techniques to a 3x3 and 5x5 median filtering technique. This was performed using different liquid phantoms. They reported that pre-processing improved the analysis of the cortical bone, however there appeared to be no improvement of the trabecular bone assessment using any of the four methods. This was attributed to the already high reliability coefficient using the raw images alone ($R \approx 99\%$) leaving minimal room for improvement as well as the high levels of noise inherent in the image, which could not be efficiently suppressed using pre-processing techniques alone. These findings therefore support the proposal that to obtain additional information on the trabecular structure within the pQCT image, enhanced pre-processing of images alone is not sufficient and additional post-processing is necessary to reveal the underlying information in the trabecular pattern.

The majority of authors who present pQCT image segmentation algorithms have used a pre-processing step to improve the algorithm's success. Filters such a 3x3 Gaussian or median filter, which replace the centre pixel with the weighted average of its neighbours, have been used successfully to reduce the effects of noise on segmentation [46, 47, 48, 49, 50]. Despite these filters degrading the image quality through blurring, they are simple and very effective tools which can be used to generate binary masks of the bone in the image which can be subsequently applied to the raw image in order to segment it from the surrounding soft tissue.

2.2 Segmentation

Image segmentation subdivides an image into unique groups or regions. It uses properties such as pixel intensity profiles or neighbourhood relationships to identify those which belong or do not belong to the same object. Segmentation algorithms are tailored to the specific requirements of each image type and resolution, and in the case of pQCT, the segmentation of bone from soft tissue is one of the major goals. Image segmentation methods have been extensively researched in the field of computer vision. A summary of the key techniques applicable to pQCT images including thresholding, contour detection and morphological segmentation, are presented here.

2.2.1 Thresholding

In its most fundamental form, histogram thresholding generates a graphical frequency plot of all of the pixel values in an image. Based on the properties of the object to be segmented, a threshold is chosen separating images into regions either above, below or between threshold values. All pixel values that are not of interest are then removed from the image. The aim is that the histogram enables the user to identify distinct 'modes' of the image, such as groups of pixels representing background, soft-tissue or bone and consequently guides the user in their choice of threshold.

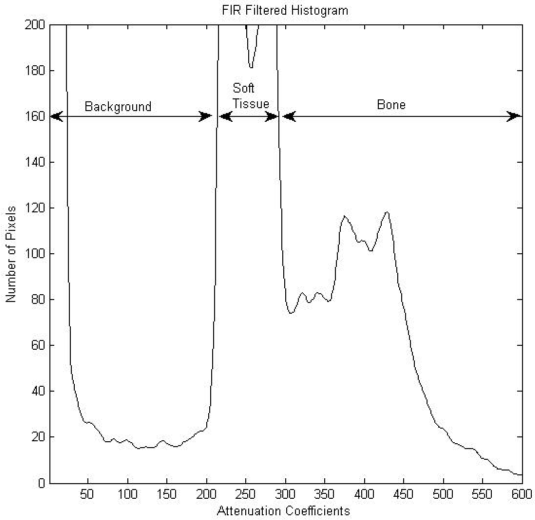

Figure 2.1: Simplified Image Histogram demonstrating 3 modes: Background, Soft-tissue and Bone

Thresholding is attractive in image processing due to its simplicity and the minimal computational power necessary to carry it out. It is for this reason that it is used extensively in the segmentation of bone from soft tissue in pQCT images. The choice of threshold is therefore the key parameter, with the manufacturer's software providing default thresholds for muscle/soft-tissue (34mg/cm^3), bone (200mg/cm^3) and cortical bone (710mg/cm^3 and above) [21]. However, what has been commented on frequently in the published literature is that a fixed threshold applied to all images has limited success. This is particulary true for longitudinal groups of images when the bones are changing, especially when gradually becoming more osteoporotic. The partial volume effect (PVE) will also influence the effectiveness of threshold choice. PVE occurs where the values of pixels located at the boundaries of objects such as bone and soft tissue are formed from a combination of the densities of both tissues, making categorisation of these pixels into either group very challenging.

For instance, Ward *et al* [51] investigated the use of the manufacturer's single threshold in the measurement of cortical bone geometry and density (710mg/cm^3) using the European Forearm Phantom and patient data. They concluded that this threshold resulted in an error of 14% when measuring cortical geometry and 13.5% when measuring its density as a result of the partial volume effect at the bone/soft tissue boundary. They therefore proposed the use of two different thresholds of 648mg/cm^3 and 1200mg/cm^3 for these respective categories. Buie *et al* [49] also presented a dual-threshold algorithm for segmentation, requiring two threshold inputs defining the periosteal and endosteal boundaries when segmenting cortical and trabecular bones using micro-CT. Hangartner [52] again used two different thresholds for measuring either density or geometry. His choice of these thresholds varied depending on the densities of the two materials that make up the boundary of the structure to be segmented. He recommended that the threshold for accurate geometric segmentation be 49% of the difference of the density between the adjacent tissues, whereas a 95% of the maximum density value of bone should be used for accurate density measurements.

Finally, a comparison was made by Davis *et al* [53] of fixed threshold choices when segmenting the radius and tibia from images acquired by High Resolution pQCT (HR-pQCT is a research tool only, generating 3D image data sets with a voxel size 82μm). Semi-automated contours were drawn to define the periosteal surface of the tibia and radius of 28 and 26 patients respectively. Three different global thresholds were applied separately to each image (one of which was the manufacturers default) to produce three different segmented images. Interestingly, these authors eroded the segmented image by 2 pixels to exclude those affected by PVE at the bone/soft-tissue boundary. The outcome showed that threshold selection did have a direct impact on the cortical parameters derived from HR-pQCT. For instance, in changing the threshold as little as ±5% from the manufacturers recommendation, a resultant change of 2-5% difference in cortical thickness measurement was observed. They concluded that a fixed threshold scheme for the measurement of cortical thickness is non-negligibly sensitive to moderate changes in threshold level and by inference to moderate, uniform changes in tissue-level mineral density.

Careful consideration is therefore necessary if a fixed threshold is to be used for segmentation, in particular for studies where changes in bone density are expected, resulting in corresponding changes in pixel value when imaging with pQCT. A threshold that was deemed suitable for segmentation of images acquired during the initial stages of a study may no longer be appropriate following disease or intervention.

With this in mind the use of an automatically generated threshold for each individual image may therefore be attractive. Helterbrand *et al* [46] proposed one such method which automatically segmented tibia and vertebrae from pQCT images of ovariectomized rats. Following smoothing using a 3x3 Gaussian filter, a histogram of the smoothed image was generated. The intensity histogram was also smoothed using a moving average filter. These two pre-processing steps were performed to minimise the noise which may affect the automated threshold choice separating the bone and soft-tissue modes. The first derivative of the smoothed histogram was then calculated and used to locate the bone/soft tissue intensity boundary. The principle behind doing this was to identify the location of the distinct modes in the image histogram using the change in gradients of its envelope from one mode to the next. The bone/soft tissue threshold was determined by locating on the 1st derivative histogram the zero crossing between the tissue mode and the bone mode, and subsequently using this value as that image's global threshold to segment bone from soft-tissue. The automatic generation of a global threshold was shown to be highly successful, with the authors reporting that a visual inspection of over 600 images yielded excellent bone/soft-tissue segmentation.

This alternative thresholding method identifies a possible solution to the previously discussed limitations of a fixed global threshold, in particular when bone changes over time are observed. However, caution must also be exercised as quite naturally, a different threshold will be obtained for each image. For example, it is important to consider how this would influence the reliability of any measurement comparisons made over time, as global thresholds may change slightly for subjects within the same study. In this instance Helterbrand *et al* [46] argue that, whilst acknowledging this, the approach adopted by this method was appropriate since variations in image production as well as bone positioning within the field of view can also lead to changes in image quality and the recorded intensity value range from image to image. In their particular study they found that 80% of the identified thresholds were within a 7% interval of the intensity scale, with 100% being within a 13% interval of the intensity scale.

It is therefore apparent that as a result of the limitations of the image acquisition process as well as inter-subject/scan variations, an appropriate threshold definition is challenging. On one hand a global threshold will maintain consistency throughout the study and across patient groups, and is straightforward to implement. There are, however, some issues with accuracy of some bone parameter measurements as well the success of this threshold if the bone mineral density changed dramatically during the period of investigation. On the other hand, an adaptive threshold would address the issue of image variability, optimising itself to the pixel densities contained within the individual patient image. This too has its drawbacks as it is slightly more computationally complex and there is a risk that comparison of measured bony attributes over time could potentially be questioned as a result of threshold variability.

2.2.2 Edge and Contour Detection

As observed in the previous section, thresholding of an image histogram does show promise when performing segmentation, and despite its associated drawbacks, these simple techniques used in combination with additional segmentation methods could potentially produce more accurate outcomes. One such method is to perform edge detection. Edge detection operators use weighted masks to identify changes in gradient across an image or in other words, where there are large changes in neighbouring pixel densities. This could be combined with adaptive or local thresholding to create a method which does not rely on tissue density assumptions. Waarsing *et al* [47] and Burghardt *et al* [48] have applied such a technique to μ-CT (generates 3D image volumes with a voxel size of 18μm) and HR-pQCT (voxel size 82μm) images respectively. The fundamental adaptation to pure thresholding which these methods have is that they apply edge-detection as a guide for localised thresholding. Both authors perform a Gaussian smoothing on the image initially (Image A in Figure 2.2 below), and then use a standard edge detection algorithm to define the surface of the bone in the smoothed dataset. In both instances a 3x3 Sobel operator was used. (Figure 2.2 was reproduced with permission of the American Society for Bone and Mineral Research in the format reuse in a dissertation/thesis via Copyright Clearance Center, [47].)

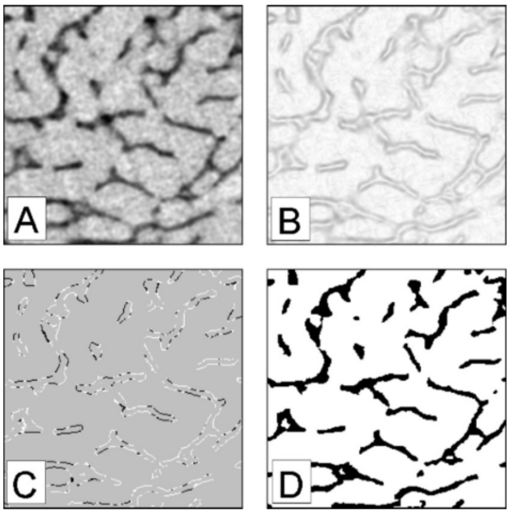

Figure 2.2: Four steps in local segmentation method, Waarsing *et al*, (A) Smoothed grayscale images, (B) 3D spatial gradient calculated (C) The local maxima in the gradient field are the edges of the bone (D) From these edges, local thresholds are derived, used to obtain the binary image

The edge detected image is shown in Image B. False edges as a result of noise were eliminated by only accepting strong edges, with a local maximum above a high threshold, in combination with a smaller maximum, which are connected to these high maxima but above a lower threshold (both thresholds were user defined). These are represented in black in Image C for strong edges and white for weak edges. These edges were then used to obtain local thresholds around the contour of the bone. The subsequent step utilised the CT number of each voxel defined as a bone edge as a local threshold value for its neighbourhood (Image D). A threshold map of the entire image was then determined using an iterative dilation of the grayscale values at these edge intensities, assigning the Gaussian weighted average of their neighbours to these border voxels. This resulted in each voxel having its own unique threshold value. Those voxels which were greater than the local threshold values were then labelled as bone.

This algorithm does appear to be more computationally laborious. However, modern hardware and software will allow for faster processing. Waarsing [47] reported almost identical results using these local thresholding algorithms when comparing their image processing results to histology, with Burghardt [48] validating HR-pQCT results with the use of concurrent μ-CT imaging. Their goal was to delineate the individual trabeculae within the image, made possible as a result of the high resolution of the scanners used in both studies (trabecular thickness 0.04 to 0.25mm [54]). With standard pQCT however it is not possible to identify individual trabeculae as the limited resolution of the scanner does not enable this separation (Stratec XCT 3000 pQCT voxel size 0.2 to 0.8mm). The key limitation of this method however, is the choice of two thresholds which define both the strong and weak edges required. Waarsing defines these thresholds using trial and error, whereas Burghardt determines theirs automatically for each image using a histogram of the gradient magnitudes. Again, ultimately a decision between a fixed or variable threshold value will still have to be made.

An alternative way of identifying the boundaries in an image is to use contour detection. This differs from edge detection in that it identifies objects or regions in an image which have salient features, using local or neighbourhood information in the image to assist its definition, as opposed to simply identifying any variations in gray-scale intensity. Contour detection for bone segmentation in Computed Tomography has been explored by Klotz *et al* [55] and Ma & Overton [56], both of whom use anatomical spatial coordinates within the 3D data set to assist their algorithms. Klotz automatically selects two anatomical landmarks within the spinal vertebrae. Using these landmarks as an anchor, contour mapping is used to define an automatically adapted ROI delineating the inner cortical wall. Edge points are determined over a range of degrees from the Centre of Mass (COM) within the spinal canal. Similarly, Ma uses the spatial coordinates of the bones' COMs to carry out a radial fan search (Figure 2.3, © 1991 IEEE [56]) to separate the bone of interest from surrounding features, in particular removing smaller adjacent bones such as the fibula or the ulna. Cross-correlation and

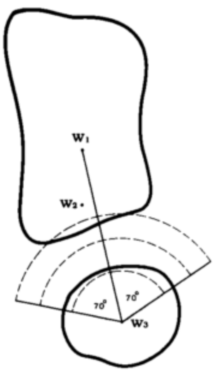

Figure 2.3: COM radial search for image edges, Ma *et al*

mathematical morphology are then used to determine the outer contour of the remaining bone. Klotz reports a success rate of better than 90% (n=822), but with the caveat that this figure was produced from a database of normal subjects. They also commented that the majority of the manual interactions required in the remaining 10% were to assist the algorithm in finding the global starting point. Ma reported an even better success rate, with only 2% of subject images requiring manual interaction (n=1251), with trabecular densities calculated using the automatically generated ROIs giving comparable results to those delineated manually.

From this small sample of contour detection references applied in the segmentation of bone from its surrounding structures, contour detection has been demonstrated to be relatively successful in this task. In addition, when the goal is to segment out individual trabeculae within higher resolution images, the extra computational investment necessary to perform contour detection with local thresholding would appear to be worthwhile. Methods which automatically determine anatomical landmarks to guide their contour detection are also not reliant on pixel-value thresholding to locate approximate positions of bones within the image field.

One of the main challenges the authors have noted with these methods is the effect noise has on the success of the contour detection. Also, in studies where there is substantial bone loss to a degree where attenuation coefficients are of a similar value to the surrounding soft tissue, these methods could potentially struggle.

2.2.3 Morphological Segmentation

The final segmentation method discussed in this review uses mathematical morphology. This is a tool which focusses on shapes and structures of objects, and can be used to describe the shapes or regions which include boundaries. It is a method which uses small sub-sets of images called structuring elements which are used to probe the image under investigation for properties of interest. Morphological analysis has been used extensively for image segmentation and analysis [57] and the segmentation of bone from soft tissue using pQCT is no exclusion. Automatic segmentation methods have been presented by Rizzo *et al* [50, 58] and Buie *et al* [49] to name two, and is also often used in conjunction with other methods (e.g. with the previously discussed Ma & Overton [56] used morphology to open and close their contour defined edges as a smoothing mechanism). The morphological approaches to bone segmentation proposed by both Buie *et al* and Rizzo *et al* are very similar, with Rizzo segmenting pQCT images of femoral neck and Buie using higher resolution QCT human and animal data from the tibia and radius. The primary steps in this segmentation technique are described as follows, using, as an example, a visual representation from [50] given in Figure 2.4:

- Gaussian smoothing and thresholding (combinations of automatic and fixed threshold values)
- Combinations of morphological dilation, erosion and connectivity operations to obtain segmented cortical and trabecular bone

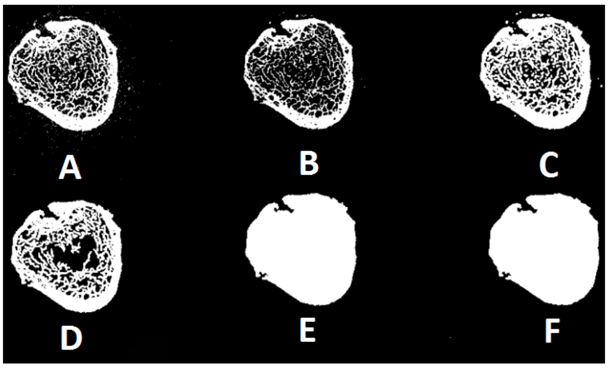

Figure 2.4: Extraction of bone regions using morphology, Rizzo *et al*

The six images in Figure 2.4 (© 2008 IEEE, [50]) are A) image thresholding and binarisation; B) erosion; C) dilation; D) deletion of small groups of connected pixels; E) filling and F) opening. This sequence of operations does successfully segment the bone from surrounding tissue, using relatively straightforward morphological operations. Its success however is also attributable to user defined thresholds as well as the size and shape of the structuring elements used to perform the openings and closings. These were determined through trial and error and consequently are a best fit for the imaging conditions used and bone under investigation.

2.2.4 Segmentation Summary

There are many methods available which can perform image segmentation. This section has touched briefly on thresholding, contour detection and morphological segmentation, primarily because these three methods appear to be the most commonly used in the segmentation of bone from surrounding soft tissue structures in pQCT. The final decision on which is the most appropriate will therefore depend upon the resolution and noise within images being segmented; the aim of the segmentation; the necessary accuracy, complexity and speed of the algorithm; and the patient group under investigation.

2.3 Image Registration

As one of the aims of this study is to look at localised changes in bone pattern using comparison to/with other images, registration of images will be necessary. This requires a process which brings corresponding points within images into alignment. Literature relating to image registration in the field of pQCT is scarce, with most of the publications arising from the registration of 3D HR-pQCT image data set volumes [59, 60]. Similarly, publications are also available on registration of spiral image data volumes from multi-detector high dose CT images [59, 61]. There has been no literature identified on registration of single slice pQCT images in peer reviewed journals.

By expanding the search outwith the field of quantitative CT into registration of medical images from other fields, it is evident that multi-modality registration is a particular topic of interest in both the research and clinical domain. This is carried out using various combinations of modalities such as MRI, functional MRI (fMRI), Single Photon Emission Computed Tomography (SPECT), CT or Positron Emission Tomography (PET), registering pairs of images which have been acquired from the same patient using two different modalities. These methods are often used to highlight physiologically functioning areas on anatomical images.

Additionally, the registration of inter-subject images to generate a composite model has also been widely researched, with a small number of these publications investigating bone turnover but the majority related to brain imaging [62]. As the shape and size of the organ of interest imaged across different subjects will vary, non-linear registration of these organs is required, using this co-registered data to generate a standard template. The outcome is a composite data-set which can be used for comparison with new data. One such study by Li *et al* [63], investigated localised bone turnover of astronauts who experience high levels of bone loss during their several months of space flight. All of the subjects' pre-flight CT scans were co-registered and then used to create a single composite model. This model was in turn compared to a similar composite model of the post-flight scans. The regions within the bone which had experienced the most bone loss across all of the astronauts were then able to be identified. Again this was carried out using a 3D image volume of the hip from spiral QCT images, which is a more flexible and forgiving data set for composite model generation with regards to registration, in comparison to the single slice pQCT acquisition. Taking the above information into account, this thesis will be restricted to intra-subject image comparisons for SCI and ACL single slice data acquisitions.

Consideration of the fundamental principals of registration of the images being utilised in this thesis is therefore given, referring to the original image as the **reference** image and the image undergoing the spatial transformation as the **target** image. The primary method used to change the position or shape of the images during the registration process is through the use of affine geometric transformations [64]. These methods spatially transform the location of pixel coordinates within an image, relocating them to their new position within the image. The four main transformations, demonstrated visually in Figure 2.5 using a black square and its associated transformation in purple, are (A) Translation, (B) Scaling, (C) Rotation and (D) Shearing.

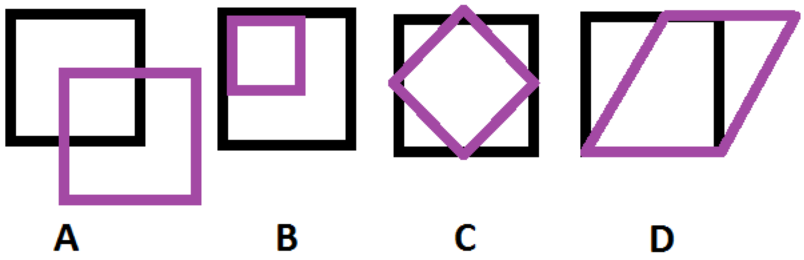

Figure 2.5: Geometric Transformations A: Translation B: Scaling C: Rotation D: Shearing

These transformations have equivalent matrix representations, the magnitude of which will vary depending on the extent of the desired transformation. Translation, scaling and rotation are linear transformations, which are global in nature and do not alter local geometric structures within the image, whereas shearing is a non-linear transformation capable of locally warping the target image to align it with the reference image. The challenge with coregistering medical images is that the specific transformation required to align one with another is unknown, and an estimate of the required geometric transformations is necessary. Two widely applied approaches to solving this problem are presented here. The first is using point mapping, which identifies identical points known precisely on both the reference image and the target image. The second is the use of intensity based alignment, which utilises similarity methods to compare intensity patterns within the image, either using the entire image or sub-images.

2.3.1 Feature Detection and Matching

Feature detection and matching is widely used to co-register image pairs, where two corresponding points which are present in both images are identified and then brought into alignment. Examples of these features can be lines such as roads, rivers, region boundaries or points, such as building corners or line intersections. The criteria for these features is that both images must contain these points, and they should be easily detectible and distinctive. Registration of images which contain significant detail, such as satellite images of towns or ordinance survey maps, will be quite successful with feature based registration [65, 66, 67]. A user will either manually identify identical multiple points across the two images, or preferentially, use an automated algorithm to detect salient features. In addition, the number of points identified should be sufficiently high in order to improve the accuracy of the registration. An example of two images requiring registration and their identified feature points is given in Figure 2.6[1]:

---

[1] Author's own images

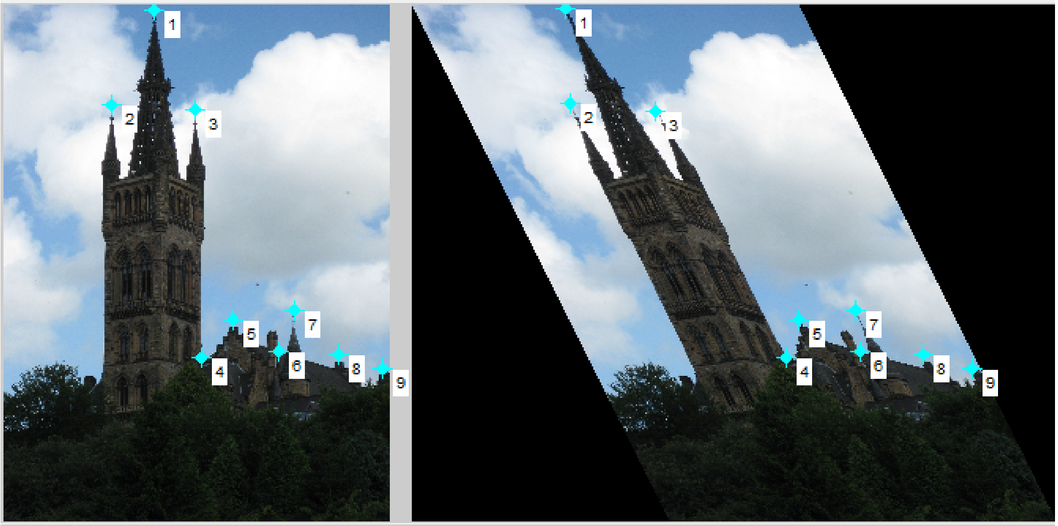

Figure 2.6: Feature pairs identified across two images prior to registration

One of the challenges with using a feature based method for registration of medical images is that these images often do not contain the level of detail required to specify multiple feature points. This is of particular relevance to pQCT images of bones in the appendicular skeleton. With the exception of the proximal femur, all the segmented images of the bones will be of a circular shape, containing no sharp edges or corners which could be used as feature pairs across images. As a result, it is almost impossible to identify pairs of anchor points in both images to be used in feature based registration either automatically or manually.

2.3.2 Intensity Based Registration

Intensity based registration can be used as an alternative to feature based identification for registration of images. This method essentially skips the step of feature identification and instead uses a correlation-based algorithm. Either areas taken from windows of data over the target image or the whole image itself are used in an attempt to match their similarity with the reference image [65]. It is a combination of performing geometric transformations and measuring the degree of similarity between the two images. This technique is generally used for images which are misaligned by small rigid transformations, with the majority of authors using cross-correlation as the measure of similarity between the reference and target images [66, 65]. Further details on other available similarity measurement methods are not provided here, but have been extensively reviewed by Penney *et al* [68]. These authors did report, however, that all of the six similarity measures compared (including cross-correlation) performed well in the application under investigation.

Firstly an assessment on the most appropriate types of geometric transformations for the two subject groups in this thesis will be made. This will be followed by how to best apply similarity measurements to these transformations during the registration process. Cross-correlation has been selected for the similarity measure due to its widespread application in medical image registration.

Geometric Transformations

Following segmentation of the bone from the surrounding soft tissue, in order to bring two images into spatial alignment, it is necessary to apply geometric transformations to one of the images (examples given in Figure 2.5). The data to be co-registered in this thesis are from the same person and from the same slice, to the best of the scanning operator's ability. These images would be acquired either between different time points or at the same anatomical location on different limbs. This by far reduces the complexity of registration necessary to align pairs of images. Moreover, the area of interest to be co-registered is not a soft tissue organ, but bone, so comparatively is less likely to experience any significant changes in shape across the image pairs. The key assumption that is therefore proposed is that there will be no gross anatomical changes of morphology within the time-frame of the studies. Using this assumption it is possible to limit the spatial transformations during registration to a set of linear constraints, using a rigid-body model which preserves all internal angles and distances. In order to justify the exclusion of any non-linear transformations, an investigation into any changes in cross sectional area (CSA) of the bones in the appendicular skeleton in both the SCI and ACL populations which may occur post-injury will be necessary during the analysis. It is known that the SCI population experience sub-lesional osteoporosis [35, 27, 69] with studies by Coupaud *et al* [70] and Frey-Rindova *et al* [71] demonstrating that a significant portion of this loss is experienced within the first year post-injury. This would therefore raise concerns regarding the assumption that the CSA diameter remains unchanged and hence the use of only rigid transformations during registration. However, a study by Eser *et al* [33] investigating the relationship between the duration of paralysis and bone structure demonstrated that there was no significant difference between SCI mid- and end- femoral and tibial shaft bone CSAs to that of a reference non-injured population. A separate study by Frotzler *et al* [72] also found that there was no periosteal diameter changes over time in both the distal tibia and femur in the chronic SCI population. Both of these studies would indicate that bone loss predominantly occurs in the endocortial regions within these bones, with no change in the cross sectional area.

Published data on the changes in bone cross sectional area following ACL injury is limited, however a DXA study by Takata *et al* [73] did find that there was no significant difference in the regional bone area when comparing the ACL injured knee to that of the non-injured knee. Although the images used in this study were areal planar images, these findings, along with those of the SCI population who comparatively experience much more extreme immobilisation conditions, the assumption that the CSA of the ACL injured limb remains unchanged would therefore seem reasonable.

Taking all of these outcomes into consideration, these results support the use of rigid transformations of the bone during registration. Such transformations would be limited to translations and rotations, as opposed to nonlinear transformations which deform the shape of the bone. The errors that would be associated with the assumption of a fixed morphology across image pairs, would be related to those of the physical processes involved in the acquisition (e.g. variations in x-ray photon flux) and reconstruction methodology, both of which may introduce artifacts into an image, as well as the ability of the operator to acquire the same slice either longitudinally or contralaterally (intra-operator variability). As these sources of error cannot be avoided, the registration will therefore be a best possible fit within the practical constraints of the study.

Similarity Measurement

To measure the strength of the similarity of two images undergoing registration transformations, a measure of correlation is required. Cross-correlation was one of the first cost functions used for image registration [74] and is a quantifiable measure of how similar two images are. The aim is to maximise the value of this cost function by varying the spatial transformations until such a point where the images are appropriately co-registered and the measure of correlation cannot be improved upon any further. A simple but useful algebraic representation of this definition is given by Pluim *et al* [75], who state that for two images A and B, their registration can be defined as the search for the geometrical transformation(s), T, that maximise the registration measure M such that

$$arg \max M(A, T(B)) \tag{2.1}$$

where $arg(x)$ is defined as the return arguments of x, which in this case are the transformation(s) T. In other words, registration is a combination of both geometric transformations and a similarity measure performed iteratively until such a time that the correlation of the two images is maximised.

Take for example two images of the distal tibia acquired at two different time points post-SCI in a subject known to experience bone loss. The correlation cost function would compute the normalised product of pixel values at the same location within the images to be registered [76]. The problem which therefore exists with this particular methodology is that the bone density of the pQCT image pairs taken from the these SCI subjects is expected to to be different. A measure of similarity at identical pixel locations would therefore be very challenging for images which will be changing with time. An alternative approach would be to eliminate the influence of any changes in pixel density which may occur across the image pairs by taking a binary mask of the bone. This instead could then be used for the registration. As it would no longer be performing a measure intensity based correlation *per se*, it would rely solely on the shape and area of the bone as the only parameters used to determine registration. As previously stated, there are no expected significant changes in CSA across the image pairs, this will result in a minor modification of the registration process to that of two binary image comparisons.

The choice of registration technique is therefore to use the latter methods, as opposed to feature based due to there being no obvious prominent features in the pQCT images of the bone which can be used as anchor points. However Zitová and Flusser [65] do raise awareness of the limitations of this method. The first, which has been discussed already, is that the reference and the sensed image must have some measure of gray-scale similarity. Secondly, if using area based methods, only shift and small rotations between images are permitted. This is a result of the large computational load and complexity associated with performing more exaggerated translations. Despite these limitations, the correlation registration methods are still widely in use. The simplification of the image to that of a binary image would reduce the computational load necessary, which in combination with good intra-operator variability should also minimise the level of complexity required.

2.3.3 Image Re-sampling

The final step in the process is to apply the registration transformation measurements calculated using the binary images to the original gray scale image data and to choose an appropriate type of resampling technique. Resampling is necessary following registration in order to determine intensity values for pixels locations which had not previously corresponded to the image grid. This is achieved by interpolation of surrounding pixel values which are within the vicinity of this point to generate the new gray scale value for the non-grid point. The choice of image resampling technique is a trade off, once again between computational complexity and increased accuracy [76, 65, 77]. In most cases the nearest-neighbour or bilinear interpolation are sufficient and relatively fast to implement. Parker *et al* [77] discuss the practical application of the nearest neighbour interpolation, stating that from a computational standpoint, it is the easiest algorithm to implement, shifting the original data to its new locations, while maintaining the magnitude of the pixel value. They did state however that the nearest-neighbour algorithm is not suitable when it is necessary to preserve sub-pixel image relations. As the resolution of the images acquired from the pQCT scanner is not high enough to distinguish individual trabecular struts, this is not a primary concern.

There are many other methods which could be used for image resampling, with Parker *et al* providing an excellent comparison between five of these techniques [77]. As the pixels across co-registered images will not be compared on a one-to-one basis, but over groups of local pixels, the nearest neighbour algorithm will be used in this thesis for pixel interpolation.

2.4 Post-Processing

So far this appraisal of the literature has focussed on how best to manipulate the original raw image data into a format such that further analysis can be carried out. Assessment of these pre-processing steps is an important part of the research and development necessary for this thesis. However, in addition to this, it also proposes additional post-processing methodologies. Specifically, those which can be used to extract further information from pQCT images of the two SCI and ACL studies. The aim of these post-processing techniques is to extract additional information relating to these groups' bone turnover, as well as assisting and providing guidance on more targeted rehabilitation. It would therefore be interesting to review existing published post-processing techniques applied to the field of bone turnover and osteoporosis in pQCT and related modalities. In doing so it will be possible to identify how these can be taken forward and developed in the assessment of localised and global BMD changes in these two groups of interest. The post-processing methodologies published can be categorised into two different groups - those which provide a global description of the bone changes, using all of the trabecular information to describe the bone pattern, and those which present a more localised assessment of bone changes, identifying particular regions within the bone itself which may be experiencing more significant changes than others.

2.4.1 Global Descriptors

In the field of bone imaging, the use of medical images as a non-invasive tool in the diagnosis of osteoporosis and other bone related diseases has generated a lot of interest in the computer vision research community. In particular, texture analysis has been extensively utilised as a means of describing the global pattern of pixel intensities and their locations relative to each other to assist in these diagnoses. Texture analysis is a descriptive technique which provides information about the properties of an image such as smoothness, coarseness and regularity. It ranges from determining first order statistical moments from the image histogram (such as mean, variance and skewness), which carry no information relating to the relative position of the pixels, to higher order statistics which consider both the distribution of intensities and their positions relative to each other. It is with these so called textural moments that researchers have demonstrated their use in providing supplementary information on bone patterns, in addition to the now well established global measurement of BMD. This is because these textural moments provide information on the bone microarchitecture, an additional factor believed to contribute to the risk of osteoporotic fracture [16, 78]. Lespessailles *et al* [79] carried out a cross-sectional multicentre study investigating the clinical interest of bone texture analysis in the assessment of osteoporosis. The study was conducted across three different centres and used a combination of both BMD measurement, obtained using a new high resolution 2D X-ray device, and selective texture parameters to assess the fracture risk of post-menaupausal women. They reported that using this new imaging device, specifically optimised to capture bone microarchitecture for the calculation of textural moments, combined with the BMD measurement, they were able to improve the prediction of fracture risk. Other similar studies have also found that texture analysis of bone images provides a useful contribution in the assessment of bone integrity [80, 81, 82, 83, 84, 85]. These results suggest that the diagnosis of osteoporosis using a measurement of bone strength by global BMD alone, although considered to be the gold standard, can also be supported further by an assessment of microarchitectural structure, as it too is a very relevant contributor to the overall bone integrity.

One of the major drawbacks to using texture analysis as a means of describing image patterns, is that the number of textural parameters which can be calculated for one image can be extremely large. Operators consequently need to identify which of these parameters either on their own or in combination with other parameters are useful in the classification of the bone into the correct etiology. The challenge of performing this feature reduction as well as developing a classification algorithm, for example using neural networks, is a complex process requiring large amounts of training data to be available for each of the different bone conditions which the operator wishes to identify. Despite these challenges, the use of these textural features for the assessment of pQCT images is potentially an avenue which could be explored, if only on a preliminary basis in this instance due to the small subject numbers available.

2.4.2 Local Descriptors

Where global image analysis aims to categorise entire image patterns, the natural extension to this is to look at localised regions within the bones themselves in more depth. Global post-processing descriptors make the assumption that any bone conditions or trabecular patterns detected are present across the entire image slice or volume. This may not necessarily be the case, as for example certain injuries may result in an altered weight bearing load on the bone, changing the trabecular bone patterns in one area preferentially over another. Frost's mechanostat theorem proposes that bones will respond to the forces exerted on them, therefore if, for example, an SCI subject experiences a high frequency of leg spasms originating from a particular muscle group, a possible consequence of this may be localised bone changes at the sites of the tendon insertions for that group. Current literature looking at localised bone changes from pQCT images focusses on dividing the image into different sections or quadrants, such as anterior, posterior, medial and lateral. These have already been introduced briefly in Chapter 1, with Boyd *et al* [13] and Bayer *et al* [30] investigating regional changes in the knee following ACL injury and similarly Dudley-Javoroski & Shields in the SCI population [40]. Additional studies assessing localised bone changes in pQCT & QCT images include following bed rest and recovery [86], assessment of ibandronate therapy in postmenopausal osteoporosis [87] and investigating regional differences in the femoral cortical shafts of postmenopausal

women [88] to name a few. As the preceding authors have all observed localised differences within the bone, it would therefore seem prudent to carry out a similar assessment of regional changes within the two subject groups within this thesis.
Expanding on this, in a similar fashion to identifying active voxels within PET images and fMRI brain maps using SPM (statistical parametric mapping) first introduced in the early 90's by Karl Friston [89], voxel-by-voxel analysis has been performed by Li *et at* [63, 90] and Zhao *et al* [91] who have looked at identifying regions within bone which have experienced statistically significant changes in BMD. Both authors perform a registration of 3D volumes of the hip generating a common reference space. They acquired images taken from astronauts pre- and post-spaceflight as well as those who had recently experienced hip fractures (<48hours), and applying voxel-by-voxel analysis, identified regions or 'clusters' of pixels which have experienced significant changes in BMD, as shown in Figure 2.7 (Reproduced with permission of Springer Netherlands in the format use in a thesis/dissertation via Copyright Clearance Center, [91]).

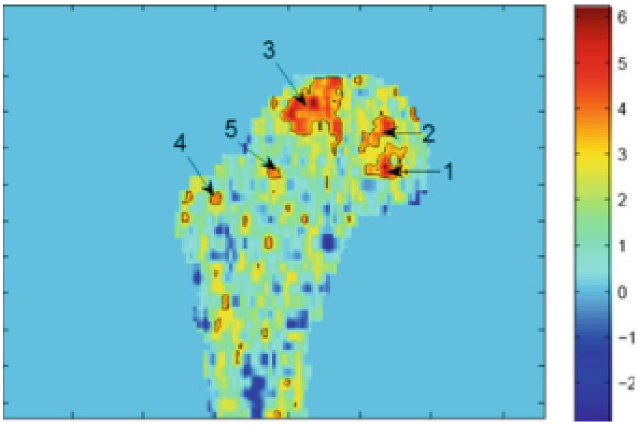

Figure 2.7: t-statistic intensity image of bone changes in 16 astronauts pre- and post-spaceflight, Zhao *et al*

Although this type of localised voxel mapping has been extensively researched in brain imaging, the application in assessing bone turnover is quite novel, and would appear to be currently limited to these listed papers. There is therefore an opportunity to use a similar method adapted to quantify and map localised bone changes in the first instance between pairs of pQCT images.

One final tool which has been used to extrapolate structural information from digital images which has already been introduced in this review, is mathematical morphology. This method is focussed on descriptions of the shapes and geometric structures contained within an image. Granulometries are one such application of mathematical morphology, which iteratively quantifies the number of structures of different sizes within an image. This generates an image signature based on the shape and size of these structures within the image, with many publications using such a technique to classify images [92, 93, 94, 95]. The application of morphology in bone imaging has also previously been investigated, for example Sakurai *et al* [96] extracted skeletal patterns from MRI bone images using skeletonization as a means of assessing bone structure and quality, and Chen *et al* [97] classified trabecular structure in MRI images using morphological granulometries. Exploring the latter paper further, the authors used a concept defined by Dougherty *et al* [98] called **local** granulometric size distributions. As the name would infer, this technique can be used to classify local windows of pixels based on the structures within those windows and Chen quite successfully applied this to the classification of bone patterns. Indications that coarse structural bone patterns are present even within the healthy population were identified by Cervinka *et al* [45] ($n = 25$) during their pre-processing analysis, who identified different clusters of BMD values in pQCT images of the tibia. As the shapes and structures within the bone images of the ACL and SCI subjects are expected to change following injury, it would seem to be a reasonable assumption that any measure of these structures, using morphology for example, will provide additional information on the localised patterns of bone loss these subjects may be experiencing. The application of granulometries to describe voxel patterns within pQCT images has the potential to provide this information and once again is an avenue which has not yet been explored using pQCT data.

2.5 Areas of open research

An excellent opportunity has been identified to develop post-processing techniques for pQCT images in the assessment of bone turnover. In particular, localisation and quantification of these processes within the bone would appear to be a current topic of interest with authors. To date, any post-processing of medical images in the field of bone densitometry have primarily been developed in imaging modalities which are currently used clinically, such as MRI or spiral CT, and not pQCT. There is however, the potential for pQCT to have its own unique role in diagnosis and rehabilitation of certain patient groups with the assistance of image post-processing.

The data-sets available for analysis using these post-processing methodologies are also unique within themselves. Assessment of bone changes within the first year post-SCI, both locally and globally, will provide a unique insight into the bone processes occurring during this critical period of bone loss. Additionally, imaging the knee using pQCT following ACL injury has only previously been reported in canines. Post-processing of these images will therefore generate novel quantifiable data which could potentially be of value in both the clinical and research domains exploring bone mass and microarchitecture.

2.5.1 Study Aims

The aims of this study will be to develop pQCT image pre- and post-processing techniques for the assessment of bone turnover in the SCI and ACL injured population. This will be performed in the Matlab® environment. The design of these techniques will also be applicable for use in any future imaging studies using pQCT.

Firstly a suitable pre-processing algorithm to segment the bone of interest from its surrounding structures will be developed using the current literature as a guide.

Subsequently two original post-processing techniques will be investigated. The first of these will perform registration of image pairs and then consider localised changes at a voxel level. The second technique will use morphological image processing to investigate whether the patterns of trabecular bone structure within a pQCT image provide any further insight into the manner in which bone losses occur. Finally, an evaluation of the two study groups available for this thesis will be made using the new software, using these findings to draw clinical conclusions about the localised and global bone turnover processes taking place in these subjects.

Chapter 3

Image Acquisition and Pre-Processing

Image acquisition using the pQCT scanner and pre-processing are two fundamental steps necessary prior to performing any data analysis. This chapter will provide a very brief introduction as to how the scanner creates these images, as well as the acquisition parameters used in both the SCI and ACL studies. It will then describe the pre-processing applied to the images. As outlined by many of the papers referenced in Chapter 2, this involves the segmentation of the bone of interest from its surrounding structures. The decisions on the most optimal methods used to perform this are discussed and tested here, using the standard manufacturer's segmentation software as a means of assessing the novel algorithm developed for this study.

3.1 pQCT Image Acquisition

A pQCT scanner uses X-rays to produce tomographical images of the appendicular skeleton. It relies on the attenuation of the X-rays as they are passed through the body to depict the patient's anatomy. An exponential relationship exists between the incident number of X-ray photons to those which have transmitted through an object, described using Equation 3.1

$$I = I_0 \exp^{-\mu x} \tag{3.1}$$

For an incident number of photons I_0 passing through a material with a linear attenuation coefficient of μ and thickness x, there will only be I photons transmitted to the detector. The linear attenuation coefficient in cm^{-1} is the probability of photon attenuation through a material of a certain density using X-ray photons of a specific energy. The X-ray image is created by the detection of the transmitted X-rays, I, which have passed through the body. Variations in attenuation as a result of different organ densities present within the field of view are represented by different gray-scale values in the image.

Planar X-ray machines transmit photons from a single projection through the patient, generating an image composed of the attenuation of organs superimposed on each other. Computed tomography, however, transmits collimated X-ray photons from different projections around the patient. The X-ray tube is rigidly linked to the detector on the other side of the patient, and as they both rotate around the patient, measurements of X-ray transmission at each angle are made by the detector [99]. The information contained within the attenuation profiles through the patient at each angle can then be reconstructed using algorithms such as filtered back projection (FBP). This algorithm determines how much attenuation is present at each *voxel* location within each rotational slice. The convention which exists is to replace the attenuation coefficient for each voxel in the reconstructed matrix with its equivalent Hounsfield Unit, HU (CT number relative to water).

The pQCT scanner used to acquire the images for this thesis was the XCT 3000 (Stratec Medizintechnik, Germany) shown in Figure 3.1, located at the Queen Elizabeth National Spinal Injuries Unit, Southern General Hospital in Glasgow. The technical specifications of this scanner are given in Table 3.1 (Stratec Medizintechnik [21]).

Figure 3.1: XCT 3000 pQCT Scanner (Image courtesy of the CRE, University of Glasgow)

It also has the ability to convert the HUs of each of the voxels to bone density values. This is achieved by calibrating the scanner using a hydroxyapatite (HA), bone equivalent material phantom of known concentration. A conversion equation applied across the image will convert the image in HUs to the corresponding image in mg/cm^3. The manufacturer supplied the conversion specific to this scanner and is given in Equation 3.2, where HUIm is the Image in HUs and BMDIm is the image in mg/cm^3.

$$BMDIm = (HUIm \times 1.495) - 341 \tag{3.2}$$

This equation only takes the mineral portion of the bone into account and all voxels, including

High Voltage	60kV
Anode current	<0.3mA
Mean X-ray energy	42keV
Detectors	12 semiconductor detectors
Slice thickness	2.3mm
Voxel size	0.2-0.8mm
No. of projections	180
Scan time	6-15s per translation
Effective Dose	<2μSv

Table 3.1: XCT 3000 pQCT Technical Data

soft tissue structures surrounding the bone, are converted to HA equivalent densities. Unlike some other pQCT scanners, the Stratec XCT 3000 is calibrated with respect to fat which is set at 0 mg HA, so that water results in 60mg HA.

The scanner comes with its own software which can calculate a wide variety of parameters, including total BMD, trabecular BMD, bone CSA, muscle CSA and Stress Strain Index. Each of these measurements can be obtained using default software parameters, with the option for the user to intervene if these algorithms fail. Default thresholds for segmentation are pre-programmed into the scanner, however users can also set their own thresholds based on the specific application.

3.1.1 Acquisition Parameters

The pQCT images in this thesis are used to investigate the regions of high trabecular bone mineral density in the long bones of the lower limbs. The slices of interest used for this analysis were consequently those located at the 4% distal femur and tibia (distance 4% of the total length of the femur/tibia from the distal epiphysis) and the 2% proximal tibia. A visual presentation of two of these anatomical locations is given in Figure 3.2 (Edited from [14]).

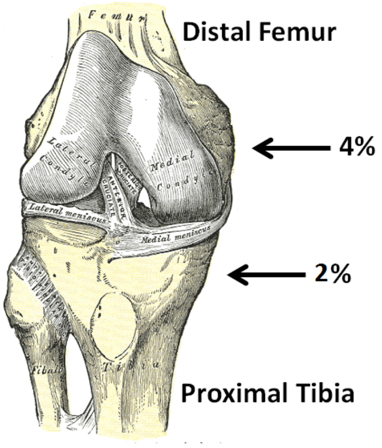

Figure 3.2: 4% distal femur and 2% proximal tibia scan locations

The length of each subject's tibia was measured from the distal end of the medial malleolus to the medial joint cleft, with the length of the femur taken to be equivalent to that of the tibia. AP scout scans were acquired at the distal femur, proximal and distal tibia, from which the operator placed reference lines at the ends of the long bones. With the reference line defined, the acquisition software could automatically locate the 4% distal and proximal slices within the bone epiphyses. The acquisition parameters used for both SCI and ACL tomographic slices are given in Table 3.2 below

Study	Slice	Slice Thickness	Voxel Size
SCI	4% distal femur	2.4mm	0.303mm^2
SCI	4% distal tibia	2.4mm	0.5mm^2
ACL	2% proximal tibia	2.4mm	0.5mm^2
ACL	4% distal femur	2.4mm	0.5mm^2

Table 3.2: pQCT Acquisition Parameters

The pQCT scanner reconstruction software uses a FBP algorithm, which combines all of the attenuation profiles from different angular positions to generate the cross sectional image of the original object. The images were exported from the scanner in comma-separated values (CSV) format, the only format available which did not compress the image data. The CSV file stores data in a tabular format, and in this case records the CT number of each voxel within the image. The CSV files were then imported into the Matlab software analysis package, with the first step in the image pre-processing algorithm converting these values in Matlab to their bone equivalent densities, using Equation 3.2.

3.2 Segmentation

Chapter 2 introduced several of many different methodologies used to segment bone from its surrounding soft tissue structures. These vary from defining a fixed threshold applied to an image histogram to more computationally complex combinations of thresholding, edge detection and morphology. Despite being more complex, it was noted that it was still necessary for authors to define a threshold value at some stage in the algorithm. These thresholds were chosen based either on previous literature recommendations, through trial and error or using a variable threshold which adapted to the pixel densities of each individual image. A review of the acquisition parameters, subject limitations and computational complexity versus time cost applied to the images under investigation in this thesis will guide the choice of a suitable thresholding technique for the pre-processing algorithm. Factors for consideration include:

- Due to the limited resolution of this scanner, the boundaries between cortical and trabecular bone cannot be reliably delineated at these epiphyseal sites.
- Individual trabecular struts cannot be delineated due to the limited spatial resolution.
- Although operators are highly skilled in patient positioning, intra-operator errors will still influence the accuracy of slice placement.
- Each SCI subject will have 2 images at 4 time points, which will ultimately result in a large volume of individual images for analysis within this group.
- There will be a wide range of bone density values in the images. The BMD in the SCI group is expected to change significantly over time, with the ACL injured legs also expected to differ in BMD compared to the control legs.
- Some form of user interaction should be available for segmentation of the more challenging images, for example when soft tissue and bone pixel BMD values are comparable or when small adjacent bones are not removed automatically.

The proposal to use a variable threshold over a fixed threshold for these two subject groups would appear to be appropriate as a result of the differences in BMD expected. Justification of this decision can be made through good software validation, performed in Section 3.4. Due to the potentially high number of images under analysis, the time cost should be kept at a minimum but without sacrificing accuracy of the bone segmentation from surrounding soft tissue. Combining a variable thresholding technique with image histogram segmentation was therefore determined to be a suitable solution.

For completeness, edge detection and morphology techniques were also tested during the preliminary investigations into an appropriate segmentation technique. The main challenge to the success of the edge detection methods was that in regions where the bone density was low and hence very similar to the surrounding soft tissue, the software failed to join up the primary edges of the bone. This can be visualised in the broken femoral outline in Figure 3.3a. For this technique to work, the user had to specify through trial and error specific thresholds for each image, which ultimately did not comply with the specification of an automated algorithm. Alternatively, performing segmentation using morphology using a combination of thresholding, dilations and erosions, it was possible to segment out the bone from surrounding structures, however again, user interaction to define the threshold and optimum size and shape of the structuring elements for each image was necessary. Figure 3.3b demonstrates why this process could not be fully automated, as areas of low bone density within the bone have not been identified. Additionally, the outline of the bone was defined by the shape of the structuring elements used.

(a) Edge Detection using Sobel Filter

(b) Segmentation using Morphology (binary mask)

Figure 3.3: Edge detection and morphology techniques for segmentation

The algorithm developed using an automatically calculated variable threshold was the most successful and is described in detail in the subsequent sections in this chapter. As a consequence of using a variable threshold histogram segmentation in images where additional small bones were also present, but not of interest in the final analysis (e.g. patella or fibula), an additional step was necessary to remove these bones. A topological segmentation method using morphology is therefore presented here for this purpose. Finally, the outline of the segmented bone image was cleaned up, removing the voxels at boundaries which were a result of the partial volume effect.

3.2.1 Histogram Segmentation

A digital image can be thought of as a matrix of numbers. In the gray-scale pQCT images of bone imported into Matlab, each of these numbers represents BMD equivalent values in mg/cm^3 as demonstrated in Figure 3.4 below.

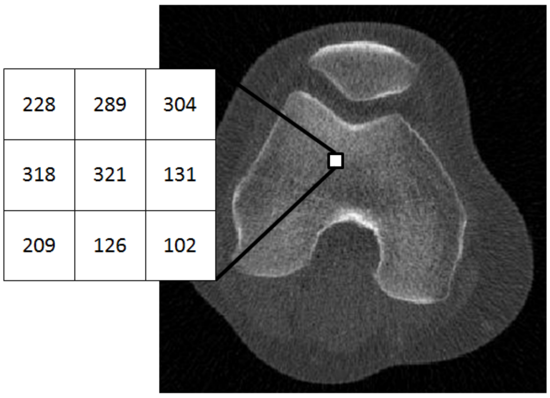

228	289	304
318	321	131
209	126	102

Figure 3.4: Digital image demonstrating matrix representation of voxels

From this matrix of numbers, a distribution plot of the image intensity levels was produced which is known as the image histogram, with the frequency of each intensity value within the image plotted on the histogram. An image histogram is one of the fundamental tools used in image processing, representing the information within the image in a more manipulatable format and as a result is used extensively in segmentation. Histograms of the pQCT images contained distinct regions, or modes, which can be grouped together to represent different components of the image such as background, soft tissue and bone.

The first step in the pre-processing software was therefore to generate a histogram of the imported images in a format which can be used for automatic segmentation. As a result of the large amount of statistical noise present within the image, a 12x12 Gaussian smoothing filter was used on the image prior to this. This is a well documented step authors use to improve signal to noise ratio prior to segmentation [64, 100]. This pre-processing algorithm will be demonstrated using the 4% femoral slice shown in Figure 3.5a, with its associated Gaussian Smoothed image given in Figure 3.5b.

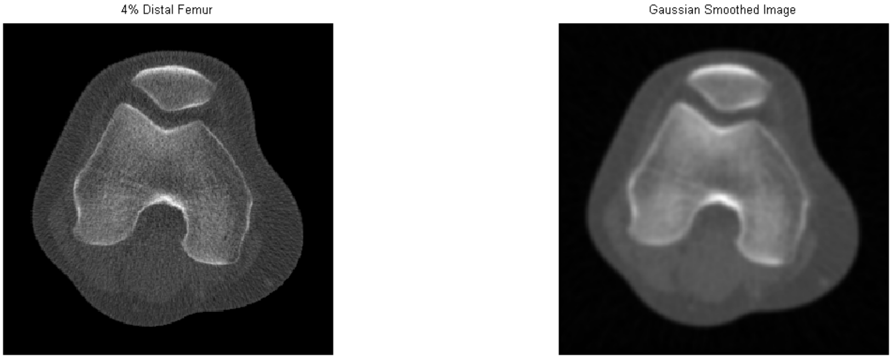

(a) Original Image

(b) Gaussian Smoothed Image

Figure 3.5: Original and Gaussian Smoothed Images

Using this Gaussian smoothed image the second step was to produce the image histogram,

Figure 3.6a (y-axis cropped for improved histogram clarity). On first visual inspection it is possible to identify a background mode (approx. 0-50mg/cm^3), a soft tissue mode (approx. 50-100mg/cm^3) and a bone mode (approx. >100mg/cm3). However, despite the Gaussian smoothing, the histogram is still quite noisy. In order to automatically detect the image specific threshold where the soft-tissue mode ends and the bone mode begins, a calculation of the bone density where the gradient of the histogram slope changes from negative to positive has to be made. Taking the first derivative of the histogram was a suitable means of identifying these locations on the graph, using the density value at zero crossing between the gradient change from soft-tissue to bone as threshold. The histogram in its current format, however, was too noisy, therefore it was smoothed using a shifting Finite Impulse Response (FIR) filter (N=10), making the distinct modes easier to identify (Figure 3.6b). The first derivative of the smoothed histogram was then taken, Figure 3.6c, plotting the rates of change of each of the main modes contained within the image histogram. When the filtered histogram peak changes from a falling slope to a rising slope, the rate of change in the 1st derivative histogram changes from a negative value to a positive value. Therefore a zero crossing from negative to positive on the 1st derivative graph would indicate the end of one mode and the start of a subsequent mode. The zero crossing of interest in this segmentation algorithm was the end of the soft tissue mode and the start of the bone mode. It is the BMD value at this location that was therefore used as the image threshold to segment the bone from the soft-tissue and background voxels.

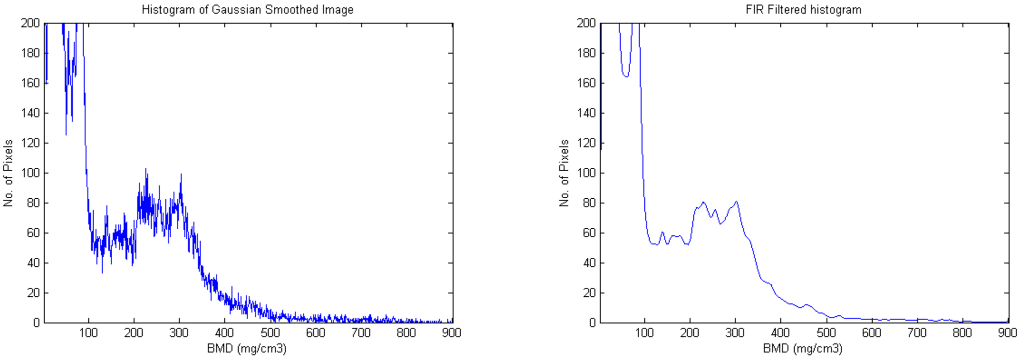

(a) Gaussian smoothed image histogram

(b) FIR filtered histogram

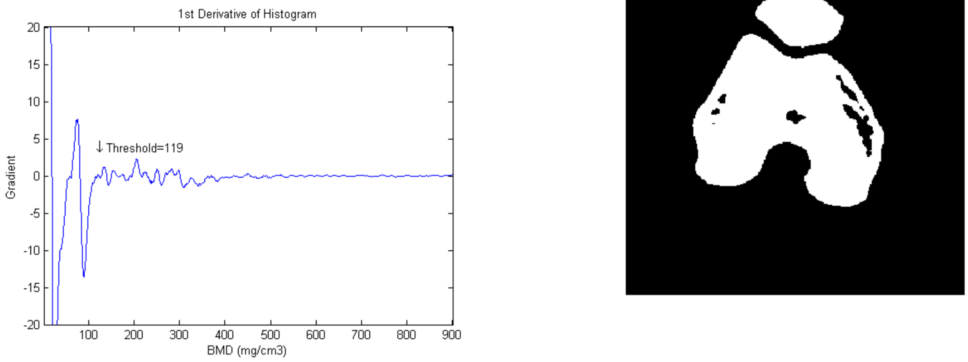

(c) 1st derivative of histogram

(d) Segmented binary image

Figure 3.6: Automated Segmentation Workflow

This proposal seems relatively straight forward, however on closer inspection of the 1st derivative graph in Figure 3.6c, there are several zero crossings transitioning from negative gradients to positive gradients. As a result, it was necessary to restrict the window of acceptable zero crossing values to the region where the soft tissue to bone boundary was expected to be found. Ruegsegger & Kalender [101] examined the distal radius of several hundred adults during the development of the European Forearm Phantom. Their results showed that close to 90% of all measurements had trabecular bone densities in the range of 50 to 200 mg/cm^3. Using this range as a guide, the first zero crossing from negative to positive which occurred at a BMD $>$ 100mg/cm^3 was used. This cut-off point was determined empirically using different tomographical slice locations as well as challenging images containing extremely low BMD, with further details on the validation of this value given in Section 3.4. The threshold calculated for the current example was 119mg/cm^3, as indicated in Figure 3.6c. Once the automatically calculated threshold, T, was determined, a binary mask was generated containing only those pixel values greater than this threshold. Any voxel value $f(x, y)$ above this threshold in the masked image $m(x, y)$, has a binary value of 1, otherwise it is set to 0:

$$m(x,y) = \begin{cases} 1 & \text{if } f(x,y) > T \\ 0 & \text{if } f(x,y) \leq T \end{cases} \tag{3.3}$$

The resultant binary mask for the image used in this example is shown in Figure 3.6d. It is clear that this mask has successfully eliminated the surrounding soft tissue, however it has also removed regions of BMD $\leq$119mg/cm^3 from within the bone as well. In addition to this, it has preserved the small patella bone in the image within the mask. These are both undesirable outcomes of using a thresholding algorithm, and an additional stage in the pre-processing software was therefore necessary.

The "holes" present in the binary mask as a result of voxels within the bone having BMD values less than the threshold was firstly resolved. A hole within the image is defined as a set of background pixels that cannot be reached by filling in the background from the edge of the image. A step which fills these holes was therefore necessary, using the assumption that despite being less than the automatically generated threshold, the voxels at these locations still represent bone based on their location within the image relative to other bone voxels. Assuming all of these missing voxels are contained within the bone mask, a flood fill operation was performed using the Matlab function *imfill.m* (Matlab R2010a) which converted connected background pixels (0's) to foreground pixels (1's), stopping when it reached object boundaries.

Secondly, the removal of smaller, unwanted bones which have remained in the image mask was then carried out. The areas of each unique region within the image mask were calculated using the Matlab function *bwlabel.m* (Matlab R2010a). Only the region with the largest area was preserved, with all others being discarded. The largest bone in this case, the 4% distal femur, is the bone of interest in the analysis (Figure 3.7a). A Boolean "AND" operation was then used to multiply the final mask with the original image, shown in Figure 3.7b.

(a) Mask with filled holes and patella removed (b) Image segmented using binary mask

Figure 3.7: Mask and Segmented Image

3.3 Partial Volume Effect

The final step in the segmentation process was to correct for partial volume effect. In this instance PVE occurs when a single voxel within an image contains multiple tissue values. As a voxel can contain only one attenuation coefficient, the resultant displayed value is the average of all of the attenuation coefficients contained at that voxel location, which either artificially reduces or increases voxel values at object boundaries. The PVE can consequently be minimised by reducing the voxel size within the image, however when this is not possible, a means of reducing its influence on the image measurements is necessary.

Following the automated segmentation process described previously, the PVE was visible at the soft-tissue and bone boundary. These blurred voxels contain a mix of BMD values for both cortical bone and soft tissue. In addition to this, the soft tissue component surrounding the bone also contained muscle tendons which insert into the bone. This also elevated soft tissue values as a result of the tendons' dense fibrous connective tissue. An example demonstrating the PVE at the patellar surface of the segmented image Figure 3.7b is given in Figure 3.8a, with the background voxels inverted to white for improved clarity. An additional step was therefore included into the pre-processing software to minimise the presence of blurred boundary voxels surrounding the periosteal margin. The segmented bone image was scanned inwards from the four outer edges of the image. Each voxel encountered with a BMD <200mg/cm^3 was removed. This figure was derived empirically as a lower threshold for a voxel containing cortical bone. Once a voxel was encountered which was greater than this threshold, this location was taken to be the true bone boundary and PVE thresholding for that row or column was terminated. The scanning procedure then repeated this process for each subsequent row or column surrounding the bone. This essentially concentrically thresholded the segmented bone removing soft tissue voxels until the cortical boundary was detected. The outcome following this PVE correction at the same patellar surface region is given in Figure 3.8b.

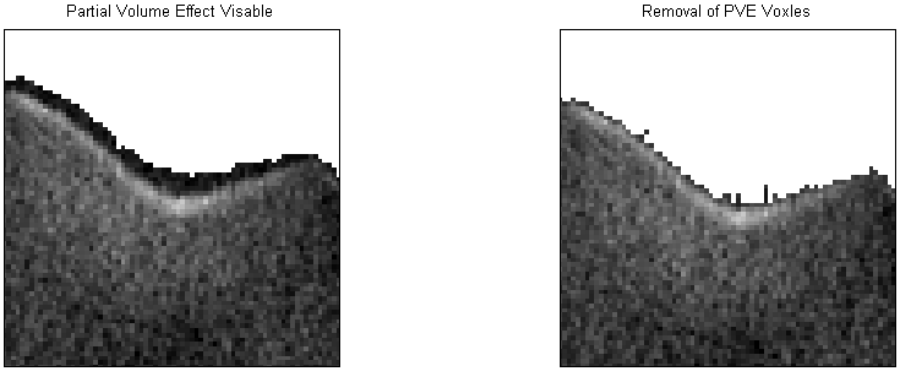

(a) PVE visible at the patellar surface of distal femur

(b) Image after correction for PVE

Figure 3.8: Correction for PVE from segmented image

This final step in the initial segmentation algorithm successfully removed the majority of the blurred boundary voxels which were contained within the original segmented image. In the more challenging cases where the cortical bone experiences significant BMD deterioration, there is an option which allows the user to modify the 200mg/cm^3 threshold so that the PVE correction does not continue past the cortical boundary.

The total BMD and total cross sectional area of the bone can now be calculated. The total BMD calculation sums the BMD values for all of the voxels present within the segmented image divided by the total number of voxels. The total CSA relies on a user input stating the voxel size of the image, multiplying the total number of voxels present in the segmented image by the area of each voxel.

3.4 Validation of Software

The existing measurement technique used to calculate pQCT image parameters is software supplied with the scanner by the manufacturer (Stratec). Only the SCI study utilised this software for analysis. For the SCI distal tibia images, a user defined threshold was chosen, which performed an initial segmentation using histogram thresholding. This then generated an outline around the perimeter of the bone. A manual modification of this outline was then carried out to create a more accurate fit for segmentation. For the femoral images in this study, the user employed a manual delineation of the femoral bone for every subject, as thresholding these images was unsuccessful. The ACL study was analysed by the author using the custom designed software developed for this thesis.

Assessment and validation of the pre-processing algorithm detailed in this chapter was therefore performed as follows:

1. A visual inspection of the segmentation as a quality control step to determine the

success of the automatic threshold selection.

2. Verification that the range of automated thresholds generated was small. This assists to justify comparisons of images segmented using different thresholds.

3. Measurement of the total BMD and total CSA calculations made by the software and compared with the Stratec technique for the same images.

For step 2, verification of thresholds, at the time of development 53 images from both the SCI and ACL study were available. The images ranged from normal BMD to osteoporotic and the automatic thresholds generated from all three anatomical locations analysed in this thesis were evaluated. From the SCI study the distal tibia and distal femur and from the ACL study, the proximal tibia. For step 3, only the distal tibia and femur images from the SCI study were used to calculate the accuracy of the novel software, as they were the only images with comparative Stratec measurements available.

3.4.1 Automated Segmentation Thresholds

As previously highlighted in Chapter 2, one of the criticisms when using a variable threshold was whether measurements taken from sequential images with potentially different thresholds could be comparable. Due to the nature of the images under assessment within the SCI and ACL groups, the use of a variable threshold does however have its benefits, as the BMD is expected to differ either longitudinally or contralaterally. Therefore, it would be appropriate to verify that the range of automated thresholds selected was small, such that comparisons could be made across images. An assessment on the range of values derived for the automatic segmentation thresholds was therefore made.

Two different types of segmentation failure were identified, requiring some form of user interaction. The first when the bone of interest had successfully been segmented out from the surrounding soft tissue, however the close proximity of smaller adjacent bones necessitated their manual removal. The second was where there was a failure to appropriately segment the bone from the surrounding soft tissue without user intervention, often as a result of extremely low BMD within the bone. Although the first failure type required manual interaction, the second type indicates failure of the automated threshold selection and is consequently the better test of the algorithm's performance. Out of the 53 images tested:

- 98% of the 4% distal tibia images were successfully segmented automatically (n=52)
- 98% of the 2% proximal tibia images were successfully segmented automatically(n=52)
- 67% of the 4% distal femur images were successfully segmented automatically(n=35)

Automatic segmentation of the tibial images was very successful, with only 1 image from each of the two distal and proximal samples not segmenting successfully. In both cases this was attributed to the partial blurring of the bone boundaries as a result of a patient movement artefact. The femoral images proved to be more challenging, with 18 images from the sample failing to accurately segment the bone from it's surrounding structures automatically. There appeared to be no obvious link between the success or failure of the algorithm with total femoral BMD as demonstrated by the box plot in Figure 3.9a. The range of total BMD values for both categories was very similar, with those that failed having a marginally lower BMD in comparison (254.7 ± 47.9mg/cm^3 compared to 283.1 ± 30.0mg/cm^3, mean±SD). On closer inspection of the femoral images that failed, localised areas of low BMD were present, as shown in the example in Figure 3.9b.

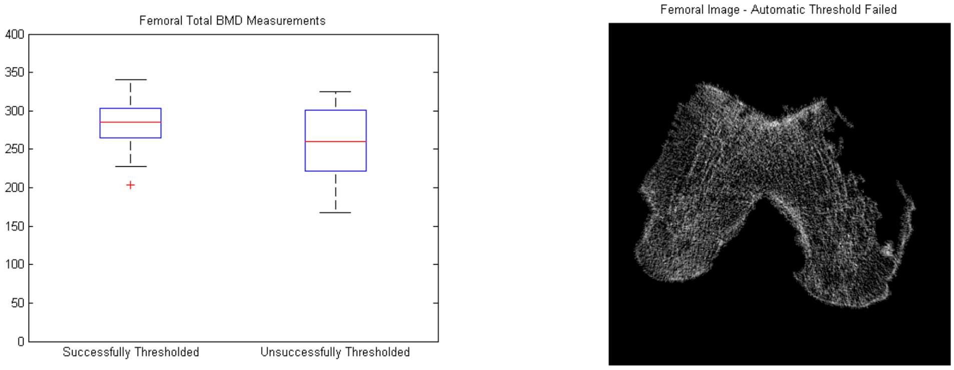

(a) Total BMD of successfully and unsuccessfully segmented femoral images

(b) Example femoral image which failed to automatically segment

Figure 3.9: Evaluation of automatic segmentation of femoral images

The cortical shell at the 4% distal location of the femur is also very thin, therefore the PI in the SCI study chose a smaller voxel size when imaging this location. The resultant finer detail contained in the femoral images, in combination with patients whose BMD was low enough to be comparable with the surrounding soft tissue, resulted in a histogram with less defined bone/soft tissue modes. Consequently, the generation of an automatic global histogram was much more challenging for these images.

The observed range of thresholds calculated for the images that were successfully segmented was

- 126.4 ± 18.1mg/cm^3 for the distal tibial thresholds,
- 113.8 ± 6.7mg/cm^3 for the proximal tibial thresholds and
- 145.7 ± 10.6mg/cm^3 for the femoral thresholds.

Box plots demonstrating this range are given in Figure 3.10, showing the median, upper and lower interquartile range values and outliers.

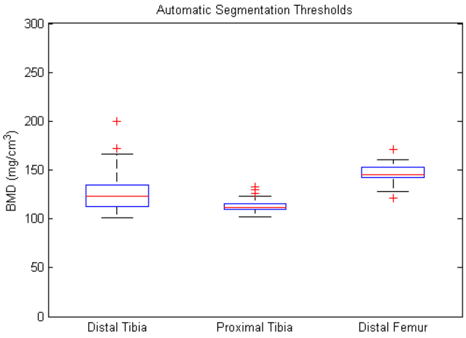

Figure 3.10: Boxplot of automatically generated segmentation thresholds

In order to assess the range of threshold values used for a given slice location, a parameter representing the breadth of threshold values was required. The breadth of threshold values were characterised using the $(mean + 2SD) - (mean - 2SD)$, i.e. 4SD. This is expressed as a percentage of available BMD values for that slice location i.e. the maximum BMD. The results are presented in Table 3.3 below.

		Thresholds (mg/cm^3)		Max. BMD Value (mg/cm^3)		
Bone	n	Mean	SD	Mean	SD	Breadth of threshold values
Distal Tibia	53	126.4	18.1	1296.8	76.2	5.6%
Proximal Tibia	53	113.8	6.7	1032.4	139.2	2.6%
Distal Femur	35	145.7	10.6	1362.3	138.1	3.1%

Table 3.3: Range of automatic BMD thresholds as a proportion of the maximum BMD

The purpose of this was to assess the use of an automatically generated threshold for each individual image. The results in Table 3.3 have demonstrated that, as a proportion of the mean available BMD values for each slice location, the range of thresholds generated is small. It is argued that this method is appropriate given the expected changes in bone density during the clinical studies. The reader must also consider other sources of variation in these studies including the errors associated with limb positioning, acquisition of the image using an X-ray photon flux which has subtle variations between each acquisition and the limitations of the resolution of the scanner. The author proposes that the relatively small breadth of threshold values indicates that the results of the segmentation of longitudinal/contralateral images would therefore be similar.

3.4.2 Assessment of Agreement

The introduction of a novel pre-processing segmentation technique will most probably generate slightly different parameter measurements compared to the existing semi-automated/manual software supplied by the manufacturer of the pQCT scanner. As the only true means of measuring the BMD within the slice would be to weigh the bone's ash *ex-vivo* being impractical, comparing the results from the new technique to the existing standard technique would be a suitable alternative. In this instance, the new Matlab measurements of Total BMD and CSA will be compared to the same measurements using the Stratec software. Although neither method will provide an unequivocally correct measure of these variables, an assessment of the degree of agreement can be made.

From the same fifty-three SCI images used previously, Stratec measurements of Total BMD and CSA made by a single operator were available for comparison. The same operator also carried out all of the SCI longitudinal scans, therefore eliminating the effect of inter-operator variability from the study. An assessment of the accuracy of the operator's positioning repeatability will not be addressed here during this assessment of the segmentation accuracy, but will be in Chapter 6 of this thesis. Comparison of the newly developed segmentation technique was made to the standard Stratec analysis using scatter, Bland Altman and percentage difference plots. Scatter plots quote the correlation coefficient for the data and display the line of equality in order to visualise the extent to which the two methods agree. Using the correlation coefficient can, however, be misleading, as a high correlation does not necessarily mean the parameter measurements are similar. A more appropriate approach of assessing the differences between the two measurements is to use the Bland Altman method, which plots the difference between the two measurements against their mean [102]. This will highlight any trends the new automated segmentation method may have in comparison to the existing method. For example, if it has a tendency to over or under-estimate parameters, or if the parameter's magnitude has an effect on the accuracy of the software. Finally, the percentage difference between the two measurements is also plotted. The purpose of this is to provide a sense of perspective of any differences in measurement as a proportion of the global measurement as a whole. What may appear to be a large numerical difference between methods, may not actually be as significant as first thought when assessed as a percentage of the overall measurement.

The results comparing the Total BMD and CSA for the 4% distal tibia and 4% distal femur measurements are presented in Figures 3.11 and 3.12 respectively. These measurements were for all 53 images, including those who required manual intervention when the automatic thresholding in the novel software failed. For each measurement, the mean difference ($\bar{d}$, green line) and the standard deviation of the differences (s, blue line) are calculated. The standard deviation of the differences between measurements made by the two methods is a good index of the comparability of the methods. Using this, it is possible to indicate on the graphs the 95% limits of agreement, where the difference between methods will be at most two standard deviations on either side of the mean for 95% of observations. Provided that the differences within $\bar{d} \pm 2s$ would not be clinically important, the new automated software could be used instead of with the existing Stratec software [103].

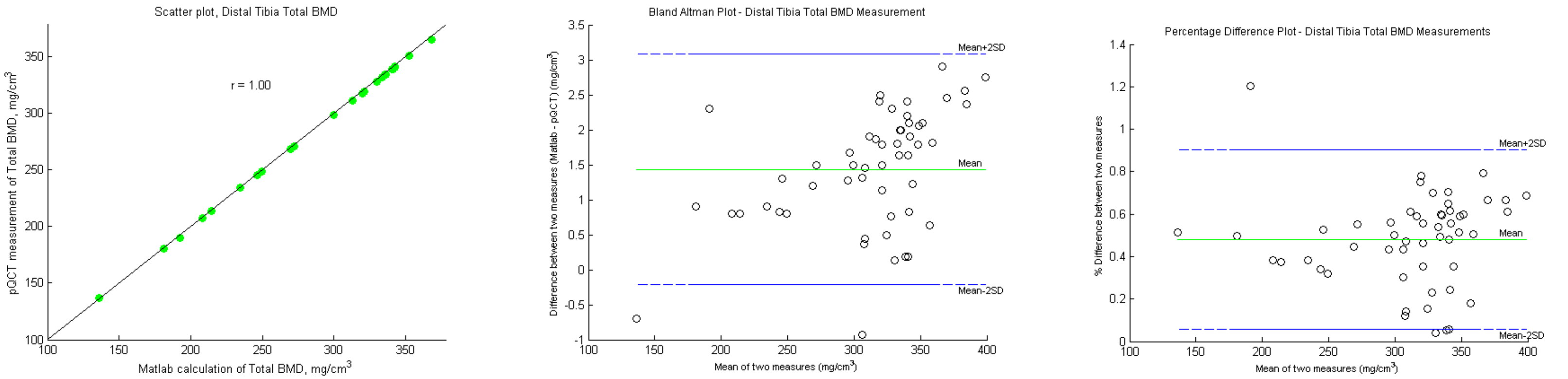

(a) Scatter Plot - Distal Tibia Total BMD

(b) Bland-Altman - Distal Tibia Total BMD

(c) Percentage Difference - Distal Tibia Total BMD

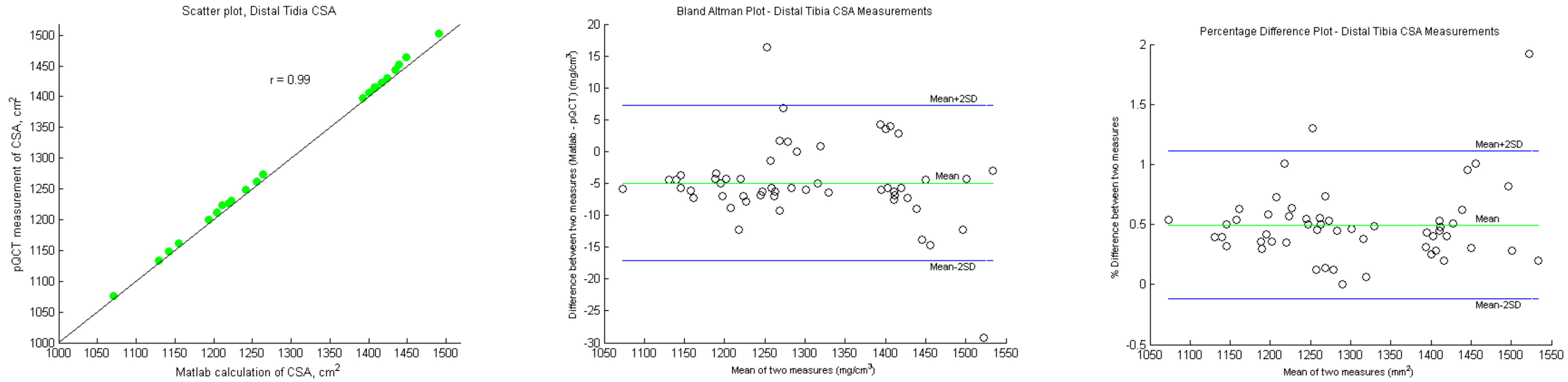

(d) Scatter Plot - Distal Tibia CSA

(e) Bland-Altman - Distal Tibia CSA

(f) Percentage Difference - Distal Tibia CSA

Figure 3.11: Agreement between Stratec and Matlab measurements of distal tibia

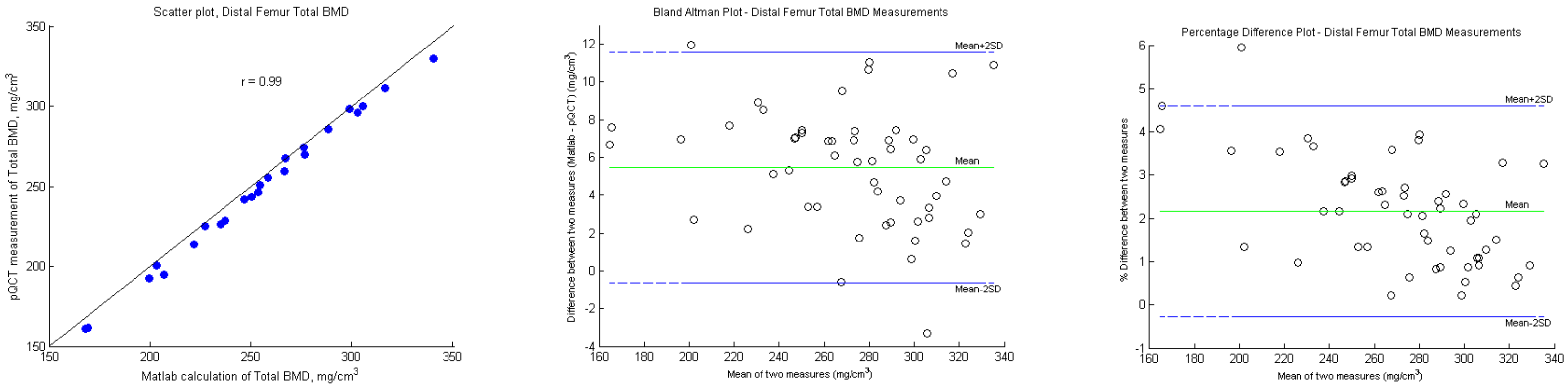

(a) Scatter Plot - Distal Femur Total BMD (b) Bland-Altman - Distal Femur Total BMD (c) Percentage Difference - Distal Femur Total BMD

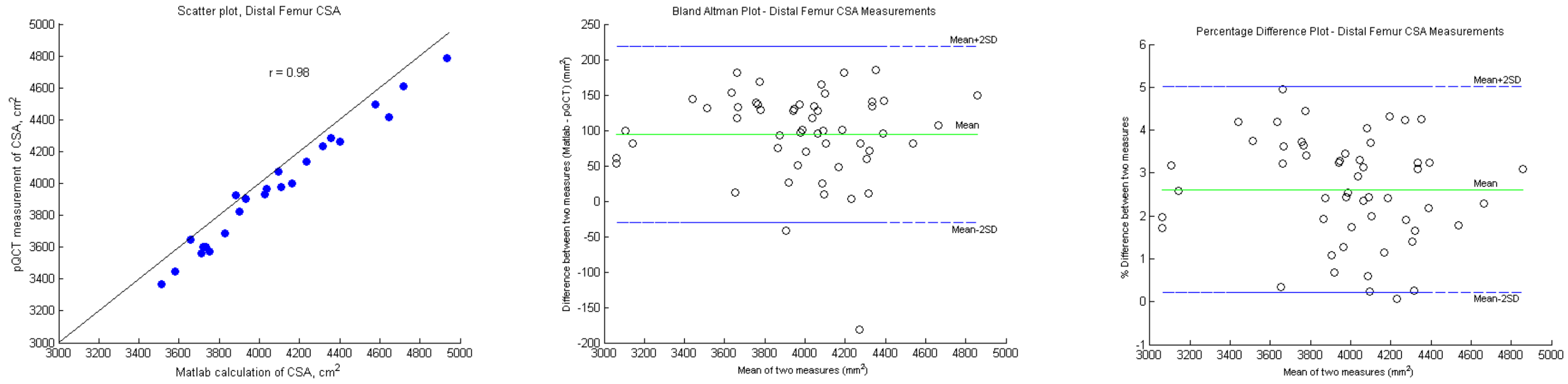

(d) Scatter Plot - Distal Femur CSA (e) Bland-Altman - Distal Femur CSA (f) Percentage Difference - Distal Femur CSA

Figure 3.12: Agreement between Stratec and Matlab measurements of distal femur

The scatter plots comparing the two techniques demonstrate a high degree of correlation for all measurements (r values>0.98), however a better sense of the differences which exist between each method is given in the Bland Altman and percentage difference plots. A summary of the results from these graphs is presented in Table 3.4 below.

Measurement	mean diff, $\bar{d}$	SD diff, s	95% limits $\bar{d} \pm 2s$	mean % diff	SD % diff
Distal tibia TotBMD (mg/cm^3)	1.43	0.85	-0.27 to 3.13	0.48	0.12
Distal tibia CSA (mm^2)	-4.94	6.25	-17.44 to 7.56	0.5	0.31
Distal femur TotBMD (mg/cm^3)	5.46	3.13	-0.8 to 11.72	2.17	1.25
Distal femur CSA (mm^2)	94.78	63.8	-32.82 to 222.38	2.61	1.23

Table 3.4: Mean and SD of measurement differences (Matlab−Stratec)

A confidence interval (CI) for the mean difference, $\bar{d}$, was also calculated, as the values in Table 3.4 are only estimates taken from a small sample of the population as a whole. If a second population of 53 images were used, there would be variations in the CI obtained. The CI determine the *bias* of the mean difference calculation and hence an indication of the precision of the estimated limits of agreement [103]. The 95% CI for the mean bias is given by

$$\bar{d} \pm t \times s/\sqrt{n} \tag{3.4}$$

where $s/\sqrt{n}$ is the standard error of the mean calculated using a sample size n, with the corresponding value of t with 52 degrees of freedom $(n-1)$ being 2.009 (Student's t table). The 95% CIs for the bias of the mean differences calculated using a sample size of 53 are given in Table 3.5.

Measurement	95% CI of mean difference bias
Distal tibia Total BMD (mg/cm^3)	1.19 to 1.67
Distal tibia CSA (mm^2)	-6.67 to -2.91
Distal femur Total BMD (mg/cm^3)	4.6 to 6.32
Distal femur CSA (mm^2)	77.18 to 112.38

Table 3.5: 95% CI of the mean difference bias

Distal Tibia Measurements

The Bland Altman plot in Graph 3.11b comparing total BMD measurements of the distal tibia shows scattered results, with a slight tendency for the Matlab software to generate measurements greater than the Stratec software as the patients' BMD increases. The mean difference between the two methods is small (1.43mg/cm^3), indicating that there is a minor overall disparity between the pQCT measurement and the new automated software. The bias of this mean difference is also small, ranging from 1.19 to 1.67mg/cm^3, thus on the basis of these data, the maximum overall bias of the calculation using the automated software over the standard method would be as little as 1.67mg/cm3, with the 95% limits of the mean difference across all of the sampled measurements ranging only from -0.27 to 3.13mg/cm^3. Proportionally, the differences between these measurements is <1% of the total distal tibia BMD (Graph 3.11c). These variations in measurement are extremely small and would not be considered clinically significant.

The mean difference of the distal tibia CSA measurement is -4.94mm^2, the negative number indicating that the new software has a tendency to underestimate this measurement (Graph 3.12e). As a proportion of the CSA measurement however, this figure equates to only 0.5% of the overall value, as demonstrated in Graph 3.11f. The 95% CI of the mean difference for distal tibia CSA ranges from -6.67 to -2.91mm^2, resulting in a maximum mean bias of -6.67 mm^2. Variations at this scale would not be considered clinically important when measuring the CSA of the distal tibia.

These distal tibia measurements show an excellent degree of agreement between the Stratec technique and the automated software developed. As expected the two methods do not calculate identical values for the total BMD and CSA, however the bias between the two is very small and in both cases would not be considered to have an effect on any clinical outcomes.

Distal Femur Measurements

The total BMD for the distal femur measured using the existing pQCT software and the new automatic software was also compared. A plot of the difference between the methods against their mean is given in Graph 3.12b. The results are scattered, with no clear evidence of any relationship between the difference and the mean (correlation coefficient $r = -0.28$). Once again, for total BMD the new software has a tendency to overestimate the measurement, and has a mean difference of 5.46mg/cm^3 with a range of -0.8 to 11.72mg/cm^3. The 95% CI of the mean difference bias for the distal femur total BMD is 4.6 to 6.32mg/cm^3 for this sample. The percentage difference between these two methods puts there results in to context (Graph 3.12c), demonstrating that the mean difference only ranges from 2.17% ± 1.25% of the total BMD measurements. For the studies used in this thesis, changes in total BMD on this scale would not be considered substantial enough to affect clinical decisions.

Finally CSA measurements of distal femur were evaluated across the two methods. The mean differences between the two methods for this parameter were $94.78 \pm 127.6\text{mm}^2$, with a mean bias of 78.18 to 112.38mm^2. This is a large bone and therefore proportionally, the percentage mean difference only ranges from 2.61% ± 1.23% of the total CSA.

It is clear that the Matlab software found the femoral images more challenging than the distal tibia when comparing them to the standard measurements of total BMD and CSA. As discussed previously, this was attributed to the smaller voxel size, thinner cortical shell and much more challenging regions of osteoporosis. Despite this, the maximum mean bias of the total BMD for the femur is still relatively small, and would not change clinical management. The segmentation of this bone using the Stratec software was completely manual for all 53 images, again due to the challenging nature of choosing a threshold for segmentation. This would consequently introduce an intra-operator error. The use of the automated software described in this chapter however would improve consistency across the images as well as reduce the overall processing time cost.

3.5 Summary

This chapter has presented a novel variable threshold segmentation technique developed to segment out bones in the apical skeleton from their surrounding soft tissue structures. The automation of this algorithm removes the requirement for an operator to manually delineate the regions of interest, improving time cost and reducing the effects of inter-operator error on parameter measurements. The automated software has demonstrated a high success rate when segmenting bones from the tibia. Segmentation of the femur has almost a 70% success rate, failing only when BMD falls to density levels equivalent to that of the surrounding soft tissue, making automated categorisation of voxels challenging. For this reason, a quality control step has also been included in the algorithm allowing the operator to visually accept or reject the segmentation, with the latter permitting a manual segmentation by hand. Previously, however, using the standard Stratec software, all images at this location were segmented manually. The range of automated thresholds generated for each location is very small. This provides reassurance that when performing longitudinal or contralateral comparisons across images that, despite being segmented using an image specific threshold, measurements can still be reliably compared. Using a variable threshold also allows a higher segmentation success rate than a fixed threshold, especially when the BMD is variable, as well as less requirement for user intervention, with the segmentation algorithm adapting itself to the image under scrutiny. When the algorithm outputs were compared to the measurements made using the standard Stratec software using SCI images with a wide spectrum of osteoporotic and non-osteoporotic conditions, it demonstrated excellent agreement with the distal tibia measurements and very good agreement of the distal femur measurements across this wide range of images.

There are many image segmentation techniques which have been studied extensively and published, all with their own benefits and limitations. For the pQCT images used in this thesis, the benefits of the method defined in this chapter outweigh the limitations which may have been identified. The production of an image specific threshold, the reduction of inter-operator variability and the fast processing time are seen as the main advantages of this software over the standard Stratec technique. Once the images have been suitably pre-processed to isolate the bone of interest, it will then be possible to perform post-processing analysis. Two novel post-processing methods were also developed in Matlab, both with the aim of extracting localised and structural information within the bone additional to global BMD measurements. Chapter 4 presents a technique which performs a spatial mapping of bone turnover across image pairs, using registration and voxel-wise comparisons and Chapter 5, an algorithm to describe the textural structure of the bone using morphological granulometries. The results and findings using these techniques are subsequently presented in Chapters 6 and 7 for both SCI and ACL subject groups.

Chapter 4

Spatial Mapping of Bone Turnover

Localisation of changes in BMD has the potential to investigate patterns of bone turnover and therefore focus rehabilitation and interventional techniques looking to restore specific areas of bone loss within the bone. Global measurements of BMD will give the user an indication of the overall bone turnover a subject may have experienced, however they do not provide information on where exactly in the bone this turnover has occurred, for example, antero-laterally versus postero-medially. These global measurements may also be diluted if, for example, the subject has experienced both decreasing and increasing changes in BMD, which may result in the extent and degree of any localised bone loss being under-estimated (Figure 4.1). Assuming that new bone is deposited where it is needed structurally along its length [5, 104], therapy for osteoporotic regions in the bone could be tailored, targeting specific muscle groups to generate the localised forces in an attempt to restore BMD in these regions.

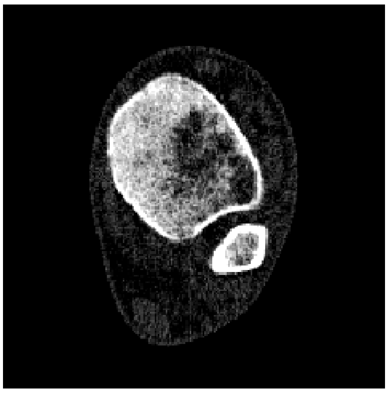

Figure 4.1: pQCT example of inhomogeneous loss in distal tibia, (global BMDTrab measurement within normal limits)

The focus of the analysis techniques presented in this thesis are to provide the user with a means of spatially identifying locations within the bone which may be experiencing increasing or decreasing bone turnover, or indeed regions which may have remained unchanged. This chapter can therefore be broken down into three distinct sections:

- The first step involves performing image registration in order to make a valid comparison between images. In the SCI population, the image pairs will be from two different time points, with the overall image time series providing longitudinal data. In the ACL population, the pairs of images will be either contralateral images taken from the same subject at the same anatomical location (using non-injured leg as the control) or longitudinal data taken from the same location in the injured limb pre- and post-operatively.
  Once registered, two different methods of spatial assessment of bone turnover were developed, defined forthwith.

- As trabecular bone is an excellent early indicator of bony changes due to its high remodeling rate, a regional assessment of the trabecular bone would accordingly highlight any specific segments or pockets which may be at a higher risk of osteoporosis compared to others. Regional trabecular assessment software developed therefore removes the cortical shell of the segmented bone images and compares the trabecular BMD of four quadrants across image pairs.

- The second method compares the registered image pairs by performing voxel wise comparisons, generating a regional map of any changes in BMD which are statistically significant at the anatomical location imaged. In a similar manner to SPM, which for example identifies functionally specialised brain responses in neuroimaging [89], this software identifies specific regions within the appendicular skeleton in order to characterise any disease related changes in the bone image.

Regional and quadrant approaches to the analysis of BMD within images has been investigated previously [86, 40, 88, 13], however techniques used to segment the bone were either performed manually or with some form of semi-automation. The software developed for this thesis removes any operator error by performing fully automated registration, cortical peeling and segmentation.

As highlighted in Chapter 2, the use of voxel mapping to assess bone turnover is quite novel, and current publications present composite images to define loss within populations using statistical voxel based analysis [63, 90, 91]. This Chapter introduces a patient specific approach to mapping changes in BMD, enabling a tailored characterisation of osteoporotic progress to be identified for the individual. This would be a more informative method than group analyses for these particular subjects/patients due to the diverse nature of the SCI and ACL subjects' injuries, backgrounds and physiotherapeutic rehabilitation undergone. In particular, the SCI population are known to experience very individual patterns of bone loss within this acute phase post-SCI [105].

4.1 Image Registration

Image registration is required to bring two images into spatial alignment enabling like for like comparisons to be made across image pairs. Geometric spatial transformations, introduced in Section 2.3, are used to rotate, translate and skew an input image into alignment with a reference image. As well as spatial transformations of image co-ordinates, voxel interpolation and re-sampling is necessary to approximate gray-scale values of voxels at their new locations. The software developed here to carry out the registration performs a rigid geometric transformation, followed by a measure of similarity (cross-correlation) between the two images undergoing registration. This is repeated until the optimal registration between the two images is obtained, while minimising any compromise in image quality through repeated interpolation.

4.1.1 Geometric Transformations

Maintaining the definitions introduced in Section 2.3, the original image will be referred to as the **reference** image and the image undergoing the spatial transformation as the **target** image. When transforming a target image coordinate (a, b) to a reference image coordinate (x, y) the following expression applies the transform matrix $\mathbf{T}$ to the input image

$$(x, y) = \mathbf{T}(a, b) \tag{4.1}$$

Any two dimensional transformation, $\mathbf{T}$, can be expressed as a three-by-three matrix[1]. Assigning the vector $[x\ y\ 1]$ to the coordinate (x, y) and $[a\ b\ 1]$ to the coordinate (a, b), Equation 4.1 therefore becomes:

$$[x\,y\,1] = \mathbf{T}\,[a\,b\,1] = [a\,b\,1]\begin{bmatrix} t_{11} & t_{12} & 0 \\ t_{21} & t_{22} & 0 \\ t_{31} & t_{32} & 1 \end{bmatrix} \tag{4.2}$$

As previously discussed in Chapter 2, only the rigid body transformations *translation* and *rotation* will be used for the registration of the pQCT bone images, as these preserve all internal angles and distances. The corresponding translation matrices for these transformations are given in Table 4.1 [64].

---

[1] The extra final column in the transform matrices below containing the value '1' ensures the geometric transformation mathematics remain correct [106]

Transformation Name	Transformation Matirx, $\mathbf{T}$	Coordinate Equations
Translation	$\begin{bmatrix} 1 & 0 & 0 \\ 0 & 1 & 0 \\ t_x & t_y & 1 \end{bmatrix}$	$x = a + t_x$ $y = b + t_y$
Rotation	$\begin{bmatrix} \cos\theta & \sin\theta & 0 \\ -\sin\theta & \cos\theta & 0 \\ 0 & 0 & 1 \end{bmatrix}$	$x = a\cos\theta - b\sin\theta$ $y = a\cos\theta + b\sin\theta$

Table 4.1: Translational and Rotational Matrix Transformations

Following each geometric transformation, intensity values have to be assigned to the voxel values which have been relocated to new positions in the image. This is achieved using image interpolation, and for the purposes of this software, a method called *nearest neighbour interpolation* is used. This technique assigns intensity-levels to the new voxel locations by finding the closest pixel in the original image to that point and assigning the intensity of that pixel to the new pixel in the grid. Although this method is simple and fast, it is noted to introduce distortions to straight lines, with some authors preferring to use either *bilinear* or *bicubic interpolation* [64]. These latter methods use the intensity levels of the surrounding voxels to generate an estimate of the voxel intensity at the new location, producing a smoother, less jagged transformed image. It is however, important to recall that the intensity values of each of the voxels in the original image are BMD values measured using the pQCT scanner. On balance therefore, the nearest neighbour method was used in order to preserve as best possible the acquired BMD values, arguing that although the outer edges of the cortical bone may be more jagged, this was deemed acceptable for this application.

4.1.2 Cross-Correlation

The concept of intensity based registration was introduced in Section 2.3.2 in the literature review. Due to the anatomical shape of the bones undergoing registration, the use of a similarity measurement was preferred over feature detection and matching, to determine the transformation, $\mathbf{T}$, necessary to register image pairs. Taking the binary mask of the bones and performing cross-correlation was proposed as an option for registering bone pairs known to have different bone densities or bony patterns. Once the geometric transformations necessary to register the images were calculated using the masks, they could then be applied to the original segmented gray-scale images.

Spatial cross-correlation is the process of shifting one image over another and calculating the sum of the products (SoP) of both images. In doing so it is possible to identify the geometric transformation arguments which will maximise the similarity between the two images. One way to explain how it obtains these arguments is by example using illustrations. Figure 4.2a and Figure 4.2b are two images represented by their numerical matrices. In order to determine the transfer function, or the shift, which will best align these two images, the target image is shifted across the reference image taking the SoP at each location.

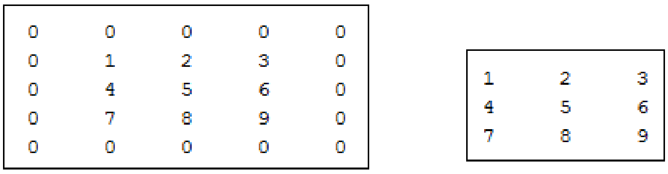

$$\begin{matrix} 0 & 0 & 0 & 0 & 0 \\ 0 & 1 & 2 & 3 & 0 \\ 0 & 4 & 5 & 6 & 0 \\ 0 & 7 & 8 & 9 & 0 \\ 0 & 0 & 0 & 0 & 0 \end{matrix}$$

(a) Reference image

$$\begin{matrix} 1 & 2 & 3 \\ 4 & 5 & 6 \\ 7 & 8 & 9 \end{matrix}$$

(b) Target image

Figure 4.2: Two images in matrix form undergoing cross-correlation

Figure 4.3 presents the target image at three different locations during the cross-correlation process. At location **A**, the SoP is
$(1 \times 0) + (2 \times 0) + (3 \times 0) + (4 \times 0) + (5 \times 1) + (6 \times 2) + (7 \times 0) + (8 \times 4) + (9 \times 5) = 94$
This value will then be placed at central pixel at that location in the output image. In this example, it is possible to see qualitatively that location **B** of the target image is the best fit. Quantitatively the SoP is 285, which is much higher than that calculated at location **A**. As the target image continues to move across the reference image, the SoP is calculated for each pixel location, with the cross-correlation of position **C** also generating a SoP of 94.

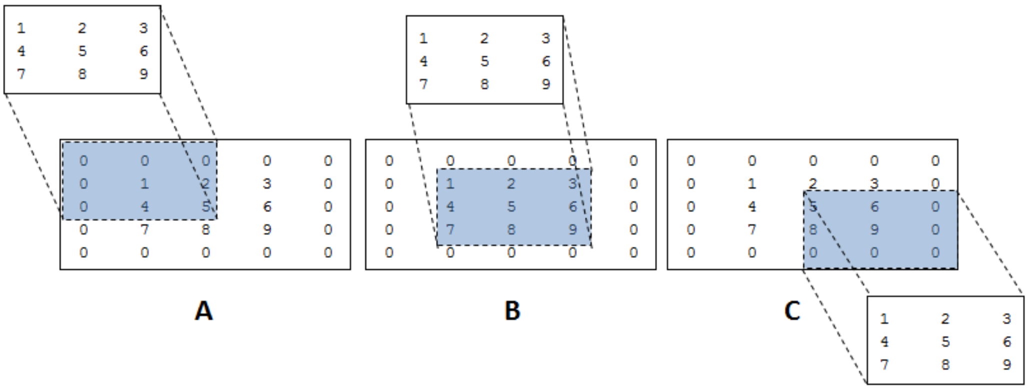

Figure 4.3: Cross-Correlation of reference image with target image

The full correlation result of these two images is shown in Figure 4.4. The arguments of displacement which maximised the cross-correlation, which in this example equated to the central SoP of 285, would therefore be used for the two dimensional transform, T, to register the image pairs. An important observation is that the full correlation result matrix is larger than the original target image, and therefore the displacement would have to be adjusted based on the image sizes under interrogation.

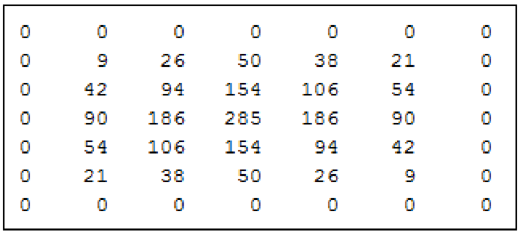

0	0	0	0	0	0	0
0	9	26	50	38	21	0
0	42	94	154	106	54	0
0	90	186	285	186	90	0
0	54	106	154	94	42	0
0	21	38	50	26	9	0
0	0	0	0	0	0	0

Figure 4.4: Full correlation result of Figures 4.2a and 4.2b

The cross-correlation of two images can be displayed mathematically using Equation 4.3, where $w(x, y)$ is the target image, $f(x, y)$ is the reference image and $w(x, y) \bigstar f(x, y)$ denotes the cross-correlation of the two. x and y are varied such that each pixel in w visits every pixel in f.

$$w(x, y) \bigstar f(x, y) \;=\; \sum_{s=-a}^{a} \sum_{t=-b}^{b} w(s, t) f(x + s, y + t) \tag{4.3}$$

For an image size of $m \times n$, the values of a and b can be determined using the relationships $m = 2a + 1$ and $n = 2b + 1$. This condition ensures that the centre coefficient of the target image $w(0, 0)$ will align with the pixel at location (x, y).

The translational shifts t_x and t_y defined in Table 4.1 (s and t respectively in Equation 4.3) were determined for binary bone image pairs using the above correlation technique, by shifting the target image across and down the reference image. t_x and t_y were calculated using the location of the maximum SoP in the result matrix. Determining the rotational angle, θ, necessary for registration was more challenging. The SoP result matrix for a range of angles would have to be calculated in order to determine which angle maximised the correlation between image pairs. In order to ensure best rotational correlation, all 360^o angles should be tested using cross-correlation, however this comes with an extremely high time cost and in the studies under scrutiny would contain a large amount of redundancy. The pQCT patient immobilisation devices ensured that the patients' limbs were held in similar positions to their previous and subsequent scanning sessions. There were therefore a limited number of rotational angles within which the leg could be held. "Challenging" scanning sessions, as can occur with SCI subjects with muscle spasms or tight hamstrings, may lead to increased variation in positional location between the two scan time-points, however the foot holder does limit the rotational angle of displacement possible. Based on this knowledge, the cross-correlation for a rotational angle range of -10^o to +20^o was calculated in the software, with the angle generating the largest SoP maxima being the best match between images.

The number of geometric transformations necessary to register the binary image pairs then had to be determined. A random sample of nine distal tibia and distal femur pairs were registered using multiple iterations of translation then rotation. During registration, the number of pixels the target image was displaced (t_x and t_y, voxels) and the angle in degrees it was rotated (θ, degrees) were recorded following each iteration, with the results given in Appendix A. These results show that after three transformations (translation, rotation, translation) only two of the distal tibia images required further minimal change (distal tibia 8 & 9), and no further displacement was necessary in any of the distal femur images. The Centre of Mass (COM) of the binary image following these three transformations, T_3, was determined and compared to six transformations, T_6. The euclidian distance in mm between the two COMs was then calculated to determine if the additional transformations in T_6 were having a significant impact on the registration. The outcome of these differences in measurements is shown in column COM diff. in Appendix A. Of the two distal tibia images requiring the additional transformations, the difference in COM locations was <0.5mm. As a percentage of the overall area of these bones, the effect of these differences would be extremely minimal.

The time cost was also measured, with $Time_3$ representing a translation, rotation, translation and $Time_6$ all six geometric transformations. On average, the $Time_6$ measurement was 3 times greater than that of the $Time_3$ measurement, with one case taking almost over 8 times longer to perform the registration (Distal tibia pair 8), with very minimal benefit to the final result. As such, the number of rigid transformations carried out in the registration software was selected to be three: translation, rotation, translation. This minimises both the number of interpolations the registered image has to undergo as well as the over all processing time cost.

4.1.3 Registration Validation

Registration validation was carried out both qualitatively and quantitatively. The registration software outputs the reference image and the registered target image. This is so that a visual inspection, checking whether they appeared geometrically aligned, is incorporated into the analysis. In order to quantitatively evaluate the registration errors, comparisons between manually identified anatomical landmarks could be made. This is challenging when considering the circular shape of the bones in the appendicular skeleton, therefore a more automated approach was taken. Using the 18 registered images from the previous example (nine distal tibia and nine distal femur), five anatomical locations were identified. Four of these specified the extrema of the binary image in both the x and y direction and the fifth the COM of the image. An example of these locations is given in Figure 4.5.

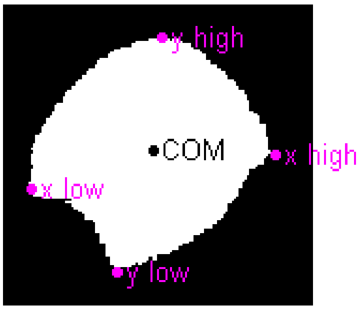

Figure 4.5: Anatomical locations used for registration validation

The four extrema in the binary image could be easily identified using an iterative scanning procedure. In the knowledge that the binary image had background pixels of 0 and foreground pixels of the bone equal to 1, the COM of the mask was defined as the average of each voxels' positions, r_i, weighted by their masses, m_i, as shown in Equation 4.4.

$$COM = \frac{\sum m_i r_i}{\sum m_i} \tag{4.4}$$

Comparisons were made between the anatomical locations of the reference image to that of the target image before and after registration. The distance between concurrent locations was used to assess the overall registration error. Tables 4.2 and 4.3 list the validation results for all five landmarks, with the statistics for all five summarised. This includes the average distance, standard deviation of the differences and the maximum distance in mm over the 9 images tested (Ave_9, Dev_9 and Max_9 respectively).

		Distance between Distal Tibia landmarks (mm)	
		Before Registration	After Registration
All 5 landmarks	Ave_9	4.35	0.41
	Dev_9	3.91	0.37
	Max_9	12.81	1.09
COM	Ave_9	6.31	0.21
	Dev_9	5.33	0.13
	Max_9	18.55	0.47
x_high	Ave_9	5.56	0.17
	Dev_9	5.38	0.25
	Max_9	17.5	0.5
x_low	Ave_9	5.17	0.78
	Dev_9	6.17	0.51
	Max_9	19.5	1.5
y_high	Ave_9	2.56	0.39
	Dev_9	1.36	0.33
	Max_9	4.5	1
y_low	Ave_9	2.17	0.5
	Dev_9	1.32	0.61
	Max_9	4	2

Table 4.2: Distances between landmarks on the reference and registered images - distal tibia

		Distance between Distal Femur landmarks (mm)	
		Before Registration	After Registration
All 5 landmarks	Ave_9	7.91	0.85
	Dev_9	10.54	0.82
	Max_9	30.72	2.24
COM	Ave_9	10.95	0.5
	Dev_9	14.12	0.44
	Max_9	42.39	1.21
x_high	Ave_9	7.64	0.74
	Dev_9	13.05	0.59
	Max_9	38.18	1.52
x_low	Ave_9	7.37	1.18
	Dev_9	10.65	1.07
	Max_9	33.33	3.03
y_high	Ave_9	7	1.38
	Dev_9	6.16	1.57
	Max_9	17.88	4.24
y_low	Ave_9	6.57	0.47
	Dev_9	8.71	0.43
	Max_9	21.82	1.21

Table 4.3: Distances between landmarks on the reference and registered images - distal femur

These results show that following registration, the average distance between all five anatomical landmarks across image pairs was extremely small. The average distance between homologous landmarks before registration was 4.35mm for the distal tibia and 7.91mm for the distal femur. After registration these differences were reduced to 0.41mm and 0.85mm respectively, indicating that the accuracy of the registration software was excellent, correlating with the qualitative visual assessment of the registration which displayed the output images adjacent to each other. In addition to calculating registration accuracy, this software also enables a measure of intra-operator error during data acquisition. The extent of the geometric transformations the target bone must undergo to register with the reference image is a quantifiable measure of patient alignment. Accuracy of patient positioning has been studied extensively in the field of radiotherapy, with assessment of accuracy also made using registration and quantification of shifts in anatomical landmarks [107, 108, 109].
The results from the registration software are therefore very promising, with the following points taken into consideration. The quantitative measure of the algorithm's accuracy was subject to human positioning error as it was based on real patient data. In addition, the CSA of the bones being registered was not taken into consideration during this assessment and the assumption was therefore made that the same anatomical location was imaged across slices under comparison. A true assessment of the accuracy would ideally be made with a phantom of a fixed shape or cadaver, translated and rotated a known distance. This gold standard in itself is challenging, subject to error and is generally not available. Woods [110] provides a comprehensive review of validation techniques used to quantify registration accuracy. He concludes that techniques such as validation by visual inspection using the expert eye and/or using point based registration comparison methods would be suitable alternatives to measurement of registration accuracy in the absence of this gold standard, provided errors in acquisition were kept minimal.

The segmented registered image pairs are now suitably aligned such that the two spatial assessments of bone turnover introduced at the beginning of this chapter can be carried out. Section 4.2 describes the first of those two, the use of a quadrant based analysis of trabecular bone to identify specific regions within the bone which may be experiencing early osteoporotic changes, information not evident from global measurements of BMD.

4.2 Regional Trabecular Bone Changes

Trabecular bone is of clinical interest as it experiences much more rapid changes in comparison to cortical bone as a result of its larger surface area and faster turnover. For the assessment of trabecular bone on its own, the removal of the surrounding cortical bone is essential. Previous studies assessing the trabecular bone in SCI subjects have carried out the Concentric peel method provided by the Stratec pQCT analysis software [33, 32, 72]. This analysis method concentrically peels the outer 55% of voxels from the outside bone circumference, leaving the central 45% core to calculate the trabecular BMD (BMDtrab). This technique does ensure that the cortical and sub-cortical bone is removed from the calculation, however it also removes a substantial portion of the trabecular bone within the image. In subjects whose bone loss preferentially occurs within the central core, an over-estimation of the total trabecular bone lost may be made when using this technique. One such case is demonstrated here. Figure 4.6a is an example of a healthy non-osteoporotic distal tibia slice, whereas Figure 4.6b demonstrates osteoporotic loss in the bone occurring through the central core of the bone. If an assessment of BMDtrab were made using the peel method described above, the measurement of BMDtrab would therefore be extremely low. This subject has a substantial amount of trabecular bone still present around the portion of centrally lost bone.

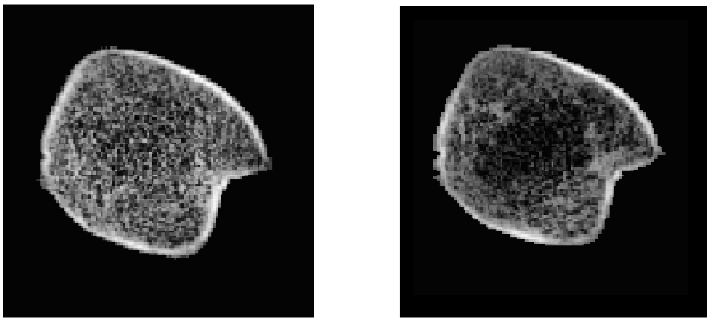

(a) Example of healthy distal tibia

(b) Example of bone loss occurring centrally

Figure 4.6: Demonstration of trabecular bone loss occurring centrally in distal tibia

A recent study by Dudley-Javoroski and Shields [111] put forward an alternative method to removing cortical bone at the 12% femoral site (mid-shaft). They proposed the use of a "Threshold" peel which removes only the cortical and sub-cortical voxels of the bone above a pre-defined threshold within the segmented image. For the ACL and SCI subject data used in this thesis, trabecular bone analysis was performed and compared using both the Concentric and Threshold peel methods. As a result of differences in anatomical location scanned in comparison to the Dudley-Javoroski study , minor modifications were made to their analysis procedure, however the fundamental principals remained the same.

4.2.1 Peel Methods

Concentric Peel

Automated software was developed which allowed the user to define what percentage of bone they wish to concentrically peel from the outside boundary of the bone. The purpose of this was to replicate the Stratec software, but with increased peel flexibility. A binary mask of the bone was taken and the area calculated. Using a morphological erosion, the peripheral voxels of the image were removed. For each iteration, a comparison was made to the desired percentage to be removed, evaluating the ratio of the new mask area to that of the original mask area. Once this area was less than or equal to the desired area, the eroded mask was used in a logical AND operation with the original gray-scale image. The outcome gave a central core of trabecular bone with the cortical bone removed.

One of the limitations of this method of concentric peeling is that the resultant eroded image will not be the exact percentage specified by the user. It will always be less than or equal to this value to the nearest peripheral erosion iteration. The true ratio is echoed to the user on the screen so that a measure of any discrepancy can be obtained.

Threshold Peel

The original Threshold peel algorithm defined by Dudley-Javoroski and Shields [40] has the following principal steps:

1. The user manually defined a region surrounding the bone which contained a small amount of periosteal muscle and soft tissue.
2. Moving from the outer edge inwards, a threshold algorithm removed voxels below 200mg/cm^3, corresponding to muscle and fat tissue still present in the segmented image.
3. Histogram thresholding classified those voxels greater than 400mg/cm^3 to be cortical and sub-cortical. Everything below this value was defined as trabecular bone. The cortical and sub-cortical voxels were removed from the analysis.
4. The remaining image was then proofed using a 3x3 voxel filter to identify any pockets of high bone mineral density. Those voxels which had substantially higher BMD than their surrounding neighbours were assigned to be cortical / sub-cortical and removed from the final image.
5. The trabecular bone mineral density was determined for the remaining voxels in image.

For the purposes of the software developed in this thesis, the following steps were modified to remove operator intervention within the peeling process and to adapt for the different anatomical locations imaged.

The first step was carried out using the automated segmentation software described in Chapter 3 as opposed to the manual segmentation. The software also removed the voxels which have been subject to the PVE at the boundary of the soft tissue and bone.

In steps 2 and 3 of the above algorithm, the soft-tissue voxels were removed below 200 mg/cm^3 at the outer edge which was subsequently followed by histogram thresholding removing voxels with BMD values greater than 400 mg/cm^3. Dudley-Javoriski's decision to make the threshold 400 mg/cm^3 was based on a visual perception of the success of the Threshold peel method at the 12% distal femur location. They felt that this value was suitable for the patient cohort within their study (specifically SCI subjects experiencing rapid bone loss), however they acknowledge that the quality and success of the Threshold based peel method relies on the appropriateness of the selected threshold for the bone region under scrutiny.

Therefore, despite this algorithm working for the 12% femoral slice, which has a very distinct cortical boundary, it was not as successful for the trabecular rich slices at the epiphyses of the bones analysed in this thesis. At these anatomical locations, there are voxels on the soft-tissue/bone boundary which experience PVE resulting in voxels ultimately containing values between the threshold values of 200-400 mg/cm^3. If the above algorithm were to be applied in its current format, these voxels would remain in the image and hence the trabecular BMD calculation, when they are actually a combination of both soft-tissue and cortical bone. This can be demonstrated visually as a ring of pixels around the bone in Figure 4.7.

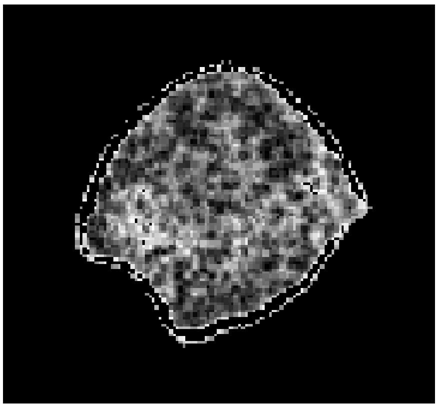

Figure 4.7: PVE voxels remaining in Threshold Peel algorithm

A method to remove this unwanted artefact was therefore necessary. As these voxels are often isolated around the periphery of the bone, one solution would be to use a spatial filter mask such as a 3x3 shifting voxel filter, to interrogate the voxel and those within its immediate neighbourhood. If a voxel were identified to be isolated within reason from the rest of the image, they could be assumed to be artefact. This was applied to the image, using the condition that if the 3x3 spatial filter contained 6 or more background values, the central voxel would also be converted to a background voxel. The Dudley-Javoriski algorithm was therefore modified as detailed below:

1. Automatically segment the bone of interest using the histographic segmentation defined in Chapter 2.
2. Moving from the outer edge inwards, a threshold algorithm removes voxels below 200 mg/cm^3 corresponding to muscle and fat tissue still present in the segmented image.
3. Histogram thresholding classifies those voxels greater than 400 mg/cm^3 to be cortical and sub-cortical. Everything below this value is defined as trabecular bone. The cortical and sub-cortical voxels are removed from the analysis.

4. The image is proofed using a 3x3 voxel filter to identify any pockets of high bone mineral density. Those voxels which have substantially higher BMD than their surrounding neighbours are assigned to be cortical / sub-cortical and removed from the final image.
5. PVE artefact is removed using a 3x3 shifting voxel filter, re-assigning any isolated voxels which have 6 or more surrounding background voxels also to background.
6. Trabecular BMD is determined for the remaining voxels in image.

The decision on a background threshold of 6 voxels or greater for the shifting filter was chosen empirically. This figure resulted in the optimum compromise between removing cortical/soft-tissue partial volume voxels without removing true trabecular voxels that exist at the cortical sub-cortical boundary. Applying the filter to Figure 4.7, the circumferential PVE artefact is almost completely removed.

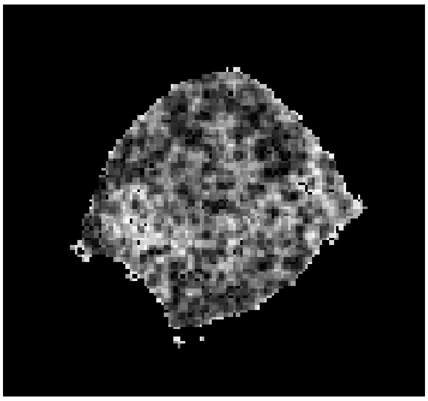

Figure 4.8: PVE voxels removed following 3x3 spatial filtering of image in Figure 4.7

When the modified Threshold Peel algorithm was applied to the SCI and ACL patient groups studies in this thesis, it was shown to be successful in all slices excluding the distal femur in the SCI population. One possible reason for this was that it was the only slice acquired at the much smaller voxel size of 0.303x0.303mm, as opposed to 0.5x0.5mm for all of the other acquired images. The cortical shell at this site is also extremely thin, in particular for SCI subjects. As a result, the Threshold peel method was unsuccessful at measuring BMDtrab in the distal femur in the SCI population, and was therefore not calculated for this data set.

4.2.2 Assessment of Peel Software

The BMDtrab measurements made by the the new Matlab software were compared to the existing Stratec software for twelve randomly selected SCI 4% distal tibia images. The percentage change of the new measurements was calculated to assess if there were any gross differences compared to the manufacturer's software. The results are presented in Table 4.4.

Slice	Stratec BMDtrab	Matlab Concentric peel BMDtrab	Matlab Thresh. Peel BMDtrab	Conc. Peel % change	Thresh. Peel % change
Dist. Tib. 1	304.2	305.5	305.6	0.43	0.46
Dist. Tib. 2	287.3	286.2	286.1	-0.38	-0.42
Dist. Tib. 3	208.2	205.5	208.2	-1.3	0
Dist. Tib. 4	283.9	284.1	283.4	0.07	-0.18
Dist. Tib. 5	284.9	281.8	281.3	-1.09	-1.26
Dist. Tib. 6	221.2	220.6	221.4	-0.27	0.09
Dist. Tib. 7	235.6	237.3	237.4	0.72	0.76
Dist. Tib. 8	284.1	281.6	283.7	-0.88	-0.14
Dist. Tib. 9	171.3	172.2	172.2	0.53	0.53
Dist. Tib. 10	177.6	177	174.1	-0.34	-1.97
Dist. Tib. 11	282.8	281.4	282.1	-0.5	-0.25
Dist. Tib. 12	87.2	86.7	87.5	-0.57	0.34

Table 4.4: Comparison of BMDtrab measurements for the distal tibia

Over the range of BMDtrab values compared (235.7±65.5 mg/cm^3), both the Concentric peel and Threshold peel software calculated very similar BMDtrab values to the Stratec software. The largest deviations from this measurement were only -1.97% and 0.76% respectively. What is interesting to note is that the Threshold peel BMDtrab measurements were very similar to the Concentric peel methods (both Matlab and Stratec). These results provide a reassurance that the peel method of trabecular bone measurement is comparable to alternative methods under these hypothesised conditions. One exception to this are the measurements from Figure 4.6, where bone loss occurs centrally (measurements not included in Table 4.4 sample). In this one example, these measurements in fact produce very different results, with Figure 4.6b having a Concentric peel BMD of 71.3mg/cm^3 but a Threshold peel BMD of 133mg/cm^3. This highlights the benefits of performing both types of BMD measurement, as it may be underestimated using the Concentric peel measurement if the bone loss occurs centrally.

4.2.3 Spatial Segmentation

Now that two different peel methods have been defined to calculate global BMDtrab, it is possible to expand on this to assess more localised regions within the bone. With the registration of pairs of images, comparison of like for like regions across the bones is now made possible. Consequently additional information can be extracted relating to regional changes of BMD within the bone. If one region within the bone was experiencing more bone loss over time than other areas, for example the posto-lateral region in Figure 4.1, intervention techniques aimed at restoring BMD could be focussed on this region. One such way could be through the stimulation of specific muscle groups which have tendon insertions within this region to exert localised forces on the bone. Any longitudinal adaptations of the bone locally to these interventions could also be monitored.

An automated approach at segmenting bone images into quadrants is proposed. This ensures there is no influence of region definition from any manual delineation. All bones (excluding the SCI distal femur) were segmented into four; the antero- and postero- medial and lateral components shown in Figure 4.9

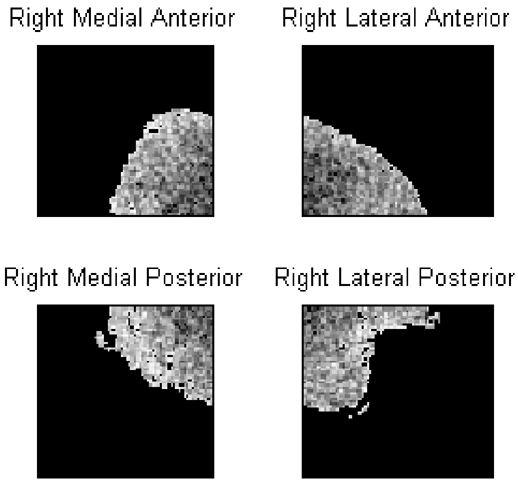

Figure 4.9: Right SCI distal tibia segmented into quadrants

The key parameter required to perform an automated spatial segmentation is the COM of the binary mask, i.e. the central voxel for the segmented bone. Section 4.1.3 already introduced how this is defined from the binary mark. Using this value, it is possible to automatically segment the bone image into the regions defined above. The segmented BMDtrab measurement can then be compared across a data series.

One of the assumptions made in this analysis is that the images are suitably registered during the previous stage of the image processing. The results given in Section 4.1.3 demonstrate that this is possible with acceptable accuracy. Consequently, the COM defined for one of the two paired images is therefore used in the definition of limits in the second image. This means that the regions are kept as consistent as possible across the images when carrying out comparisons and are not affected by any patient positioning error.

Example data demonstrating the benefit of both the segmented analysis as well as the Threshold peel method are given in Figure 4.10. These data are from two different longitudinal SCI subjects, scanned at 4 different time points.

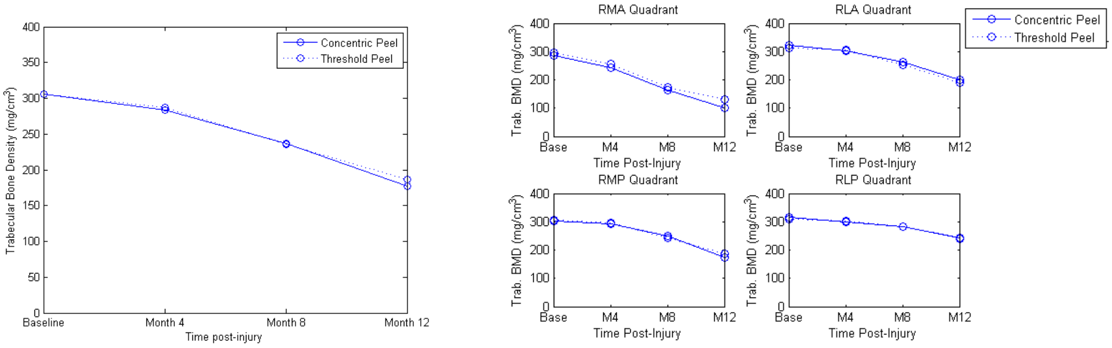

(a) Global longitudinal BMDTrab measurement in subject with inhomogeneous loss

(b) Inhomogeneous loss visualised graphically

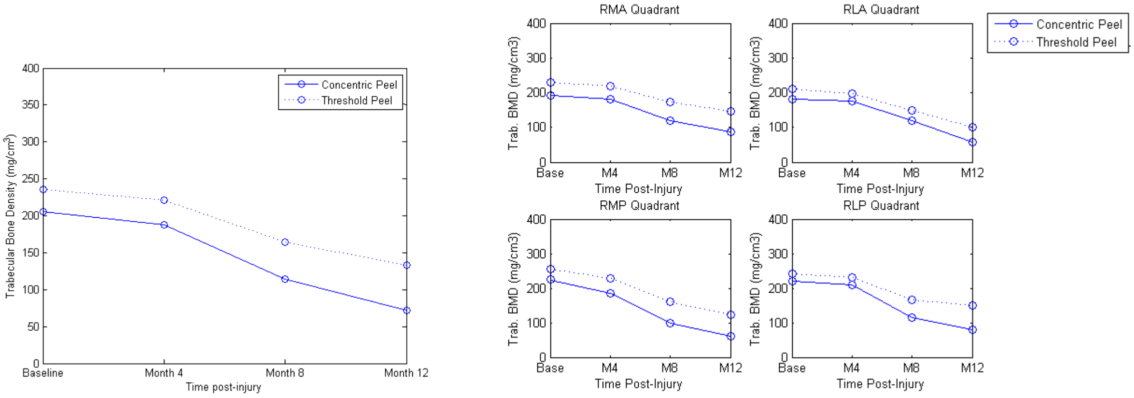

(c) Global longitudinal BMDTrab measurement in subject with central loss

(d) Central loss visualised graphically

Figure 4.10: Example demonstrating quadrant analysis of BMDtrab measurements of distal tibia in SCI subjects

The first subject's global BMDtrab measurements are shown in Figure 4.10a. This graph demonstrates a gradual loss in BMD over time, with no obvious difference in BMDtrab values measured using either peel technique. However, when the image was segmented and the quadrants were analysed individually, it becomes apparent that the right medial-anterior (RMA) quadrant is contributing to a substantial proportion of this overall loss in comparison to other regions of the bone. This particular quadrant drops to approximately 100mg/cm^3 by Month 12 whereas the other regions have values of at least twice this density. It is not apparent from the global graph that this inhomogeneous loss is occurring.

A second example, again measured from a SCI subject undergoing longitudinal imaging is also presented. Global BMDtrab and segmented BMDtrab measurements are displayed graphically in Figures 4.10c and 4.10d, with the quadrant data appearing to decline uniformly across the bone with time. This example demonstrates quite a clear difference between the Threshold peel algorithm's measurements to those of the Concentric peel measurement. The latter BMDtrab values are much lower than that of the Threshold peel algorithm. This would suggest that bone loss is occurring centrally within this subject, however the BMDTrab loss could possibly be overestimated if the Concentric peel measurements were taken on their own.

This software developed to measure regional trabecular bone changes has the potential to provide medical professions with additional information complimentary to the existing global BMDTot and BMDtrab measurement currently used in clinical practice. Regions within the bone at higher risk of osteoporosis could be targeted, or appropriate lifestyle advice given to the patient.

The segmented graphs provide a useful presentation of any localised bone changes, however it would also be interesting to offer a spatial map of bone turnover in an image format. Images convey information easily and quickly, with the visualisation of the loss understandable by both medical professions as well as the patients themselves. Therefore a second spatial analysis method was also developed, performing voxel wise comparisons across pairs of images. This software will identify those voxels which have experienced statistically significant changes in BMD and generate a statistical map which will convey this information visually within an image.

4.3 Voxel Wise Comparisons

The registered image pairs are used once more, in this case to perform voxel-wise comparisons of BMD. Broadly speaking, small windows of data are sampled at the same location across two images and the BMD values compared. The difference between each small window of BMD data is plotted onto a lower resolution output image, ΔBMD (as demonstrated in the Figure 4.11 example). The voxel size on this output image is the sum of voxels from the original image used for the statistical test. If the statistical test was significant, the voxel in the output image was assigned to be the difference, denoted by a colour scale. If the statistical test was non significant, the voxel in the output image was assigned to zero (white).

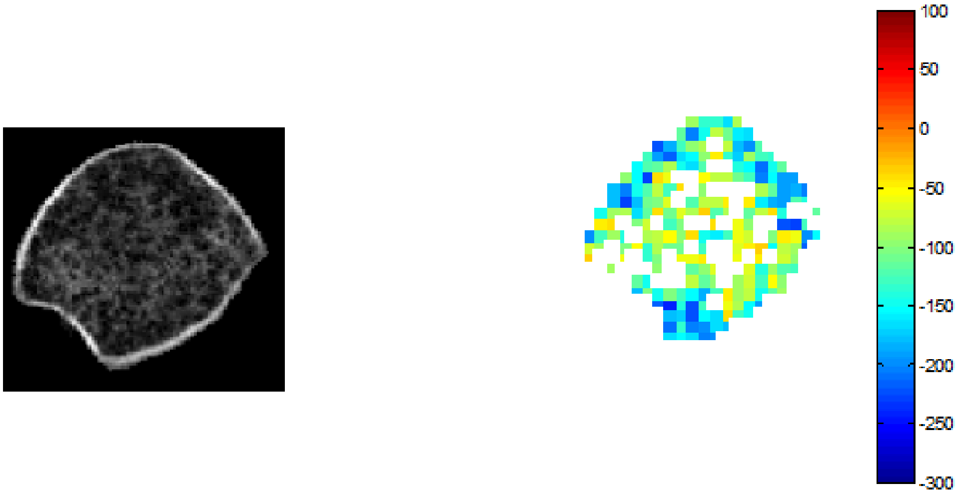

(a) Example pQCT image of 4% distal tibia

(b) Lower resolution output image from ΔBMD map, mg/cm^3

Figure 4.11: High resolution pQCT image versus low resolution ΔBMD map

Although the voxel based approach has some similarities with SPM, this analysis is in fact quite different. SPM type methods perform voxel based comparisons on the original, high resolution images, using groups of data sets (i.e. multiple data sets from the same subject or different subjects). This technique to map changes in BMD however, groups local pixels within each of the two individual high resolution images and performs statistical comparisons between these. Novel software is therefore necessary to perform these comparisons.

There are many considerations necessary when developing software which performs this type of analysis, in particular those concerning its statistical parameters. There are three primary statistical questions which need to be answered:

1. How big should the sample size of voxels be?
2. Which statistical test should be used to compare samples?
3. How does the analysis compensate for multiple comparisons?

An understanding of the statistical errors which may occur when carrying out these analyses is necessary, as well as a definition of the null hypothesis, H_0, for the study. In this instance the null hypothesis is that there is no change in BMD across image pairs.

4.3.1 Statistical Errors

When carrying out statistical testing which investigates a null hypothesis, there are four possible outcomes (Table 4.5)

A Type 1 Error is when the Null Hypothesis is rejected, when in fact it is true. In this study this would correlate to a voxel being declared as having a statistically significant change in

	Reject H_0	Fail to Reject H_0
Null Hypothesis, H_0 is True	Wrong Decision Type 1 Error False Positive	Right Decision
Alternative Hypothesis (H_1) is true	Right Decision	Wrong Decision Type 2 Error False Negative

Table 4.5: Statistical Testing Outcomes

BMD when in fact it does not, or in other words a False Positive. Studies try to keep Type 1 Errors as small as possible, which relates to the Significance Level, α, commonly set at 0.05 or 5%.

Type 2 errors, or False negatives, are often the result of the sample size being too small. In this study a Type 2 error would result in the voxel not being declared as having a significant change in BMD where in fact there was one. The probability of a Type 2 error, β, is generally unknown and it is often defined in terms of the error not occurring, β-1, or the Power of the test.

4.3.2 Sample Size Calculation

Statistical tests require a sample of data representative of the population of data, which in this case is within a region of bone. It is therefore necessary to determine a suitable sample size of voxels for comparison, which can be used to determine whether there is a statistically significant change in BMD between the two data set samples. In this study however, there are conflicting requirements to optimal sample size: a larger sample size would improve the statistical power and accuracy of the analysis however this would also result in a lower spatial resolution in the output image. In order to determine the required sample size of voxels needed to carry out voxel-wise testing across two bone images, it is necessary to define two parameters:

1. The statistical significance level, alpha (α) which is normally defined as 5%. α=0.05 is the false-positive rate.
2. The power of the study, or in other words the probability it will reject the null hypothesis. Typically power is defined as 1-β and is between 80-95%. A power of 80% would have a false-negative %, β, of 20

It is also necessary to know the mean value of the two groups of data under comparison as well as their standard deviation (SD). The sample size is the number of samples required which is of a sufficient statistical power, which can be used to make inferences about a larger population of data. There are many software packages that exist which perform sample size calculations. In this thesis, G*Power 3.1 was used [112] utilising a paired two-tailed t-test, with $\alpha = 5\%$ and $1\text{-}\beta = 80\%$.

The mean and SD voxel values were calculated for a sample of eight randomly selected subjects from both the SCI and ACL studies for 80% of the total bone area (cortical bone removed), for both tibial and the femoral slices. These calculations were then repeated for a second time-point, where a difference in BMD was expected to be present but at a minimum between the two scans. For the SCI study, the smallest difference in BMD predicted to be detected would be between the baseline scan and the month 4 scan and for the ACL study between contralateral limbs. Using the means and SD's of data from these two time points, the sample size, and therefore the voxel window size was calculated. A two-tailed t-test was used so that the sample size would be large enough to detect both significant increases and decreases in BMD (based on a Normal distribution).

The results from both SCI and ACL calculations can be found in Table 4.6. These values are the mean and SD across all eight subjects for both studies, where mean_8_1 BMD (SD_8_1 BMD) is for the first group, and mean_8_2 BMD (SD_8_2 BMD) the equivalent values for the second group.

Sample	mean_8_1 BMD	SD_8_1 BMD	mean_8_2 BMD	SD_8_2 BMD	Sample size calculated	Window size calculated
SCI distal tibia	285.7	11.5	273.3	11.7	9	3x3
SCI distal femur	276.2	24.9	257.2	27.6	18	5x5
ACL proximal tibia	225.3	24.8	206.7	23.1	17	5x5
ACL distal femur	289.1	40.3	268.5	39.4	32	5x5

Table 4.6: Sample size calculations

From the mean and SD values of the SCI data sets, a 3x3 window containing 9 voxels would provide sufficient power to characterise BMD changes between these two image pairs in the SCI distal tibia, with a 5x5 window suitable for the SCI distal femur. For the ACL study, a 5x5 window was chosen for both the proximal tibia and distal femur. For the ACL distal femur, this was selected as a reasonable compromise between statistical power of the test and the spatial resolution in the ΔBMD maps.

4.3.3 Statistical Test

The decision on a suitable statistical test to determine whether the differences in BMD are statistically significant is also required. The data in this thesis are "paired" (repeated measures) data sets, i.e. they are from the same person taken at two different time points/opposite legs. As a result of this there exists a natural correlation between the two data sets which has to be taken into consideration during the statistical analysis. The data are also "continuous" meaning that they can take any value on a given scale. In this study the data points are mg/cm^3 on a BMD scale. Finally, it is necessary to determine whether a parametric or non-parametric test should be used to compare the data sets. The main assumptions which need to be met when using parametric tests are that the data are Normally distributed, there is an adequate sample size and there is equal variance among sample populations [103]. As a result, it is difficult to determine if all these data are Normally distributed. The use of parametric tests, such as the Student's t-test in this instance, may therefore not be the most appropriate given the presence of smaller sample sizes and the uncertainty associated with the data's Normality. Non-parametric tests are an alternative means of determining statistical inference which do not make strict assumptions on the sampled data. The Wilcoxon signed rank (WSR) test is one such method, analogous to the paired t test, which uses rank order to accept or reject the null hypothesis. The primary obstacle with using non-parametric tests over parametric tests is that there is the possibility of them being less powerful i.e. ability to reject the null hypothesis. However, this is only the case if all of the assumptions underlying the parametric test are met, with comparison studies demonstrating non-parametric test frequently being as powerful as their parametric equivalents, especially when the sample size is small [113]. Therefore, for this study, the WSR test will be used to determine if the voxel samples taken from image pairs either accept or reject the null hypothesis that there is no change in BMD at that location within the bone. The p value returned is the probability that the null hypothesis is true, and will therefore be rejected if $p<0.05$ (5% significance level).

4.3.4 Multiple Comparisons

Ideally a voxel-by-voxel statistical test would be carried out and using a suitable threshold, typically $p<0.05$, to identify voxels which have a significant difference in BMD between images. However the problem with voxelwise hypothesis testing is that for every single test carried out, there is a 5% probability that the Null Hypothesis will be rejected when in fact it is true. If for example, 100 tests were carried out, an expected 5 of those tests will have a $p<0.05$ just by chance. In other words, there would be 5 results that would manifest themselves as positive when they were not. When this test is carried out on over 2000 voxels, such as the ΔBMD map images used in this thesis from the 3x3 windows, there will be approximately 100 voxels with a Type 1 error, which is much more substantial. This complication of multiple comparisons has been extensively investigated in the field of neuroimaging, where researchers are identifying active voxels in functional neuroimaging data sets across 10's of thousands of voxels. These studies have used methods which adjust the significance level threshold with which voxels are declared active, in order to appropriately reduce the number of Type 1 errors. There are a variety of methods which exist to control the effect of multiple comparison errors. One such technique is the Bonferroni method [114], which replaces the threshold, α=0.05, with α/k, where k is the number of tests carried out. This has been shown to control the quantity of Type 1 errors, however there are limitations to this method. These include the findings being dependent on the number of tests performed, focussing on the Null Hypothesis when this is generally not the main interest, as well as an increase in the number of Type 2 errors [115]. For these reasons improved methods of correcting for multiple comparisons in imaging have been developed, such as random field approaches [116, 117], permutation based methods [118, 119] and the False Discovery Rate (FDR) controlling technique [120, 121, 122]. Nichols and Hayasaka [123] carried out a comparative review of techniques used to control the familywise error rate (FWE) in functional neuroimaging, which included Bonferroni, random feld and the permutation test. They also commented on the FDR-controlling procedures, stating that they are *"...more powerful than FWE procedures, yet still control false positives in a useful manner. We predict that FDR may soon eclipse FWE as the most common multiple false positive measure."*. In 2007, Chumbley and Friston argued that the FDR is not appropriate for SPM, arguing that controlling the FDR of voxels is not equivalent to controlling the FDR of features, as used in neuroimaging [124]. Bennett *et al* [125] also discuss the advantages and disadvantages between the FWE rate and FDR controlling techniques. Using example images, the FDR corrected images had a greater power, with 4.9% of pixels identified as false positives, whereas on the other hand the FWE controlled images virtually eliminated all false positives, but the amount of detected signal (i.e. the power) was dramatically reduced. What they concluded was that when multiple testing is known to be a major issue, the type of correction used can be debated. However the implementation of some means of Type 1 error protection is necessary in order to move forward. Therefore, using the methodology of Li *et al* [63] as a basis, an FDR control technique was developed in this thesis for the purposes of Type 1 error control of the statistical test used to determine the ΔBMD output images.

FDR Control Technique

The ratio of False Positives, N_{FP}, to the total number of voxels declared active is given by the ratio shown in 4.5, also known as the False Discovery Rate (FDR)

$$FDR = N_{FP}/(N_{TP} + N_{FP}) \tag{4.5}$$

where N_{TP} is the number of True Positives. What this ratio demonstrates, is that if the number of True Positives is quite small, this ratio can be significantly higher than the desired significance level of 5%.

The False Discovery Rate controlling procedure was first presented by Benjamini and Hochberg in 1995 [120] and then expanded by Benjamini and Yekutieli in 2001 [126]. Genovese *et al* 2002 [121] provided a detailed account of its application in voxel based analysis.

The fundamental principal behind controlling the FDR is to ensure that the ratio in Equation

4.5 does not exceed a predefined threshold, q. Despite not knowing how many True or False Positives there are, it is still possible to control the FDR ratio. This will control the proportion of False Discoveries declared as active voxels. The procedure of controlling the FDR is as follows:

1. Define a desired threshold, q, between 0 and 1 that will be the maximum FDR tolerable (on average).
2. Order the p-values, $P_{(1)},\ P_{(2)}\ \ldots P_{(V)}$, where V is the number of simultaneous tests such that
$$P_{(1)} \leq P_{(2)} \leq \ldots \leq P_{(V)}$$
letting $v_{(i)}$ be the voxel corresponding to the P value $P_{(i)}$
3. Let r be the largest i for which
$$P_{(i)} \leq \frac{i}{V}\frac{q}{c(V)} \tag{4.6}$$
where $c(V)$ is a constant.
4. Declare all of the voxels $v_{(1)},\ v_{(2)}\ \ldots v_{(r)}$ active. This thresholds the image of test statistics using a P-value of $P_{(r)}$.

The value of $c(V)$ varies under different conditions. $c(V) = 1$ is used when the P values are independent test statistics [120], whereas if there is some form of dependency between the statistics, $c(V) = \sum_{i=1}^{V} 1/i$, as defined in [126]. In some imaging studies, there may be a dependency between pixel values due to factors such as smoothing the data (used widely when registering groups of images to a common size and orientation). However, strict independence is hard to verify and $c(V) = 1$ has been proposed as a good default (for neuroimaging [121]). Therefore $c(V) = 1$ has also been used in this study, where no smoothing has been applied to the data. Also, any dependency between voxels which are close neighbours in the original pQCT images, will be diluted during the process of producing statistic maps where the voxels are sets of 3x3 or 5x5 of the original voxels.

The application of the FDR correction can be demonstrated graphically using p-values generated from a longitudinal comparison of registered images from an SCI subject in Figure 4.12.

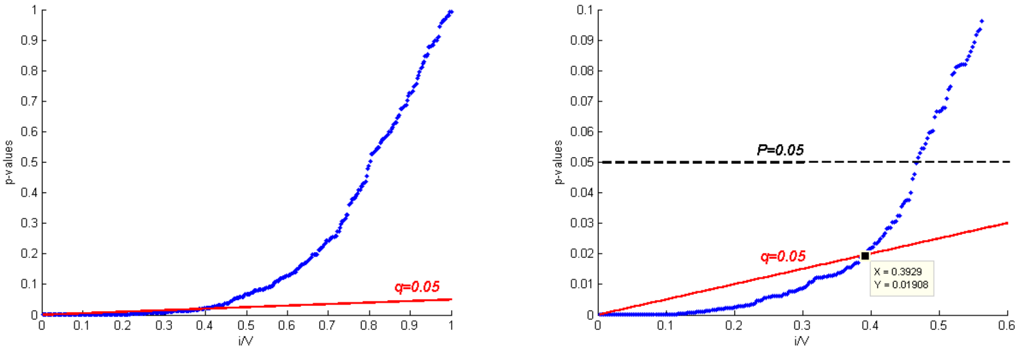

(a) Ordered p-values plotted with FDR control threshold, *q=0.05*

(b) Graph 4.12a zoomed to highlight the difference between *P* and *q* thresholds

Figure 4.12: Graphical demonstration of FDR controlling technique

The sorted *p*-values with an index *i* are plotted in order against i/V for $i=1, \ldots, V$. A line through the origin with gradient *q* is plotted and the largest *p*-value below the line corresponds to the FDR-corrected threshold. All voxels with a *p*-value less than or equal to this threshold are declared active. The non-corrected threshold of $p=0.05$ is also plotted on the graph for comparison. For this particular subject, where previously 170 voxels would have been declared active using a threshold of $p=0.05$, applying the FDR-correction results in a total of 143 voxels now being declared active with a *q*-value of 0.05. The new *p*-value threshold is p=0.019 (highlighted on Figure 4.12b).

One of the obvious advantages of this method is its adaptation to the individual signal. There is no requirement to define an arbitrary fixed threshold, the operator simply defines the rate of false discoveries they are willing to tolerate. It is also important to note that this method will ensure that *on average* the FDR will not exceed the defined threshold *q*. As the number of False Positives is actually unknown, the guarantee would be that if the experiment were repeated several times, the overall average of FDR voxels would not exceed *q*. For any one particular analysis within that repeated data-set of experiments, the FDR may actually exceed *q*.

4.3.5 Voxel-Wise Comparison Maps

One of the main goals of this methodology is to generate an image showing a map of statistically significant differences in BMD across pairs of images for a particular individual. As a reminder, this map could be two registered longitudinal images from a SCI subject, or two contralateral images comparing injured or non-injured knees of ACL injured subjects. Once a particular voxel has been declared active, as having experienced a significant change in BMD over the 3x3 or 5x5 neighbourhood at that location, an mean change in BMD difference across the two samples is assigned to that voxel on the ΔBMD output map.

Example images of the final display from the distal tibia, proximal tibia and distal femur are given below. The colour map presents the user with a visual identification of where the subject is experiencing the largest significant changes in BMD.

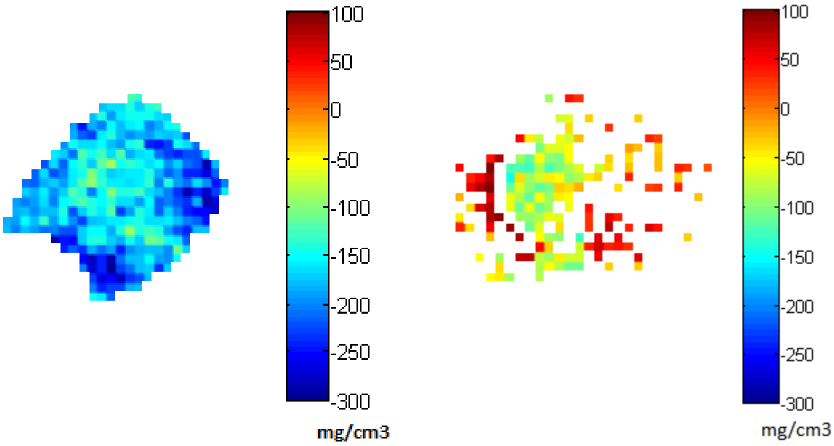

(a) SCI distal tibia ΔBMD example (b) ACL proximal tibia ΔBMD example

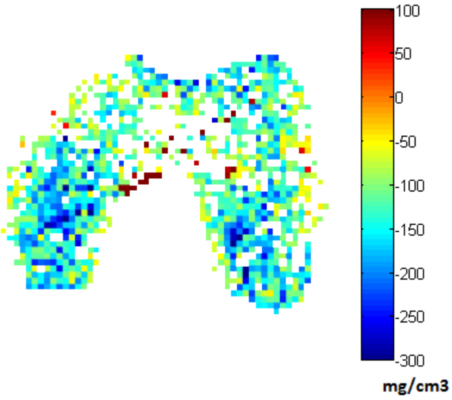

(c) SCI distal femur ΔBMD example

Figure 4.13: ΔBMD maps for distal tibia, proximal tibia and distal femur

In Figure 4.13a the 3x3 ΔBMD map informs the user that this subject has experienced BMD loss globally, however in particular there are some areas medially and posteriorly which are proportionally experiencing more significant loss compared to the rest of the bone. Figure 4.13b is an example from the proximal tibia from the ACL study, which uses samples from a 5x5 shifting voxel window across the pairs of images. This image identifies regions within this bone which have also experienced bone loss, which appear to be occurring primarily centrally, with some increases in BMD also being visualised. Those regions which have had no statistically significant change in BMD are represented by the white voxels. Finally, Figure 4.13c compares two images of the distal femur again from the SCI population, using a 5x5 neighbourhood window for the statistical test. In this example the majority of voxels have experienced a decrease in BMD, some of which are losses >200mg/cm^3. In this image there is again, a small proportion of voxels demonstrating no significant change.

It is clear that these images provide additional useful information, which is complimentary to the measurement of total BMD. It is important to bear in mind that healthy bone still does experience normal bone turnover, therefore increases and decreases in BMD would still be present in healthy subjects to some degree. However, using these images it is now possible to characterise the localised changes in BMD an individual is experiencing, which is new information the clinicians currently do not have. In subjects who are experiencing osteoporotic changes, the distribution of bone loss within the bone may be a link to identifying individuals who are more susceptible to low impact or fragility fractures.

4.3.6 Validation of Software

Testing was performed in order to determine how well the software developed for the FDR correction method removed false positives. Simulated data was generated by adding normally distributed pseudorandom noise to segmented bone images. A voxel wise comparison was carried out comparing the noisy image with it's original parent image.

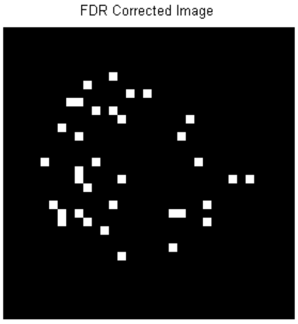

Figure 4.14: False Positives identified after FDR correction

An example is given in Figure 4.14 of a distal tibia image with noise following FDR correction. For this example, the number of false positive voxels which remained active following FDR correction was approximately 8%. This was repeated for an additional ten images randomly selected from the distal and proximal tibia and distal femur. In most cases the FDR correction completely removed all of the false positives, with only three still containing a small proportion of false positives following FDR correction, including the example given in Figure 4.14.

These simulations have demonstrated that the false positive error rate for the FDR correction did not exceed 8%. If this were to be averaged across all 10 images tested, there would be an agreement with Benjamini and Hotchberg's statement that the proportion of false hypotheses will not exceed the q threshold [120], which in this case is 5%.

4.4 Summary

This chapter has presented the first of two novel post-processing methods developed using Matlab. In order to perform accurate spatial mapping of bone turnover, it was necessary to initially register image pairs. Following this, software was developed which analysed trabecular changes within different quadrants of the bone. Finally, a technique which performed voxel-wise comparisons on pairs of registered images was described and tested. The development of this method was necessitated by a need for comparison of two individual images. Existing techniques which compare an image to that of a group of images were not appropriate for either the SCI or ACL studies, due to each individual's unique response to injury in these two studies. It was therefore necessary to go back to the fundamental principals of voxel analysis techniques and develop something suitable for analysis of two individual images. The overall aim of these methods is to provide clinicians with information additional to the global BMD measurement, generating either graphically or as a bone map image any potential regions within the bone which may be experiencing more extreme rates of bone loss. Conversely, it could also be used to inform researchers if interventional techniques were successfully managing to restore bone, either globally or in more localised focussed regions.

The next chapter describes the second of the two post-processing methods. It differs from these techniques in that it assesses the *patterns* of bone within a segmented image. As bone becomes more osteoporotic, the structural integrity of the trabecular struts changes becoming weaker and more porus, which can ultimately lead to fracture. Information on these trabecular patterns is inherent within pQCT images. There is therefore an opportunity to explore whether these patterns can provide additional information on the condition of the bone. As osteoporosis is defined as a combination of both low bone density and microarchitectural deterioration [16], Chapter 5 presents a technique which performs a structural assessment on the bone's architecture using mathematical morphology, in an attempt to compliment the measures of BMD and assist in the characterisation of osteoporosis.

Chapter 5

Morphological Descriptors of Trabecular Architecture

Mathematical morphology is a methodology used to describe the shape, size and distribution of structures present within an image. As opposed to linear transformations where there is a relationship between the image and its building blocks, such as the Fourier transform decomposing an image into its constituent frequencies, morphology is a non-linear technique which uses set theory and geometry to extract information from an image. It was first introduced by Matheron [127] and Serra [128] who were investigating geological patterns of core samples, using the concept of size and structures of these patterns to quantify properties of the samples. The theory was later extended by Heijmans in terms of lattices [129]. This was then applied to fields such as microbiology, aerial image processing and medical diagnostics to name a few [130, 131, 132, 133]. Mathematical morphology examines the geometric structure of an image using a small pattern of pixels known as a *structuring element*. The closer a structuring element (SE) is to the shapes of objects within the image, the stronger the signal that is produced during the interrogation. By marking the locations where the structuring element fits, information related to the structure of the image can therefore be derived.

For example, the blue circle, A in Figure 5.1a[1] is completely contained within the yellow circle B, A is therefore a **subset** of B ($A \subseteq B$). However, the same blue circle A, does not fit in the red rectangle C (Figure 5.1b) and is **not a subset** of C ($A \nsubseteq C$).

---

[1] This, and all subsequent figures in this chapter are original examples created by the author

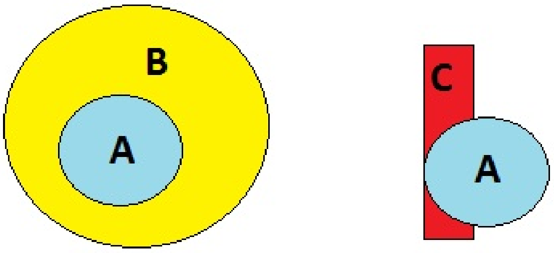

(a) A is a subset of B (b) A is not a subset of C

Figure 5.1: Set Theory Examples

It is this simple model of A either being completely contained within a structure or not that can be used to assist the description of the basic morphological operations, where the blue circle A would constitute the structuring element and both the yellow circle B and red rectangle C would be the images under interrogation. If A fits into B or C, this provides information about the image's shape and size relative to that of the structuring element. The basic operators used in mathematical morphology are called Erosion, Dilation, Opening and Closing. For simplicity, descriptions using Euclidian binary images will be used to illustrate these methods (as opposed to discrete images). This concept can then be expanded and applied to much more complex gray-scale pQCT images. Applying morphological analysis to the shapes and patterns of trabecular architecture present within these medical images could be used to provide additional information on how the bone is responding to change or whether certain patterns of bone structure are more susceptible to bone loss in comparison to others.

5.1 Morphological Processing of Images

Practically speaking, morphological image processing applies a structuring element to the pixels within an original image to create an output image based on the structural properties of the pixels within it. Erosion and dilation produce contrasting results when applied to an image, with erosion shrinking the structures within an image and dilation expanding them.

5.1.1 Erosion

The **erosion** of an image A by structuring element B at point x within the image is denoted by $A \ominus B$ and is defined by

$$A \ominus B = \{x : B_x \subseteq A\} \tag{5.1}$$

where $\subseteq$ denotes the subset relation and where B_x is the translation of the SE B by a point x, i.e.

$$B_x = \{b + x \mid b \epsilon B\} \tag{5.2}$$

$A \ominus B$ exists for all points of x for which the translation of B by x fits inside A. Equations 5.1 and 5.2 can be described visually using the diagrams below.

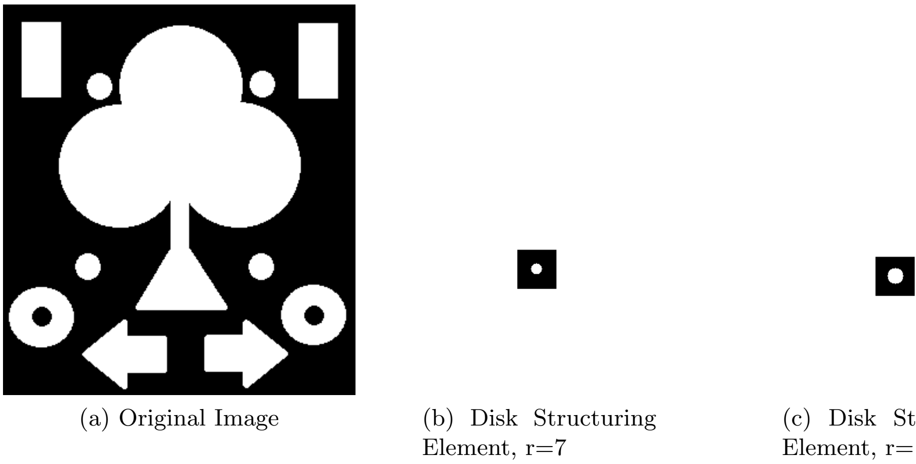
(a) Original Image
(b) Disk Structuring Element, r=7
(c) Disk Structuring Element, r=10

Figure 5.2: Original Binary Image and Two Structuring Elements

Figure 5.2a is the original image, consisting of several different shapes each of varying size. Eroding each of these shapes with a structuring element will produce different output shapes depending on how well the structuring element fits within the shapes. 5.2b and 5.2c are two disk shaped structuring elements of radius, $r=$ 7 and 10 pixels respectively. When both are applied to the original image, the following output images are produced:

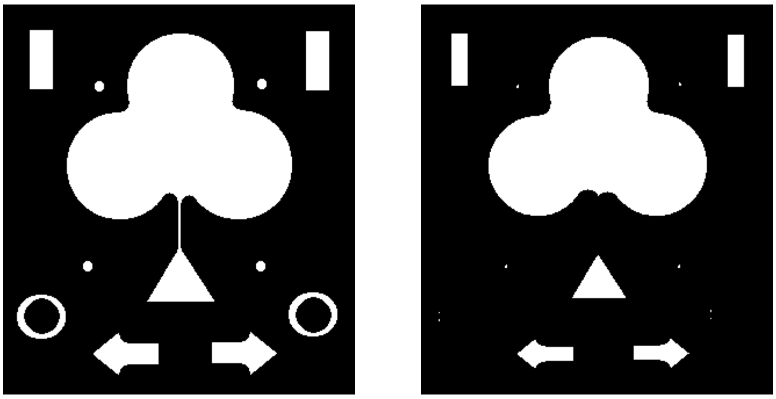
(a) SE Radius=7
(b) SE Radius=10

Figure 5.3: Original Image eroded with structuring elements (a) r=7, and (b) r=10

In this instance the origin of the structuring elements are the central pixels, and as a result the eroded images are subsets of the original. What has become apparent in Figure 5.3a, is that the four small circles surrounding the tree structure have almost completely disappeared, with the two larger doughnut shapes also having shrunk in size. The hole in the centre of these circles has also grown in diameter following erosion. Some of the once previously sharp lines within the shapes have became more rounded as a result of the disk shaped SE, for example, the bottom of the arrow heads. This is a result of the structuring element being unable to fit into small sharp corners of objects, which has the effect of removing these sharper edges. Performing erosion with a structuring element which has only a two pixel increase in radius (r=10), demonstrates quite a considerable difference in the output image. In Figure 5.3b the stem of the tree object did not survive this process, neither did the four small circular structures. The reason for this is that the width of these objects is now less than the size of the structuring element, whereas previously they had not been. Increasing the structuring element even more would eliminate some of the larger structures, such as the rectangles or the arrows.

Using a simple binary image, these two examples demonstrate that erosion shrinks or thins objects within an image, and as a result can be thought of as a *morphological filtering* operation, where image details smaller than the size of the structuring element are filtered (or removed) from an image.

5.1.2 Dilation

Whereas erosion shrinks or thins the objects within an image, dilation is the opposite, growing or thickening objects. Dilation can be thought of as a shrinking of the background i.e. dilation takes the complement of an image and then performs an erosion - it is a dual operation to erosion. The **dilation** of a set A by B is denoted as $A \oplus B$ and is defined by

$$A \oplus B = \left(A^C \ominus \breve{B}\right)^C \tag{5.3}$$

where A^C denotes the set-theoretic complement of A and $\breve{B}$ is B rotated around the origin. Once again, a description of the Equation 5.3 can be demonstrated visually using the binary image of simple shapes from Figure 5.2a and the two disk structuring elements with r=7 and r=10.

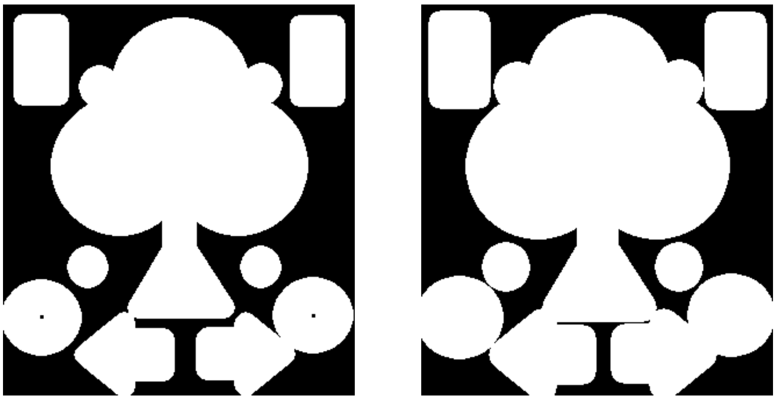

(a) SE Radius=7 (b) SE Radius=10

Figure 5.4: Original Image dilated structuring elements (a) r=7, and (b) r=10

Following dilation, it is now possible to observe the thickening of objects associated with this operation from Figure 5.4a. Two of the small circles which were once distinct objects situated in close proximity to the tree structure have now merged with the tree. Many of the sharp edges from the original image present in the rectangles and arrows are now more rounded, a direct result of the expansion of these objects using a disk shaped structuring element. Incidently, if a square SE had been used this would not have been the case. The smoothing of these sharp edges becomes even more apparent following dilation of the original image using a structuring element or r=10 (Figure 5.4b). Dilation has also filled in the small holes (relative to the structuring element) within the doughnut shapes. Where erosion eliminates small components and extrusions of the image, dilation fills in small holes and protrusions into the image. Since dilation involves a fitting onto the complement of an image, it represents a filtering on the outside.

5.1.3 Opening

Where erosion and dilation would be considered the two primary operations of mophological image processing, **opening** and **closing** are the two secondary operations, both of which expand on the notion of using morphological operators as image filters. This chapter will focus primarily on opening, as its definition is key to understanding Granulometries (Section 5.2). However the properties of closing are simply analogous to opening via complementation [134].

The opening of an image A by image B is denoted by $A \circ B$ and is defined using a combination of erosion and dilation by

$$A \circ B = (A \ominus B) \oplus B \tag{5.4}$$

Hence, the opening of A by B is the erosion of A by B, followed by the dilation of **the result** by B. Conversely the closing of A by B is denoted by $A \bullet B$ and is defined by

$$A \bullet B = (A \oplus B) \ominus B \tag{5.5}$$

Opening by a disk structuring element has the effect of smoothing from the inside of the object, or in other words rounding the corners that extend into the background of the image. (Closing smooths from the outside, rounding corners that protrude into the image from the background). Equation 5.4 can be represented visually by opening an image containing simple shapes (Figure 5.5a) with the disk shaped structuring element, $r = 7$, used previously (Figure 5.2b).

(a) Original Image

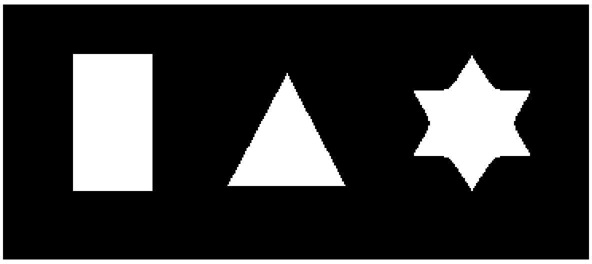

(b) Original Image Eroded

(c) Original Image Opened (Erosion then Dilation)

Figure 5.5: Original Binary Image, Erosion and Opening

During opening with a circular structuring element, the resultant boundary of the three shapes above is defined by the furthest points inside each shape that the structuring element will fit inside. The ball will not fit into the extreme corners of each shape and consequently the resulting union removes these sharp edges. Using the triangle as an example, this is demonstrated in Figure 5.6.

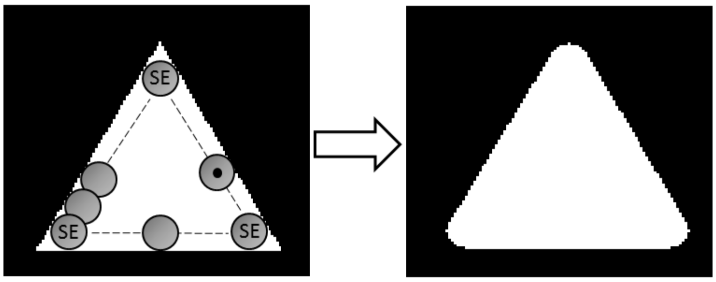

Figure 5.6: Structuring element translating along the inner boundary of triangle. Corners are removed.

The boundary of $A \circ B$, where A is the triangle and B is the circular structuring element in the above example, is defined as the furthest points B can reach within the inside boundary of A. The set theoretic equivalent of this description would be that the opening of A by B is obtained by taking the **union** of all translations of B that fits in A, which expressed algebraically gives:

$$A \circ B = \bigcup \{B_x : B_x \subseteq A\} \tag{5.6}$$

where $\bigcup$ denotes the union of all the sets inside the brackets. Once again, the resultant image would be quite different if a square or a triangular structuring element were used. In this instance, using a disk shaped structuring element, opening can be thought of as a *smoothing filter*, removing sharp edges from the image. It can also be used to remove noise from an image as demonstrated in Figure 5.7. The image containing three simple shapes used in the previous example is this time corrupted by some noise. Opening this image with the circular structuring element in Figure 5.2b has a restorative effect on this image. This is because, in a similar way that the structuring element does not fit into the small corners of the shapes, is also does not fit inside the noise. Consequently, the noise does not survive the opening process, and with the exception of the rounded corners, the original shapes have been restored.

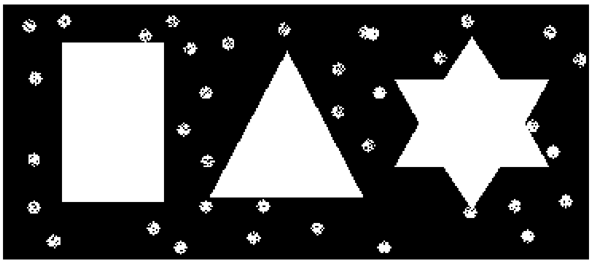

(a) Original Image + Noise

(b) Original Image with noise removed

Figure 5.7: Example of noise removal using morphological opening

Although this is a very basic example of the filtration properties of morphological opening, this example sets the foundations upon which the measurement of trabecular survival can be built. The notion of how well a trabecular bone pattern within an image can survive a morphological opening, has the potential to describe how densely or sparsely spaced the trabecular struts or pores are situated within each subject's tomographical bone image. This information could provide further insight into investigating whether subjects with particular bone structures experience specific bone responses in response to stimuli (or lack thereof).

5.2 Granulometries

A granulometry is a measurement of the size and distribution of a collection of particles or grains. In image processing, granulometries using mathematical morphology is a method used to characterise granular images in terms of a sieving analogy (conceived by Matheron, 1975 [127]). For example, consider a sample of small grains of different sizes in a sieve, the ability for each grain to pass through the mesh of this sieve will depend on its size and shape relative to the mesh. As the size of the holes in the mesh is gradually increased, more and more of the grains will pass through the sieve until no more grains remain. By counting the residual grains after each sieving, an estimate can be made of the size distribution of the total sample of grains.

In terms of image morphology, the sample of grains would correlate with the pixel groups within the image itself and the size and shape of the mesh to that of the structuring element. The sieving action itself shares all of the same properties as a morphological opening [135]:

- what is left in the sieve can only be a *subsample* of the input image (anti-extensivity),

- when sieving a subsample of a larger sample, what remains in the sieve is a subsample of what would remain when sieving the whole sample (increasingness), and
- sieving a sample twice through the same sieve does not sieve further this sample (idempotence).

This therefore means that the granulometry concept can be applied to images by performing a series of openings using structuring elements of increasing size. With each progressive opening, fewer and fewer pixels will remain in the residual image, until such a point where no more pixels remain. It is this sequence of sieved images that are called the granulometry images. This process will in turn generate a unique image signature based on the rate that pixels are removed after each "sieving". This method is not exclusively limited to images of grains, but is also an effective means of describing image texture and the distribution of pixels within an image, say for example, those within a trabecular bone structure.

5.2.1 Granulometries using Sequential Opening

As discussed in section 5.1.3 and defined in Equation 5.4, opening is an erosion followed by a dilation. Equation 5.4 defined A as the image under interrogation, with B as the structuring element performing the opening. Introducing a variable t, where $t > 0$, the class of operators Ψ_t defined by $\Psi_t(A) = A \circ tB$ is called a **granulometry**, and the primitive B is said to be the **generator** of the granulometry. If $\Omega(t)$ is the area removed by opening with tB, then

$$\Omega(t) = v[A] - v[A \circ tB] \tag{5.7}$$

where v denotes area (or volume). $\Omega(0) = 0$ and $\Omega(t)$ is an increasing function of t. A can be defined as having finite extent in the application to images, therefore for a sufficiently large t, $\Omega(t) = v[t]$. $\Omega(t)$ is known as the image **size distribution**.
A normalised size distribution is defined by

$$\Phi(t) = \frac{\Omega(t)}{\Omega(\infty)} = \frac{\Omega(t)}{v[A]} \tag{5.8}$$

$\Phi(t)$ increases from 0 to 1 and can be shown to be a probability distribution function. Thus, its derivative $d\Phi(t)$ is a probability density. Both $\Phi(t)$ and $d\Phi(t)$ are known as the **pattern spectrum** of the image relative to the shape of the generating structuring element.
For this model to hold true, the opened image must be a sub-image of the previous. Therefore accordingly, the construction of the sequential structuring elements requires a systematic approach. Both of these conditions are met by defining the sequence of structuring elements, B_t, for $t = 1, 2, \ldots$ as

$$\begin{aligned} B_1 &= B, \\ B_2 &= B \oplus B, \\ B_3 &= B \oplus B \oplus B, \ldots \end{aligned} \tag{5.9}$$

and so forth, where B_0 is a single pixel. The opening of A using this set of structuring elements will in turn satisfy the condition that each opened-image is a sub-image of the previous, or in other words

$$A \circ B_1 \supset A \circ B_2 \supset A \circ B_3 \supset \ldots \tag{5.10}$$

Once again, it is helpful to describe the process of generating image granulometries and their associated pattern spectrum distribution with the use of an illustration. Figure 5.8a has circles of 3 different radii randomly scattered throughout the image. The same disk shaped structuring element as in the previous two examples is used as the generator of the granulometry, however in this instance a sequence of SE's will be created as described in Equation 5.9. As the size of the structuring element increases, the different sizes of circles are removed, or "sieved" from the image. Figures 5.8b and 5.8c demonstrate two key moments during the sequence of openings. Once the radius of the structuring element reaches 9, the smallest of the 3 circles are removed from the image (Figure 5.8b), and again when the radius reaches 14, the medium sized circles are eliminated (Figure 5.8c).

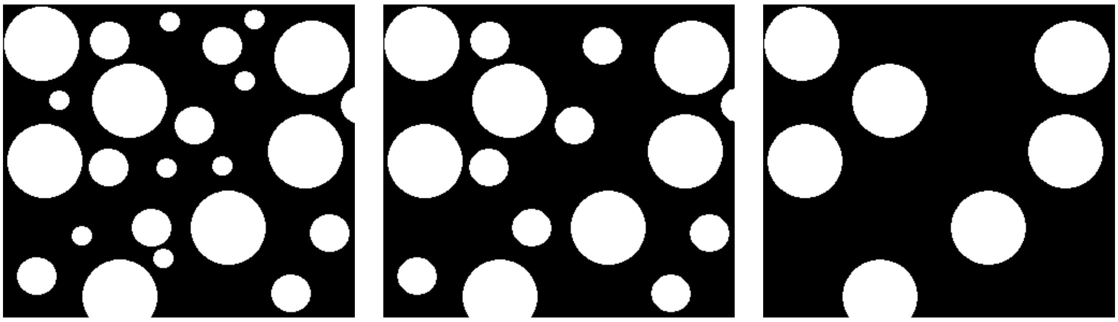

(a) Original Image

(b) Residual Image Following 9 Openings

(c) Residual Image Following 14 Openings

Figure 5.8: Binary Granulometry Example

Following each opening, the area removed is determined using Equation 5.7. Normalising the result using Equation 5.8 generates the following graph.

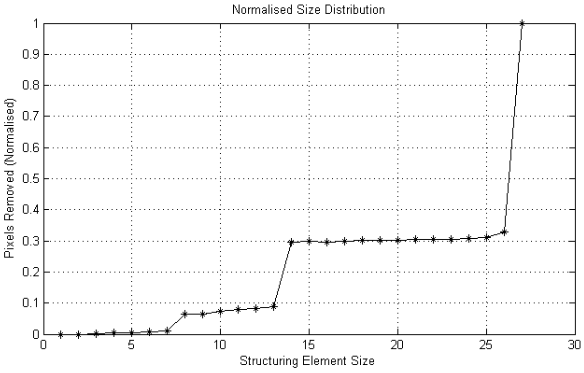

Figure 5.9: Granulometry Size Distribution

The discrete **pattern spectrum** of the image taken from the derivative of this probability size distribution, relative to the disk generator can then be produced - Figure 5.10.

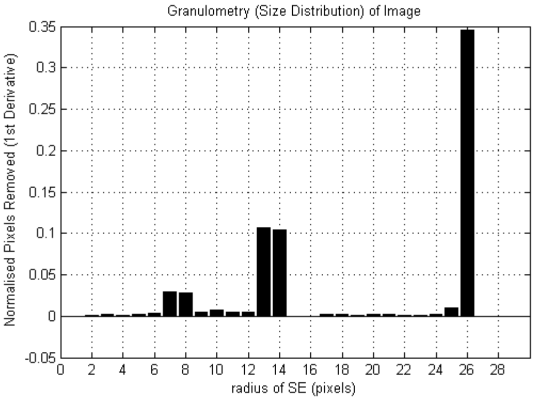

Figure 5.10: Discrete Derivative of Size Distribution Plot - Pattern Spectrum

This derivative pattern spectrum distribution graph, $d\Phi(t)$, identifies the proportion of pixels removed by each radius of the structuring elements during the sequential opening. There are three locations where there are distinct peaks, at $r = 7$ and 8, 13 and 14 and $r = 26$. These radii therefore identify the approximate size of the three circles within the image. What this has demonstrated is that this technique is a useful way of extracting information related to the shapes within an image.

It is worth noting at this stage however, that the outcome of this pattern spectrum distribution (PSD) would not be as clear cut if the circles were overlapping within the image. The combination of two smaller circles would result in a larger object within the image, which would survive the opening process much longer than if the circles were independent objects. There would only be distinct peaks in the pattern spectrum if the SE is a similar shape to the image structure. In the above example, a circular SE was used to open an image containing circles and as a result, distinct peaks are obtained.

A second example giving the pattern spectrum distribution of a simplified drawing of bone (crude trabecular struts contained within a circle), is given in 5.11a. When an image contains random shapes and structures, the resultant granulometric pattern spectrums are also random distributions, as demonstrated by its corresponding $d\Phi(t)$ in Figure 5.11b.

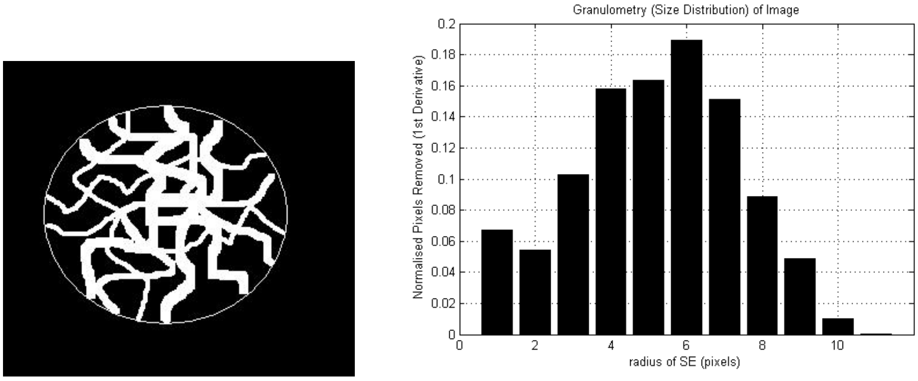

(a) Binary Bone Demo

(b) Pattern Spectrum Distribution of Bone Demo Image

Figure 5.11: Binary Granulometry Example 2

As each individual image will create its own unique pattern spectrum, the spectrum itself will in turn have its own **granulometric moments**, such as the *pattern spectrum mean* (PSM), *pattern spectrum variance* (PSV), or the *pattern spectrum skewness* (PSS). These measurements are a means of quantifying the image's granulometric signature and are calculated using the occurrence probability $P(i)$ of a structuring element size, i, and its ability to remove voxels from an image. It is obtained from a pattern spectrum distribution histogram such as in Figure 5.11b, and is defined in Equation 5.11

$$P(i) = \frac{N(i)}{M} \tag{5.11}$$

where $N(i)$ is the number of voxels removed from the image with a structuring element size i and M is the total number of voxels in the histogram. Using this occurrence probability, it is possible to calculate the properties specific to the pattern spectrum distribution (granulometric moments) such as it's mean, variance and skewness, as defined in Equations 5.12, 5.13 and 5.14, where N_g is the number of structuring element sizes used to generate the pattern spectrum.

$$\text{Mean}\,(\mu) \qquad f_1 = \sum_{i=0}^{N_g-1} iP(i) \tag{5.12}$$

$$\text{Variance}\,(\sigma^2) \qquad f_2 = \sum_{i=0}^{N_g-1} (i-\mu)^2 P(i) \tag{5.13}$$

$$\text{Skewness} \qquad f_3 = \frac{1}{\sigma^3}\sum_{i=0}^{N_g-1} (i-\mu)^3 P(i) \tag{5.14}$$

The pattern spectrum moments associated with the graph in Figure 5.11b are therefore given in Table 5.1.

	PSM	PSV	PSS
Disk SE	5.21	4.58	-0.14

Table 5.1: Demo Pattern Spectrum Moments

These moments have parallels with texture analysis, where they are also known as First Order Features. As with texture analysis, it is by using these features, or moments, that makes it possible to extract hidden content on the structures and patterns contained within an image.

5.3 Gray-Scale Granulometries

So far discussions and examples have been based on binary images, however the same theoretical processes can be extended to gray-scale images. This evidently would be the case if applying the methodology to pQCT images of the bone. The primary difference when using gray-scale images is the additional dimension associated with the image i.e. the pixel density. The different densities of the pixels within the image can be visualised using the gray-scale image of a 4% distal femur slice, Figure 5.12a and its 3D representation, Figure 5.12b.

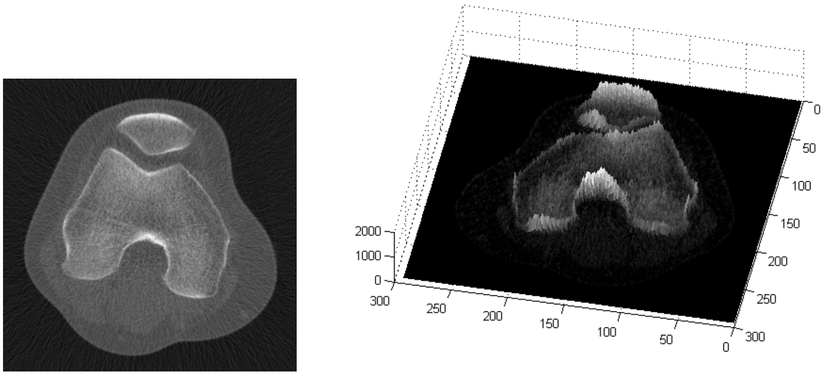

(a) Distal Femur Image (b) 3D Representation of Distal Femur

Figure 5.12: Gray-scale Image and Corresponding 3D Surface Image

Instead of only removing groups of pixels when the structuring element matches the size of the objects within an image, granulometric analysis of gray-scale images results in a gradual decrease in the pixel density values. An example using a subset of the above femoral image, Figure 5.12a which has been segmented to remove the surrounding structures is presented. Applying sequential openings to this image using a circular structuring element generates the following four granulometries for structuring elements of radius 1, 3, 5 and 7.

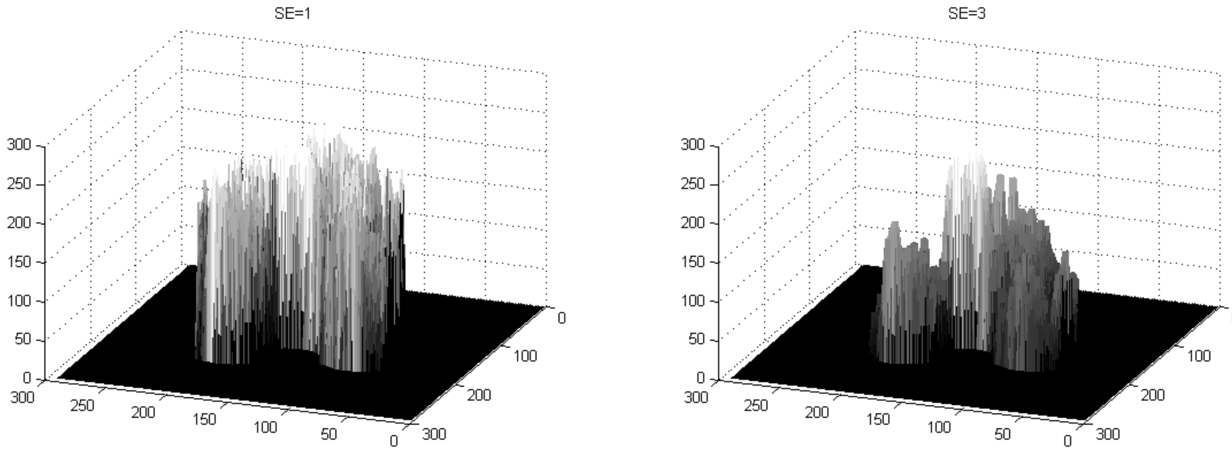

(a) SE1

(b) SE3

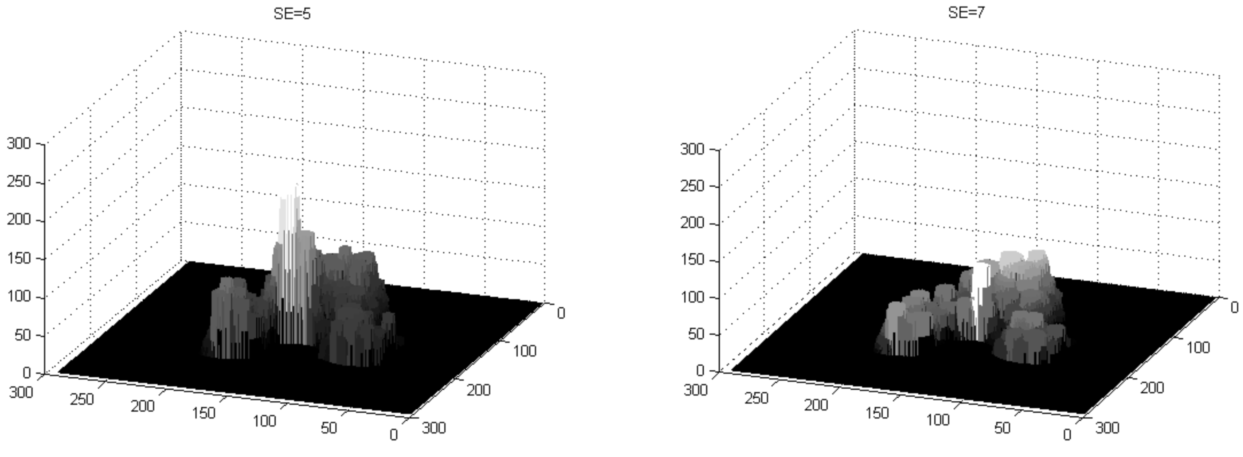

(c) SE5

(d) SE7

Figure 5.13: Granulometries of Femur

The main observation which can be made from this sequence of four images is that the images become much less ‘spiky’ as the structuring element size increases, and by Figure 5.13d the shape of the structuring element can almost be visualised within the gray-scale pattern in the bone. In order to take a closer look at what is happening to the amplitude of the image pixels, a 1-D profile signal from across the centre of the femur at each of the above four stages is presented.

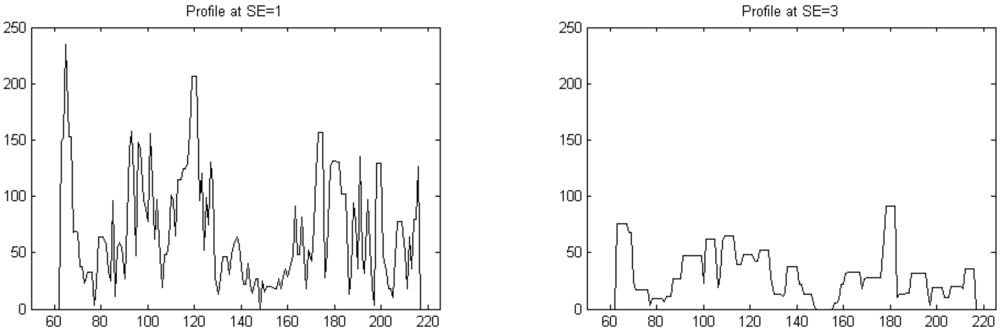
Profile at SE=1

Profile at SE=3

(a) SE1 Profile

(b) SE3 Profile

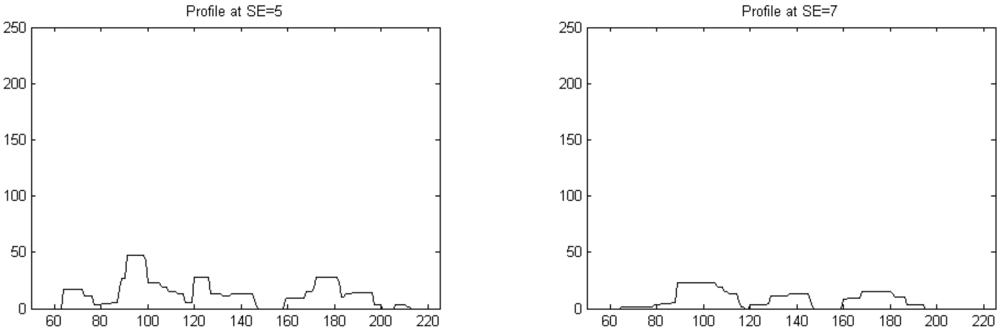
Profile at SE=5

Profile at SE=7

(c) SE5 Profile

(d) SE7 Profile

Figure 5.14: 1-D opening profiles through centre pixel of femur

It is now possible to see from both Figures 5.13 and 5.14 that there is a decrease in pixel density value of the images and a flattening out of the profiles as the size of the structuring element increases. The reason for this is that for each opening, the structuring element is pushed up against the bottom of the underside of the image surface and translated across the entire domain. The granulometry is constructed by finding the highest points reached by any part of the structuring element as it is moved along the undersurface of the image. The 1-Dimensional profiles demonstrate a graphical illustration of this occurrence quite nicely. The sharp peak at location 70 on the x-axis in Figure 5.14a, does not survive the 7th iteration of the opening (as it is missing in Figure 5.14b). By this point, the structuring element is now too large to fit up inside this peak. What the process is therefore doing is suppressing the brighter fine details within the image with each iteration.

5.3.1 Global Pattern Spectrum Moments

As with the previous binary example in Figure 5.11, a gray-scale image will also generate a Pattern Spectrum Distribution plot. This too will have its own granulometric moments. Figure 5.15 is the pattern spectrum distribution of the segmented knee image discussed in the previous example.

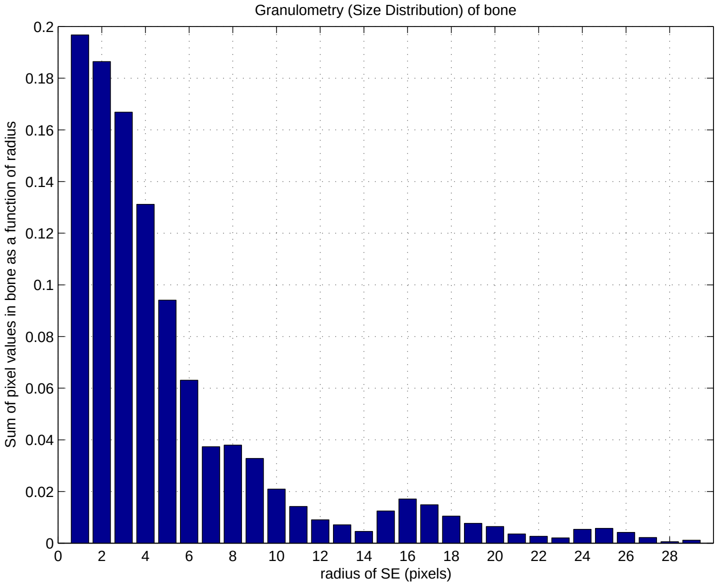

Figure 5.15: Pattern Spectrum Distribution of Knee Image

The pattern spectrum moments associated with this graph are

	PSM	PSV	PSS
Disk SE	5.26	26.91	2.03

Table 5.2: Pattern Spectrum Moments of Knee Image (disk SE)

Notice how in this example the variance is much larger that the black and white demo image. The image has survived openings up to a SE radius of 26, however the majority of the pixel density is removed during the first few openings.

The pattern spectrum distribution graphs and their moments will only start to have meaning when they are compared across data-sets. Ideally, the moments either individually or in combination with other moments could provide a user with additional information related to the structures within the image, for example changes in bone patterns following a certain time period. For instance, the changes in granulometry PSD of an SCI subject during their first year post injury, can be observed in Figure 5.16, with each graph's associated moments given in Table 5.3 (generated using segmented 4% distal tibia images).

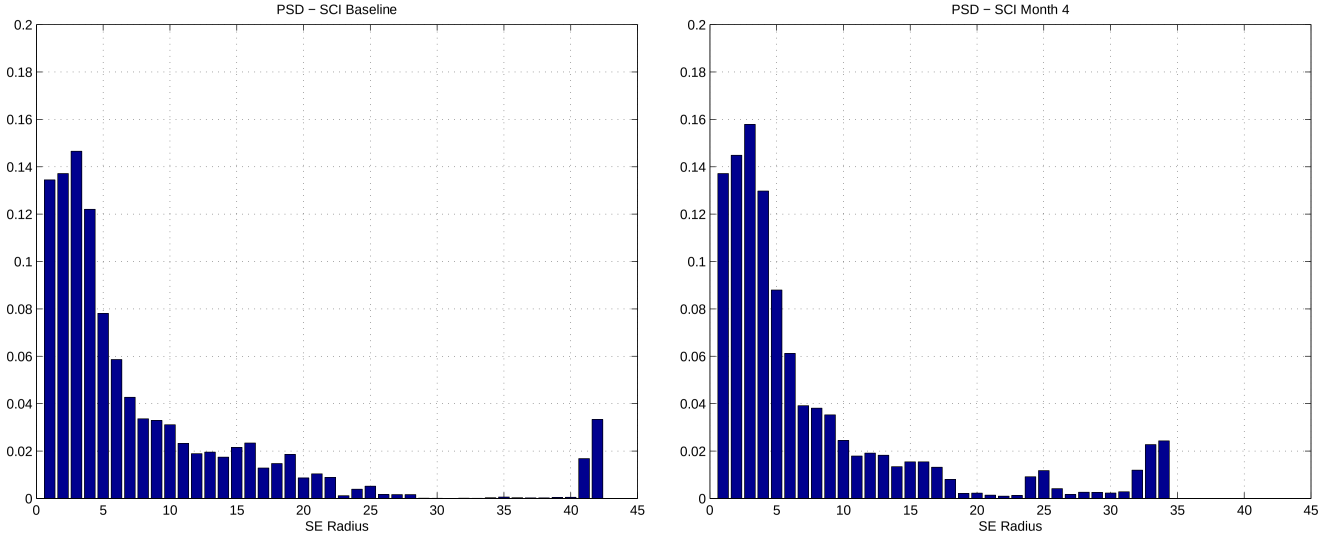

(a) Baseline Image PSD

(b) Month 4 Image PSD

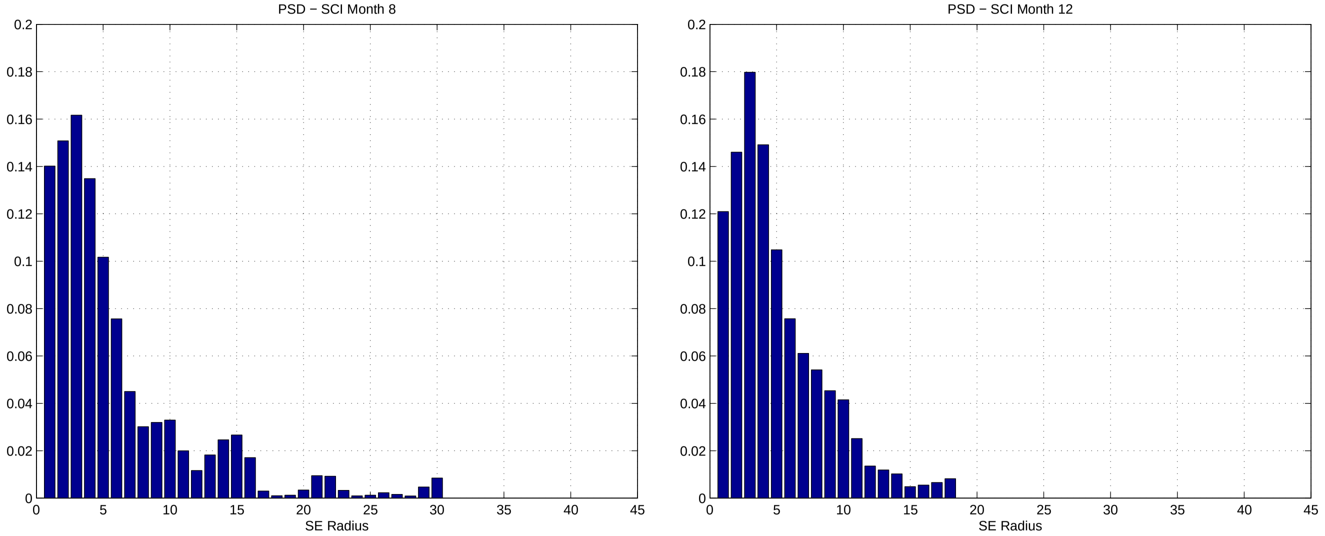

(c) Month 8 Image PSD

(d) Month 12 Image PSD

Figure 5.16: Pattern Spectrum Distributions of Example SCI Longitudinal data

	PSM	PSV	PSS
Baseline	8.25	88.28	2.25
Month 4	7.55	69.67	1.95
Month 8	5.99	31.02	1.98
Month 12	5.04	12.53	1.28

Table 5.3: Pattern Spectrum Moments of SCI Longitudinal Images (disk SE)

Even although no visual image data has been given, there are indications from both the shape of the PSD graphs and their moments, that there are changes occurring during this time period. In particular, the pattern spectrum variance changes quite considerably from 88.28 to 12.53. Using this data alone, a hypothesis could even be proposed as to the physical structure of the bone within these four images. For instance, the 12 month PSD given in Figure 5.18d has more sparsely distributed trabecular struts compared to that of the Baseline PSD in Figure 5.18a. This is apparent because a large proportion of its pixel densities do not survive past a SE size of 3, with the entire image being completely removed after only 18 openings. The baseline image however survives much longer, up to 42 openings. This would indicate by inference, that the Baseline image has more densely packed trabecular bone structures throughout its image, whereas the Month 12 image this has become a much more sparse pattern of trabecular bone within the image. This emerging information therefore has the possibility to represent a descriptor of the bone structure's texture within a pQCT image.

5.3.2 Local Pattern Spectrum Moments

Expanding on the idea that information present within these pQCT images can be extracted to provide an insight into the patterns of bone structure, the next step after generating global pattern spectrum moments is to investigate what structures are present locally, at pixel level. The concept of a **local granulometric size distribution** was first introduced by Dougherty and Pelz *et al* in 1992 [98] who proposed that rather than generating a single size distribution based on the whole image, local size distributions can be calculated over windows within the image. Each of these windows would generate its own granulometric PSD and moments for each pixel location within the image. The benefit of this is the ability to identify where there are groups of similar patterns contained within the image, as the local moments will be homogeneous over regions of comparable texture.

The generation of each granulometry ('sieved', or opened image) remains unchanged, with the entire image being opened using the first structuring element in the series. The difference however, takes place at this stage in the process, between each successive granulometry. The flow chart in Figure 5.17 can be used to assist the description of the generation of local pattern spectrum distributions for each pixel location, x, in the image.

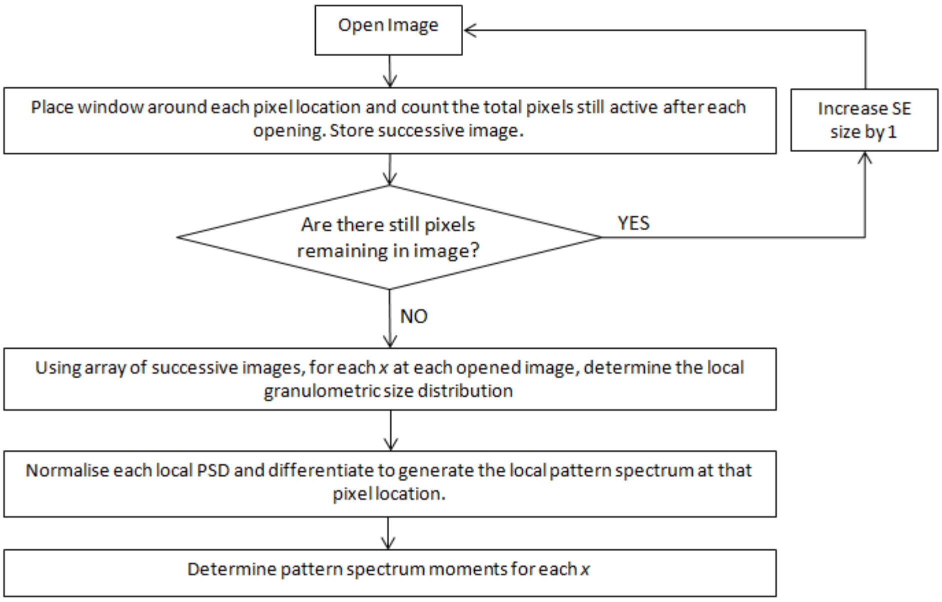

Figure 5.17: Flowchart: Local Granulometric Size Distribution Generation

Instead of simply calculating the number of pixels that are removed from the image after each opening as was the case with global granulometries, a local window is placed over each pixel location, and the total pixel count still active after the opening is counted and stored in each location. This process is repeated, with a count taken at each x location following each opening with successively increasing structuring element sizes, until no more pixels remain in the image. For each x location, there is now a local size distribution, $\Omega_x(t)$. As before, each of these local distributions are normalised to give the probability distribution function, $\Phi_x(t)$, and again its derivative, $d\Phi_x(t)$ gives a local pattern spectrum for each x in the image. It is this variable which will act as a descriptor for the local patterns of bone within a pQCT image. Once again using the local pattern spectrum, moments can be calculated for each x (mean, variance, skewness etc). These moments will be comparable in localised regions within the image that contain similar textures or structures. It is now possible to create a corresponding moment image for the original image, and Dougherty recommends this is done using the pattern spectrum means. The justification for focussing on the local means of an image is because of the way the PSM has been generated, as this variable best reflects the texture in the window around x, relative to the structuring element.

The example images used to generate the global pattern spectrum distributions in Figure 5.16, were the 4% distal tibia of a spinal cord injury subject involved in the longitudinal study. These data are now used to demonstrate local pattern spectrum distributions. For each of the four images, taken at Baseline, Month 4, Month 8 and Month 12 post-SCI, its corresponding moment image is calculated (using a window size of 11x11 [97]). These are shown in Figure 5.18. The PSM values are represented using the colour bar to the right of the image, displaying a range from 0 to 10.

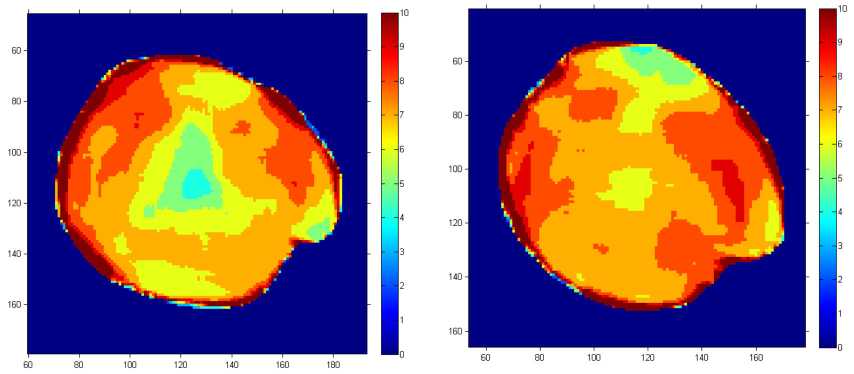

(a) Baseline Image Local PSD (b) Month 4 Image Local PSD

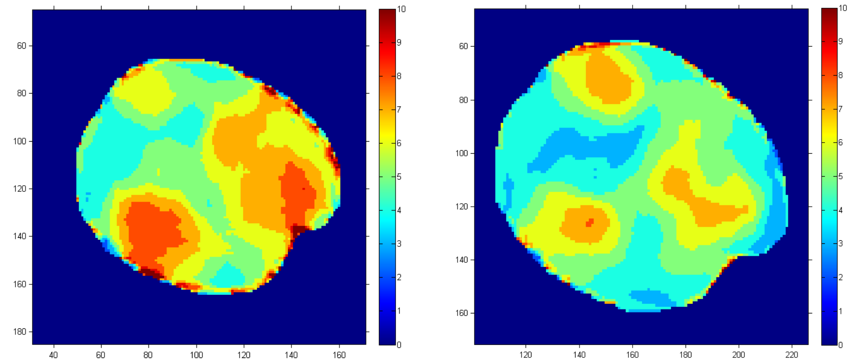

(c) Month 8 Image Local PSD (d) Month 12 Image Local PSD

Figure 5.18: Local Pattern Spectrum Distributions of Example SCI Longitudinal data

Similarly to the global pattern spectrum distributions observed changing over time, there are quite noticeable local structural changes occurring in the bones' textural properties during this period of 1-year post-injury as well. Whereas before it was hypothesised that the Month 12 image contained much finer structures compared to the Baseline image, it is now possible to locate within the image itself where both the finer and denser bone are located (colder colours and warmer colours respectively). Where the global pattern spectrum moments would have been an averaged result of all of these different textural patterns in each image, localised pattern spectrum moments identify and group more specific patterns of bone structure. This gives a more representative indication of the bone turnover occurring within the image under investigation.

The natural progression of calculating local pattern spectrum images would be to perform some form of classification, using training data to teach a classification algorithm how to identify the different types of bone structure from normal, to osteopaenic to osteoporotic. Once a classification algorithm had been developed, test data which had not been previously used in its construction would then be analysed to assess whether it can predict bone structure based on the local granulometric moments.

The data sets available for this thesis are however quite small in number compared to that required for a successful classification algorithm. However a preliminary assessment of both the SCI and ACL data using this analysis technique will provide an insight into whether the use of mathematical morphology it is a feasible method when describing trabecular architecture within a pQCT image.

5.4 Summary

This chapter has outlined the concept of using mathematical morphology as a technique to describe bone microarchitecture. The main principal behind this idea is that, should the bone structure within the image be very dense, then it will survive the granulometric sieving process longer than if the trabecular bone struts were more sparsely structured. The outcomes from these findings should provide the operator with a better understanding of an individual's bone patterns, with the aim of using this to aid fracture risk assessment and/or rehabilitation treatment plans.

Chapter 6 is the first of two clinical studies the image processing tools outlined in Chapters 3 to 5 were applied to. It investigates the changes in bone density in the first year following spinal cord injury. The second clinical study, evaluating BMD changes in the knee following ACL injury and surgical repair, is then presented in Chapter 7. Application of the software to these two very different clinical patient groups will be a good evaluation of its true flexibility.

Chapter 6

Subject Group 1: Acute Spinal Cord Injury Population

In this chapter, the results from the application of the different image analysis methods developed applied to the acute SCI population are presented. To date, these methods have never been applied to low dose pQCT images. The investigation of their value when applied to longitudinal SCI pQCT images of the tibia and femur within the first year post-injury is also an original concept. The application of these image processing techniques to patient data is one of the principal aims of this thesis, and the culmination of work described in previous chapters.

The chapter will therefore begin with an introduction to the clinical study carried out at the Queen Elizabeth National Spinal Injuries Unit (QENSIU), and calculate the intra-operator variability of the patient positioning for the images acquired. It will then proceed to investigate whether there are any localised changes in the participants' BMD throughout the duration of the study. Following this, morphological analysis will be used to evaluate whether the subjects' bone patterns present in the pQCT images can provide additional information on the integrity of their bones. Finally, an evaluation of the clinical outcomes and value of each of the image processing methods used in the analysis of this study will be discussed.

6.1 Summary of Clinical Study

A collaboration between the department of Clinical Physics, University of Glasgow, the Centre of Rehabilitation Engineering (CRE), University of Glasgow and the QENSIU, NHS Greater Glasgow and Clyde, was set-up by the author. A clinical study entitled *"Longitudinal study of bone demineralistion following spinal cord injury using peripheral Quantitative Computed Tomography (pQCT)"* is an ongoing research project being undertaken by Principal

Investigator (PI) Mr David Allan, Clinical Director of the QENSIU. The author's role was to work with the key investigator, Dr Sylvie Coupaud (CRE & QENSIU), on the image analysis of the the patients in this study. All research parties involved in the collaboration would be acknowledged in any novel findings which may arise from using data from this clinical study. The principal research aim of this study is to describe the decline in bone mineral density and other bone parameters following SCI, with the secondary objective to identify the relationship between bone strength at the time of injury and the rate and extent of decline in bone strength in the first year after SCI. These findings are important in the SCI population as these patients are known to be susceptible to sub-lesional osteoporosis and consequently low-energy fractures in these limbs e.g. after a fall from a wheelchair. Using these results, an additional potential outcome would be to identify the most suitable time point for introducing osteoporosis intervention treatments in SCI. Its ultimate aim is to provide clinicians with information on osteoporosis screening and guide patient management plans for patients following SCI injury.

6.2 Methods

Full ethical approval for this project was granted by the South Glasgow & Clyde Research Ethics Committee. All subjects provided their informed consent prior to participation in the study, in line with the Declaration of Helsinki. Inclusion criteria were the candidate must be

- An in-patient at the QENSIU, Glasgow.
- No more than 5 weeks post-injury at the start of participation.
- Neurologically stable.
- Motor complete Spinal Cord Injury.

A written information sheet was provided to each patient and they were invited to discuss participation in the study with clinicians, family, friends or colleagues. Patients were under no obligation to participate in the study and they had one week to decide whether or not to take part. Every patient who participated in the longitudinal study was allocated an 'L' ID. Patients were scanned at four time points. Baseline scans at various anatomical locations on the dominant tibia, femur and non-dominant radius were made as soon as possible following injury but within 5 weeks post-injury. Patients then returned for repeat scanning sessions at 4-monthly intervals up to and including one year post-injury. Scans at all four appointments were made at the same anatomical locations as the Baseline scan and were carried out by a single operator. Contralateral limbs were used if there was a history of fracture in the limb or if it contained any metal components at the scan site.

Data from 15 subjects who were successfully scanned at all four time points are used for the image analysis in this chapter. Table 6.1 presents further detail on these subjects, where C is an injury in the cervical spine, T thoracic and L lumbar, with the associated number relating to the vertebral level of the injury.

Subject	SCI Level	Age	Sex
L1	C4	17	M
L4	C4/5	72	M
L5	T3	17	M
L6	T4	29	M
L7	T6	18	M
L10	L1	37	M
L12	T4	21	M
L14	C5	17	M
L15	C4/5	67	M
L16	C5	52	F
L18	C6/7	53	F
L19	T11	47	M
L21	T12	44	M
L22	C6/7	27	M
L29	T11	22	M

Table 6.1: Subjects in SCI Longitudinal Study

Although images of the radius were acquired, the analysis in this chapter will focus on the distal tibia and distal femur scans, however the methods would also be applicable to the radius and would unquestionably be of interest in future work. Acquisition parameters for the tibial and femoral locations are provided in Table 3.2, with the 4% distal tibia acquired using a voxel size of 0.5mm^2 and the 4% distal femur a voxel size of 0.303mm^2. The 5% distal locations were chosen because they are rich in trabecular bone and therefore a good site to monitor any rapid bone turnover. For this reason, however, they also have the highest fracture incidence in SCI [32], making assessment of BMD at these locations even more relevant. The choice of voxel size for the tibia was based on the measuring protocol as recommended by the manufacturer; there were no such recommendations for the femur at the time of the study and therefore the choice was based on previous research by Eser *et al* [33], choosing a smaller voxel size due to the thin cortical shell at the distal femur. The bones contained in all images were segmented from their surrounding soft tissue structures using the automated thresholding technique described in Chapter 3. The data were then analysed using the image processing methods described in Chapters 4 and 5 of this thesis.

6.3 Results

6.3.1 Patient Positioning Intra-Operator Variability

A common area of weakness identified in the analysis of data, from either longitudinal or cross-sectional imaging studies, is the inclusion of an intra- and inter-operator error measurement. The reason that an estimate of this error is not often included is that it involves taking multiple scans of the same patient either using different operators or following removal and repositioning of the same patient into the scanner by the same operator. In addition, if the scan uses ionising radiation, this would involve an additional radiation exposure which would be of no extra benefit to the patient. Finally, it would double the scan length duration, resulting in additional patient discomfort. The latter is of particular concern when working with people with SCI as it can cause an increased frequency of muscle spasms, increased risk of pressure sores on the skin and in the worst acute case scenario, can result in an autonomic dysreflexia which has very serious medical complications. For these reasons previous authors in this field sensibly proposed alternative methods to assess the repeatability of patient positioning by an operator. Eser *et al* determined a correction factor based on repeated measurements of healthy volunteers [38], whereas Marjanovic *et al* scanned two adjacent slices of the radius and chose the slices which were the best fit between Baseline and follow up [136]. Rittweger *et al* minimised the operator variability by ensuring that the scans were only carried out by two experienced operators [137] while Cervinka *et al* excluded repeat scans which had total CSA differences greater than 25mm^2 [45]. A means of calculating the inter-operator error for this study was briefly introduced in Section 4.1.3. It uses a quantification of the geometric transformations necessary for registration of follow-up images to the Baseline image. The publications in Radiotherapy quoted previously have used a similar method of image registration measurements to quantify the positioning accuracy. The registration software developed as part of the image processing in this thesis therefore enables an assessment of the operator's positioning repeatability, without the need for any additional scans or radiation exposure.

The patient data used to validate the registration software were also used to calculate the intra-operator variability. As there was only one operator performing all of the scanning sessions for this study, this eliminated any errors which would be a result of inter-operator variability. The operator was also very experienced in performing pQCT scans with the SCI population.

Prior to each scan, the patient's limb lengths were measured to assist the localisation of the required slice. An AP scout view was then performed and reference lines were positioned at either the distal tibial endplate or the lateral femoral condyle. SCI patient data from both the distal tibia and distal femur pairs were registered using the geometric transformations defined in Chapter 4. Intra-operator variability was calculated at both of these sites by measuring the average euclidian distance between the Baseline COM and the COM in subsequent scans (x-y displacement), the average difference in CSA between sequential scans during the 1 year time frame (z-displacement) and the average rotational displacement necessary to rotate the images into alignment (θ displacement). The results are presented in Table 6.2 quoting the mean ± 2SD of the displacements for the two anatomical locations.

Slice	COM displacement ($\overline{mm}$)	CSA ave. diff. ($\overline{mm^2}$)	θ displacement ($\overline{deg}$)
Distal Tibia	6.3 ± 10.7mm	23.7 ± 25mm^2	5.3 ± 12.3^o
Distal Femur	11 ± 28.2mm	50.5 ± 66.1mm^2	6.9 ± 14.4^o

Table 6.2: Intra-operator variability for SCI study

In order to put these results into context, the COM and θ displacement can both be resolved with good registration software. The primary concern would be whether the location scanned was the same as previous or subsequent scans, as this would effect any comparisons between BMD measurements across the longitudinal data set. The average difference in CSA is therefore the best indicator for this. Research by Sun *et al* [138] used cadaver bones as a means of quantifying the repositioning errors in pQCT at both the distal radius and distal tibia. BMD measurements were performed three times consecutively without repositioning at 11 locations of the distal tibia and the relationship between CSA change and bone density change was investigated. Their results showed that *“At the distal tibia, the change of trabecular bone density around the ultradistal location of 4% location, showed no significant changes if the CSA change fell within* $\pm 20mm^2$ *or the longitudinal distance fell within* $\pm 0.5mm$*”*. The results from the operator in the SCI study were on average over this limit for the distal tibia at 23.7 ± 25mm^2. This will result in a higher variation in the statistical noise, however due to its nature it is random and non-systemic. Given the challenges associated with the positioning of SCI subjects, who can frequently experience involuntary leg spasms, the reproducibility of patient positioning was therefore considered acceptable for this patient group. The mean total CSA±2SD for the distal tibia and femur is 1308 ± 226mm^2 and 3947 ± 760mm^2 respectively. With this in mind, the maximum shift in CSA for the distal tibia as a percentage of the minimum CSA of this bone would be 4.5% of the overall area, with an equivalent distal femur percentage of 3.7%. The presence of these intra-operator variability errors will however still need to be taken into consideration when drawing conclusions from any results.

6.3.2 BMD Analysis

While this chapter focusses primarily on the image analysis of the data from the longitudinal SCI study, a brief summary of the results generated from the raw image data itself are presented here. This provides a starting point from which the image analysis results can be discussed.

Tables 6.3 and 6.4 display the BMDTot measurements calculated from the segmented pQCT images for all 15 subjects using the software outlined in Chapter 3. In addition to these measurements, the amount of bone lost by 12 months as a percentage of each subject's Baseline value is also provided.

Subject	Baseline (mg/cm^3)	Month 4 (mg/cm^3)	Month 8 (mg/cm^3)	Month 12 (mg/cm^3)	% loss B-12M
L1	368	343	272	209	43
L4	336	341	329	321	6
L5	313	250	215	136	57
L6	300	270	188	181	40
L7	353	341	247	235	34
L10	343	336	333	320	7
L12	358	342	328	308	14
L14	400	386	385	371	7
L15	339	341	331	325	4
L16	309	307	298	296	4
L18	322	317	307	306	5
L19	360	349	335	322	11
L21	342	322	306	244	29
L22	350	345	306	296	16
L29	340	292	264	238	30

Table 6.3: Total BMD measurements of distal tibia calculated from segmented images

Subject	Baseline (mg/cm^3)	Month 4 (mg/cm^3)	Month 8 (mg/cm^3)	Month 12 (mg/cm^3)	% loss B-12M
L1	306	277	222	207	32
L4	254	251	247	237	7
L5	299	267	227	203	32
L6	255	200	168	169	34
L7	288	276	259	235	18
L10	341	317	303	267	22
L12	303	296	291	278	8
L14	331	323	312	308	7
L15	292	285	265	254	13
L16	308	325	301	293	5
L18	295	284	277	274	7
L19	284	286	273	240	15
L21	322	304	268	242	25
L22	308	286	250	226	27
L29	308	302	298	284	8

Table 6.4: Total BMD measurements of distal femur calculated from segmented images

What is apparent when considering both the distal tibia and distal femur results is that there is quite a marked inter-subject variation in the bone loss experienced during the first year post-injury. For example, in the distal tibia the biggest loss observed was 57% with the smallest as low as 4%. Although not as dramatic, the same can be said for the distal femur, with the largest and smallest losses being 34 and 5% respectively. This is an extremely interesting finding as it is clear that some subjects are much more susceptible to bone loss compared to others. This finding also supports that of de Bruin *et al* [36] who found a similar variation in bone loss between a 5 week post-injury pQCT scan with a 2 year follow-up despite having an even smaller sample of subjects (n=8). The concept of categorising people into "fast" and "slow" bone losers has already been proposed by other authors, with Müller *et al* using the term to identify a sample of women who are predisposed to osteoporosis (n=39) [139] and Coupaud *et al* identifying the two distinct groups from the preliminary results of the SCI longitudinal study (n=6) [70]. For these data, the method of determining a suitable cut-off separating the fast and slow losers proposed by Müller *et al* was used. A frequency distribution of the rates of individual bone loss was plotted for the distal tibia in the first instance and shown in Figure 6.1.

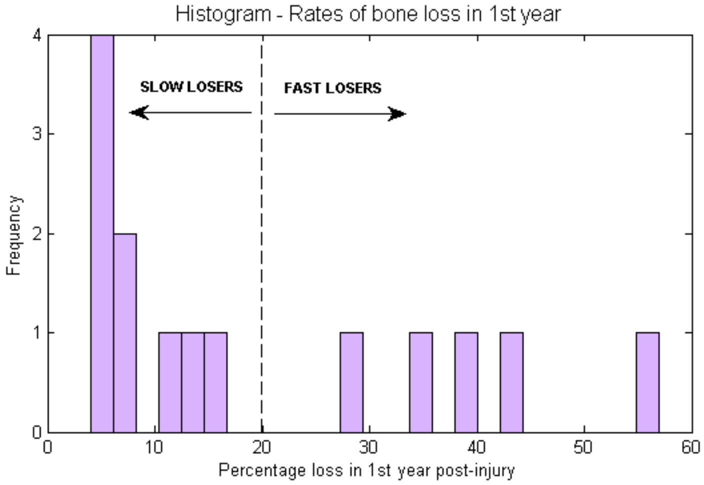

Figure 6.1: Frequency distribution of rates of individual bone loss for SCI distal tibia - % loss from Baseline to month 12

In Müller's study, the histogram was described as being "bi-modal", with a gap between the two modes. Figure 6.1 could also be described as having two different groups of subjects, with a proposed cut-off of those having experienced a BMDTot loss >20% of Baseline as being identified on the histogram as fast losers.

Similarly, the bone loss distribution for the distal femur was also plotted (Figure 6.2).

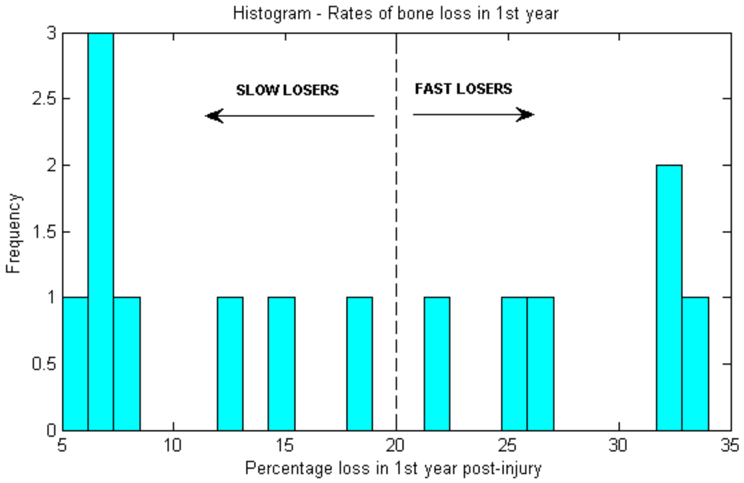

Figure 6.2: Frequency distribution of rates of individual bone loss for SCI distal femur - % loss from Baseline to month 12

The cut-off between fast and slow losers is less evident for this anatomical location, showing a wide distribution of varying bone loss rates. It was therefore proposed to use the same threshold as the distal tibia of 20% difference from the Baseline measurement, also indicated on the histogram in Figure 6.2.

With this threshold in mind, it is clear that classification as a fast loser based on one anatomical location does not automatically infer that the subject is a fast loser in another location. The following summary can be made from the subjects in this study:

- Subjects L1, L5, L6 and L21 are classified fast losers at both the distal tibia and distal femur location.
- Subjects L7 and L29 are fast losers at the distal tibia only, whereas L10 and L22 are fast losers at the distal femur only.
- Subjects L4, L12, L14, L15, L16, L18 and L19 are all classified slow losers at both the distal tibia and distal femur location.

In this acute-SCI cohort, there are proportionally more slow losers than fast losers. One of the surprising findings from this sample is that a large proportion of subjects are not experiencing rapid bone loss within the first year post injury as would otherwise be expected from current publications [35, 27]. What has resulted in these subjects experiencing minimal bone loss during this period is unknown. It is proposed therefore to look at these two groups in more depth using the image processing techniques developed. Example subjects from both groups will be used to demonstrate the software as well as to further investigate potential reasons behind this inter-subject variation.

6.3.3 Quadrant Analysis of Bone Mineral Density

Regional assessment of trabecular bone changes over the duration of the study for the distal tibia were analysed using the method outlined in Section 4.2. The majority of publications looking at changes in BMD in SCI quote global measurements such as BMDTot or BMDTrab, however information on where any bone loss takes place within the bone is not apparent from these measurements. Of those authors who have looked at regional BMDTrab changes within pQCT images, the techniques used to segment the regions have at best been semi-automated. The quadrant analysis presented in this thesis is fully automated and therefore free from any operator error during the segmentation process.

Longitudinal segmented images from the distal tibia for all 15 subjects were registered to their Baseline reference image. The cortical bone from each image was removed using both a threshold peel and a concentric peel, the latter of which removes 55% of voxels from around the outside bone circumference, leaving a central 45% core. Once the cortical bone had been removed, the images were then segmented into quadrants and the BMDTrab for each quadrant was measured for each time point and plotted on a graph.

Two examples each from both fast and slow loser groups at the distal tibia identified in the previous section are presented in Figures 6.3 and 6.4 respectively.

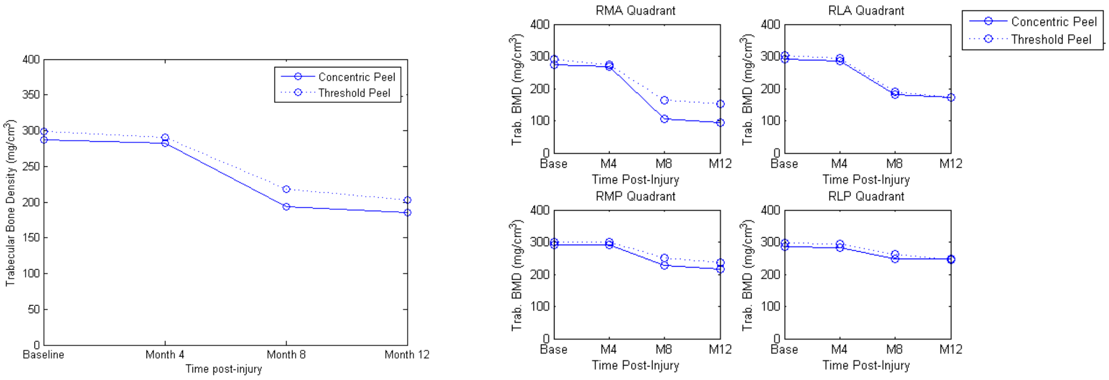

(a) Global longitudinal BMDTrab measurement - Subject L7

(b) BMDTrab measurements from each quadrant - Subject L7

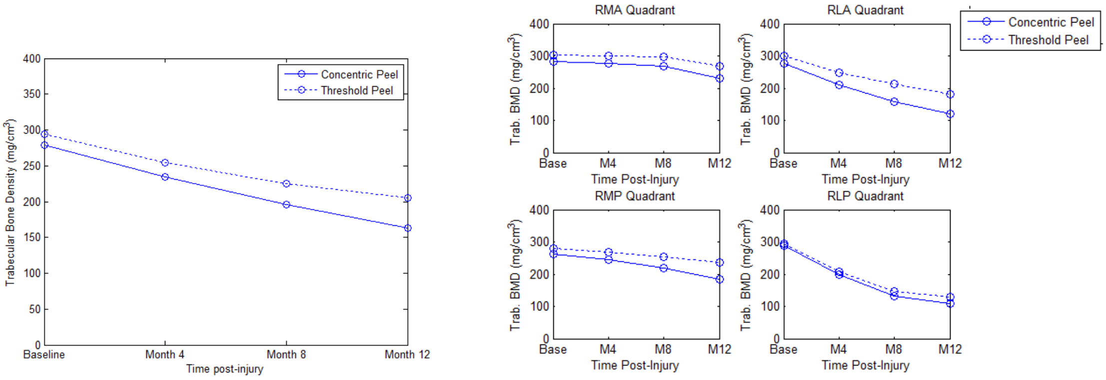

(c) Global longitudinal BMDTrab measurement - Subject L29

(d) BMDTrab measurements from each quadrant - Subject L29

Figure 6.3: Quadrant analysis of the distal tibia from two fast loser subjects

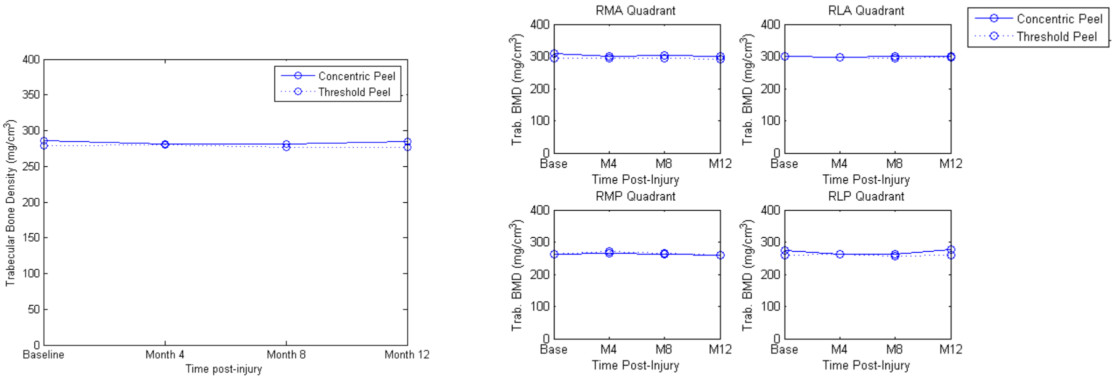

(a) Global longitudinal BMDTrab measurement - Subject L4

(b) BMDTrab measurements from each quadrant - Subject L4

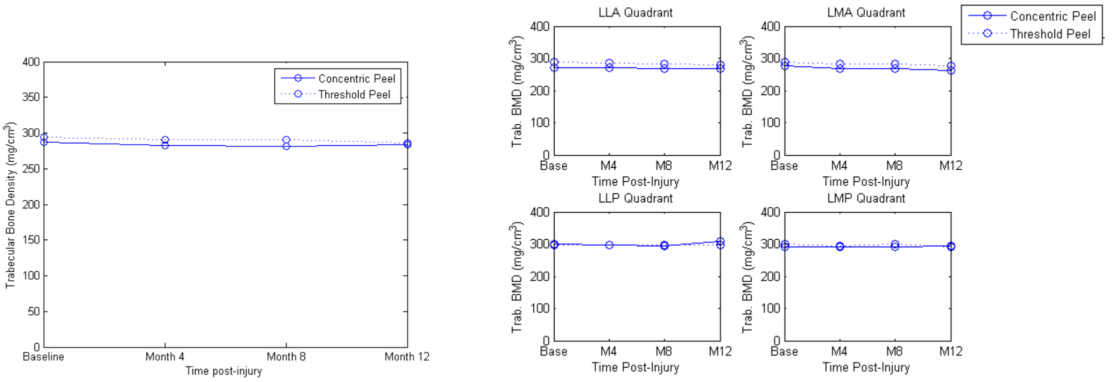

(c) Global longitudinal BMDTrab measurement - Subject L10

(d) BMDTrab measurements from each quadrant - Subject L10

Figure 6.4: Quadrant analysis of the distal tibia from two slow loser subjects

Looking at the global measurements of the fast losers in Figures 6.3a and 6.3c, the data presented indicates that these subjects are losing bone. In performing a more detailed interrogation of the BMDTrab values in each of the four quadrants of the slice, the majority of that loss which would have previously been assumed to be global but is in fact occurring in only one, or at most two quadrants. The implications of these findings clinically are that lifestyle advice could be given to the patient, counseling them to avoid stresses or trauma to the weakened portion of the bone. In addition, interventional techniques could be more tailored, for example, focussing on the antero-medial quadrant for Subject L7 (Figure 6.3b) or both the postero- and antero-lateral quadrants for Subject L29 (Figure 6.3d).

The quadrant analysis of the BMDTrab for the slow losers shows that this steady-state occurs in all regions of the bone, with two representative examples from this group given in Figure 6.4. These graphs are typical of all ten subjects who did not experience any significant bone loss within the first year.

The evaluation of BMDTrab using both the global and quadrant analysis described here has raised an interesting finding in the acute SCI population, in particular for those subjects who are classified as fast losers. Where previously when using the pQCT system data analysis alone it was possible to identify by 12 months that some subjects were more susceptible to bone loss than others, it is now known that this loss is sometimes quite focussed in certain regions within the bone rather than a diffuse weakening of the trabecular structure as a whole. Taking global measurements alone when analysing each image could potentially mask the extent of bone loss in regions within the bone. For example, if the trabecular structure had been significantly destroyed in one quadrant, this would make it a weak point in the bone and at high risk of low impact fracture.

6.3.4 Voxel Wise Comparisons

The results presented in the previous section indicate that in some of the acute injury SCI subjects there are inhomogeneous changes in BMD occurring during the first year post injury. The natural extension from quadrant analysis is therefore to perform voxel wise comparisons on intra-patient images to determine bone turnover at each anatomical location. This method of intra-subject comparison applied to pQCT data, to date, has not been investigated. It is a novel means through which magnitudes of bone loss across image pairs can be displayed visually at a voxel level in the form of a ΔBMD map of bone density changes.

Longitudinal segmented images from the distal tibia and distal femur from all 15 subjects were registered to their Baseline reference image. Voxel wise comparisons were performed on image pairs as outlined in Section 4.3, comparing each follow up scan to the Baseline scan.

Distal Tibia

Results from the distal tibia are discussed first. Figure 6.5 and 6.6 present four of the six subjects identified as being fast losers at the distal tibia location and Figure 6.7 ΔBMD maps of two subjects typical of those who do not appear to experience any significant bone loss during the first year post-SCI (slow losers). The voxels in each image display the absolute change in BMD in mg/cm^3 on the colour scale provided. Each image displays the difference in BMD which has occurred between the two time points indicated.

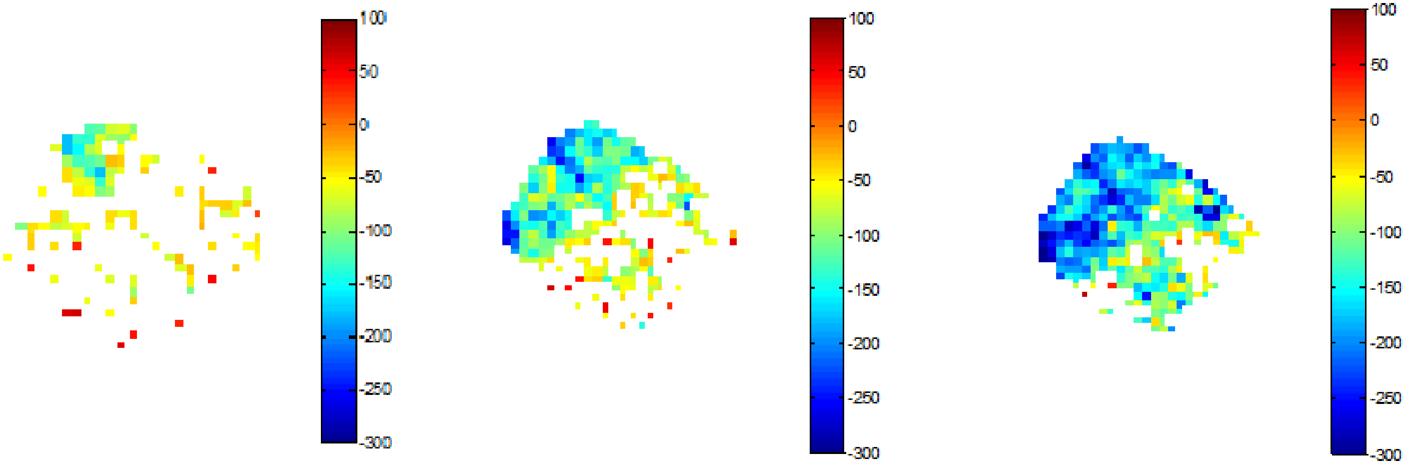

(a) L1: Baseline to Month 4 comparison

(b) L1: Baseline to Month 8 comparison

(c) L1: Baseline to Month 12 comparison
Total % BMD loss from Baseline: 43%

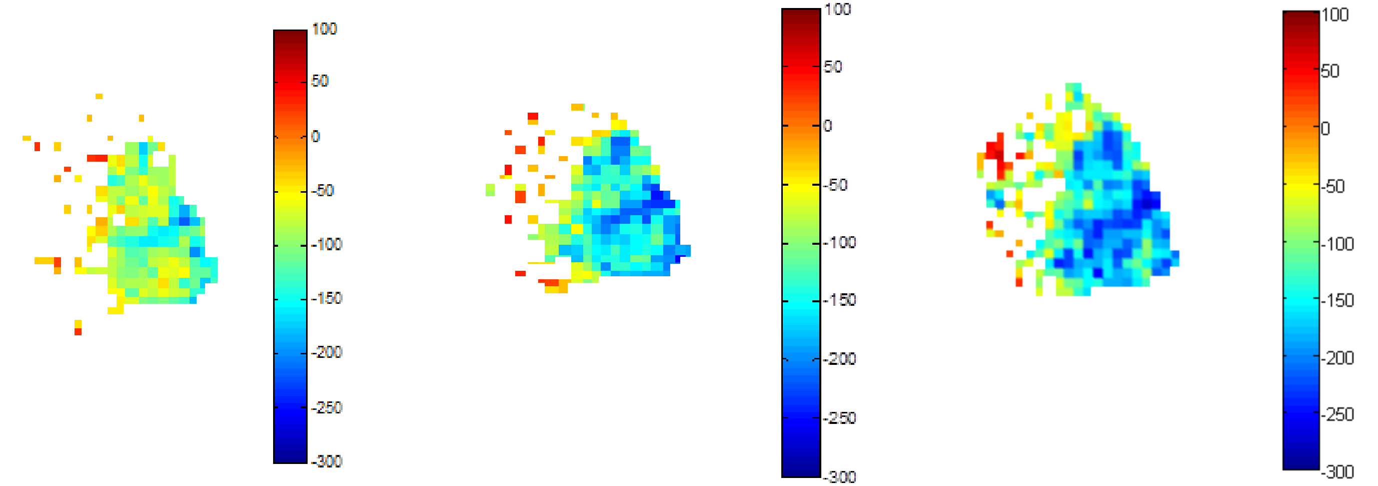

(d) L29: Baseline to Month 4 comparison

(e) L29: Baseline to Month 8 comparison

(f) L29: Baseline to Month 12 comparison
Total % BMD loss from Baseline: 30%

Figure 6.5: Distal tibia ΔBMD maps of SCI injury subjects demonstrating inhomogeneous bone loss patterns during 1st year post-injury

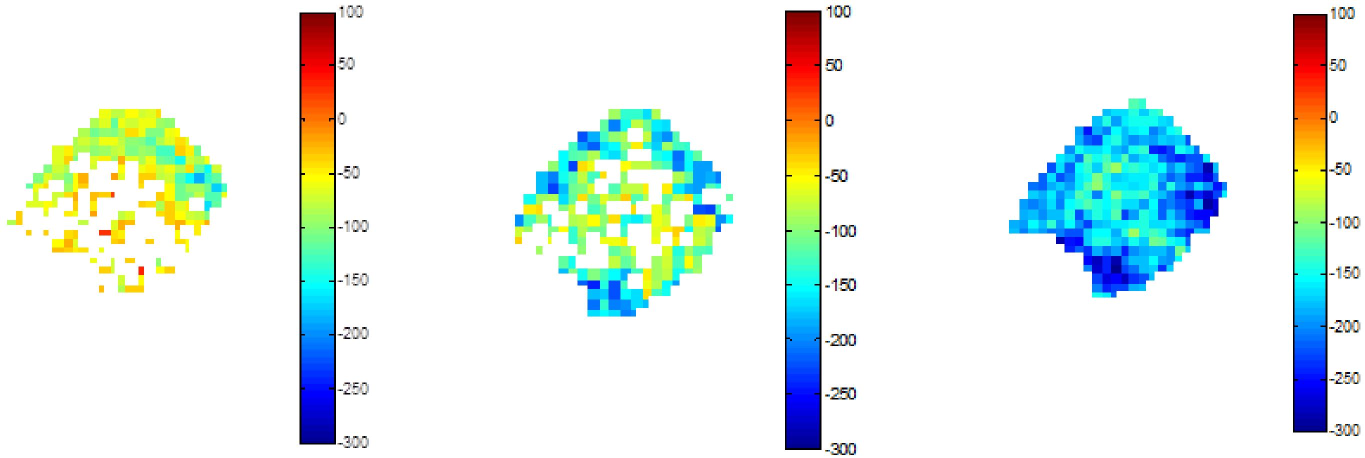

(a) L5: Baseline to Month 4 comparison

(b) L5: Baseline to Month 8 comparison

(c) L5: Baseline to Month 12 comparison
Total % BMD loss from Baseline: 57%

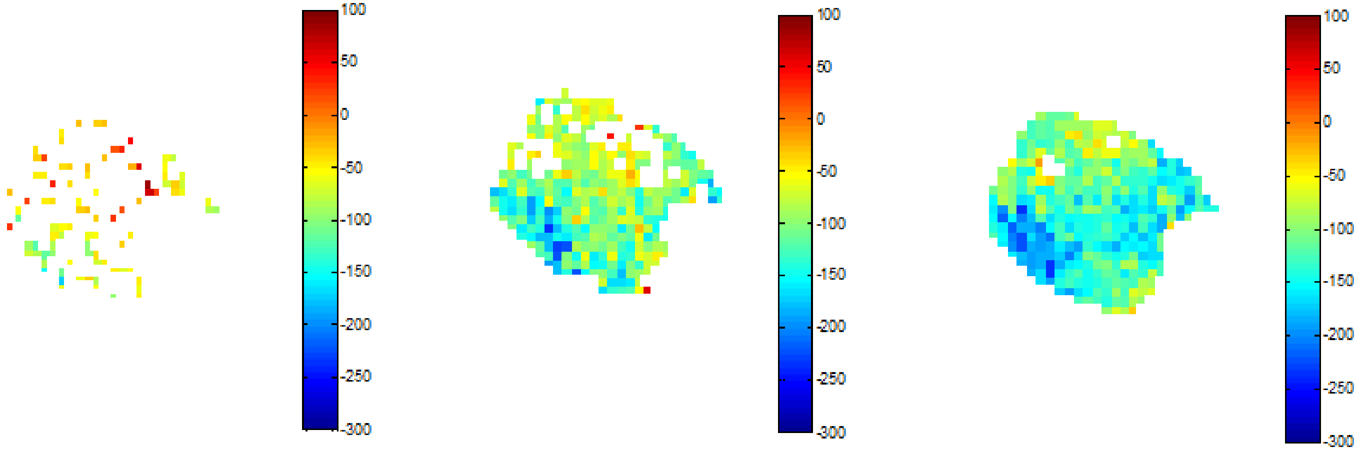

(d) L6: Baseline to Month 4 comparison

(e) L6: Baseline to Month 8 comparison

(f) L6: Baseline to Month 12 comparison
Total % BMD loss from Baseline: 40%

Figure 6.6: Distal tibia ΔBMD maps of SCI injury subjects demonstrating inhomogeneous bone loss patterns during 1st year post-injury

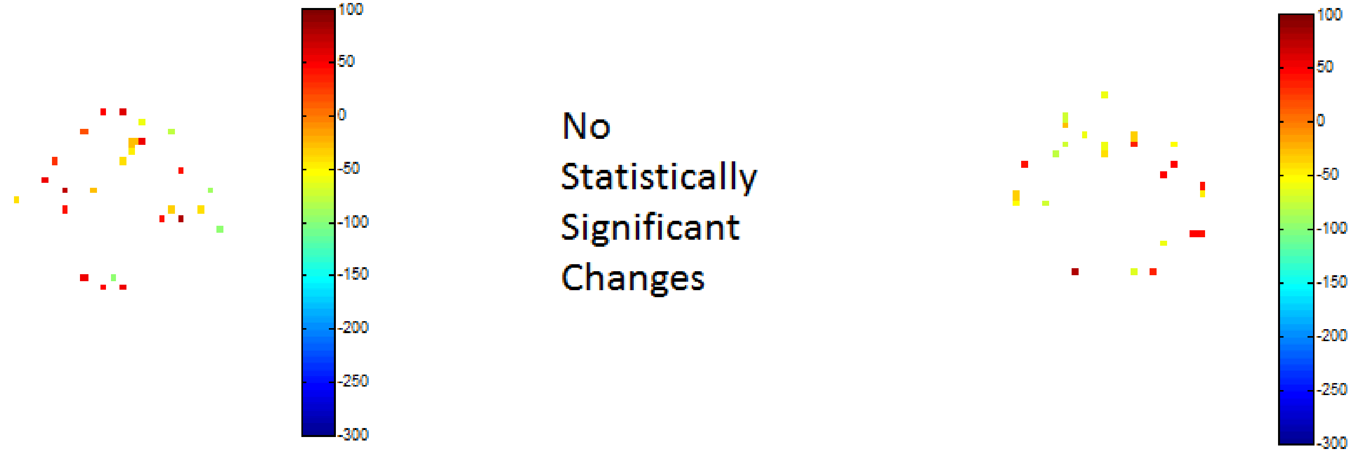

(a) L4: Baseline to Month 4 comparison
(b) L4: Baseline to Month 8 comparison
(c) L4: Baseline to Month 12 comparison
Total % BMD loss from Baseline: <u>**6%**</u>

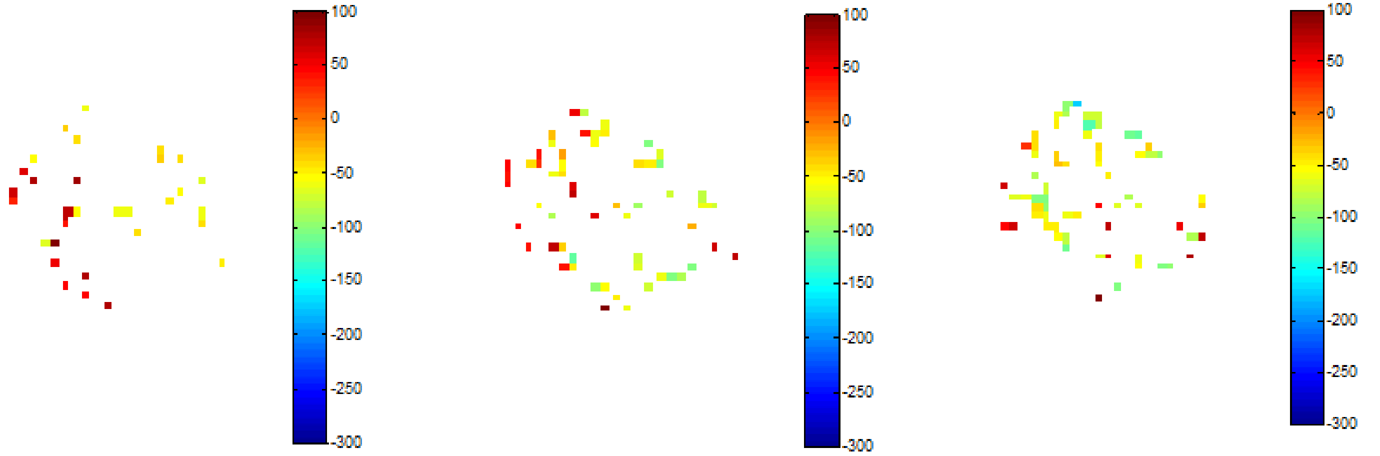

(d) L14: Baseline to Month 4 comparison
(e) L14: Baseline to Month 8 comparison
(f) L14: Baseline to Month 12 comparison
Total % BMD loss from Baseline: <u>**7%**</u>

Figure 6.7: Distal tibia ΔBMD maps of SCI injury subjects demonstrating no obvious bone loss patterns during 1st year post-injury

Figures 6.5a to 6.5c are the comparisons of the distal tibia of subject L1's right leg. At 4 months it is not obvious whether this subject will go on to lose significant amounts of BMD within their first year, however there is a small indication in the anterior section of the bone that some bone demineralisation has started to take place. By 8 months however it is clearly evident that the rate of bone loss has drastically increased, in particular medially and anteriorly, with a small proportion of voxels in these areas demonstrating loss of >200mg/cm^3. The postero-lateral portion of the bone conversely still appears to maintain the majority of its Baseline structure. At 1 year post-injury the proportion of bone loss is now larger, with a significant number of the voxel comparisons in the antero-medial region indicating loss >200mg/cm^3. Subject L29, whose comparison maps are shown in Figures 6.5d to 6.5f interestingly once again demonstrates an asymmetric bone loss in the right distal tibia however in this instance it is in the entire lateral portion of the bone. This is clear even from the Baseline to month 4 comparison, the bone loss is occurring much more rapidly than subject L1. By month 12 this subject has lost significant proportions of their Baseline BMD and will be at an increased risk of low-energy fracture.

Subjects L5 (Figure 6.6a to 6.6c) and L6 (Figure 6.6d to 6.6f) are two examples of fast losers who have experienced different patterns of bone loss across the bone. Initially subject L5's left distal tibia has a tendency for loss anteriorly at month 4, however by month 8 and month 12 this becomes more diffuse across the entire bone, with the 1 year scan exhibiting a loss of >200mg/cm^3 at the majority of voxels. It is not clear by month 4 whether subject L6's right distal tibia will actually experience any loss (Figure 6.6d), however between month 4 and month 8 there has been a rapid decline in BMD, once again showing a significant loss across the slice by month 12.

Two voxel maps representative of those subjects who did not experience any obvious bone loss during their first year post injury are shown in Figure 6.7. The majority of voxels in these two comparisons are white, indicating no statistically significant change in BMD, with any voxels which are highlighted as having experienced changes, being a combination of increasing and decreasing BMD. This could be attributed to natural osteoblastic and osteoclastic activity involved in normal bone turnover or indeed measurement error associated with patient position and for the use of a significance cutoff of $p < 0.05$ (5% of voxels will be false positives).

What has been demonstrated by these images, in particular for those subjects who are fast losers, is that even within this grouping of subjects there is a lot of inter-subject variation related to how these loses actually manifest themselves within the bone. It is for this reason that the use of ΔBMD voxel maps displaying changes in BMD are extremely useful in conveying this additional clinical information which had previously been unavailable.

Distal Femur

Voxel wise comparisons were also performed on the distal femur of the 15 subjects. Again, each subject's follow up scan was compared to their Baseline image. Representative results from 6 of those subjects are presented here, four from the fast loser group and 2 from the slow loser group. The first two subjects in Figure 6.8 demonstrate loss which appears to be preferential to the femoral condyles of the distal femur, with Figure 6.9 demonstrations of subjects who have experienced other patterns of inhomogeneous loss. Finally, two examples representative of those who did not experience any obvious bone loss during the first year post-injury are given in Figure 6.10

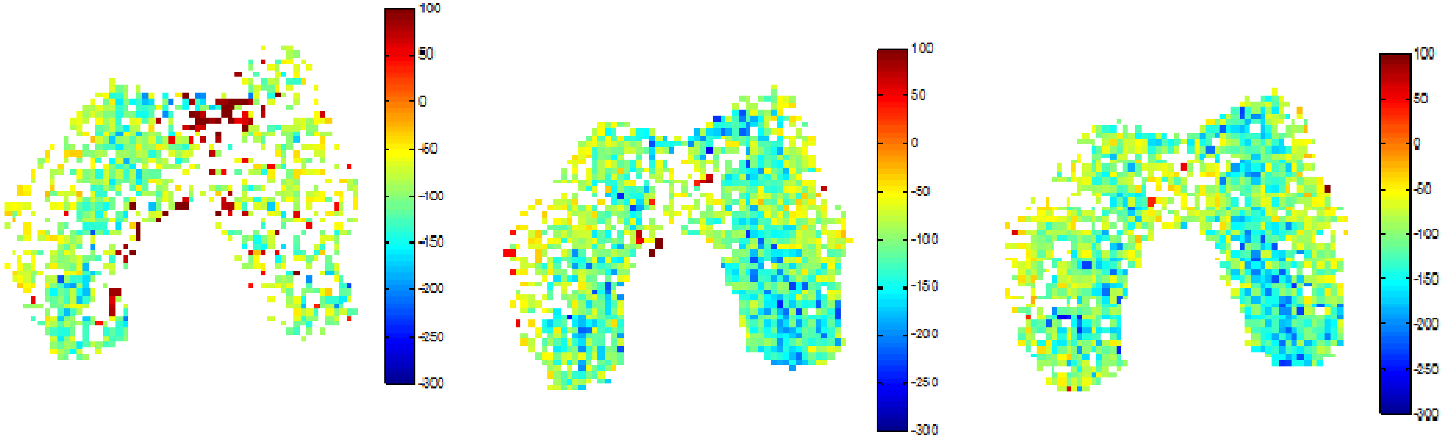

(a) L6: Distal femur Baseline to Month 4 comparison

(b) L6: Distal femur Baseline to Month 8 comparison

(c) L6: Distal femur Baseline to Month 12 comparison
Total % BMD loss from Baseline: 34%

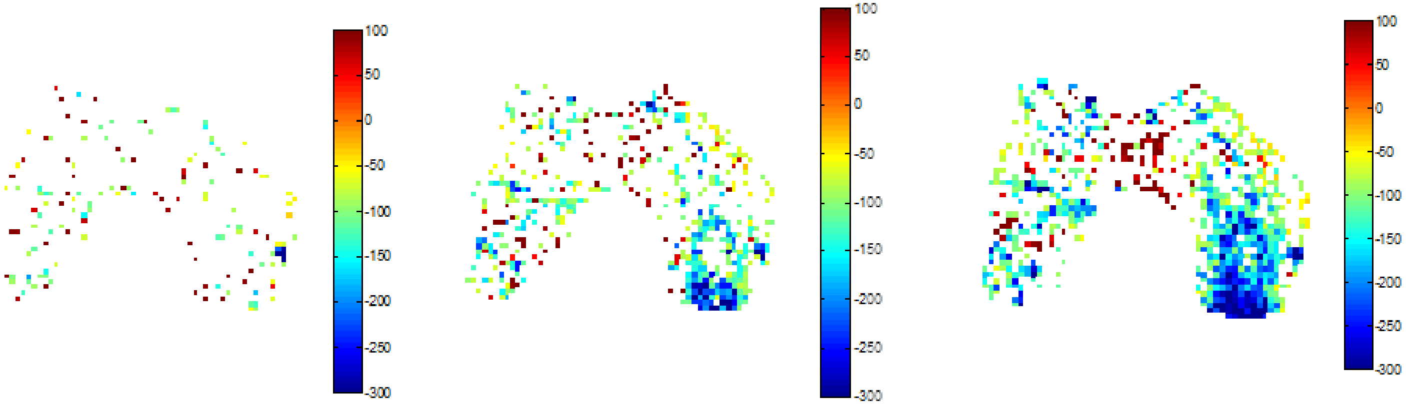

(d) L21: Distal femur Baseline to Month 4 comparison

(e) L21: Distal femur Baseline to Month 8 comparison

(f) L21: Distal femur Baseline to Month 12 comparison
Total % BMD loss from Baseline: 25%

Figure 6.8: Distal femur ΔBMD maps of SCI injury subjects demonstrating bone loss patterns in femoral condyles during 1st year post-injury

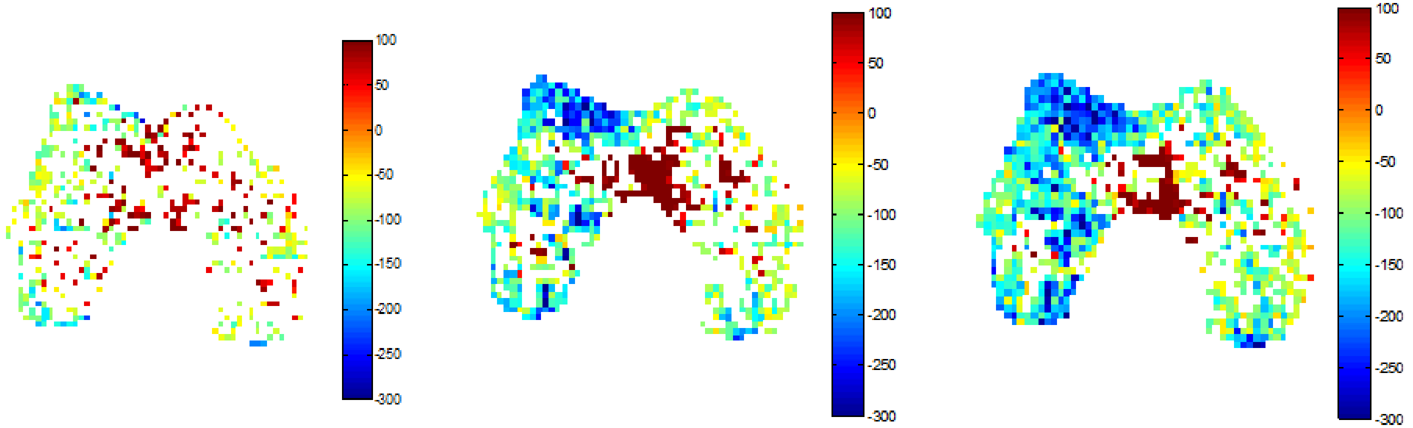

(a) L5: Distal femur Baseline to Month 4 comparison

(b) L5: Distal femur Baseline to Month 8 comparison

(c) L5: Distal femur Baseline to Month 12 comparison
Total % BMD loss from Baseline: 32%

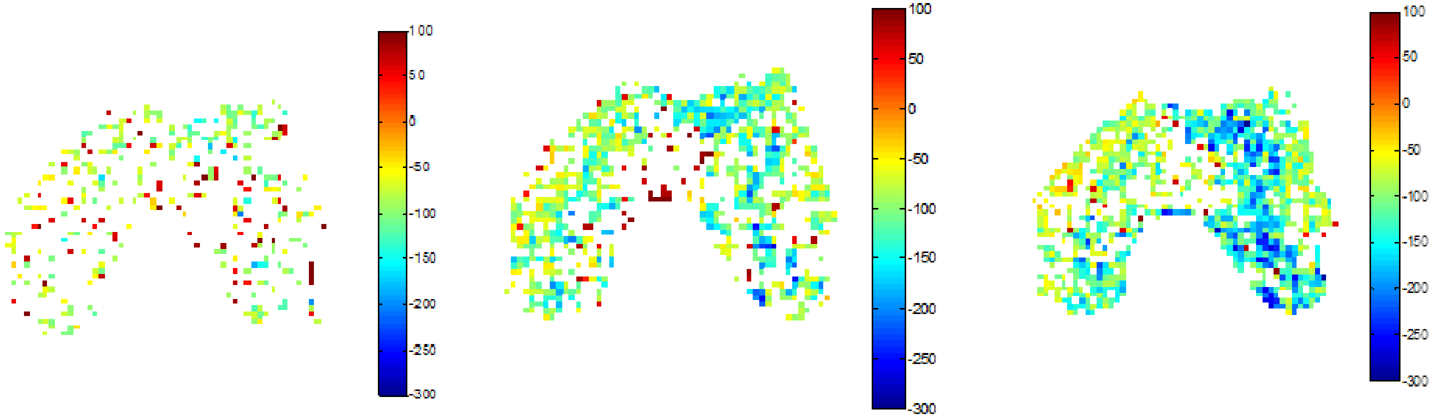

(d) L22: Distal femur Baseline to Month 4 comparison

(e) L22: Distal femur Baseline to Month 8 comparison

(f) L22: Distal femur Baseline to Month 12 comparison
Total % BMD loss from Baseline: 27%

Figure 6.9: Distal femur ΔBMD maps of SCI injury subjects demonstrating inhomogeneous bone loss patterns during 1st year post-injury

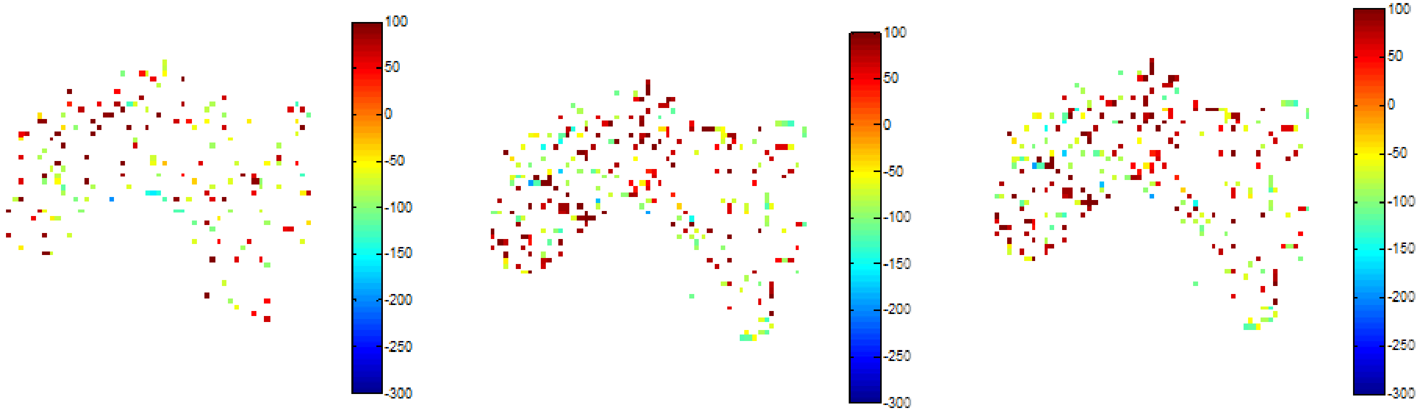

(a) L4: Distal femur Baseline to Month 4 comparison

(b) L4: Distal femur Baseline to Month 8 comparison

(c) L4: Distal femur Baseline to Month 12 comparison
Total % BMD loss from Baseline: **7%**

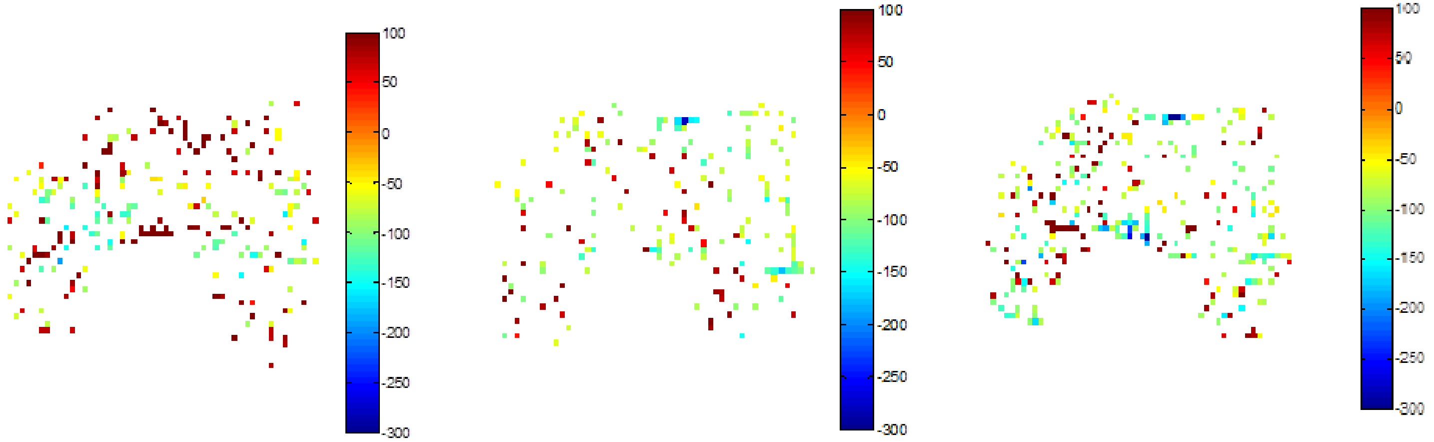

(d) L14: Distal femur Baseline to Month 4 comparison

(e) L14: Distal femur Baseline to Month 8 comparison

(f) L14: Distal femur Baseline to Month 12 comparison
Total % BMD loss from Baseline: **7%**

Figure 6.10: Distal femur ΔBMD maps of SCI injury subjects demonstrating no obvious bone loss patterns during 1st year post-injury

Subject L6's right distal femur at 4 months (Figure 6.8a) shows early indications of bone loss, in particular in the medial condyle. Between month 4 and month 8, both femoral condyles start demonstrating quite significant drops in BMD. Interestingly, between month 8 and month 12 the changes are not quite as dramatic, however the majority of voxels with statistically significant changes have lost >100mg/cm^3. Another example of bone loss evident in the femoral condyles is demonstrated in subject L21's longitudinal changes in Figures 6.8d to 6.8f. Initially, L21's left distal femur appears to be quite stable, with the Baseline to month 4 scan showing very minor bone turnover. By month 8 there is some indication that bone loss at this site may be commencing, as the proportion of voxels with statistically significant changes has increased and the postero-medial femoral condyle has a small pocket of voxels with loss >250mg/cm^3. By the end of the study at month 12, this pocket has started to extend outwards demonstrating a very considerable amount of bone loss in the medial femoral condyle, with the start of pockets of loss in the lateral femoral condyle. One possible explanation for loss preferentially occurring in these regions is that they were previously key weight bearing points within the femur. In accordance with the Mechanostat theorem [5], the removal of the previously very high stresses and strains on the femoral condyles should result in bone remodeling in response to the now very low forces which act upon this region. Subjects L5 (left leg) and L22 (right leg) are two examples given in Figure 6.9 which demonstrate different patterns of inhomogeneous loss in the distal femur over the duration of the study. Subject L5 has very interesting patterns of bone turnover. By month 4, there is nothing of significance occurring, with the pattern map containing a mixture of both increasing and decreasing BMD voxels. However by month 8 there are two noteworthy regions within this 5% femoral location. Firstly, there is a small area with a large loss of bone in the antero-lateral region of the bone, at it's boundary with the patella (not included in the image). Generally, the entire lateral condyle looks like it is beginning to show signs of significant bone loss, whereas the medial condyle has losses of a much smaller magnitude. The second area of interest in Figure 6.9b is the posterior region of the inter-condyle fossa. This subject appears to have quite a marked region of increasing BMD at this location at both month 8 and month 12 in comparison to the Baseline scan. This is noteworthy as it would indicate that some processes are occurring in this subject resulting in an increase in BMD. Where it is known that following SCI the removal of weight-bearing forces on the bones results in bone loss, the cause of any increase in BMD following SCI without any intervention is not clear. One possible explanation for this is that it may be highlighting the limitations of both the clinical study and the software. These have been identified previously as patient positioning error, registration errors or the presence of false positives within the voxel map of BMD change.

The right distal femur of L22 has loss evident in both femoral condyles by month 8 however by month 12 this has become much more pronounced in the lateral condyle, with no real change in BMD occurring in the inter-condyle fossa.

The final examples of changes in BMD occurring in the right distal femur are those demonstrating no obvious signs of bone loss, despite the fact that these subjects are no longer weight bearing on the limbs. All comparisons to Baseline made in Figure 6.10 primarily have no statistically significant changes (represented by white voxels), with a small mixture of increasing and decreasing BMD values across the slice, thought to be attributed to statistical noise.

6.3.5 Morphometric Analysis

In this clinical study of bone demineralisation following SCI, what is becoming clear from the image analysis already presented is that based on these small numbers, each subject experiences their own pattern of bone loss and at varying rates. From the available data in this study, it is therefore not possible to conclude a general hypothesis of bone turnover for the acute SCI population as a whole. An individualistic approach is necessary, as there appears to be no obvious pattern which categorises subjects into those who will experience rapid declines in BMD or not. Based on the initial findings of this study (n=6), Coupaud *et al* [70] have proposed patient-specific predictions of global bone loss based on a Baseline pQCT scan performed as soon as possible after injury at fracture prone sites. By using the results from this measurement and those at an 8-month acquisition, these values could be compared to predicted values of loss in this population, flagging up any patients who are losing bone at a faster rate than expected and hence at greater risk of experiencing low-impact fractures.

In parallel with Coupaud's investigation into predicting patient specific fracture risk, gray-scale granulometric analysis defined in Chapter 5 was also performed on the pQCT images at each time point. The purpose of this was to investigate whether there was a possible link between the subject's bone structure and patterns to their susceptibility to bone loss following post-SCI immobilisation. Recalling that granulometric analysis of an image is analogous to a sieving process, where depending on the voxel patterns present in the image i.e. their size, density, shape and proximity to surrounding voxels, they will either pass through the sieve (morphological opening) or survive to the next iteration which will subsequently use a sieve mesh with slightly larger holes. Measuring the survival of voxels at each iteration provides information on the texture and patterns of bone present in the image. Although the exploration of granulometric analysis of bone in the investigation of disease has been studied previously in MRI [140, 97], whether it has a clinical application with lower resolution pQCT images is unknown. This final analysis section of the SCI data will therefore examine whether it can provide useful information on bone structure and if it has any relationship with rate of bone loss.

Both global pattern spectrum analysis and local pattern spectrum analysis were performed on the longitudinal segmented images from the distal tibia of all 15 subjects using morphological granulometries. The results from these analyses generated local pattern spectrum images and global pattern spectrum moments (mean, variance and skewness).

Local Pattern Spectrum Distribution Maps

The purpose of generating local pattern spectrum distribution (local PSD) maps was to identify any obvious changes in bone pattern over time and relate this to the changes in BMD, in addition, whether an assessment of the bone texture using this method would provide any additional information in relation to bone loss patterns or susceptibility. It is important to note at this stage that unlike the ΔBMD voxel wise comparison images presented in Section 6.3.4, these images are a measure of the bone's structural pattern and not it's BMD.

Examples of local pattern spectrum mean images generated from two fast losers and one slow loser are presented. Recalling from Chapter 5, for each x location in the image, there is a corresponding local PSD. The local pattern spectrum image is generated from the moments of each local PSD. In this instance the mean of the local PSD is presented as these images were the most informative.

The first subject, L6, is a fast bone loser at the distal tibia location, who had experienced the majority of their bone loss centrally. The local PSD (mean) of their images is shown in Figure 6.11 along side their segmented raw pQCT images.

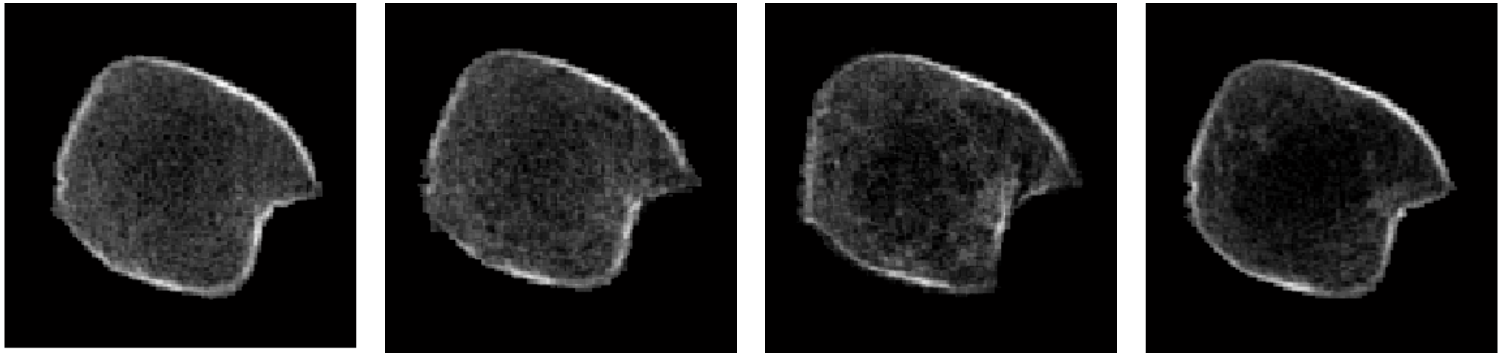

(a) L6: Segmented distal tibia Baseline image
Total BMD: 300mg/cm^2

(b) L6: Segmented distal tibia Month 4 image
Total BMD: 270mg/cm^2

(c) L6: Segmented distal tibia Month 8 image
Total BMD: 188mg/cm^2

(d) L6: Segmented distal tibia Month 12 image
Total BMD: 181mg/cm^2

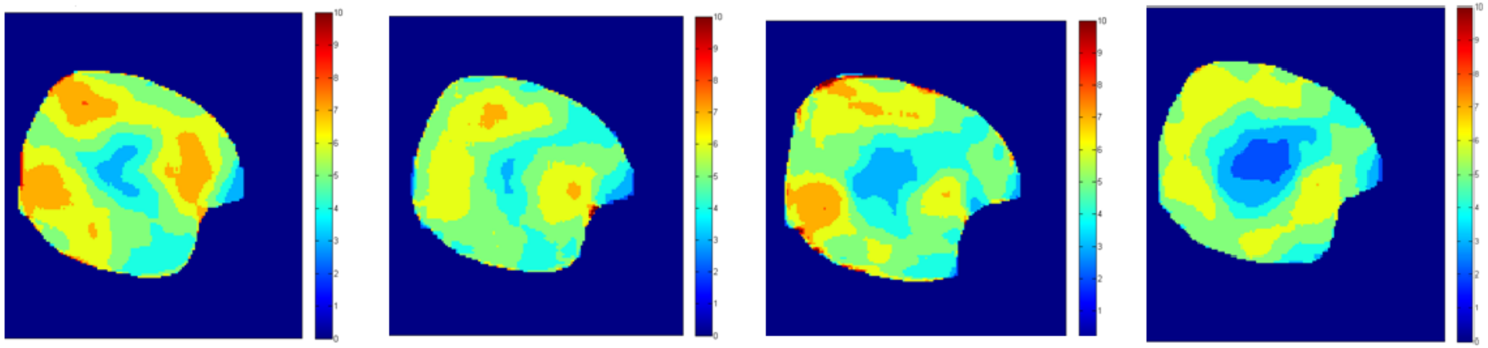

(e) L6: Baseline Local Pattern Spectrum Image

(f) L6: Month 4 Local Pattern Spectrum Image

(g) L6: Month 8 Local Pattern Spectrum Image

(h) L6: Month 12 Local Pattern Spectrum Image

Figure 6.11: L6: Local Pattern Spectrum mean images of distal tibia with corresponding pQCT images - fast loser

The colour scale indicates number of iterations each neighbourhood of voxels has survived the morphological opening. By inference, the lower the number, the less dense the voxel neighbourhood and hence pattern of trabecular bone is in that region. These images inform us that the bone structure centrally is finer and more sparse than that of the peripheral bone, and it is the former bone structure which has been more susceptible to loss as opposed to the more densely packed bone. This is observed by the blue and green colours which appear within the central core of the bone.

An example of the bone structures present in the distal tibia of another subject experiencing rapid loss (L5), in this instance globally across the entire slice, is also presented (Figure 6.12)

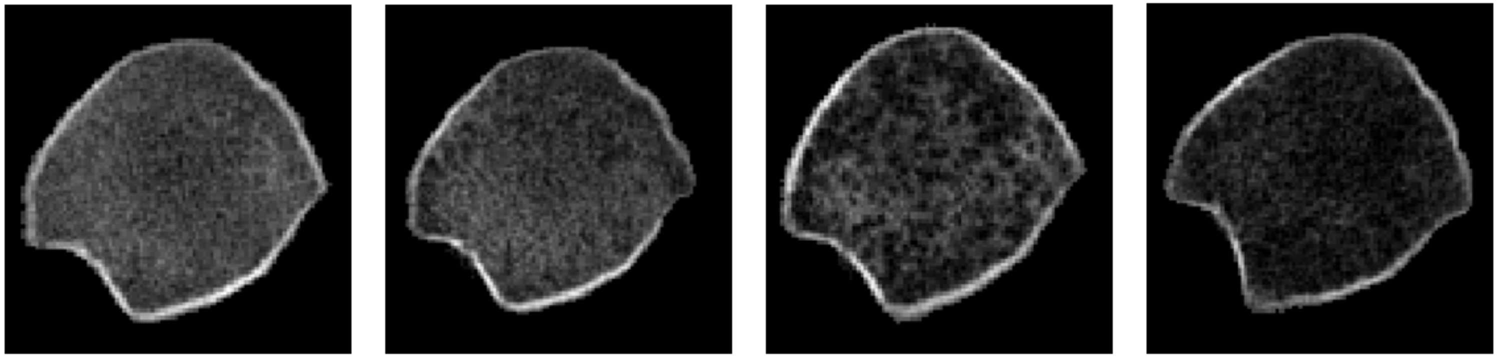

(a) L5: Segmented distal tibia Baseline image **Total BMD: 313mg/cm^2**

(b) L5: Segmented distal tibia Month 4 image **Total BMD: 250mg/cm^2**

(c) L5: Segmented distal tibia Month 8 image **Total BMD: 215mg/cm^2**

(d) L5: Segmented distal tibia Month 12 image **Total BMD: 136mg/cm^2**

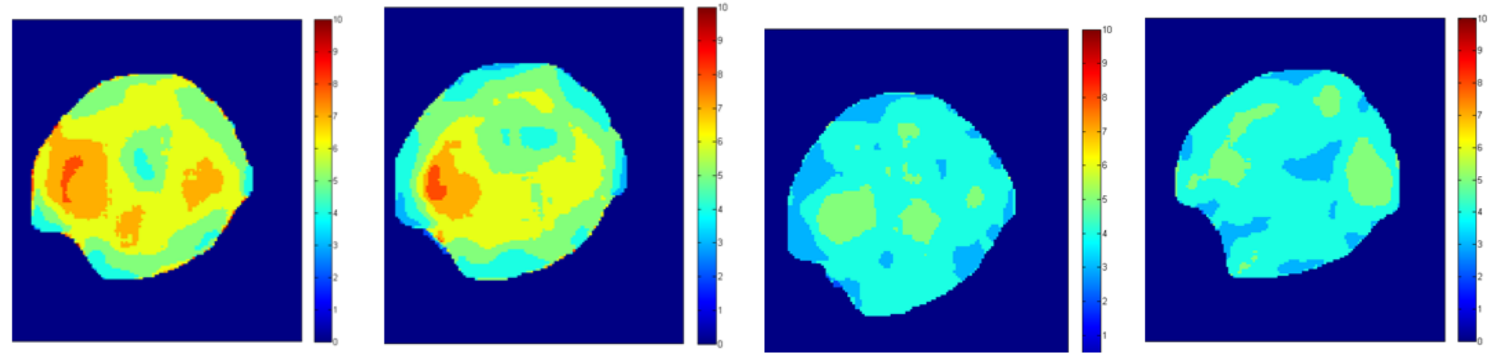

(e) L5: Baseline Local Pattern Spectrum Image

(f) L5: Month 4 Local Pattern Spectrum Image

(g) L5: Month 8 Local Pattern Spectrum Image

(h) L5: Month 12 Local Pattern Spectrum Image

Figure 6.12: L5: Local Pattern Spectrum mean images of distal tibia with corresponding pQCT images - fast loser

The more diffuse nature of this subject's bone loss is visible in both the raw pQCT images as well as the local pattern spectrum images, the latter again demonstrating that as the trabecular structure becomes more sparse (Months 8 and 12), the survival rate of the granulometric sieving process is much shorter.

The third example of longitudinal image analysis using local PSD granulometries is of subject L10 shown in Figure 6.13, a subject who has been identified as having no real change in BMD with time.

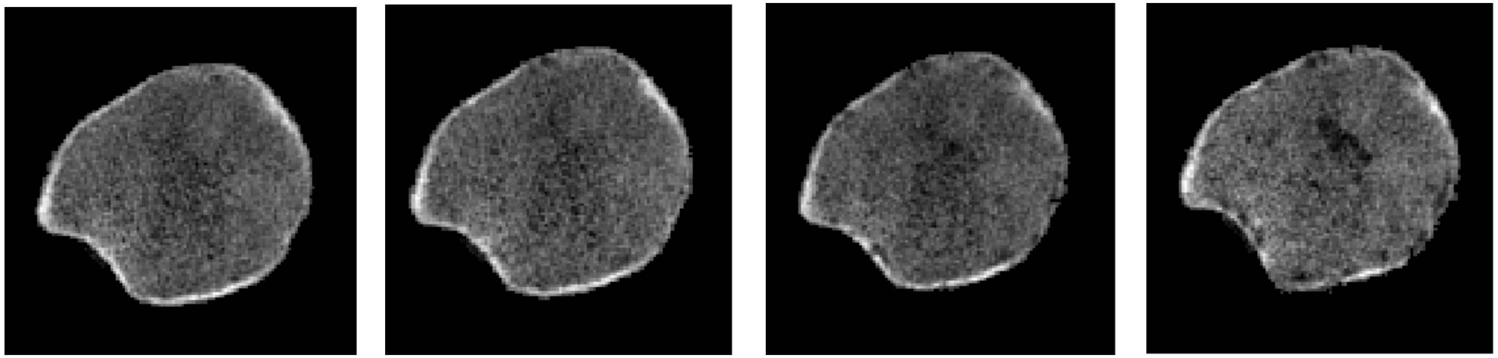

(a) L10: Segmented distal tibia Baseline image **Total BMD: 343mg/cm^2**

(b) L10: Segmented distal tibia Month 4 image **Total BMD: 336mg/cm^2**

(c) L10: Segmented distal tibia Month 8 image **Total BMD: 333mg/cm^2**

(d) L10: Segmented distal tibia Month 12 image **Total BMD: 320mg/cm^2**

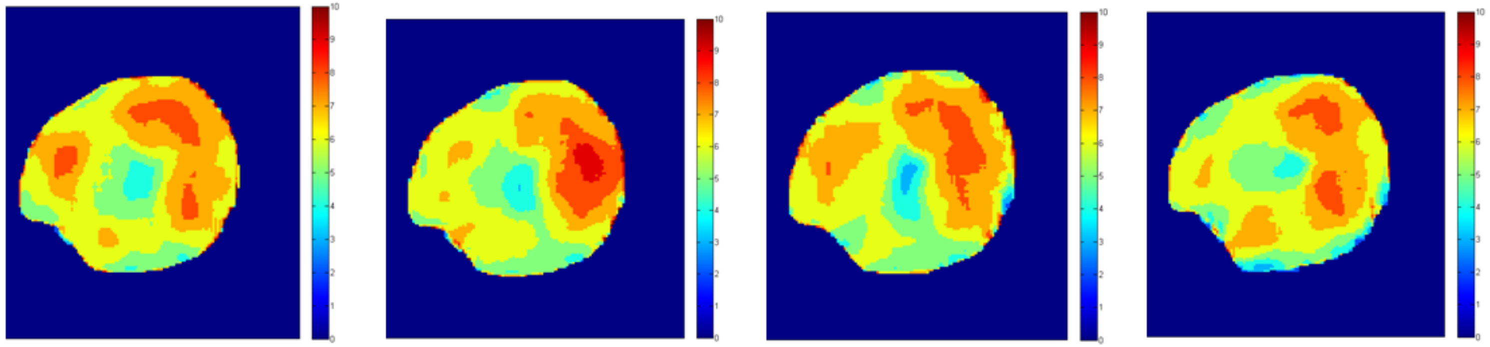

(e) L10: Baseline Local Pattern Spectrum Image

(f) L10: Month 4 Local Pattern Spectrum Image

(g) L10: Month 8 Local Pattern Spectrum Image

(h) L10: Month 12 Local Pattern Spectrum Image

Figure 6.13: L10: Local Pattern Spectrum mean images of distal tibia with corresponding pQCT images - slow loser

Although there appear to be minor changes in the bone structure over time, the local granulomerty images remain largely unchanged. This would support the assumption that no changes in physiological bone turnover are occurring in these subjects at this site despite their radical change in physical mobility.

An alternative approach to looking at the additional information these images provide on the bone structure is to compare local pattern spectrum distribution images corresponding to BMD images which have the same BMDTot measurements. Figure 6.14 presents three images which all have a BMDTot measurement of ≊306mg/cm^3 alongside their local granulometry images.

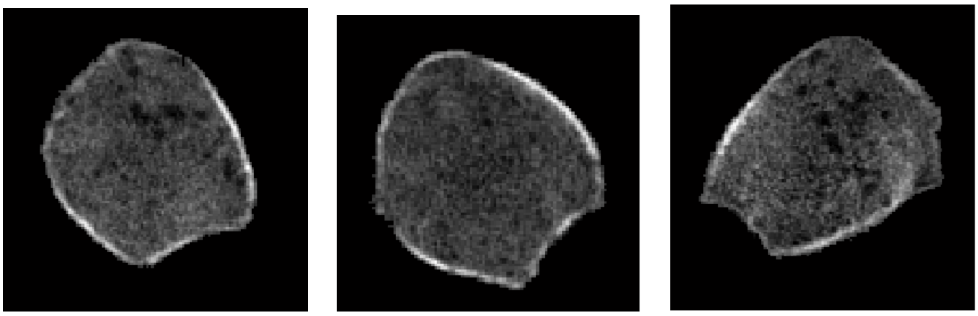

(a) L22 Month8, BMD=306mg/cm^3 (b) L16 Month4, BMD=307mg/cm^3 (c) L21 Month8, BMD=306mg/cm^3

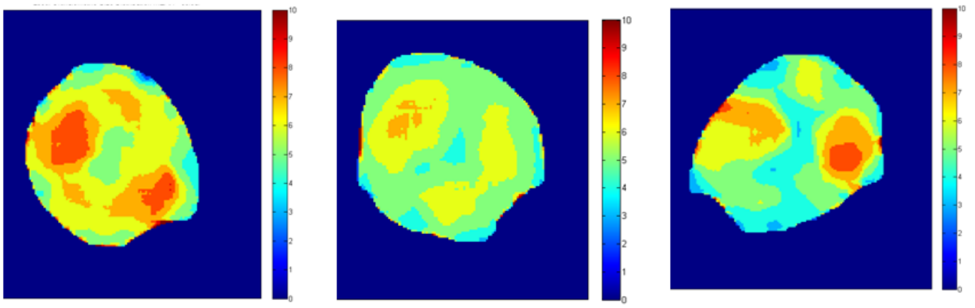

(d) L22 Month8, PSM image (e) L16 Month4, PSM image (f) L21 Month8, PSM image

Figure 6.14: Granulometry images of 3 subjects with the same BMDTot measurements

It is possible to see from the raw pQCT images in Figures 6.14a-6.14c that there are perhaps some structural differences present within the bone, despite the identical measurement in global BMD, however this becomes much more obvious when a qualitative assessment of the local pattern spectrum images is made (Figures 6.14d-6.14f). More dense pockets of bone are represented by the red and orange colours, whereas thinner bony networks are displayed with the blues and light greens. What this demonstrates is that the BMDTot measurement on its own is only one factor of many when assessing osteoporotic risk factors in the acute SCI population, with other indicators almost certainly playing a role in parallel with this.

Patterns Spectrum Moments

From the visual indications using the local PSD mean images, it would suggest that there are remodeling processes occurring early in post-SCI injury. Although visually informative, these images are qualitative in nature. It would be interesting and clinically relevant to see if some quantitative measure from the granulometry analysis could be of value e.g. early predictor of outcome in terms of later changes in BMD. One such measure would be to look at the pattern spectrum moments of the global granulometry analysis as outlined in Chapter 5, taken from the pattern spectrum distribution of the sequentially opened gray-scale image as a single entity.

The following four graphs present three global pattern spectrum moments alongside BMDTot values for 4 typical subjects who were fast losers, experiencing significant bone loss over the 1 year period following injury (>20% Baseline measurement). The values are displayed as a percentage of the Baseline measurement.

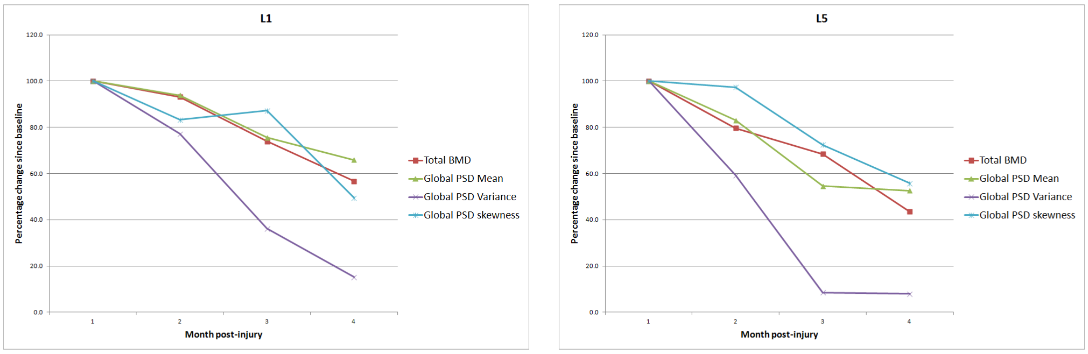

(a) Pattern Spectrum Moments for Subject L1, Baseline to Month 12

(b) Pattern Spectrum Moments for Subject L5, Baseline to Month 12

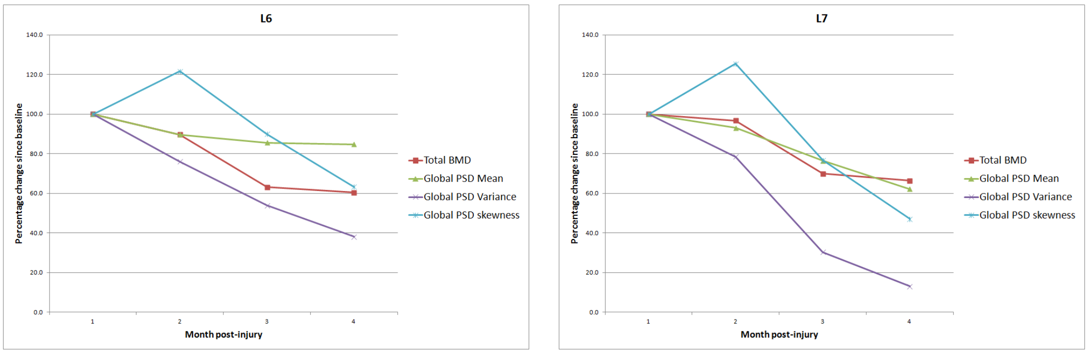

(c) Pattern Spectrum Moments for Subject L6, Baseline to Month 12

(d) Pattern Spectrum Moments for Subject L7, Baseline to Month 12

Figure 6.15: Global Pattern Spectrum Moments of fast loser SCI subjects

In order to evaluate the usefulness of this data, a comparison of the global pattern spectrum moments of typical subjects who did not experience bone loss would be sensible. These are given in Figure 6.16.

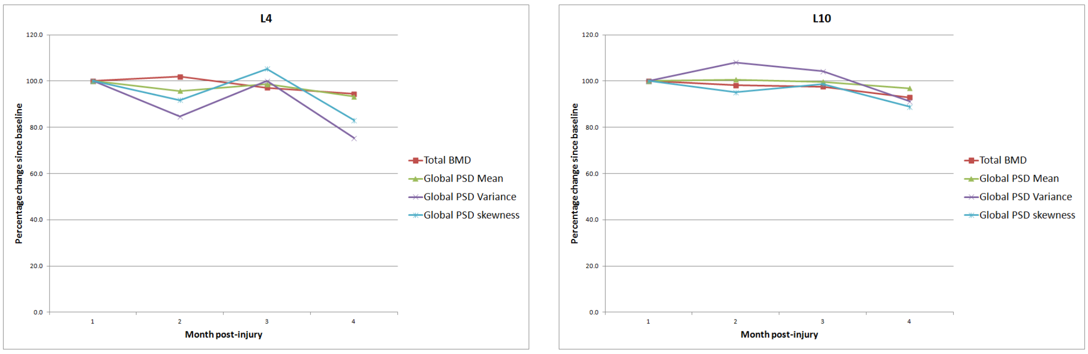

(a) Pattern Spectrum Moments for Subject L4, Baseline to Month 12

(b) Pattern Spectrum Moments for Subject L10, Baseline to Month 12

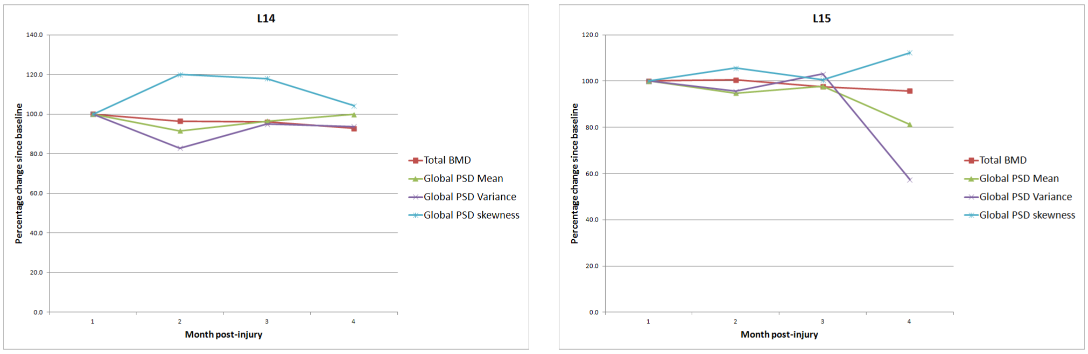

(c) Pattern Spectrum Moments for Subject L14, Baseline to Month 12

(d) Pattern Spectrum Moments for Subject L15, Baseline to Month 12

Figure 6.16: Global Pattern Spectrum Moments of slow loser SCI subjects

The difference between these two groups of graphs is quite contrasting, which is to be expected given the very different responses in BMD turnover during this period of investigation. The following observations from these results can be made:

- **Global PSD mean:** These values tend to follow and reflect BMDTot values for both fast and slow losers.
- **Global PSD skewness:** No obvious reflection of the changes in BMDTot.
- **Global PSD variance:** There are quite marked differences in the response of this variable between the two groups. For this reason it may have value in the categorisation of fast and slow losers within the group.

Based on these initial observations, an assessment on whether Global PSD variance could be a better early predictor (e.g. at the 4 month scan) of a subject's classification as a fast or slow bone loser, compared to its equivalent 4 month Total BMD would be interesting. If a SCI-patient could be flagged as being high risk of experiencing sub-lesional osteoporosis as early as 4 months post-injury, interventional treatments could be implemented much earlier with the aim of minimising any further losses in BMD.

The mean and 95% Confidence Intervals (CI) of the BMDTot and Global PSD variance values as a percentage of their baseline at 4 months was firstly calculated for the slow losers.

- Total BMD measurements: mean (95% CI) at 4 months of slow losers:
  98.4 (94.5 - 102.4)

- Global PSD variance measurements: mean (95% CI) at 4 months of slow losers:
  89 (45.9 - 132)

Based on a classification paradigm which would flag a subject as a fast loser at 4 months should their BMDTot or Global PSD variance fall below the 95% CI (mean-2SD), Table 6.5 presents the categorisations of the fast losers that would be made from the 4 month scans.

Classification at 4 months post-SCI using % of baseline measurement

Total BMD Measurement		Global PSD variance Measurement	
Prediction as fast loser at 4m (measurement $<$ 95% BMDTot CI)		Prediction as fast loser at 4m (measurement $<$ Global PSD var 95% CI)	
Subject	**Prediction**	**Subject**	**Prediction**
L1	YES	L1	NO
L5	YES	L5	NO
L6	YES	L6	NO
L7	NO	L7	NO
L21	YES	L21	NO

Table 6.5: Assessment of Global PSD variance versus BMDTot as a predictor of bone loss

Despite the Graphs in Figure 6.15 displaying some initial indications that Global PSD variance may a good early predictor of bone loss, the results in Table 6.5 would disagree. The explanation for this is because there are large fluctuations in the range of values the Global PSD variance can take, which ultimately results in a very poor classification at the 4 month stage. The BMD Tot values conversely demonstrated much better classification.
Although the Global PSD variance values have not demonstrated good early predictive value, it is clear that this granulometry variable is providing some additional information which is known to relate to the image structure, different from that of the BMD value. Up to this point, categorisation into fast or slow losers has been done using 12 month BMD measurements. Those categorised as fast losers were consequently identified as being at a higher risk of osteoporosis and/or fracture and flagged as requiring preventative intervention. However if a different parameter were used for the classification, would the classification of the subjects change, or indeed, if combinations of parameters were used? The use of pattern spectrum moments is therefore explored here to determine whether the additional information these variables provide on the bony structure within the image can be used to compliment the Total BMD measurement when identifying those SCI subjects at greatest risk of osteoporosis.

The information contained in the BMD frequency distribution plot in Figure 6.1, which displays the rates of individual bone loss for the SCI distal tibia and categorises into fast and slow losers, can also be displayed as a scatter plot, demonstrated in Figure 6.17.

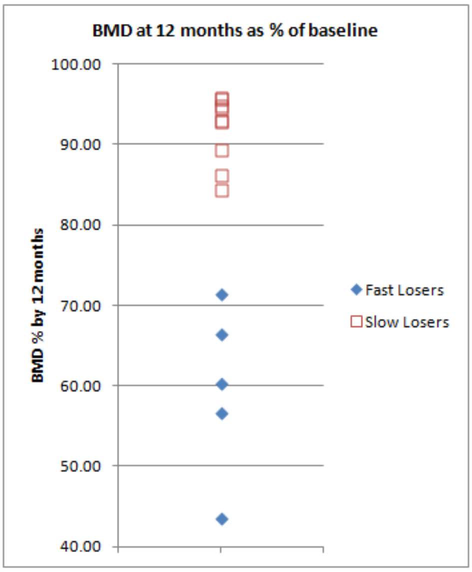

Figure 6.17: Scatter distribution of rates of individual bone loss for SCI distal tibia - Month 12 as a % of Baseline

This representation of the data has allocated different marker types for the two different groups into which the subject has been classified. Fast losers are represented by filled blue diamonds and slow losers unfilled red squares. As was apparent in Figure 6.1, the bi-modal distribution of these two groups is also clear in this graph. Displaying the data in this format will assist in the evaluation of global PSD moments as novel classifiers.

Firstly, the Global PSD mean values are very similar to those of the BMDTot measurements. These were therefore excluded from further analysis as it is not felt they will provide any novel clinical information. Global PSD variance and skewness however are quite different and are hypothesised to be describing different properties of the bone from BMDTot. The frequency distribution plots are presented in Figure 6.18 for change in Global PSD skewness (Δ PSD skewness) and change in Global PSD variance (Δ PSD variance).

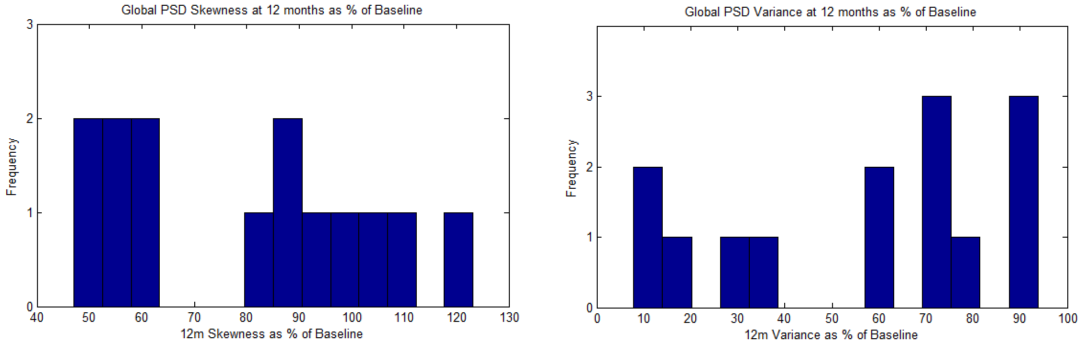

(a) Frequency Distribution for Δ PSD Skewness (b) Frequency Distribution for Δ PSD Variance

Figure 6.18: Frequency distributions for Global Granulometries

Once more, it is possible to see bimodal distributions within these two histograms. In Figure 6.18a Δ PSD Skewness, there are 6 subjects whose images have experienced a sizable change in the global PSD skewness (values <70% of the original baseline value), and a group of 8 of the subjects with 12 month values between 80-125% of the Baseline measurement. As all changes are relative to the best case value at baseline, it is proposed that the group with the more rapid changes are likely to be associated with a worse prognosis. Similarly, the Δ PSD variance (Figure 6.18b) indicates one group (n=5) with large reductions in PSD variance (<50% of baseline values) and another group (n=9) with smaller changes (>50% baseline value). Again, as values are relative to Baseline, sizeable changes are proposed to be associated with a worse prognosis. The scatter plots associated with these frequency distribution graphs are given in in Figures 6.19a and 6.19b, using the icons for each patient which they were allocated during their original classification with Total BMD.

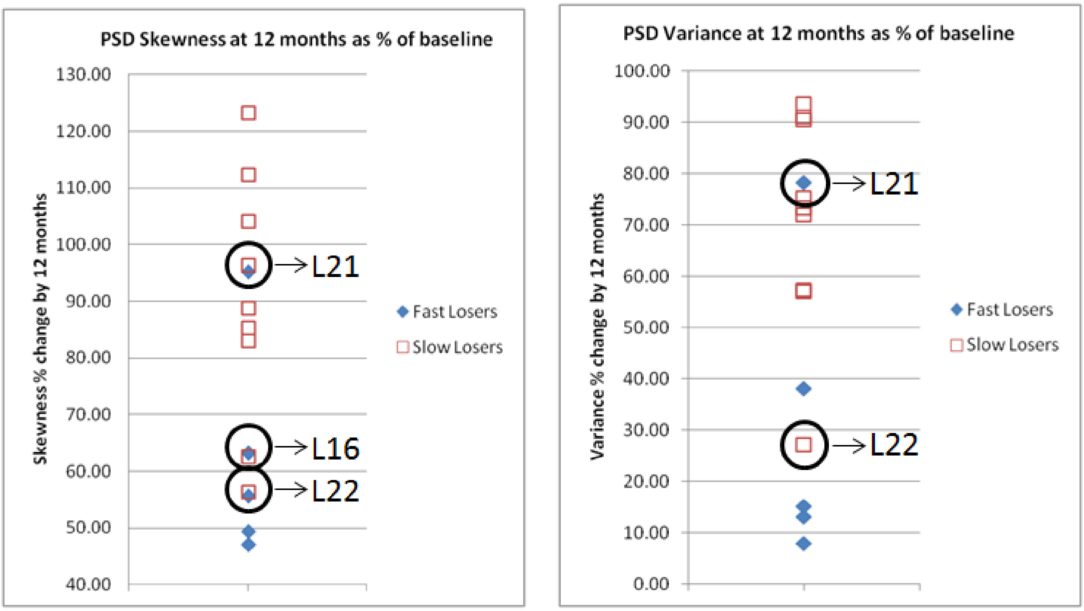

(a) Scatter plot for Δ PSD Skewness (b) Scatter Plot for Δ PSD variance

Figure 6.19: Scatter distributions for Global Granulometries

Both the Δ PSD skewness and Δ PSD variance at 12 months appear to categorise the subjects into two independent groups. How these groups vary from those using the 12 month BMD measurement are discussed below.

- **Δ PSD skewness:** Using a cutoff of 70% of the baseline value, 11 of the 14 subjects remain in the groups as defined using total BMD loss at 12 months. Three of the subjects would have been grouped differently (L16, L21 and L22).

- **Δ PSD variance:** Using a cutoff of 50% of the baseline value, 12 of the 14 subjects remain in the groups as defined using total BMD loss at 12 months. Two of the subjects would have been grouped differently (L21 and L22).

From the 14 subjects analysed, both of these granulometry parameters would allocate the grouping into the same fast and slow losers as 12 month BMDTot for the large majority of subjects (11 out of 14). This in itself is reassuring that the Total BMD values have strong associations with the structural integrity of the bone. There were however 3 subjects who would have been classified differently and consequently merit further investigation into why this may be the case.

L22 This subject was defined as a **slow loser** using the 12 month Total BMD classification and therefore at lower risk. On closer inspection this subject had the largest loss of BMD of all the subjects in the slow losers group (83% of Baseline). Both Δ PSD skewness and Δ PSD variance categorise this subject as a fast loser.

L21 This subject was defined as a **fast loser** using the 12 month Total BMD classification and therefore at higher risk. The BMD at 12 months was approximately 70% of the original value, which was the smallest loss of BMD of all subjects in the fast-losers group. Both Δ PSD skewness and Δ PSD variance categorise this subject as a slow loser.

L16 This subject was defined as a **slow loser** using the 12 month Total BMD classification and therefore at lower risk. Δ PSD variance results agree with this classification. The Δ PSD skewness measurement would categorise this subject as a fast loser, although it is near the cutoff between the two categories.

The Baseline and Month 12 images for one of these outliers (L22) are presented in Figure 6.20. A visual comparison between both of these images highlights some visible structural changes occurring within the bone, with the 12 month image having a more "speckled" bone pattern compared to it's Baseline image.

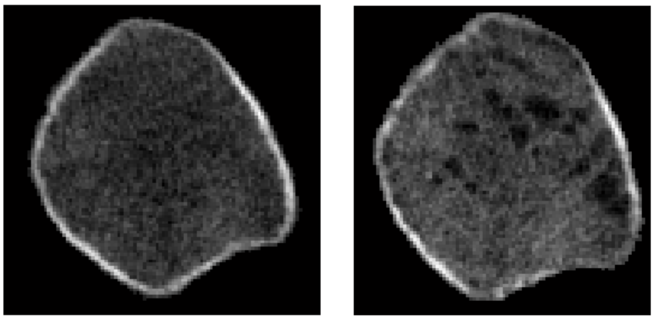

(a) L22 pQCT Baseline image (b) L22 pQCT month 12 image

Figure 6.20: L22 "Speckled" bone pattern present by month 12 not evident at Baseline

Where using the BMDTot value alone at 12 months this subject would have been classified as a slow loser, the granulometric analysis for both PSD variance and skewness categorised this subject as a fast loser. One hypothesis for this could be that classification using the latter values is based on the structural pattern of the bone which evidently has changes as opposed to the total BMD measurement.

Figure 6.21 presents the Baseline and 12 month images of subject L21, another example from the outliers. This subject was classified as a fast loser using 12 month total BMD and a slow loser using both 12 month PSD variance and skewness.

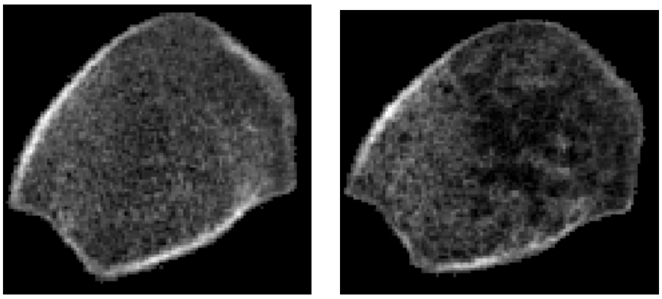

(a) L21 pQCT Baseline image

(b) L21 pQCT month 12 image

Figure 6.21: L21 asymmetric bone loss pattern present by month 12 not evident at Baseline

In this instance it is clear that L21 is experiencing bone loss in the entire medial portion of the distal tibia image. As mentioned previously, this subject experienced approximately 30% of their baseline BMDTot bone loss, the smallest loss within the fast losers group. The asymmetric nature of this loss would however be a cause for concern, and quantification of the actual extent of the bone loss within this region could be facilitated using either a quadrant analysis or voxel wise comparisons. What this also demonstrates is the need for an assessment of osteoporosis risk to be made using both Total BMD as well as that of the bone structure. For this particular subject the BMDTot measurement at 12 months would have been a better classification of risk compared to the structural image analysis using Δ PSD skewness or variance.

In the absence of granulometry analysis of the structural patterns within the bones, within this study each subject's serial pQCT scans would be classified according to BMD alone. For the majority of the longitudinal SCI subjects, both classifications of risk using 12 month BMDTot and 12 month granulometry variables are in agreement. However the presence of outliers from the slow and fast BMD losers groups are noted, with granulometry values for these subjects more in keeping with those of the alternative group. It is therefore proposed that granulometry analysis of the bones' structure may be a useful adjunct to BMD for characterisation of SCI subjects post injury. Further follow up is required to determine the clinical utility of these parameters, however in the interim, using a combination of both BMD and structural assessment can "red-flag" users as requiring osteoporosis interventions who may have been classified as slow losers using one variable but fast losers using another.

6.4 Discussion

6.4.1 Review of Software

A case study of 1 subject is presented here as a means of reviewing the additional clinical benefits the outcomes developed in this thesis can add. The images from subject L1 are used, a subject who was classified as a fast bone loser.

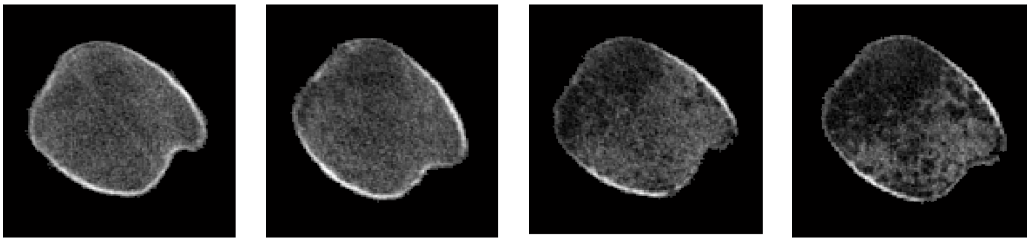

(a) L1 Baseline pQCT (b) L1 Month 4 pQCT (c) L1 Month 8 pQCT (d) L1 Month 12 pQCT

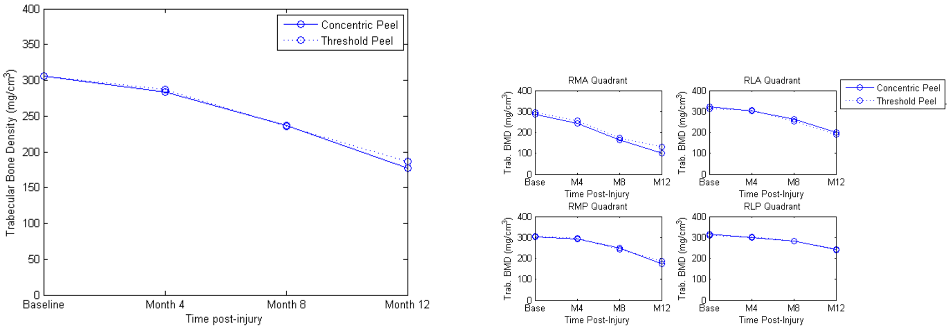

(e) L1 BMDTrab global loss (f) L1 BMDTrab quadrant loss

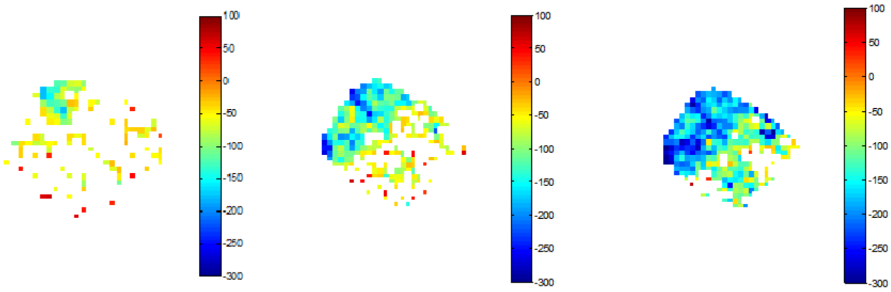

(g) L1 ΔBMD Baseline to month 4 comparison (h) L1 ΔBMD Baseline to month 8 comparison (i) L1 ΔBMD Baseline to month 12 comparison

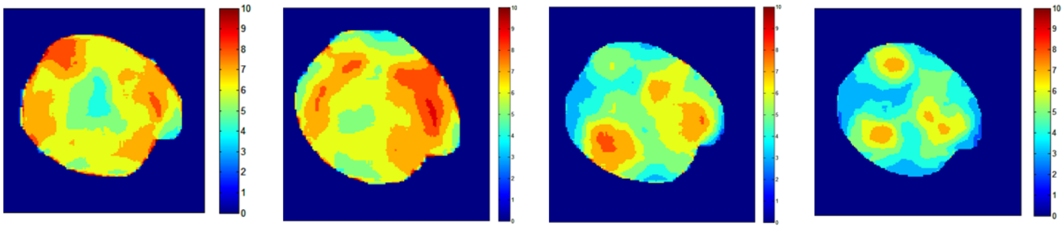

(j) L1 Baseline local PSD (k) L1 Month 4 local PSD (l) L1 Month 8 local PSD (m) L1 Month 12 local PSD

Figure 6.22: Case study - Subject L1

Figure 6.22 brings together all four different image data sets processed using the software developed for this thesis. Currently, analysis is carried out using the manufacturer's software using a predefined threshold for segmentation. If the manufacturer's software fails to segment the image, the operator can either modify the threshold or manually draw around the bone of interest. Figures 6.22a to 6.22d are the automatically segmented longitudinal pQCT images, from which BMDTot and CSA are automatically calculated. It is also possible to see from the trabecular quadrant analysis that in this subject the right medial anterior quadrant is preferentially losing bone (Figure 6.22f). Further analysis of this in the ΔBMD voxel wise comparisons quantifies this loss locally, providing the operator with a visual representation of the bone loss over time (Figures 6.22g-6.22i) conveying clinical information previously unavailable. Finally a visual representation of the changes in bone structure using granulometries is presented in Figures 6.22j to 6.22m. All of these images provide the operator with additional information on the bone turnover occurring during the first year post-injury which had not been previously available. The representation of the subject's bone loss in the form of the gradient colour scale image used in the ΔBMD voxel wise comparison images is simple and straightforward for both health care professionals and the patient to understand. Where the numbers from granulometry analysis and the graphical descriptors are useful, the visual representation on the bone loss helps them picture what is happening to the bones. This in turn will help consolidate targeted therapies and enable the use of any follow-up imaging to see if these interventions are having any effect. The value of the local pattern spectrum distribution images is instinctively less obvious. A background on their generation and what these images are describing would be necessary so that the observer understands that these images are describing bone pattern and structure, as opposed to BMD. Finally there is the potential additional clinical benefit of assessing the bone structure using global granulometries. When used in conjunction with the BMDTot measurement, an informed risk assessment on the rate at which the patient will potentially lose bone following injury can be made.

6.4.2 Clinical Study Outcomes

Based on the findings derived from the medical image analysis in this thesis, the following novel clinical outcomes were able to be concluded from the SCI longitudinal study:

1. Automatically calculated BMD and CSA measurements can be generated with none or minimal user interaction.

2. The intra-operator variability of patient positioning was able to be calculated and was good for this particular clinical study given the challenges associated with positioning in this population.

3. The global value of BMDTot does not convey information on the pattern of bone loss.

It has been identified through the use of trabecular quadrant analysis and ΔBMD voxel wise comparisons that the acute SCI-population can often experience an inhomogeneous bone loss during the first year post-injury. These additional image processing techniques were required to reveal this.

4. Some regions of bone gain have been observed in the inter-condyle fossa of the distal femur. These are highly unexpected in this population and their cause cannot currently be explained. These may be attributed to patient positioning, registration error or statistical error therefore should be regarded with some scepticism due to their surprising presence in this particular subject group.

5. The use of granulometries to describe information pertaining to bone patterns within an image can be demonstrated visually via local pattern spectrum images.

6. Although granulometries have not demonstrated having early predictive value with regards to bone loss, they have shown to be a useful adjunct to BMD in the assessment of bone structure when assessing their risk of rapid bone loss. Further work with larger subject numbers is needed to validate these findings.

There are consequently several clinical implications of these findings. It would now be possible to implement more focussed interventional techniques looking to minimise further bone loss or ideally restore it in specific regions within the bone. The image analysis could also be used to monitor outcomes, providing a more detailed picture of whether these interventions have had any success. Granulometries as an image processing technique has been identified as a possible avenue for assessing bone structure. Osteoporosis as defined by the World Health Organization is a disease which affects both BMD and microarchitectural bone structure [16]. These preliminary results would indicate that there is potentially information present in these grey scale pQCT images which could be extracted using granulometries to identify those at a higher risk of future fracture. It therefore acts as a complimentary measure to global BMD.

There are some limitations to these findings. Currently these hypotheses are made using a single slice. This may not necessarily be representative of the processes happening elsewhere in the limb. The Baseline scan is acquired within a window of 5 weeks post-injury and as a result some degree of bone loss may have already occurred prior to the scan taking place (although Baseline BMD from the subjects in this study were all within the normal range). The reason behind the inhomogeneous loss seen in some of these patients also cannot currently be explained using this software alone. Coupaud *et al* are looking at correlations between flaccid and spastic paralysis as one explanation, as well as tendon and muscle insertion points. Although this image analysis has demonstrated fast and slow losers with the age of the subjects known, there is no information available on the patient's size, exercise patterns, hormone levels or diet to name a few of many additional factors which will influence BMD during this period. Finally, these findings have been derived from a very small sample of subjects (n=15). The nature of this study makes recruitment very challenging as it takes place at a difficult stage of a devastatingly life-changing injury. Additionally, it requires the patient to have a complete SCI with a commitment to return for 4 scanning sessions during this first year post-injury. Despite these challenges, this study is ongoing with the goal of obtaining a better insight into acute bone loss post-SCI.

6.5 Conclusions

This clinical study into the acute changes in BMD following SCI has brought to light some very interesting findings related this population's bone turnover. Evidence from the image processing in this chapter suggests that it is unique to the individual, with the some experiencing more rapid bone loss than others and often with an inhomogeneous pattern of loss as demonstrated by the ΔBMD voxel wise comparisons. The use of granulometries as a means of describing bone architecture shows promise as an early feasibility study, with further work using larger subject numbers enabling this to be developed further into a means of combining bone mineral content with micro-structural architecture as a descriptor of osteoporosis.

Measurements taken from bone densitometry alone however are only one piece of the overall picture in the assessment of susceptibility to bone loss. Many additional clinical factors will also have an influence, for example the disruption of hormone regulation following a SCI, neurological or vascular changes, complete or incomplete injury, could all affect the bone regulation processes. Although not the purpose of this thesis, what has been developed here is a sensitive tool which could be used in the future to assess the influence of these factors, for example, to what extent are fast losers in this category because of their genetic make-up and to what extent is it lifestyle? Furthermore, the risk of fracture ultimately cannot be assessed using these data alone as correlative data on fracture incidence is unavailable for these subjects. However, the software developed here can be used in conjunction with other clinical diagnostic assessments to assess fracture risk in future studies. As proposed by Coupaud *et al*, it is also the author's belief that pQCT imaging should be incorporated into the acute SCI patient's patient management as one means of assessing and managing bone loss following spinal cord injury.

Chapter 7

Subject Group 2: Post-Anterior Cruciate Ligament Injury Population

The application of the image processing techniques developed for this thesis to a second, very different population, will evaluate their overall efficacy as flexible image processing tools. This chapter carries out image analysis of pQCT images from a population of subjects who had experienced an ACL injury to the knee. As detailed in Chapter 1, it is known that bone loss occurs both following ACL injury and after reconstructive surgery [12, 13, 30, 29, 141, 41]. Performing localised and global image analysis on this subject group will therefore offer further insight into the patterns of bone loss these subjects are experiencing. The potential clinical outcomes of these findings include better guidance as to the timing of surgery post-injury, implant placement during surgery as well as rehabilitation management focussing on BMD recovery in the knee.

In a similar format to the preceding chapter, this chapter will begin with an introduction to the ACL clinical study carried out at the Southern General Hospital (SGH), Glasgow. Patient positioning intra-operator variability for the images acquired will be calculated, followed by BMD analysis, quadrant analysis and investigation into the ΔBMD patterns of loss post-injury but prior to reconstructive surgery. These analyses will also be performed for a small sample of subjects who were imaged post-surgery following a period of recovery. Morphological analysis will be used to assess whether the trabecular structure influences BMD loss in the ACL injured subjects, finishing with an evaluation of the image processing techniques when applied to this unique population.

7.1 Summary of Clinical Study

A clinical study entitled *" Bone density adaptation around the knee before and after ACL reconstruction"* was carried out between 2004 and 2007 by PI Mr Colin Walker, Consultant Orthopaedic Surgeon, SGH. This was a joint study between the orthopaedic department and the nuclear medicine department at SGH, Glasgow. The author's role in this clinical study was to perform both the data and image analysis from the recruited subjects' pQCT images related to their BMD changes following ACL injury. Both of these aspects are presented in this chapter. All research parties involved in the collaboration would be acknowledged in any novel findings which may arise from using data from this clinical study.
The principal research aim of this study was to investigate how the bone in the knee behaves following an ACL injury as well as establishing what happens following hamstring tendon graft reconstructive surgical repair of the tear. Imaging the contralateral knee as well as the injured knee provides a patient specific control for comparison. Although the ACL reconstruction surgery is a successful operation in restoring knee stability, improving patients' function, ability to undertake work and sporting related activities, evidence would suggest that it does not necessarily restore bone loss which has occurred as a result of the injury within the limb. If the bone density is not restored back to normal after a period time, this may ultimately result in the development of osteoarthritis in the injured joint. The findings from this clinical study are therefore important clinically as they will provide an insight into global and regional BMD changes in the human knee, following both ACL injury and surgical repair. These results could provide guidance on the best time to perform reconstructive surgery and guide the patient's rehabilitation to try and restore previous pre-injury BMD levels.

7.2 Methods

Full ethical approval for this project was granted by the South Glasgow & Clyde Research Ethics Committee. All subjects provided their informed consent prior to participation in the study, in line with the Declaration of Helsinki. Candidates who were about to undergo ACL reconstruction at SGH Glasgow, were approached to take part in the study. Exclusion criteria included:

- Having sustained any previous knee injury, on either limb.
- Any metal implants within the field of interest to be scanned.
- Pregnancy.

A written information sheet was provided to each patient and they were invited to discuss participation in the study with clinicians, family, friends and/or GP. Patients were under no obligation to participate in the study. Patients were scanned immediately prior to their ACL reconstruction surgery. A 2% proximal tibia and 4% distal femur scan was taken of both the injured knee and the contralateral knee, the latter to be used as a control measure. Both images were acquired using a 0.5mm^2 voxel size and a 2.4mm slice thickness. Patients were invited back post-operatively following a suitable period of recovery for follow up scans of the same anatomical locations. All image acquisitions were performed by a single operator and all image analysis was performed using the automated software developed in this thesis. Nineteen subjects were successfully recruited to this study from the orthopaedic out-patients clinic at SGH, Glasgow. Details of their demographics, injury and imaging dates are presented in Table 7.1. Date of injury was determined using the patient's history of trauma to the knee, either verbally from the patient or via the clinical radiology information system. In one case the date of trauma which resulted in the ACL injury was unknown. Pre-op imaging was performed within one week prior to the ACL surgical repair operation. The duration of injury is presented in years (y) and months (m), and the mean values are presented with their standard deviations in brackets.

Subject	Gender	Age at pre-op scan	Duration between injury and pre-op scan
A1	Male	37	Chronic
A2	Male	16	0y 8m
A3	Male	39	1y 6m
A4	Male	42	0y 5m
A5	Male	30	1y 4m
A6	Male	30	1y 1m
A7	Male	31	1y 11m
A8	Male	20	0y 4m
A9	Male	35	8y 5m
A10	Male	44	3y 5m
A11	Male	23	0y 10m
A12	Male	30	2y 2m
A13	Male	33	5y 4m
A14	Male	20	0y 9m
A15	Male	26	1y 8m
A16	Male	16	0y 11m
A17	Male	33	0y 9m
A18	Female	17	0y 10m
A19	Male	39	1y 11m
		30y (9y)	**1y11m (2y)**

Table 7.1: Patient demographics for ACL study

From this patient sample, subjects A1 to A8 returned for post-ACL reconstruction imaging. The dates these scans took place are given in Table 7.2.

Subject	Date of post-op scan	Time between pre-op & post-op scan	Time between injury & post-op scan
A1	21/02/07	1 year 6 months	Unknown
A2	28/03/07	1 year 10 months	2 years 6 months
A3	31/01/07	2 years 2 months	3 years 8 months
A4	21/03/07	1 year 7 months	2 years
A5	31/01/07	2 years	3 years 4 months
A6	07/02/07	1 year 4 months	2 years 5 months
A7	19/02/07	2 years	4 years
A8	10/12/05	1 year	1 year 4 months
	Mean (SD)	**1y8m (5m)**	**2y11m (11m)**

Table 7.2: Dates of ACL post-op imaging

The post-op scan should have ideally been performed at 1 year post-reconstruction. The variation in the times when this was actually performed was a result of the scanner breaking down during the period of the study. This resulted in the scanner having to be returned to the manufacturer for several months for repair. Additionally, only 8 subjects in this clinical study returned for follow-up imaging. With a sample size of only 8 and using a significance level of 0.05, this will ultimately reduce the power of any calculations involving the post-op data. The results will therefore be analysed within these limitations, with any conclusions derived having the caveat that they are based on a much lower statistical power.

7.3 Results

7.3.1 Patient Positioning Intra-Operator Variability

The data acquired in this study was also carried out by a single operator. This eliminated the effect of inter-operator variability. The operator was very experienced in performing densitometry imaging using a DXA scanner. Prior to each scan, each patient's limb lengths were measured to assist the localisation of the required slice. An AP scout view was then performed and reference lines were positioned at either the proximal tibial endplate or the lateral femoral condyle. Intra-operator variability of the patient's position was calculated at both of these sites by comparing the 19 control and injured pre-op image pairs (assuming left-right symmetry) as well as the pre-op and post-op scans for the 8 subjects who were imaged after surgery. The euclidian distance was measured between the COM of these image pairs (x-y displacement), the average difference in CSA between image pairs (z-displacement) and the rotational displacement needed to bring the images into alignment (θ displacement). The results are presented in Table 7.3 quoting the mean ± 2SD of the displacements for the two anatomical locations.

The average areas of the proximal tibia and distal femur for this study are $3584 \pm 340\text{mm}^2$

Slice	COM displacement ($\overline{mm}$)	CSA ave. diff. ($\overline{mm^2}$)	θ displacement ($\overline{deg}$)
Proximal Tibia	9.7 ± 13.9mm	47.3 ± 74.4mm^2	-0.7 ± 7.8^o
Distal Femur	8.7 ± 13.6mm	33.5 ± 43.2mm^2	-0.37 ± 8.3 ^{o}

Table 7.3: Intra-operator variability for ACL study

and 4059±319mm^2 respectively. With this in mind the relative COM and θ displacements were both very small. The discrepancies of these two variables between registered images were once again resolved using the registration software outlined in Chapter 4. The variation in CSA however is investigated further, as significant differences along the z-direction would indicate that the two images under comparison were not anatomically in alignment. The variation in CSA of the distal femur for the ACL study was 33.5 ± 43.2mm^2. In comparison to the 50.5 ± 66.1mm^2 displacement for the same image in the SCI study, the discrepancies as a result of positioning error in this study were smaller. This is not unexpected. ACL injuries are commonly associated with fit and healthy patients who would be easier and more flexible to position during set up, compared to the acute SCI population who can have high levels of muscle tone and often experience involuntary leg muscle spasms.

Although it is not possible to quantify the error in BMD measurement associated with the variation in CSA placement without carrying out phantom or cadaver studies similar to that of Sun *et al* [138], it is possible to postulate the worst case shift as a percentage of the location being imaged. For example, the maximum difference in CSA for the proximal tibia as a percentage of the minimum CSA of this bone would be 3.75% of the overall area, with an equivalent distal femur percentage of 2%. These errors associated with patient positioning add noise, resulting in a higher variation in statistics, however they are nonsystematic, with the location imaged assumed to be randomly varying up or down the limb.

7.3.2 BMD Analysis

In the first instance, results from the global BMD analysis are presented here, as the findings from this clinical study are novel in this investigation field. Subsequently, image analysis will be carried out which will also provide original information on the bone turnover in response to an ACL injury.

Nineteen subjects participated in the study pre-operatively. They had a mean age of 30±9years and an average duration between injury to imaging & operation 1year 11months±2years. One of the participants were unsure of the date their injury occurred and two had waited over 5 years following injury before seeking treatment. The remaining participants (n=16) waited on average 1year 3months±10months between their injury date and them having surgery. BMDTot and BMDTrab measurements using both a 45% concentric peel and a threshold peel (BMDTrab45 and BMDTrabTP respectively) are included in the analysis. The results from the data acquired pre-ACL reconstruction surgery are discussed first for the n=19 subjects. Analysis on the post-operative data from the 8 returning subjects will then be investigated. Finally a review of these results in relation to the length of time since injury will be presented to investigate any relationship between time since injury with extent of BMD loss.

Pre-ACL Reconstruction Surgery

Table 7.4 presents the mean and SD BMD values for the control and injured leg pre-operatively for both the proximal tibia and distal femur for all subjects (n=19) who participated in the study.

	Proximal Tibia (mg/cm^3)	Distal Femur (mg/cm^3)
BMDTot		
Control	243 (24)	280 (20)
Injured	220 (21)	255 (21)
BMDTrab45		
Control	200 (25)	253 (20)
Injured	177 (21)	230 (21)
BMDTrabTP		
Control	212 (19)	228 (12)
Injured	189 (27)	212 (14)

Table 7.4: Pre-op ACL control versus injured BMD comparison (mean(SD))

From the table it is possible to see that the average BMD measurement for the injured limbs pre-operatively is consistently lower than the control limbs. The 3 measurements listed for the control and injured groups were compared using a t-test in Matlab. For both the proximal tibia and the distal femur these differences were all significant for all measurements ($p < 0.05$). Assuming the control leg is a valid reference, percentage changes between the control and the injured images for each subject were calculated using Equation 7.1.

$$Percentage\,change \;=\; 100\% \left[\left(\frac{Injured}{Control} \right) - 1 \right] \tag{7.1}$$

The mean percentage change results with standard deviations in brackets are given in Table 7.5 for both the proximal tibia and the distal femur, for all 3 BMD measurements calculated.

Variable	Proximal Tibia % change	Distal Femur % change
BMDTot	-9.1 (5.6)%*	-8.8 (4.6)%*
BMDTrab45	-11 (7.3)%*	-9 (6.3)%*
BMDTrabTP	-10.5 (11.9)%*	-6.9 (4.1)%*

$^*p < 0.05$, n=19

Table 7.5: Pre-op ACL control versus injured percentage changes

Table 7.5 demonstrates that for the 2% proximal tibia slice, on average the BMDTot of the injured leg is -9.1% (5.6) less than that of the same patient's control leg. Similarly for the distal femur, the BMDTot is -8.8% (4.6) less than the control uninjured leg. The trabecular bone measurements also display lower BMD values for the injured leg at both anatomical locations, and all differences are statistically significant ($p < 0.05$). Based on these findings, the loss in the proximal tibia appears to be marginally greater than that of the distal femur however this difference is non-significant ($p = 0.8$). The limitations of these findings are that the duration between injury and pre-surgery imaging was quite variable as demonstrated in Table 7.1, with a mean duration of 1year 11months±2years (and 1 subject of unknown duration).

Overall these findings would agree with similar studies carried out by Boyd [13] in canines and Bayer [30] and Leppälä *et al* [12] using DXA, confirming that rapid bone loss is observed in the ACL injured knee which has not undergone any surgical repair. These findings add additional value to these publications in that they have been carried out in the human knee, and through the use of pQCT an assessment of both BMDTot and BMDTrab can be made following this injury.

Post-ACL Reconstruction

Eight of the nineteen participants returned for post-operative knee imaging at an average of 1year 8months (±5months) post-surgery (ranging from 1year to 2years 1month). pQCT images of both the control and injured knees were again acquired at the same anatomical locations as the pre-operative scan slices. Examples of femoral and tibial images before and after ACL reconstruction are shown in Figure 7.1.

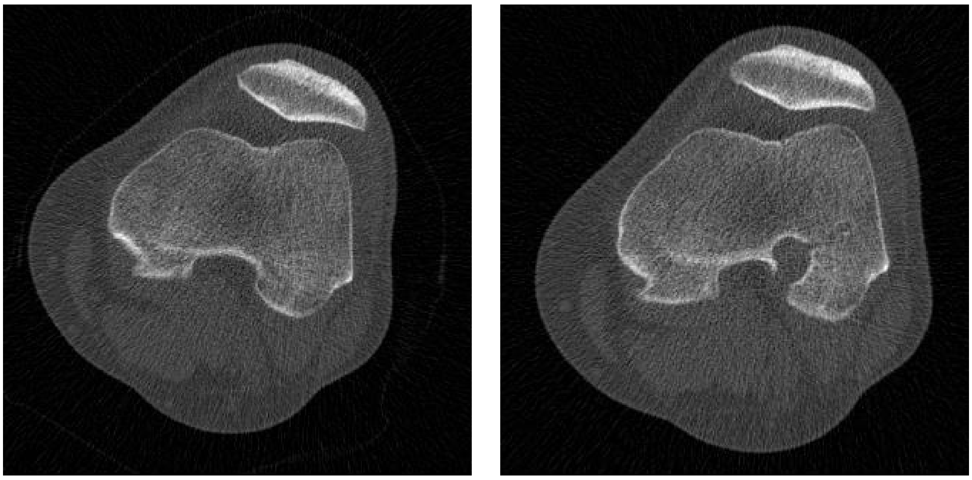

(a) Subject A3 distal femur image pre-op (b) Subject A3 distal femur image post-op

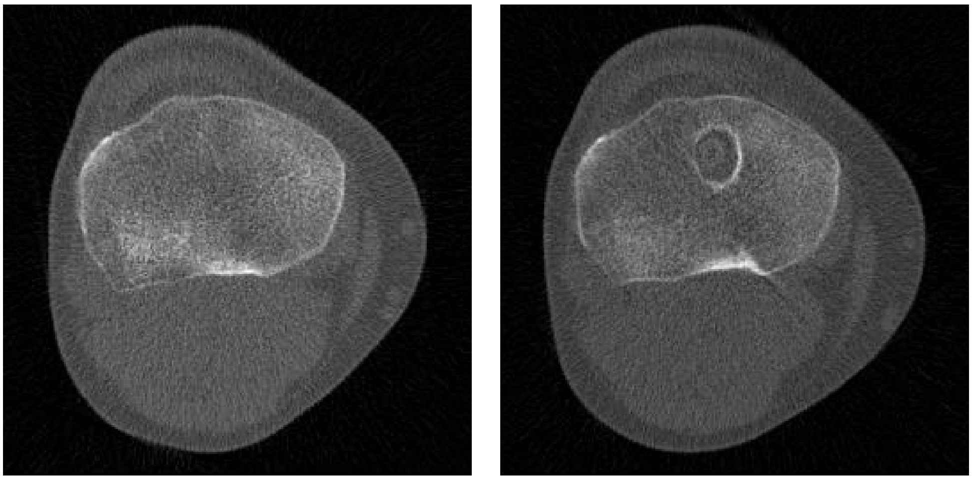

(c) Subject A4 proximal tibia image pre-op (d) Subject A4 proximal tibia image post-op

Figure 7.1: Comparison between pre- and post-op ACL images

It is now possible to visualise the canal where the graft is situated following the ACL reconstruction operation, with the small circular implant visible in Figure 7.1d. Around the perimeter of these grafts it is apparent that there is some high density compact bone. With the presence of the surgical tunnel, ACL graft and compact bone in the post-op image, like for like comparisons between the injured leg and control leg are more challenging. Rittweger *et al* [41] performed a similar pQCT post-operative comparison in a retrospective cross-sectional study of injured versus control images at the same anatomical locations, including the graft canal in the image analysis (n=9 for the femur and n=5 for the tibia). They investigated side to side comparisons of both pQCT image pairs, calculating the percentage difference in BMD between the control and injured knee. Their study demonstrated that the injured knee had on average -4.2% (1.1) less BMDTot pooled across both tibial and femoral locations post-operatively than the control non-operated side, with a statistical significance of $p < 0.05$. It would therefore be interesting to expand on these findings and investigate the differences in BMD without the canal and graft contained within the analysis. An additional sub-routine was therefore appended to the software outlined in the preceding chapters. Following segmentation and registration, the user is presented with the post-operative image and prompted to draw a perimeter around the implanted region they wish to exclude from the analysis. As the images are already registered, the sub-routine also removes an identical area from the corresponding location in the non-implanted slice under comparison.

In the first instance, longitudinal results are analysed. These look at the changes in the same anatomical location which have occurred over time in this study, i.e. pre-op injured limb versus post-op injured limb, in order to identify any changes in BMD which may have occurred following surgical intervention. Following this, the results from post-operative contralateral comparisons are presented. These compare the post-op control with the post-op injured BMD values for both the distal femur and proximal tibia.

Pre- to Post-op Longitudinal Comparisons

The longitudinal assessment of control limbs are considered first. The purpose of doing this is to determine whether there are any changes in BMD in the uninjured limb as a result of the ACL injury, for example as a result of altered loading. Additionally, when performing contralateral comparisons before and after surgery, should the control limb experience any changes, these will influence any differences between these measurements. Table 7.6 presents the mean (SD) BMD of the control limb pre- and post-op where Table 7.7 displays the percentage change between the two, with all statistical comparisons carried out using a Wilcoxon signed-rank test.

	Proximal Tibia (mg/cm^3)	Distal Femur (mg/cm^3)
BMDTot		
Control pre-op	239 (17)	280 (17)
Control post-op	234 (13)	278 (19)
BMDTrab45		
Control pre-op	197 (20)	251 (18)
Control post-op	191 (15)	251 (20)
BMDTrabTP		
Control pre-op	209 (11)	225 (7)
Control post-op	206 (9)	224 (9)

Table 7.6: Pre-op control versus post-op control BMD comparison (mean(SD))

Variable	Proximal Tibia % change	Distal Femur % change
BMDTot	-1.7 (3.5)	-0.8 (1.3)
BMDTrab45	-2.7 (4.8)	-0.3 (1.1)
BMDTrabTP	-1.4 (2.8)	-0.2 (1.1)

$^{*}p < 0.05$, n=8

Table 7.7: Pre-op control versus post-op control % change (mean(SD))

It is clear from both of these tables that using the global measurements of BMD, there is no statistically significant difference in the control limb BMD at either the proximal tibia or distal femur following surgery on the injured limb. This information is useful in that the null hypothesis of no difference in BMD between these time points for this limb cannot be rejected. Any subsequent analyses of the contralateral comparisons will therefore use these initial findings with the assumption that any changes between the control and injured limbs over time will be a result of the injured limb alone.

The pre- to post-op longitudinal comparisons of the injured limb are now presented. The post-operative injured limb images contain the ACL implant, therefore results with both the implant included as well as excluded are given for both the mean (SD) BMD (Table 7.8) and % change (Table 7.9) measurements.

	Proximal Tibia (mg/cm^3)	Distal Femur (mg/cm^3)
BMDTot		
Injured pre-op	221 (22)	257 (22)
Injured post-op	221 (22)	251 (22)
BMDTrab45		
Injured pre-op	176 (19)	231 (26)
Injured post-op	174 (18)	224 (24)
BMDTrabTP		
Injured pre-op	192 (13)	211 (12)
Injured post-op	188 (12)	206 (12)
BMDTot (Implant Removed)		
Injured pre-op	228 (22)	252 (22)
Injured post-op	223 (24)	246 (22)

Table 7.8: Pre-op injured versus post-op injured BMD comparison (mean(SD))

Variable	Proximal Tibia % change	Distal Femur % change
BMDTot	0.1 (7)	-2.5 (4.7)
BMDTrab45	-1.0 (5.1)	-2.8 (4.6)
BMDTrabTP	-1.9 (2.8)	-2.7 (2.9)
BMDTot (Implant Removed)	-1.6 (7)%	-2.4 (4.7)%

$^{*}p < 0.05$, n=8

Table 7.9: Pre-op injured versus post-op injured % change (mean(SD))

An initial inspection of these data would indicate that the BMD in the injured limb after surgery does not change from its pre-surgery levels. With the implant region still contained in the image, there is no statistically significant difference between the two images. However, as highlighted previously, this is not a true comparison as the implant will influence the overall BMD measurements. On removal of this region from both the pre- and post-implant images the results are relatively unchanged. The % change in BMD remains very small and non-significant for both limbs. These findings would indicate that following surgery, the injured knee does not appear to either lose or recover BMD.

Post-operative Contralateral Comparisons

The second type of analysis which can be carried out with the post-operative data is the same contralateral comparisons that were carried out pre-op, looking at the post-op control limb versus the post-op injured limb. The BMDTot, BMDTrab45 and BMDTrabTP post-operative contralateral measurements with the implant included in the image are presented in Table 7.10 alongside BMDTot equivalent values with the implant area removed from both images. Table 7.11 displays the contralateral percentage changes.

	Proximal Tibia (mg/cm^3)	Distal Femur (mg/cm^3)
BMDTot		
Control post-op	234 (13)	278 (19)
Injured post-op	221 (22)	251 (22)
BMDTrab45		
Control post-op	191 (15)	251 (20)
Injured post-op	174 (18)	224 (24)
BMDTrabTP		
Control post-op	206 (9)	225 (9)
Injured post-op	188 (11)	206 (13)
BMDTot (Implant Removed)		
Control post-op	241 (14)	273 (18)
Injured post-op	224 (23)	246 (22)

Table 7.10: Post-op ACL control versus injured BMD comparison (mean(SD))

Variable	Proximal Tibia % Change	Distal Femur % Change
BMDTot	-5.6 (6.7)%	-9.7 (5.1)%*
BMDTrab45	-8.8 (8.4)%*	-10.6 (6.2)%*
BMDTrabTP	-8.6 (5)%*	-8.4 (3.1)%*
BMDTot (Implant Removed)	-7.2 (7.3)%	-9.8 (5)%*

$^*p < 0.05$, n=8

Table 7.11: Post-op ACL control versus injured percentage change

The results with the implant still included in the images are considered first. As with the pre-op contralateral comparison (Table 7.4), the BMD values for the injured limbs are lower than those of their contralateral control limbs. The post-operative BMDTot percentage change comparison of the proximal tibia with the implant still contained in the image is now no longer significant ($p = 0.08$), however both trabecular measurements have stayed significant (BMDTrab45 $p = 0.02$, BMDTrabTP $p = 0.02$). Otherwise, all comparisons between the control and injured limbs remain significant, with a percentage change of just below 10%, indicating that the injured leg BMD continues to stay lower than the control.

On removal of the implanted regions from both images, the magnitude of the percentage change remains generally unchanged, however the proximal tibia contralateral comparison is now borderline significant ($p = 0.055$). The injured distal femur still remains significantly lower than the control by -9.8%. These findings are similar to those of Rittweger *et al*, although the measured percentage differences in the study in this thesis are comparatively over twice those of Rittweger, with a -5.6 (6.7)% versus their -2.0 (2.3)% difference for the proximal tibia for BMDTot (borderline/ non-significant) and a -9.7 (5.1)% versus their -5.4

(1.7)% difference for the distal femur (both significant). It is important to recall the low statistical power of both the study analysed in this thesis (n=8) as well as that of Rittweger (n=9 for femur and n=5 for tibia) when considering the conclusions of significance derived from these results. What can be concluded from the results of these 8 subjects is that a lower BMD is still observed in the injured limb compared to the control. This would indicate that the BMD in the injured limb does not recover well following surgical reconstruction of the ACL. The clinical study in this thesis was able to expand on Rittweger's results as there were now both the pre- and post-operative data available for each subject. This enabled BMD contralateral comparisons made pre-operatively to be evaluated against those made post-operatively. During the longitudinal analysis, it was demonstrated that the BMD % changes were extremely small, with no statistically significant changes identified for either the control or injured limbs. The contralateral % BMDTot changes pre-operatively were significant at -9.1% for the proximal tibia and -8.8% for the distal femur (Table 7.5). Post-operatively, the distal femoral comparisons remain significant, with the proximal tibia measurements borderline significant. This would indicate that the drop in BMD in the injured limb is pre-surgical, with little evidence of change post-surgery. Although the surgical repair restores stability, other factors associated with the injury, surgery to the knee and rehabilitation may also be having a continued influence on the bone density of the knee.

The limitations of the findings using the post-operative data are that they are based on very small numbers (n=8) and consequently their statistical power is reduced. There are also variable durations between injury, surgery and follow-up imaging. Although the intra-operator variability was demonstrated to be less than that of the SCI population, it's presence will still have an influence on the overall measurements. As the changes in BMD being measured in the ACL population are relatively much smaller than those of the SCI fast losers, this variation in positioning may proportionally have a larger effect on the BMD comparisons made in this study. It is noted that the trabecular BMD is significantly lower in the injured proximal tibia and distal femur both pre- and post-surgery. This is a novel finding but has not been discussed further due to lack of similar measurements in other studies. It does however support the finding that BMD in the injured limbs is reduced pre-surgically, with little evidence of change following ACL repair.

Duration of Injury Versus Bone Loss

It is clear from these findings that statistically significant bone losses are present in the knee following ACL injury pre-operatively for both limbs and following post-surgical repair for the distal femur. What is unknown is the rate of decline this loss occurs pre-operatively. There will undoubtedly be other factors which affect this decline in BMD following injury such as age, original BMD, duration of immobility, activity levels, pain, altered blood flow and modification of gait/loading to compensate to name a few. Therefore the presentation of the time duration since injury variable versus bone loss will only be one piece of the overall picture.

For the 18 subjects whose injury date was known, Figure 7.2 displays the BMDTot percentage change of the pre-op injured knee against time since injury. Those subjects who had pre- and post-op data are indicated by blue diamonds, with the remaining pre-op only subjects indicated by red squares.

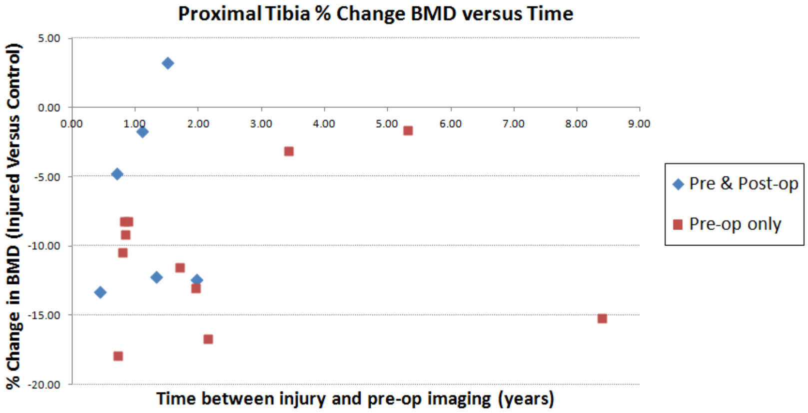

(a) Proximal Tibia BMD Versus Time since injury at pre-op

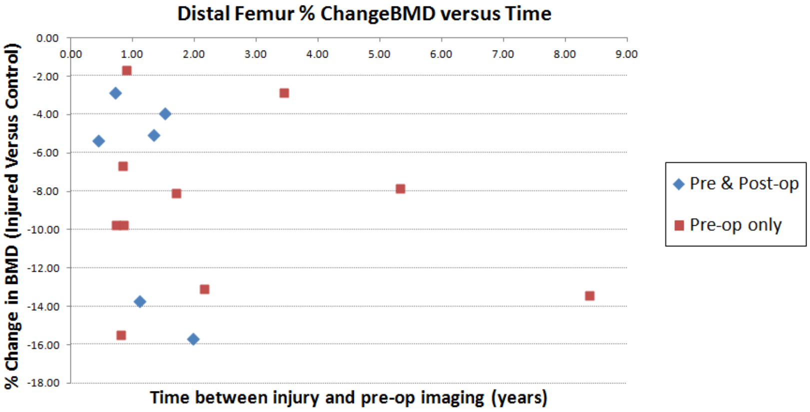

(b) Distal Femur BMD Versus Time since injury at pre-op

Figure 7.2: Duration of injury versus Bone Loss

These graphs demonstrate that there is no visible trend relating these two variables alone from the data available, with each subject demonstrating its own unique rate of loss. What can be concluded is that, at both femoral and tibial locations, this loss can occur very rapidly following ACL injury. This would agree with the findings of Boyd *et al* [13] who observed significant changes in the canine ACL injured knee as early as 3 weeks post-ACL injury. The majority of subjects in this study were operated on within two years of experiencing their injury. As significant bone losses are observed in many of them within this period of time, where the knee is unstable following ACL injury, a rapid surgical reconstruction would be advisable in order to minimise/reduce significant BMD losses in the injured limb.

7.3.3 Quadrant Analysis of Bone Mineral Density

Up to now, the quadrant analysis in this thesis has been used to compare longitudinal changes occurring within the bone over the period of a year in the SCI population. The data from this study are quite different in that all subjects have contralateral imaging, with only a small proportion with longitudinal imaging. Boyd *et al* [13] published findings on regional adaptations of BMD in the canine knee following ACLX at 3 weeks and 12 weeks (n=10). Images of the injured and control proximal tibia and distal femur of euthanaised bones were scanned and semi-automated software segmented the femur into quadrants, with the manual segmentation of the tibia into 2 compartments (medial and lateral). 3mm radius circular cores from each quadrant in the ACLX versus control images were compared. At 3 weeks, only the postero-medial portion of the ACLX canine femoral images had statistically significant changes. However by 12 weeks all compartments of both the tibia and femur in this limb demonstrated statistically significant changes. The rate of loss observed in the canine knee in Boyd's study is quite dramatic. A similar comparison of any compartmental losses in the knee using the subjects from the clinical study described in this chapter was therefore carried out in order to investigate the losses in humans.

Quadrant comparisons of BMDTot were carried out for both contralateral and longitudinal data. The registered proximal tibia and distal femur pairs were automatically segmented into four as demonstrated in Figures 7.3a and 7.3b.

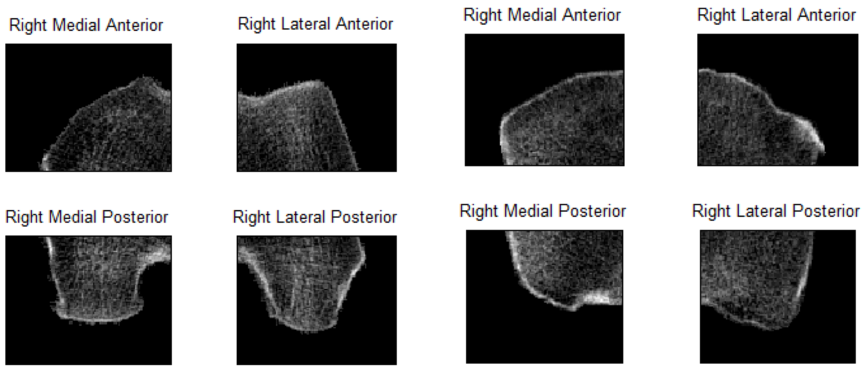

(a) Quadrant segmentation of distal femur

(b) Quadrant segmentation of proximal tibia

Figure 7.3: Quadrant segmentation of ACL knee images

Tables 7.12 and 7.13 present the contralateral quadrant comparisons, displaying the mean and SD of the injured limb BMDTot over the contralateral control for both the pre-op data (n=19) and post-op data (n=8). Tables 7.14 and 7.15 present the longitudinal quadrant comparisons, comparing the pre- to post-op control limbs as well as pre- to post-op injured limbs. Any statistical significance in each individual quadrant is denoted by an $*$ (t-test for pre-op comparisons, WSR-test for longitudinal and post-op comparisons). The statistical analysis was carried out independently for the proximal tibia and distal femur. Post-operative comparisons were made with the implant *in situ* as it's removal eliminated a large proportion of voxels from the quadrant under comparison. This therefore affected the comparisons made in the antero-medial quadrant of the proximal tibia and the postero-lateral quadrant of the distal femur and as such are not included in the comparison.

Proximal Tibia - Contralateral Comparisons, (mg/cm^3)				
	Antero-Lateral (Injured/Control)	**Antero-Medial** (Injured/Control)	**Postero-Medial** (Injured/Control)	**Postero-Lateral** (Injured/Control)
Pre-op (n=19)	189 (26)/216 (27)*	211 (27)/234 (26)*	239 (22)/256 (24)*	238 (27)/261 (33)*
Post-op (n=8)	184 (20)/207 (22)*	N/A	243 (27)/250 (20)	233 (41)/247 (22)

$^*p < 0.05$

Table 7.12: BMDTot contralateral quadrant analysis of proximal tibia

Distal Femur - Contralateral Comparisons, (mg/cm^3)				
	Antero-Lateral (Injured/Control)	**Antero-Medial** (Injured/Control)	**Postero-Medial** (Injured/Control)	**Postero-Lateral** (Injured/Control)
Pre-op (n=19)	246 (28)/274 (27)*	196 (22)/218 (19)*	281 (28)/299 (28)*	293 (23)/323 (27)*
Post-op (n=8)	248 (29)/273 (30)*	191 (20)/216 (14)*	274 (30)/300 (29)*	N/A

$^*p < 0.05$

Table 7.13: BMDTot contralateral quadrant analysis of distal femur

Proximal Tibia - Longitudinal Comparisons, (mg/cm^3)				
	Antero-Lateral (pre/post)	**Antero-Medial** (pre/post)	**Postero-Medial** (pre/post)	**Postero-Lateral** (pre/post)
Control (n=8)	213 (28)/207 (22)	229 (15)/229 (15)	256 (23)/250 (20)	253 (26)/247 (22)
Injured (n=8)	187 (22)/ 184 (20)	N/A	240 (28)/243 (27)	244 (30)/233 (41)

$^*p < 0.05$

Table 7.14: BMDTot longitudinal quadrant analysis of proximal tibia

Distal Femur - Longitudinal Comparisons, (mg/cm^3)				
	Antero-Lateral (pre/post)	**Antero-Medial** (pre/post)	**Postero-Medial** (pre/post)	**Postero-Lateral** (pre/post)
Control (n=8)	282 (24)/273 (30)	218 (14)/216 (14)	302 (27)/300 (29)	313 (17)/312 (18)
Injured (n=8)	252 (30)/248 (29)	197 (21)/191 (20)*	283 (29)/274 (30)	N/A

$^*p < 0.05$

Table 7.15: BMDTot longitudinal quadrant analysis of distal femur

The contralateral comparisons are discussed first (Tables 7.12 and 7.13). Pre-operative results for all quadrants of both limbs were significantly lower for the injured knee compared to the control ($p < 0.05$). This finding is not surprising given that the subjects were imaged a mean duration of 2 years (2 years) post-injury, and that Boyd *et al* found significant differences as early as 12 weeks after ACLX in canines. Post-operatively however these findings are slightly different, and with the exception of the two regions containing implants, are summarised below:

- **Proximal Tibia:** Only the Antero-lateral quadrant of the injured limb remains significantly lower than the control. Both posterior quadrant comparisons are now non-significant (postero-medial $p = 0.46$, postero-lateral $p = 0.25$).
- **Distal Femur:** All injured quadrants remain significantly lower than their contralateral controls.

In the preceding section, initial post-operative comparisons using the global measurement indicated that surgical intervention had little impact on BMD in either limb. The findings from the quadrant analysis may however indicate that in fact this is not a global process. Although preliminary findings, some with a low statistical power (when n=8) and with variable time periods between surgery and imaging, these outcomes would suggest that the bone deposition and demineralisation process may vary across some regions of the injured knee, e.g in the proximal tibia, whilst other regions (distal femur) demonstrate relatively global changes.

Longitudinal quadrant analysis (Tables 7.14 and 7.15)for all four control quadrant comparisons in both limbs are non-significant, suggesting no change globally. The longitudinal injured analysis for the proximal tibia, with the exception of the implanted quadrant, show no significant change in BMD whereas the distal femur has one quadrant where the injured post-op BMD is significantly lower than the pre-op scan. Global longitudinal comparisons of the injured limbs were visited in Table 7.9, which found that there was no significance globally with or without the implant *in-situ*. Performing the quadrant analysis enables a more in-depth evaluation of where any change may be occurring.

The use of the software which registers images and automatically segments them into quadrants has therefore been demonstrated to be a useful tool in the assessment of bone changes within different regions in the bone. Other authors who study this field have performed similar compartmental comparisons and therefore like for like analysis can be made between studies.

A novel continuation and the next logical step in this analysis is to localise even further the patterns of bone loss in the knee following ACL injury using ΔBMD voxel wise comparisons. These pattern maps could potentially provide further insight into the bone turnover processes such that they could be used to guide surgery and rehabilitation interventions, or even provide clarification on how the loading distribution of the bone changes with the presence of the ACL implant within the knee.

7.3.4 Voxel Wise Comparisons

From the initial findings in this study it is clear that, in agreement with the current published consensus, the injured ACL knee experiences bone loss and is at risk of becoming osteoporotic despite surgical intervention. Performing voxel wise comparisons on registered images will help to identify any particular regions which may be more susceptible to bone loss following injury. To date, this method of intra-subject comparison applied to pQCT data from the ACL injured patient has not yet been explored.

Images acquired for all 19 subjects were all automatically segmented and registered. The following voxel-wise comparisons between image pairs were then carried out for both proximal tibia and distal femur:

1. Pre-op control knee versus pre-op injured knee (n=19).
2. Pre-op injured knee versus post-op injured knee (n=8).

Proximal Tibia

Results from the proximal tibia are discussed first. A representative sample of eight pre-op comparisons between the control and injured limbs are presented in Figure 7.4, with the change in BMD displayed as a gradient colour scale in mg/cm^3.

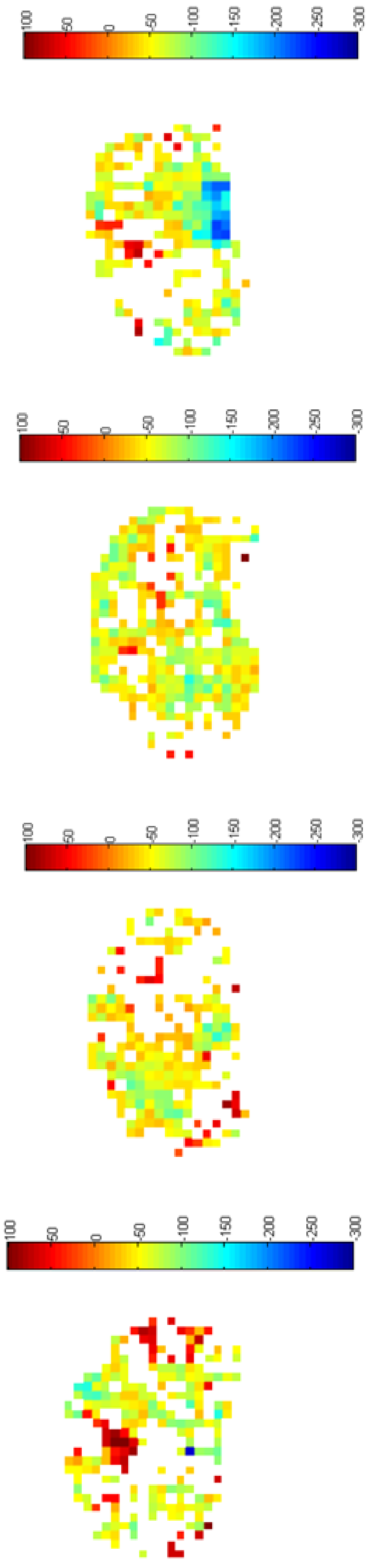

(a) A1: Unknown time since injury

(b) A4: 5months since injury

(c) A7: 1year 11months since injury

(d) A9: 8years 5months since injury

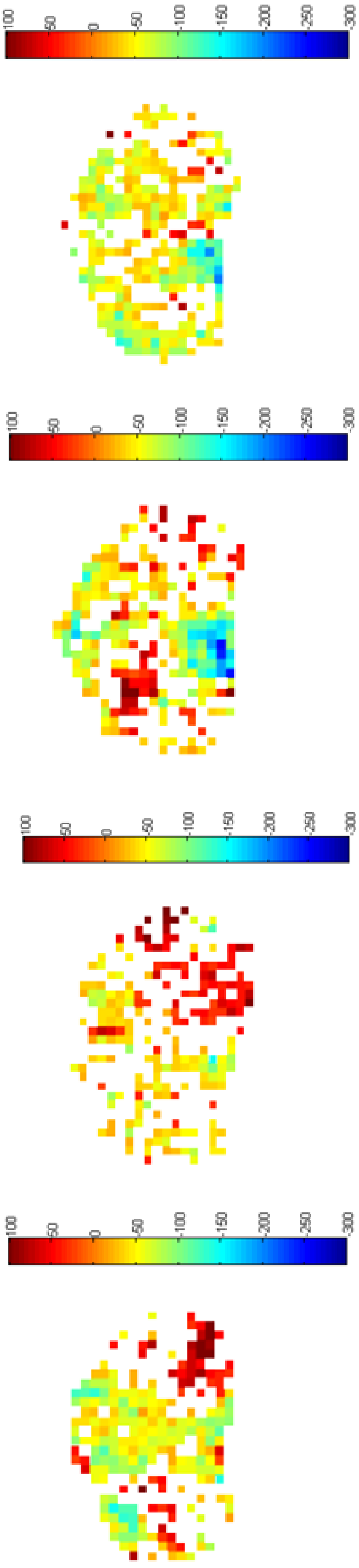

(e) A11: 10months since injury

(f) A13: 5years 4months since injury

(g) A16: 11months since injury

(h) A17: 9months since injury

Figure 7.4: Proximal tibia ΔBMD change maps comparing ACL pre-op control and pre-op injured, Δmg/cm^3

It is clear from these images that there is no obvious pattern to the bone loss which occurs following injury based on a contralateral comparison. Proportionally, there are substantially more voxel regions with reduced BMD in the injured knee versus the control. These images are also quite contrasting to the previous longitudinal SCI study. Where the images from the latter are generated during the first year post-SCI, these images are taken on average 2 years post-ACL injury. Direct comparison of the voxel maps is complex, due to the bi-modal losses observed in SCI, however it is clear that the BMD changes occurring in "fast loser" SCI population are much more rapid and extreme in comparison to those from the ACL study. The majority of voxels quantifying bone loss in this study appear to go only up to approximately 100mg/cm^3, whereas some of the subjects in the acute SCI population experience losses of >300mg/cm^3 for each voxel (e.g as demonstrated in Figure 6.5).

Similarly to the SCI subjects however, the patterns of bone loss visualised from these images are unique to each subject. From the sample of subjects in this clinical study, there is no obvious correlation between the pattern or extent of the loss visualised in these images and the duration of injury. As mentioned previously, it is the rate at which the bone loss occurs that is concerning. Subject A4 shown in Figure 7.4b for example had the shortest duration between injury and imaging (5 months) but has already experienced losses in certain voxels of around 100mg/cm^3. Subjects A16 and A17 (Figures 7.4g and 7.4h) whose time between injury and imaging was 11 months and 9 months respectively are also starting to demonstrate small pockets of loss >150mg/cm^3 . In contrast to this however, subject A13's injury occurred 5 years and 4 months before imaging and globally their loss appears to be minimal across the bone as demonstrated in Figure 7.4f.

It is difficult to hypothesise on the nature of the regions of increasing BMD that can also be visualised across these pairs of images, considering the trauma this bone has experienced. These could be true regions of BMD which are greater in the injured knee compared to the control, however consideration must also be given to the possibility that they are a result of statistical noise inherent to the clinical study, such as patient positioning error and right/left asymmetries in BMD.

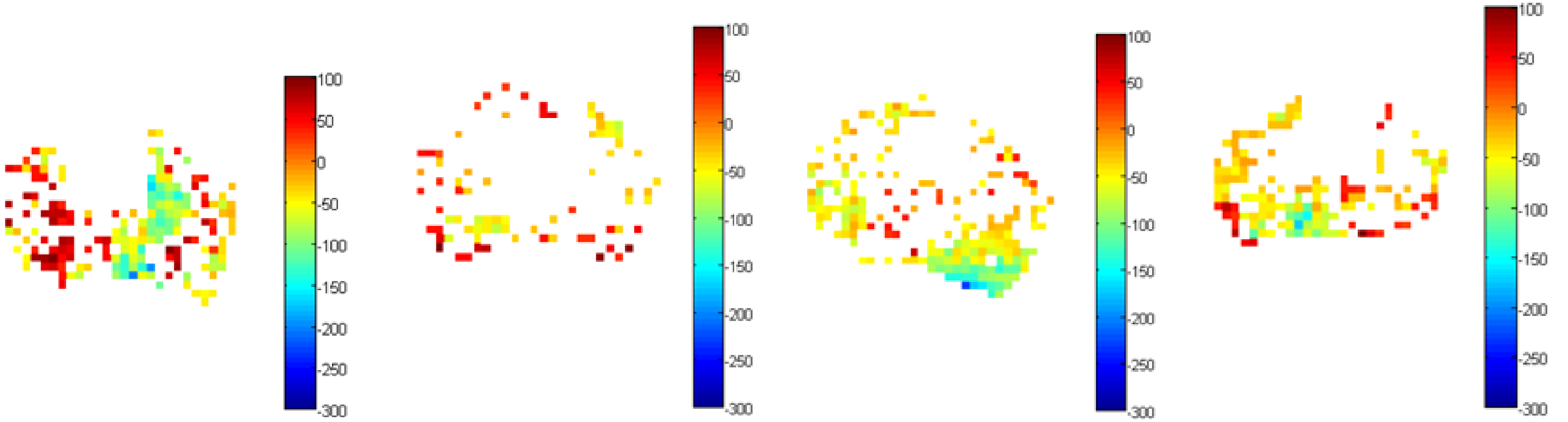

(a) A1: Pre to post-op 1year 6months (b) A2: Pre to post-op 1year 10months (c) A3: Pre to post-op 2years 2months (d) A4: Pre to post-op 1year 7months

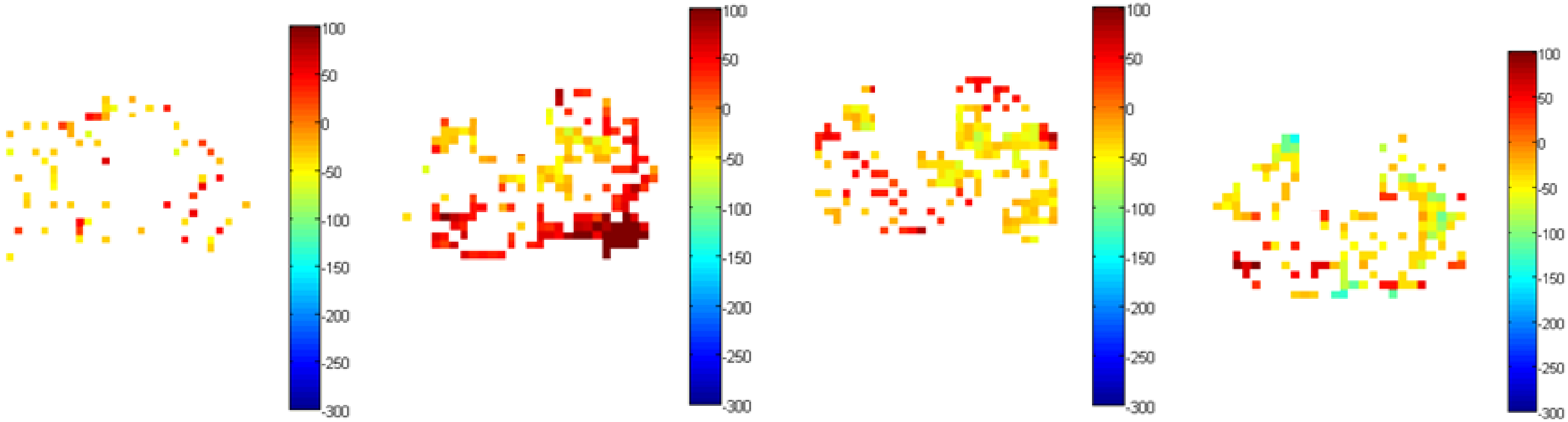

(e) A5: Pre to post-op 2years (f) A6: Pre to post-op 1year 4months (g) A7: Pre to post-op 2years (h) A8: Pre to post-op 1year

Figure 7.5: Proximal tibia ΔBMD change maps comparing ACL pre-op injured and post-op injured - Implant removed, $\Delta mg/cm^3$

Figure 7.5 presents the ΔBMD voxel wise comparisons of the pre-op to post-op injured proximal tibia images for the 8 returning subjects with the implanted region removed from the comparison. From the analysis performed previously, it is known that there are no statistical changes in BMD in the injured proximal tibia globally (Table 7.9) or in any specific quadrant (Table 7.14). Observation of the longitudinal voxel wise comparison images actually demonstrates that the response of the bone is quite variable across these 8 subjects. For example, subjects A2 and A5 (Figures 7.5b and 7.5e) demonstrate minimal changes in BMD, with a large proportion of the voxels in the comparison remaining white (no statistically significant change). On the other hand, the ΔBMD comparisons of subjects A1, A6 and A7 (Figures 7.5a, 7.5f and 7.5g) would suggest that there are small amounts of bone loss occurring peripheral to the implant. This could be attributed to the change in load across the bone or perhaps stress shielding as a result of the implant's presence, however the surgical reconstruction also appears to have had a positive effect in small areas of the bone, with regions of increasing BMD also indicated.

From this sample of 8 subjects, the response to ACL reconstructive surgery to the proximal tibia appears to be patient specific and it is challenging to summarise the group as a whole. Although the injured longitudinal ΔBMD voxel comparisons are generally no greater than 100mg/cm^3, it is still concerning that a continued loss of bone is indicated in several of these subjects. One possible explanation could be that it is due to factors such as patient immobility during recovery, reduced functionality of the knee and whether the patient has been able to return to their pre-injury level of activity. What this does highlight is that there is a potential need for long-term follow-up of BMD in the knee following ACL injury.

Distal Femur

ΔBMD voxel comparison maps of the distal femur are now discussed, with Figure 7.6 providing a representative sample of 8 images from the 19 subjects comparing the contralateral pre-op control to pre-op injured limbs.

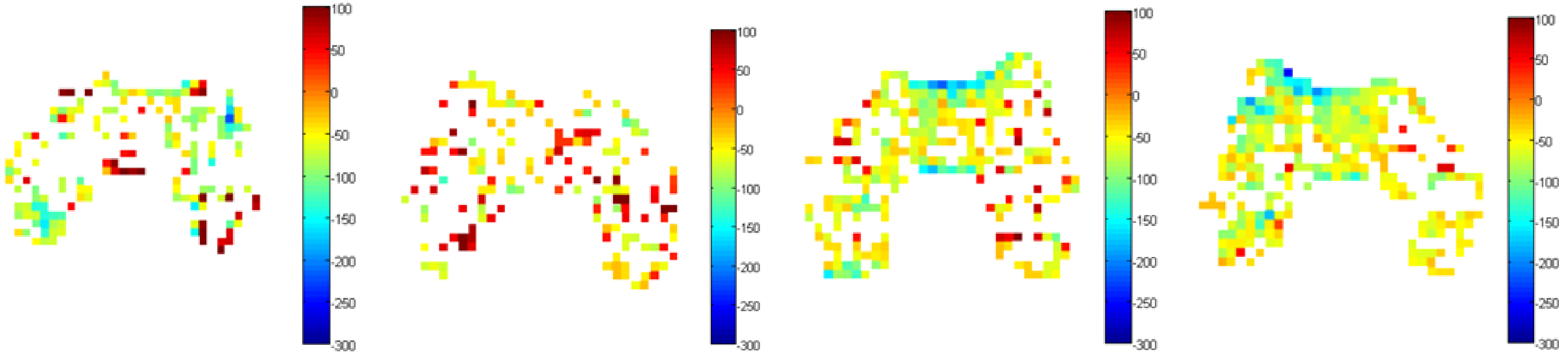

(a) A1: Unknown time since injury (b) A2: 8months since injury (c) A6: 1year 1months since injury (d) A7: 1year 11months since injury

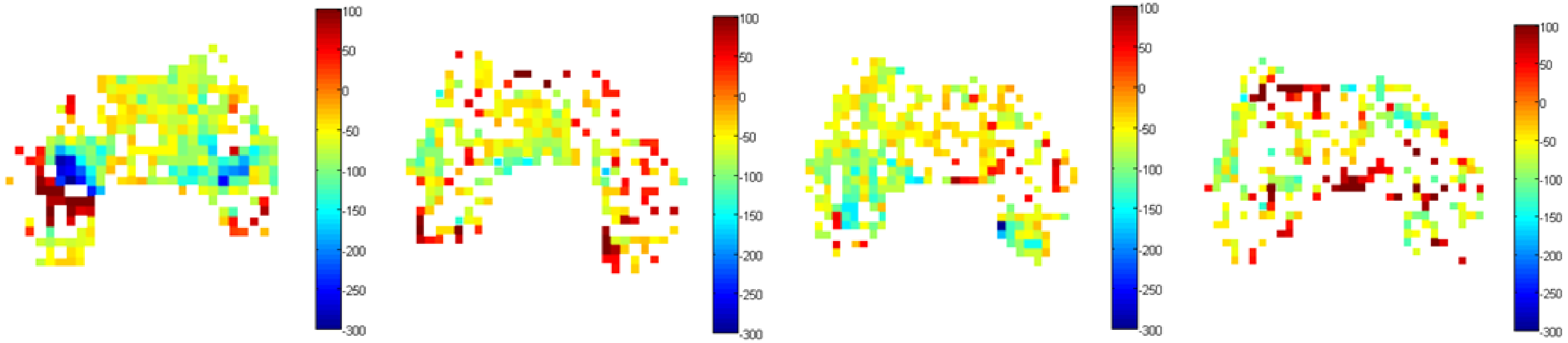

(e) A9: 8 years 5months since injury (f) A11: 10months since injury (g) A17: 9months since injury (h) A19: 1year 11months since injury

Figure 7.6: Distal femur ΔBMD maps comparing ACL pre-op control and pre-op injured, Δmg/cm^3

Globally again it is noticeable that following injury the pre-op injured limb has suffered bone loss when compared to its contralateral control. These losses tend to range from 50 to 100mg/cm^3. Where subjects A1 (Figure 7.6a), A2 (Figure 7.6b) and A19 (Figure 7.6h) show minimal changes in bone turnover between the two limbs, subjects A6, A7, A9 and A17 are starting to show more dense regions of bone loss.

These results are in agreement with the global BMDTot measurements, which calculated a significant drop in BMD following injury of -8.78 (4.6)% ($p < 0.05$) given in Table 7.5. Like the tibia, the patterns of bone loss in the distal femur can be described as variable and patient specific with no obvious visual correlation with duration post-injury.

Post-op comparisons of the distal femur from the 8 subjects who returned for follow-up imaging are now presented. The implant remains *in situ* for these comparisons as the presence of the compact bone surrounding the implant is not as evident as in the post-op images of proximal tibia.

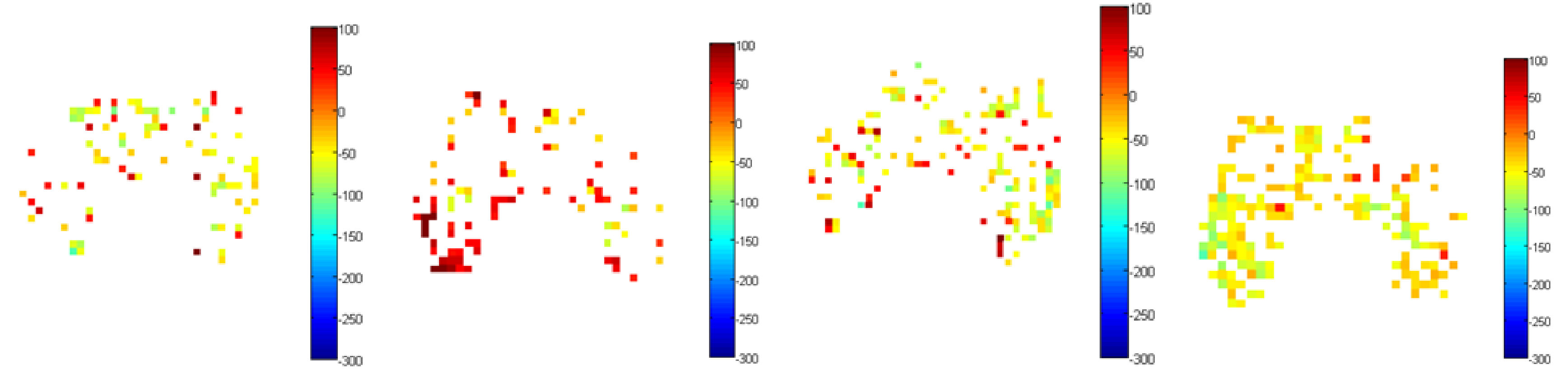

(a) A1: Pre to post-op 1year 6months (b) A2: Pre to post-op 1year 10months (c) A3: Pre to post-op 2years 2months (d) A4: Pre to post-op 1year 7months

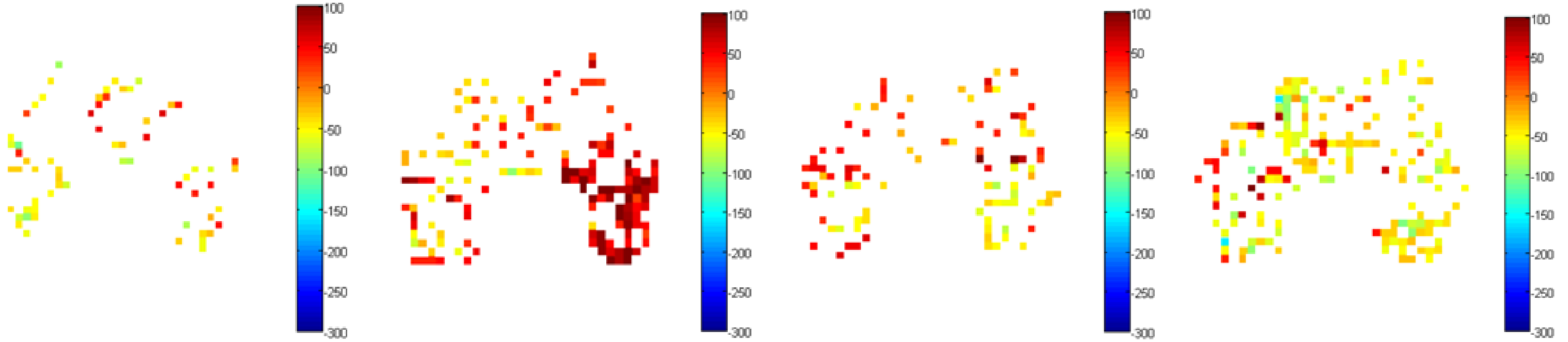

(e) A5: Pre to post-op 2years (f) A6: Pre to post-op 1year 4months (g) A7: Pre to post-op 2years (h) A8: Pre to post-op 1year

Figure 7.7: Distal femur ΔBMD maps comparing ACL pre-op injured and post-op injured, $\Delta\text{mg/cm}^3$

Once more, from Table 7.9, it is known that globally there is no evidence of a statistically significant change in the injured distal femur following surgery. Further investigation using the ΔBMD maps does not demonstrate any evident localised changes in the BMD following reconstructive surgery. Subjects A2 and A6, Figures 7.7b and 7.7f respectively, were the only two subjects from the 8 who experienced a global increase in BMD. From the ΔBMD maps, it is possible to see that this increase is quite localised for subject A6 in the postero-lateral condyle, whereas is more diffuse for A2.

Where it was possible to roughly classify the SCI subjects into categories according to their ΔBMD patterns of bone loss, this has not been possible in this ACL study. The rate of bone loss following injury has been demonstrated as being variable and potentially rapid, both in this study and by other authors. The patterns obtained from voxel wise comparisons appear to be unique to the individual, inferring that additional factors not evaluated in this clinical study are also influencing the rate of bone loss in the individual, as opposed to the injury alone. The ΔBMD voxel wise comparisons have demonstrated that the loss pre-implant may be present in the region the surgeons use to fix the ACL implant. This could ultimately have a detrimental affect on the integrity and longevity of the implant. It would also indicate surgical ACL reconstruction in the unstable knee should be performed as soon as possible following injury in order to minimise bone loss and maximise the success of the implant.

7.3.5 Morphometric Analysis

The results discussed in this chapter thus far demonstrate that patients who have suffered an ACL injury are at risk of developing osteoporosis in the injured knee, which can take place despite surgical intervention. From the voxel wise comparisons there appears to be no one location particularly susceptible to bone loss following this injury. However this analysis does not provide information on any processes which may be occurring at a microarchitectural level. Once more, it is of value to investigate these bone patterns within the images of the ACL injured knee using granulometries. In the SCI longitudinal study, global pattern spectrum moments were identified as having potential in providing additional information on the structure of the bone. The data available for this study however are quite different. In 11 of the cases, data were acquired for only one time point (post-ACL injury, pre-ACL reconstruction), with just 8 having longitudinal data available post-surgery. Assessment of the images using granulometries may therefore be best made visually using local pattern spectrum images, comparing the injured knee to that of the contralateral knee post-injury. In this case a similar evaluation in the change in pattern with time that was carried out in the SCI study will not be possible. In the 8 subjects who did have one follow-up imaging scan, a comparison of the local pattern spectrum moments pre- to post-op can be made to determine whether the surgical implant has had any affect on the bone structure itself. In addition to the local pattern spectrum map, the global pattern spectrum moments for these 8 subjects are also presented.

Local Pattern Spectrum Distribution Maps

Local pattern spectrum distribution maps present information on the relationship of the pixels within the image to their neighbours and are a representation of the bone structure as opposed to BMD. The ΔBMD voxel maps and granulometry local pattern spectrum distribution maps therefore provide complementary information to each other. A selection of different results from both the proximal tibia and the distal femur are presented in this section.

Granulometry analysis was carried out on the images of all 19 subjects. The proximal tibia is discussed first and representative images from two subjects are given in Figures 7.8 and 7.9. These particular subjects were also chosen because they had images available both pre- and post-operatively. Each example displays the segmented raw pQCT image along side its associated local pattern spectrum map (mean).

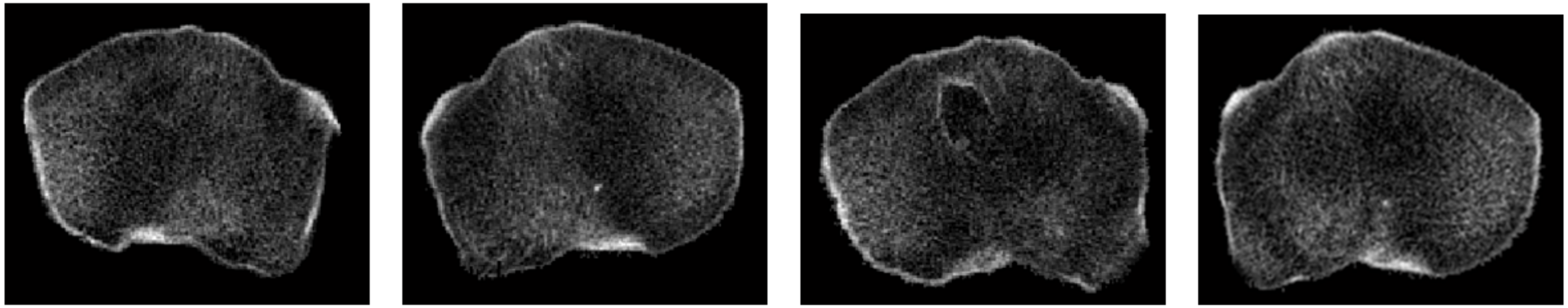

(a) A1: Injured pre-op pQCT image

(b) A1: Control pre-op pQCT image

(c) A1: Injured post-op pQCT image

(d) A1: Control post-op pQCT image

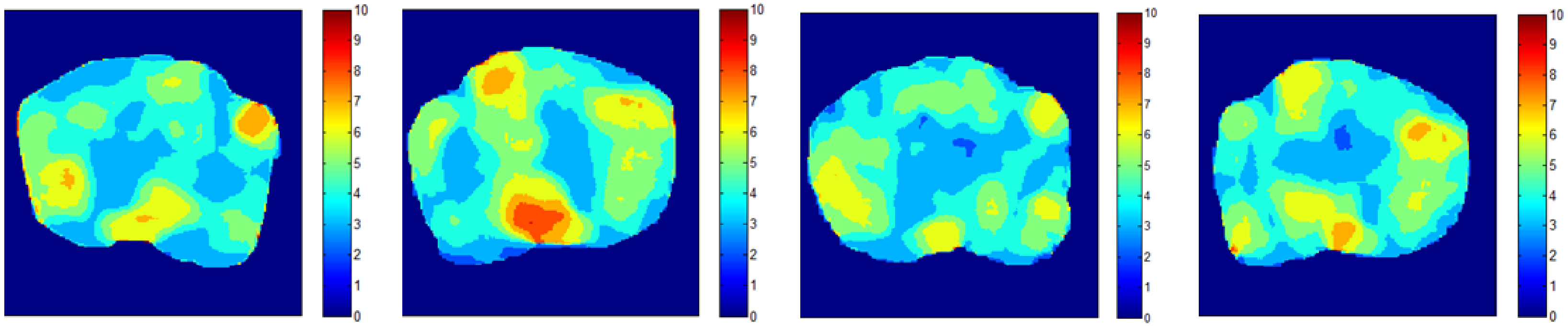

(e) A1: Injured pre-op local pattern spectrum image

(f) A1: Control pre-op local pattern spectrum image

(g) A1: Injured post-op local pattern spectrum image

(h) A1: Control post-op local pattern spectrum image

Figure 7.8: A1: Local pattern spectrum mean images of proximal tibia with corresponding pQCT images

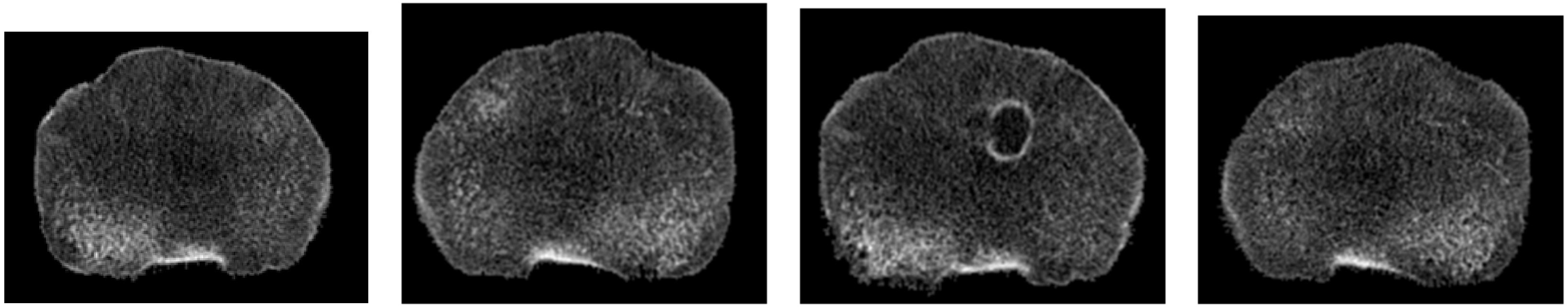

(a) A2: Injured pre-op pQCT image (b) A2: Control pre-op pQCT image (c) A2: Injured post-op pQCT image (d) A2: Control post-op pQCT image

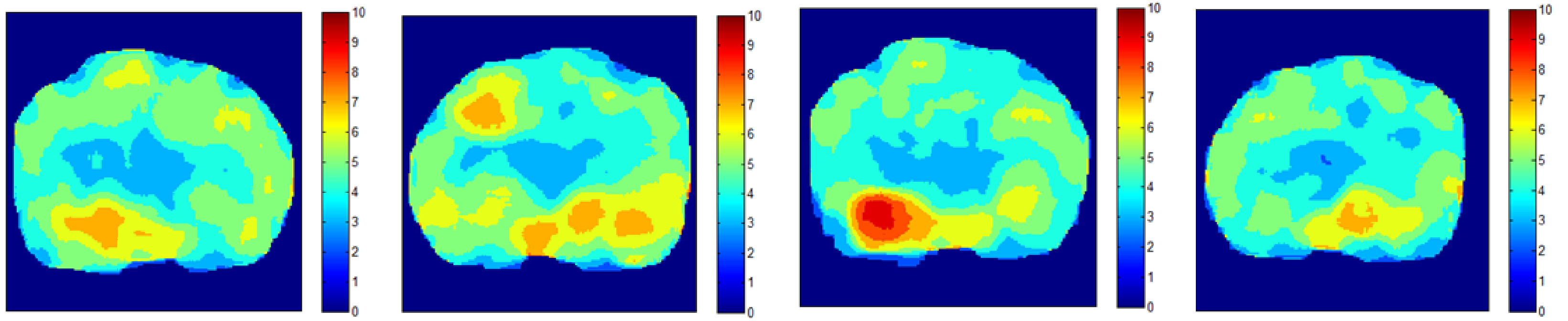

(e) A2: Injured pre-op local pattern spectrum image (f) A2: Control pre-op local pattern spectrum image (g) A2: Injured post-op local pattern spectrum image (h) A2: Control post-op local pattern spectrum image

Figure 7.9: A2: Local pattern spectrum mean images of proximal tibia with corresponding pQCT images

The local pattern spectrum maps of the proximal tibia in this ACL study are quite different compared to those of the distal tibia in the SCI population. They do not survive the granulometric sieving process as long, with the majority of voxels only lasting 3 to 5 iterations, represented by the blue colours in Figures 7.8e-7.8h and 7.9e-7.9h. There is therefore little variation within and between images. Comparatively, some of the SCI distal tibia images survived as many as 10 sieving iterations. A closer inspection of the bone patterns of the pQCT data images of the two extremities of the tibia would offer one possible explanation. The proximal tibia is a much larger bone, with an average CSA of 3529 (360)mm^2 whereas the distal end of the tibia is much smaller with a CSA average of 1313 (117)mm^2. In contrast to this the average BMD of the distal tibia is 1.4 times that of the proximal tibia (figures derived from distal tibia SCI Baseline versus proximal tibia ACL pre-op control acquisitions). This make the distal tibia proportionally a much more structurally dense bone over a smaller area in comparison to the proximal end and the compact nature of the trabecular struts consequently survive the granulometric iterative sieving much longer.

On comparing the local pattern spectrum images of the pre-op injured proximal tibia to those of the pre-op control tibia, there does not appear to be any major differences in bone structure between the two images (noting that due to their contralateral nature the images are flipped around the central axis). This may seem surprising, considering the SCI local pattern spectrum images demonstrated some quite significant visual changes in bone pattern during the 1st year post-SCI in the “fast-loser” group. However as demonstrated in the voxel-wise comparisons, the extent of bone loss experienced by the ACL-injured subjects compared to that of the SCI fast-losers is substantially smaller. In addition to this, there does not appear to be any observable difference in proximal tibia contralateral bone patterns pre-operatively or post-operatively. This is unexpected, as the outcomes from the injured versus control pre-op BMDTot analysis are statistically significant (Table 7.5) and borderline different post-op (Table 7.11). In addition to this, the trabecular bone analysis was also significantly different both pre- and post-operatively. What these patterns do demonstrate is that for this particular anatomical location, the local pattern spectrum maps appear to have limited value in this population.

A representative example of the distal femur pQCT images alongside their associated local pattern spectrum (mean) images from a subject who had both pre- and post-operative images available is given in Figure 7.10.

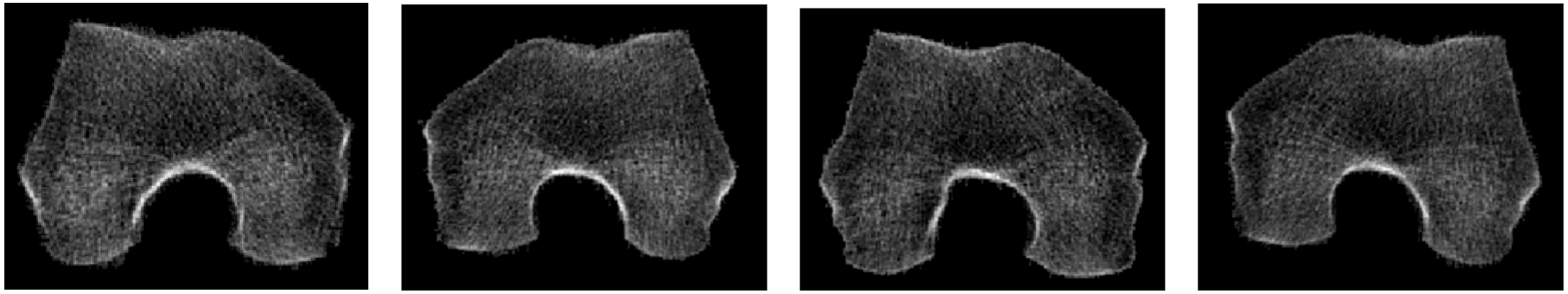

(a) A4: Injured pre-op pQCT image

(b) A4: Control pre-op pQCT image

(c) A4: Injured post-op pQCT image

(d) A4: Control post-op pQCT image

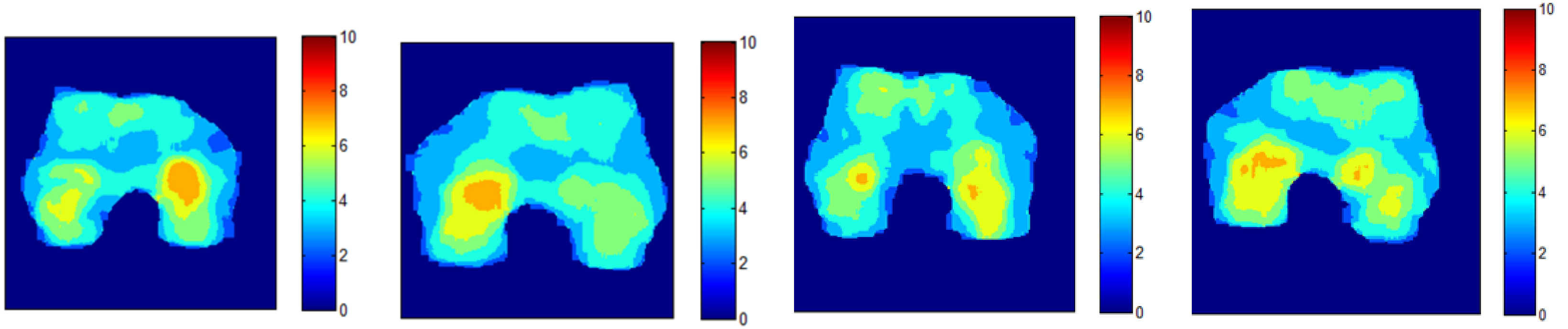

(e) A4: Injured pre-op local pattern spectrum image

(f) A4: Control pre-op local pattern spectrum image

(g) A4: Injured post-op local pattern spectrum image

(h) A4: Control post-op local pattern spectrum image

Figure 7.10: A4: Local pattern spectrum mean images of distal femur with corresponding pQCT images

At first glance along the raw pQCT images of the distal femur, it is not possible to see any obvious visual changes in the bone's pattern as was possible with the longitudinal SCI images of fast losers. A further evaluation using the local pattern spectrum images would confirm this. Once again, the images generated as a result of this analysis are limited in the information they convey on the bony structure following ACL injury. The reasons for this are similar to those described previously for the proximal tibia location: The changes in BMD, although statistically significant when measured using group BMDTot values, are still relatively much smaller than those that occur following SCI in individual fast losers. Also, the bone structure under evaluation is spread across a large surface area with an average BMD of 280 (21)mg/cm^3 over a CSA of 4015 (327)mm^2, an almost identical BMD to CSA ratio as the proximal tibia.

These initial findings when applying granulometries to the ACL images of the knee have not been able to demonstrate any discernible changes in bone pattern following injury or surgery. As mentioned in the previous chapter, the findings are however qualitative in nature providing only a visual representation of these changes. Global granulometries have already been demonstrated to provide complementary quantitative additional information to BMDTot in the longitudinal analysis of acute SCI. An evaluation was therefore carried out using these outcome measurements from the available longitudinal ACL images.

Patterns Spectrum Moments

The following four graphs present three global pattern spectrum moments alongside BMDTot values of the injured proximal tibia for 4 of the 8 subjects who returned for follow-up imaging post-surgery. In this study, there are only 2 time points available therefore comparisons of any changes in the injured limb can only be made pre-operatively to post-operatively as demonstrated in Figure 7.11.

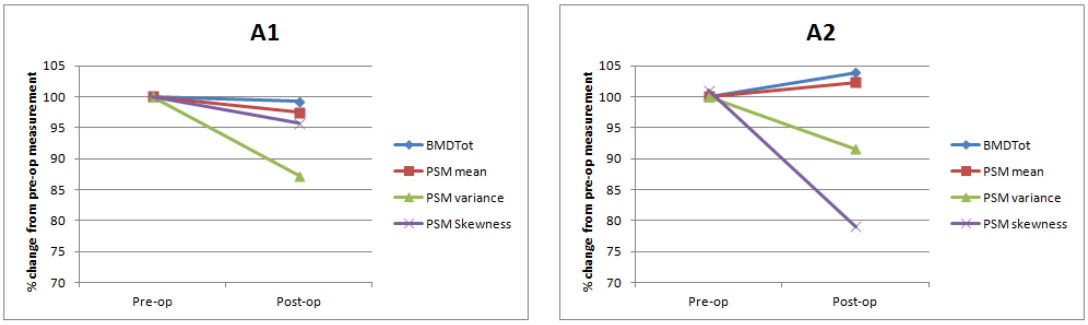

(a) Pattern Spectrum Moments for Subject A1, Pre-op to Post-op proximal tibia

(b) Pattern Spectrum Moments for Subject A2, Pre-op to Post-op proximal tibia

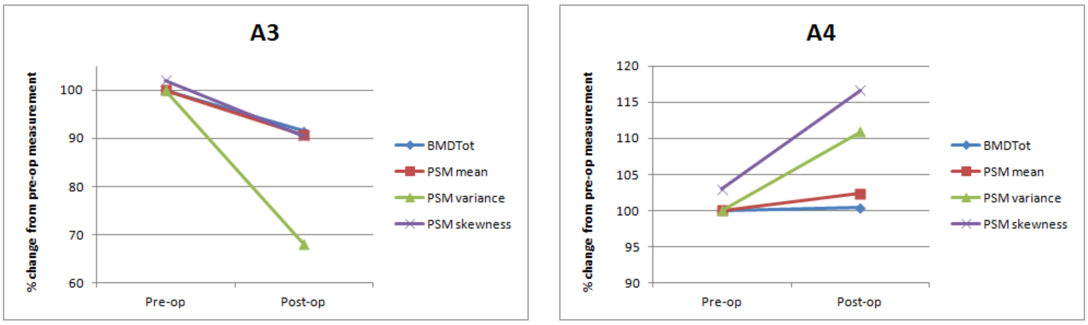

(c) Pattern Spectrum Moments for Subject A3, Pre-op to Post-op proximal tibia

(d) Pattern Spectrum Moments for Subject A4, Pre-op to Post-op proximal tibia

Figure 7.11: Global pattern spectrum moments of proximal tibia - longitudinal ACL subjects

It is not unexpected given the results from the local pattern spectrum images, that the global granulometry graphs presented here do not appear to provide any obvious additional useful information to the BMDTot measurement. Consequently there are several reasons why at this point these data are not investigated further for both the proximal tibia and distal femur. The first is that they were only acquired at 2 time points, therefore a longitudinal assessment of the bone patterns following ACL injury is extremely limited. Additional acquisitions following a further period of recovery may provide further information for evaluation. The second reason has already been alluded to in the previous section. The value of granulometric structural analysis of the bone at both the proximal tibia and distal femur anatomical locations is extremely limited. This is due to the smaller ratio of BMD to CSA compared to that of the distal tibia, resulting in a comparatively poorer survival of the trabecular struts than the distal tibia during granulometric sieving. As this survival is concentrated within a small range of iterations with low variation, it is not possible to obtain any discriminatory information related to the trabecular structure.

7.4 Discussion

7.4.1 Review of Software

The application of the software developed in this thesis to a second, very different clinical study to that of the longitudinal SCI, demonstrates that it's overarching functionality has different strengths (and weaknesses) depending on the nature of the bone under investigation, its associated losses or gains as well as the individual bone patterns. The BMDTot analysis using the automatically segmented images was performed using BMD and CSA values generated from the software, presenting a good foundation of findings describing the bone turnover occurring following an ACL injury. The segmentation and registration software facilitated group changes in BMD to be explored in relation to contralateral limbs and longitudinally following surgical intervention. This was performed both globally and using quadrant analysis to explore specific regions of the bone. Currently these results remain novel to this field of study.

Analysis of the images acquired for the subjects in this study using ΔBMD maps demonstrated that there was no obvious pattern of bone loss occurring either pre-operatively or post-operatively. Although no generalisation in patterns of bone loss could therefore be made, this information in itself is useful. It demonstrates that it is not simply the injury or even the duration since injury which governs the extent to which a patient will experience bone demineralisation. As the patterns of loss are unique, additional external factors must be influencing the rate of decline in bone loss. These could be due to many factors including altered loading as a result of immobility following injury or participation in physiotherapeutic rehabilitation.

Although shown to have additive value to distal tibia BMDTot measurements in the SCI study, granulometries applied to the 2% proximal tibia or 4% distal femur were not able to provide any clear additional information on the structural integrity of the bone in the ACL images. Although disappointing given previous results, on closer inspection it is not surprising given the fundamental principals of the granulometric analysis. This particular technique used to describe bone pattern employs a sieving analogy, using structuring elements which sequentially increase in size. For these two anatomical locations the trabecular struts do not survive this process very long in comparison to the distal tibia therefore providing little discriminatory information. This is true for both the local pattern spectrum images as well as the pattern spectrum moments obtained from the global granulometry analysis.

7.4.2 Clinical Study Outcomes

Based on the findings derived from the medical image analysis in this thesis, the following novel clinical outcomes were able to be concluded from the ACL BMD clinical study:

1. Similarly to the outcomes outlined in Chapter 6, automatically calculated BMD and

CSA measurements can be generated with no or minimal user interaction

2. The intra-operator variability of patient positioning was able to be calculated and was good for the operator in this clinical study.

3. The automatically generated BMDTot, CSA and quadrant analysis of these images proved to be useful in describing the group global BMD differences across these subjects which occurred post-injury as well as post-surgery. ΔBMD voxel wise comparison maps demonstrated bone loss in the injured limb unique to the individual with no obvious patterns of loss present across all 19 subjects..

4. Previous studies by Leppälä *et al* [12] and Rittweger *et al* [41] have concluded that despite surgery, the BMD in the injured limb remains less than that of a contralateral control. Analysis in this thesis assessing both pre and post-op injured and control limbs would agree with this finding, however the extent of the loss in the injured limb is analysed further through the removal of the implanted region in both registered images. This removes any influence the post-surgical compact bone and implant may have on the comparative measurements. The availability of longitudinal pre- and post-operative pQCT data in this study also enabled a more in-depth analysis of the response to both the injury as well as surgery.

5. Closer inspection of these pre- and post-operative losses in the injured limb using automated quadrant analysis quantified that pre-operatively, all four quadrants of the injured proximal tibia and distal femur were significantly lower than the contralateral controls. Post-operatively, it highlighted quadrants which were no longer significantly different. Although preliminary findings with high inter-subject variability between injury, surgery and imaging, the results suggest some anatomical variation in bone loss within the injured limb. Longitudinally, the quadrant analysis was able to demonstrate that the injured limb did not generally experience any further bone demineralisation following surgical intervention.

There are consequently several clinical implications of these findings. It confirms that bone loss occurs in the ACL injured limb following injury and that the rate of bone loss appears to be quite rapid. Based on the 8 patients who had both pre- and post-operative imaging, surgery appears to have halted the decline of bone loss in the injured limb. Therefore the risk of the knee developing osteoarthritis later on in life will be influenced by extent of loss the patient experiences between injury and surgery. Using imaging and the software presented in this thesis, it would be possible to ascertain the extent of loss that has already occurred immediately prior to surgery and localise specific regions which may require more focussed interventional rehabilitation techniques to try and restore BMD to the patient's pre-injury levels. The quadrant analysis has generated some promising findings. Whereas previously the bone loss in the injured limb was assumed to be global across the bone, this may in fact be located to specific quadrants. Unlike some of the SCI subjects whose bone loss is so dramatic during the first year post-SCI, the best outcome of any physiotherapeutic intervention would be simply to slow this loss down, in the fit and mobile ACL subjects, the prospects for bone recovery may be more hopeful if they could be given the right therapy and lifestyle advice.

There are some limitations to these findings. Firstly, the statistical power of the conclusions drawn from the 8 subject post-operative data was reduced due to poor recruitment. The results from these findings were able at best to provide only an indication of the bone changes taking place following ACL surgical intervention. Secondly, the variation between injury and time of surgical intervention in this cohort of subjects is quite large. One recommendation for the future would be to ensure a much tighter period between injury and surgery, however this in itself is a challenging requisite. Patients do not always present immediately following injury, and timescales are extended further still by surgical waiting times.

Another challenge encountered during this clinical study was a result of equipment malfunction and repair. Desirably, the post-op scan should have been performed at 1 year post-injury, however during this study the pQCT scanner broke down and was returned to the manufacturer for several months for repair. This ultimately resulted in a larger variation in the durations between surgery and follow-up imaging than was intended (2y8m (5m) Table 7.2). Furthermore, the participation of the subjects returning for post-surgical imaging was quite poor with only 8 of the 19 coming back for follow up imaging, limiting the power of the statistical tests performed. One reason for this was a result of the age group involved in this study. These subjects tended to be young and mobile, resulting in many having moved on from their pre-implant addresses and could not be contacted. In addition, the time commitment was often a challenge in this young population, with a scanning session of both limbs at both anatomical locations taking up to 3 hours.

Additional factors which would have an influence on BMD apart from the injury were not recorded. No comparative information was available on each subject's physical activity before and after the injury/surgery. There was also no information available on the duration of their immobility and recovery or the extent of any rehabilitation they undertook.

Finally the premise that the contralateral limb is unaffected by the ACL injury and is a normal control was based on only 8 subjects who returned post-surgery. This is therefore limited due to the small numbers, with Boyd *et al* also noting this limitation in their canine study. The advantages however of using the contralateral limb for comparison is that it reduces intra-subject variation of the clinical study.

7.5 Conclusions

This study into the changes in BMD following ACL injury and surgical repair has enabled further evaluation of this known risk factor which can lead to disuse osteoporosis. Currently the only pre- and post-ACL transection cross-sectional imaging data available is in canines (Boyd *et al* [13]). The findings of the current study in the human population have identified parallels with those found in the canine model. BMD in the injured limb across the entire knee has been shown to be significantly lower than that of the contralateral control pre-operatively and post-operatively for the distal femur. These findings agree with those of Rittweger *et al*'s retrospective post-operative cross-sectional study investigating BMD using pQCT (n=10). From both the voxel wise comparisons and the quadrant analysis, the comparative contralateral loss generally appears global across the bone for both the proximal tibia and distal femur pre-operatively. In addition to this, the contralateral trabecular analysis of the proximal tibia remained significant post-operatively as well as pre-operatively. The longitudinal changes however would appear to be patient specific as demonstrated by the varying ΔBMD maps for the 8 returning patients. For this particular study, the structural information provided by granulometric analysis was limited.

The question remains unanswered about whether a significant recovery could possibly be made with suitable intervention given the altered load distribution caused by the presence of the implant in the knee. However, as with the SCI study, the image processing analysis presented here could again be used as a sensitive image analysis tool in the future.

What these results, as well as those from other authors who have studied the effects of an ACL injury on BMD would suggest, are that should the ACL injury require surgical intervention, this should be carried out as soon as possible following injury in order to minimise the initial rapid bone loss within the knee. Performing a pre-operative pQCT scan of the control and injured knee would also enable the surgeon to evaluate the integrity of the trabecular bone using the quadrant analysis and/or the ΔBMD voxel wise comparisons. This could potentially provide them with additional information on the estimated success or longevity of the ACL-surgical repair.

Chapter 8

Conclusions and Recommendations for Further Work

The purpose of this PhD was to develop automated software which can be used clinically in the analysis of BMD in the appendicular skeleton, using pQCT imaging. It's application and flexibility has been demonstrated in two very different clinical studies, using the findings from the software to make novel hypotheses on the characterisation of bone turnover in these two patient groups.

An automated method of segmenting the images removing the requirement for user interaction was developed. The measurements obtained from the software were validated against the existing semi-automatic protocols and showed excellent correlation. The software has incorporated flexibility in that, where the images are very challenging and the segmentation algorithm fails, operator intervention is enabled. Chapter 3 demonstrated that the algorithm works extremely well in a range of anatomical scenarios, facilitating successful segmentation of bone from surrounding soft tissue structures.

Assessment of the osteoblastic and osteoclastic processes which are occurring in the appendicular skeleton are generally made using global measurements of BMD, however any regional differences within the limb can be obscured by this global averaging of the bony compartment. Chapter 4 presented novel software which can be used to characterise the bone turnover spatially as well as globally. In order to perform the spatial analysis, registration software was written and applied to the segmented images which maximises correlation of images both translationally and rotationally. Spatial evaluation was carried out using the automated quadrant analysis and ΔBMD voxel wise comparisons. The latter analysis had not to date been carried out in registered images of the limbs of individual subjects using pQCT densitometric images. This novel approach to voxel based analysis facilitates comparisons between a pair of images, as opposed to group comparisons. Such a technique is excellent for describing bone turnover in clinical populations who experience individualistic changes in BMD, where global descriptions would not be appropriate.

The relationship between bone turnover and trabecular bone microarchitecture in the characterisation of osteoporosis has been studied extensively in other fields of medical imaging. Whether the images from pQCT scanners had a role is this domain is still under exploration. Software which used a sequence of morphological openings of pQCT images was developed in this thesis as one such method, which could potentially provide further information into the inherent structure of the bone contained within the images. Chapter 5 described the fundamental principles of this software and the theory behind the concept of its use in describing bone patterns.

Two novel clinical studies were presented in Chapters 6 and 7. The image analysis component of both these studies was carried out using the software developed in this thesis. The first study investigated the longitudinal changes in BMD in the acute SCI population. Initial findings using global BMD measurements were published by Coupaud *et al* (n=6) [70]. Further analysis of the acquired images was then presented in Chapter 6 of this thesis. It was identified that a proportion of these subjects experienced rapid bone loss within the first year post SCI, with inhomogeneous bone loss patterns occurring within the paralysed lower limbs. Applying the spatial analysis tools developed to the distal tibia, it was possible to observe this loss graphically using quadrant analysis, as well as visually using ΔBMD maps with varying colour scale depicting the extent of the bone loss. The remaining subjects in this cohort did not experience the same dramatic decreases in BMD as expected from the current literature.

The images from the distal tibia of the SCI subjects were then processed using morphological granulometries. Local pattern spectrum moment images provided a qualitative assessment of the bony microarchitecture, where global pattern spectrum moments enabled a more quantitative evaluation. The results from the latter were investigated for their predictive ability in determining whether a subject would be susceptible to rapid bone loss or not based on the bone patterns present from their pQCT scan. Based on the data available for this study, granulometries did not appear to have a better prediction at 4 months post injury than BMDTot. On the other hand, granulometry analysis of bone patterns at 12 months demonstrated promising findings as a useful adjunct to BMDTot, in particular when trying to characterise BMD in SCI patients at risk of osteoporosis and ultimately fracture. Further work with larger subject numbers is needed to validate these findings.

The second clinical study which was evaluated using these software tools, investigated the BMD response of the knee following ACL injury and surgical repair. Images were acquired at the distal femur and proximal tibia of both the injured knee and the contralateral control knee. For this study the author performed both the data analysis, using the global measurements of BMD, as well as the image analysis, investigating the spatial changes in bone post-injury. Automated segmentation of the bone from it's surrounding soft tissue, as well as registration with automated quadrant analysis, facilitated an impartial global assessment of the changes in BMD post-ACL injury. The majority of findings derived from this analysis were in line with current publications. There were however some indications of variation in bone density within the limbs following surgical repair which had not previously been observed.

Information on patterns of bone loss from ΔBMD maps describing the ACL population as a whole was relatively inconclusive. Each subject observed their own individual patterns of loss, which would indicate that other factors associated with the person and the injury also influence the bone turnover. Rapid bone loss was however observed in all subjects following injury, with the tibial trabecular post-op measurements demonstrating a significant loss that had not previously been evident in published BMDTot measurements. These losses could potentially be an issue regarding the success of the repair and the longevity of the implant.

Granulometric analysis of bone microarchitecture in the ACL study was not fruitful. It was hypothesised that this was due to the nature of the bone structure at the anatomical locations imaged and the resolution limits of the pQCT images used in this thesis. Granulometries would not appear to be the optimal method for assessing bone patterns in the proximal tibia or distal femur in this instance.

8.1 Future work

The future work associated with this thesis can be divided into two different categories: technical and clinical. The technical considerations are discussed first.

The SCI study demonstrated the potential application of granulometries in providing additional information on bone structure to its BMD measurement in the distal tibia. Due to the limited patient numbers in this study, these results would be considered a good grounding as a feasibility study. If the number of subjects recruited to the study was much larger, more global pattern spectrum features could be calculated. Feature reduction algorithms could be used to determine the optimal parameter, or combination of parameters, which best describe underlying changes in bone microarchitecture. In addition to this, these granulometry results were based on the use of a disc shaped structuring element, a shape chosen based on its similarity to the porous nature of trabecular bone. Evaluating a range of additional different structuring elements could potentially generate features which have improved classification power over the disc. In contrast, assessment of bone patterns in the knee following ACL injury using granulometries was not as successful. There may still be merit in investigating any changes in bone patterns using an alternative technique such a texture analysis. Although this performs a similar neighbourhood analysis of the voxels in the image, its analysis methods differ from granulometric sieving and perhaps would be more successful at generating descriptive textural features.

A potentially exciting development of this software would be to feed the findings from these studies into whole-body biomechanical modeling software, such as AnyBody^{TM} Technology (`www.anybodytech.com`). This is an object oriented piece of software developed in C^{++} which is a modeling system developed for musculoskeletal analysis. Patient specific data such as weight, height and mobility, for example, whether they have a spinal cord injury, or an ACL implant in the bone, are entered into the model. The AnyBody^{TM} Technology has the capability to interface with software such as finite-element analysis or image-based bone and muscle data. The simulation will calculate the mechanical properties for the body-environment system, from which the user can then obtain information on individual muscle, joint, tendon forces etc within the model. Using the localised data generated from this thesis on bone loss following SCI or ACL-injury as an additional parameter in the simulation, the modeling system could potentially be used to identify exact individualised muscles or movements which would be predicted to work towards restoring BMD. Modeling software such as this would be the next step towards creating a personalised tailored rehabilitation plan for each patient. This would not just be limited to SCI or ACL subjects, but any patient group scanned with pQCT, as this thesis has demonstrated the flexibility of the spatial and longitudinal software analysis.

There are several different clinical avenues which would be interesting to explore further. For example, the radius of the paraplegic SCI subjects who still have mobility in their upper limbs. Research has shown that following injury, the BMD in these limbs remains no different from a control group [33], but is there any remodelling taking place as a result of wheelchair propulsion which is not reflected in this global measurement? A preliminary assessment could be made using the data available in this clinical study, as radius data are available and 8 of the subjects had injuries at T4 and below.

Another avenue would be to evaluate whether other contributing factors influence the rate of bone loss in SCI, such as muscle tone, frequency of spasms, hormone levels, to name a few.

With the time window for analysis only being 1 year, it was not possible to correlate these findings with fracture risk which is the ultimate goal. Annual follow-up would be of interest, recording any incidence of fracture during this period. This would also allow the “slow lowers” to be monitored, in order to characterise their bone demineralisation.

Although the pattern maps provide much more detail on how and where the bone is lost (or gained) in the limb, it ultimately raises more questions than answers: Why do some SCI subjects experience significant loss in their tibia but not in their femur? What determines the inhomogeneous patterns of bone loss they experience? Finally, why do some subjects

experience no apparent bone loss at the anatomical sites investigated in this thesis in their first year post-SCI, despite the dramatic change in their physical circumstances? Correlations with their pre-injury activity levels and maturation of the limbs may provide a key explanation, as the majority of "fast" losers in this sample were young males.
Further longitudinal assessment of the ACL subjects would also be very interesting. Has the bone demineralised further after several years post-surgery? For those subjects who had already experienced significant losses prior to surgery, how successful was their implant in the longer term? Again, an evaluation of factors such as age and activity levels pre- and post-ACL injury would perhaps provide the additional information necessary to correlate patterns of bone loss observed in this study.

Although this thesis has only detailed the osteoporotic challenges associated with SCI and ACL, it is also important to remember that it is a condition which is a major issue for many other patient groups. pQCT research by Hosie in Glasgow almost 20 years ago [142] was driven by the need for a good surrogate marker of bone characteristics that relate to fracture probability. This was necessary for clinical trials of preventive therapies. Very recent publications have also demonstrated the added value of structural analysis over global BMD and T-scores in terms of fracture risk [143, 144, 145]. The software presented in this thesis could therefore potentially be used as a tool to enhance the findings derived from such clinical trials.
Clinically, the findings presented in this thesis have prompted additional questions into the processes surrounding bone demineralisation, however what is apparent is that these losses are influenced not only by the forces, or lack thereof, on the bone but also by additional lifestyle factors. The World Health Organisation has also identified this correlation, having recently developed a Fracture Risk Assessment Tool (also known as FRAX®, `www.shef.ac.uk/FRAX`). It generates a patient specific model which integrates their BMD values with the patient's clinical risk factors to provide a 10 year probability of fracture. In addition to this, newer models of DXA scanners are performing bone morphology analysis, which also confirms the appreciation that architecture is a contributory factor to fracture risk in addition BMD.

What is clear from the studies presented, as well as all of the other clinical research studies mentioned in this thesis, is that the understanding of bone turnover in response to injury, illness, age or even unknown factors still has many unanswered questions. It is therefore a subject which will continue to drive researchers towards a better understanding of the processes involved in restoring and maintaining healthy strong bones.

Appendix A

Optimisation of Geometric Transformations

Coregistered Image	t$_{x1}$	t$_{y1}$	θ_2	t$_{x3}$	t$_{y3}$	θ_4	t$_{x5}$	t$_{y5}$	θ_6	COM diff. (mm)	Time$_3(s)$	Time$_6(s)$
Distal tibia pair 1	9	8	15	-1	4	0	0	0	0	0	6.39	17.36
Distal tibia pair 2	3	22	0	0	0	0	0	0	0	0	6.49	16.63
Distal tibia pair 3	3	-37	10	-10	10	0	0	0	0	0	7.83	20.71
Distal tibia pair 4	4	1	1	1	1	0	0	0	0	0	4.79	13.55
Distal tibia pair 5	8	4	6	0	2	0	0	0	0	0	6.47	18.38
Distal tibia pair 6	1	-6	8	0	4	0	0	0	0	0	6.28	17.29
Distal tibia pair 7	7	6	0	0	0	0	0	0	0	0	5.13	14.26
Distal tibia pair 8	2	3	-2	0	0	-1	0	0	0	0.18	1.86	15.33
Distal tibia pair 9	7	8	12	3	3	-1	0	-1	0	0.43	5.19	14.26
Distal femur pair 1	14	6	13	5	-8	0	0	0	0	0	176	512
Distal femur pair 2	-61	-60	10	-10	5	0	0	0	0	0	123.04	374.71
Distal femur pair 3	-61	-121	7	-8	4	0	0	0	0	0	125.22	390.8
Distal femur pair 4	-23	4	-4	0	0	0	0	0	0	0	170.12	485.77
Distal femur pair 5	5	13	8	4	-3	0	0	0	0	0	152.09	437.55
Distal femur pair 6	3	1	0	0	0	0	0	0	0	0	161.29	492.2
Distal femur pair 7	-10	-6	-1	0	-1	0	0	0	0	0	100.39	291.89
Distal femur pair 8	-16	4	11	-1	8	0	0	0	0	0	110.68	319.24
Distal femur pair 9	-21	-1	18	-4	13	0	0	0	0	0	103	303.91

Appendix B

Conference Abstracts

IMAGE ANALYSIS OF BONE DENSITY FOLLOWING ANTERIOR CRUCIATE LIGAMENT INJURY

C.Findlay[1], SS.Jameson[2], S.Marshall[3], B.Walker[1], C.Walker[2], RD.Meek[2], A.Nicol[1]
[1]Nuclear Medicine, Southern General Hospital, Glasgow
[2]Orthopaedics, Southern General Hospital
[3]Dept EEE, Strathclyde University

Journal of Bone & Joint Surgery, British Volume, 94-B(SUPP XVIII):31, 2012.
Presented at British Orthopaedic Research Society annual conference, Cardiff, 2010

Background
Following an anterior cruciate ligament (ACL) injury, the affected knee is known to experience bone loss and is at significant risk of becoming osteoporotic. Surgical reconstruction is performed to attempt to restore the function of the knee and theoretically restore this bone density loss. Cross-sectional analysis of the proximal tibia using peripheral quantitative computed tomography (pQCT) enables localised analysis of bone mineral density (BMD) changes. The aim of this study was to establish the pattern of bone density changes in the tibia pre- and post- ACL reconstruction using pQCT image analysis.

Methods
Eight patients who underwent ACL reconstruction were included. A cross sectional analysis of the proximal tibia was performed using a pQCT scanner pre-operatively and one to two years post-operatively on both the injured and contralateral (control) knee. The proximal two and three percent slices [S2 and S3] along the tibia were acquired. These were exported to Matlab and automated segmentation was performed to remove the tibia from its surrounding structures. Cross correlation was applied to co-register pairs of images and patterns of change

in BMD were mapped using a t-test (p¡0.05). Connected components (CC's) of pixels with significant change in BMD were created and used to assess the impact of ACL injury & reconstruction on the proximal tibial BMD.

Results

Prior to surgical ACL reconstruction, the BMD in the injured leg was significantly reduced relative to the control leg [S2: p=0.002, S3: p=0.002]. Post surgery, the proximal tibial BMD did not change in either leg [Control S2: p=0.102, S3: p=0.181; Injured S2: p=0.093, S3: p=0.439]. The post surgical images demonstrated patterns of increasing BMD surrounding the tunnel in the form of compact bone.

Discussion

A significant reduction in proximal tibial BMD was observed in the ACL injured legs relative to control legs. The pattern of pre-operative bone loss was generally observed to be global across the entire slice. No change in BMD was observed following ACL reconstruction, in either injured or control leg. These results indicate that proximal tibial BMD is reduced and does not change after ACL reconstruction.

LOCALISED TEMPORAL AND SPATIAL IMAGE ANALYSIS OF BONE TURNOVER USING PQCT

C.Findlay[1], A.Nicol[1], S.Marshall[2]
[1]Nuclear Medicine, Victoria Infirmary, Glasgow
[2]Dept. Electronic & Electrical Engineering, University of Strathclyde, Glasgow

Bioengineering 10, IPEM, 2010
Presented at The Bioengineering Society (UK) annual conference, Nottingham University, 2010

Background and purpose

Longitudinal studies of bone response to external stimuli such as stress-shielding from metal implants or the removal of weight bearing forces have been investigated using medical imaging techniques such as DXA (Dual energy X-Ray Absorptiometry) or pQCT (peripheral Quantitative Computed Tomography). Many published reports state total bone mineral density (BMD) changes over a particular area of interest [13], however limited results are available describing patterns of change throughout the bone. An image processing technique is presented which maps the pattern of bone change in pQCT images of the appendicular skeleton. It is demonstrated in this instance using image data from a patient group following anterior cruciate ligament (ACL) reconstruction.

Method

Longitudinal pQCT images of the appendicular skeleton are imported into Matlab. Automated image segmentation of the bone from surrounding soft tissue is performed by thresholding the 1st derivative of the image histogram [46]. Pairs of images, e.g. from the same subject acquired at different time points, are coregistered and areas of statistically significant change in BMD are identified using a t-test (p¡0.05). The magnitude of these changes is plotted across the tomographic slice producing a visual representation of BMD change. This analysis can also be applied to compare BMD in left and right limbs e.g. following surgery, using the contralateral limb as a control.

Results

The technique has been applied to pQCT images from the 2 and 3%, femoral and tibial slices of 8 patients who underwent ACL reconstruction [146]. Data was acquired pre-op and at 1-2 years post-op. Analysis was performed on the pre-op data using comparison with the contralateral knee. Pre- and post-op data were compared of the injured knee.

Pre-operatively, there were areas of reduced BMD in the injured knee when compared with the contralateral knee, although there was inter-individual variability observed in regional patterns. Post-operatively, all subjects had an area of bone formation around the tunnel made for the ACL insert. Regional analysis of the post-op vs pre-op images indicates that there is an inhomogeneous response to the ACL reconstruction surgery. Example of pre- and post-op pQCT images with their associated pattern map of BMD change are presented. Areas in white on the map indicate a statistically significant decrease in BMD across the two co-registered images, areas in grey show a statistically significant increase in BMD and black regions indicate no significant change in BMD. The example given identifies a BMD increase around the ACL implant. It also identifies a region laterally to the implant that has experienced significant bone loss 2 years post surgery, despite the surgical intervention.

Conclusions

Patterns of bone loss across transverse pQCT images allow investigators to identify regions within the bone that are more susceptible to bone loss. Global measurements of BMD may mask underlying areas of significant bone loss if subject groups experience a combination of both increasing and decreasing in BMD. An image analysis technique is presented which gives an indication of regions of increasing and decreasing BMD. This may permit more focused intervention techniques or physiotherapeutic exercises which may assist in bone restoration in these regions.

References

[1] P Dolan and D J Torgerson. The Cost of Treating Osteoporotic Fractures in the United Kingdom Female Population. *Osteoporosis International*, 8(6):611–617, November 1998.

[2] C P Iglesias, A Manca, and D J Torgerson. The health-related quality of life and cost implications of falls in elderly women. *Osteoporosis international*, 20(6):869–78, June 2009.

[3] L Gutiérrez, N Roskell, J Castellsague, S Beard, C Rycroft, S Abeysinghe, P Shannon, M Gitlin, and S Robbins. Clinical burden and incremental cost of fractures in postmenopausal women in the United Kingdom. *Bone*, 51(3):324–331, June 2012.

[4] H M Frost. *The Utah Paradigm of Skeletal Physiology. Volume 1: Bone and Bone Associated Problems.* International Society of Musculoskeletal and Neuronal Interactions, Greece, 2004.

[5] H M Frost. Bone "mass" and the "mechanostat": a proposal. *The Anatomical record*, 219(1):1–9, September 1987.

[6] H M Frost. Perspectives: a proposed general model of the "mechanostat" (suggestions from a new skeletal-biologic paradigm). *The Anatomical record*, 244(2):139–47, February 1996.

[7] H M Frost. The Utah paradigm of skeletal physiology: an overview of its insights for bone, cartilage and collagenous tissue organs. *Journal of bone and mineral metabolism*, 18(6):305–16, January 2000.

[8] H M Frost. From Wolff's law to the Utah paradigm: insights about bone physiology and its clinical applications. *The Anatomical record*, 262(4):398–419, April 2001.

[9] W S Jee. Principles in bone physiology. *Journal of musculoskeletal & neuronal interactions*, 1(1):11–3, September 2000.

[10] M Järvinen and P Kannus. Injury of an extremity as a risk factor for the development of osteoporosis. *The Journal of bone and joint surgery. American volume*, 79(2):263–76, February 1997.

[11] D B Burr. Muscle strength, bone mass, and age-related bone loss. *Journal of bone and mineral research*, 12(10):1547–51, October 1997.

[12] J. Leppala, P. Kannus, A. Natri, M. Pasanen, H. Sievänen, I. Vuori, and M. Järvinen. Effect of Anterior Cruciate Ligament Injury of the Knee on Bone Mineral Density of the Spine and Affected Lower Extremity: A Prospective One-Year Follow-Up Study. *Calcified Tissue International*, 64(4):357–363, April 1999.

[13] S K Boyd, J R Matyas, G R Wohl, A Kantzas, and R F Zernicke. Early regional adaptation of periarticular bone mineral density after anterior cruciate ligament injury. *Journal of applied physiology*, 89(6):2359–64, December 2000.

[14] H Gray. *Anatomy of the human body, 20th Ed.* Lea & Febiger, Philadelphia, 20th edition, 1918.

[15] F Martini. *Fundamentals of Anatomy & Physiology.* Prentice Hall, fifth edition, 2001.

[16] WHO Scientific Group. Prevention and Management of Osteoporosis, Report 921. Technical report, Geneva, 2003.

[17] S L Bonnick. *Bone Densitometry in Clinical Practice.* Humana Press, Totowa, NJ, 2010.

[18] H K Genant and D Boyd. Quantitative bone mineral analysis using dual energy computed tomography. *Investigative radiology*, 12(6):545–51, 1977.

[19] P. Rüegsegger, P. Niederer, and M. Anliker. An extension of classical bone mineral measurements. *Annals of Biomedical Engineering*, 2(2):194–205, June 1974.

[20] W Huda and R L Morin. Patient doses in bone mineral densitometry. *The British journal of radiology*, 69(821):422–5, May 1996.

[21] J Willnecker. Manual XCT 3000 Software wersion 5.50, 2004.

[22] C Formica, M L Loro, V Gilsanz, and E Seeman. Inhomogeneity in body fat distribution may result in inaccuracy in the measurement of vertebral bone mass. *Journal of bone and mineral research*, 10(10):1504–11, October 1995.

[23] P Tothill, M A Laskey, C I Orphanidou, and M van Wijk. Anomalies in dual energy X-ray absorptiometry measurements of total-body bone mineral during weight change using Lunar, Hologic and Norland instruments. *The British journal of radiology*, 72(859):661–9, July 1999.

[24] H H Bolotin, H Sievänen, J L Grashuis, J W Kuiper, and T L Järvinen. Inaccuracies inherent in patient-specific dual-energy X-ray absorptiometry bone mineral density

measurements: comprehensive phantom-based evaluation. *Journal of bone and mineral research*, 16(2):417–26, February 2001.

[25] J Hong, J a Hipp, R V Mulkern, D Jaramillo, and B D Snyder. Magnetic resonance imaging measurements of bone density and cross-sectional geometry. *Calcified tissue international*, 66(1):74–8, January 2000.

[26] A E Comarr, R H Hutchinson, and E Bors. Extremity fractures of patients with spinal cord injuries. *American journal of surgery*, 103:732–9, June 1962.

[27] D E Garland, C A Stewart, R H Adkins, S S Hu, C Rosen, F J Liotta, and D A Weinstein. Osteoporosis after spinal cord injury. *Journal of orthopaedic research*, 10(3):371–8, May 1992.

[28] M G Lazo, P Shirazi, M Sam, A Giobbie-Hurder, M J Blacconiere, and M Muppidi. Osteoporosis and risk of fracture in men with spinal cord injury. *Spinal cord*, 39(4):208–14, April 2001.

[29] P Kannus, H Sievänen, M Järvinen, A Heinonen, P Oja, and I Vuori. A cruciate ligament injury produces considerable, permanent osteoporosis in the affected knee. *Journal of bone and mineral research*, 7(12):1429–34, December 1992.

[30] A Bayar, S Sarikaya, S Keser, S Ozdolap, I Tuncay, and A Ege. Regional bone density changes in anterior cruciate ligament deficient knees: a DEXA study. *The Knee*, 15(5):373–7, October 2008.

[31] P Vestergaard, K Krogh, L Rejnmark, and L Mosekilde. Fracture rates and risk factors for fractures in patients with spinal cord injury. *Spinal cord*, 36(11):790–6, November 1998.

[32] P Eser, A Frotzler, Y Zehnder, and J Denoth. Fracture threshold in the femur and tibia of people with spinal cord injury as determined by peripheral quantitative computed tomography. *Archives of physical medicine and rehabilitation*, 86(3):498–504, March 2005.

[33] P Eser, a Frotzler, Y Zehnder, L Wick, H Knecht, J Denoth, and H Schiessl. Relationship between the duration of paralysis and bone structure: a pQCT study of spinal cord injured individuals. *Bone*, 34(5):869–80, May 2004.

[34] S Coupaud, A N McLean, and D B Allan. Role of peripheral quantitative computed tomography in identifying disuse osteoporosis in paraplegia. *Skeletal radiology*, 38(10):989–95, October 2009.

[35] F Biering-Sorensen, H H Bohr, and O P Schaadt. Longitudinal study of bone mineral content in the lumbar spine, the forearm and the lower extremities after spinal cord injury. *European journal of clinical investigation*, 20(3):330–5, June 1990.

[36] E D de Bruin, V Dietz, M A Dambacher, and E Stüssi. Longitudinal changes in bone in men with spinal cord injury. *Clinical Rehabilitation*, 14(2):145–152, April 2000.

[37] E M Leeds, K J Klose, W Ganz, A Serafini, and B A Green. Bone mineral density after bicycle ergometry training. *Archives of physical medicine and rehabilitation*, 71(3):207–9, March 1990.

[38] P Eser, E D de Bruin, I Telley, H E Lechner, H Knecht, and E Stüssi. Effect of electrical stimulation-induced cycling on bone mineral density in spinal cord-injured patients. *European journal of clinical investigation*, 33(5):412–9, May 2003.

[39] A Frotzler, S Coupaud, C Perret, T H Kakebeeke, K J Hunt, N N Donaldson, and P Eser. High-volume FES-cycling partially reverses bone loss in people with chronic spinal cord injury. *Bone*, 43(1):169–76, July 2008.

[40] S Dudley-Javoroski and R K Shields. Asymmetric bone adaptations to soleus mechanical loading after spinal cord injury. *Journal of musculoskeletal & neuronal interactions*, 8(3):227–38, 2008.

[41] J Rittweger, N D Reeves, M V Narici, D L Belavý, C N Maganaris, and N Maffulli. Persisting side-to-side differences in bone mineral content, but not in muscle strength and tendon stiffness after anterior cruciate ligament reconstruction. *Clinical physiology and functional imaging*, 31(1):73–9, January 2011.

[42] J Rittweger, N Maffulli, C N Maganaris, and M V Narici. Reconstruction of the anterior cruciate ligament with a patella-tendon-bone graft may lead to a permanent loss of bone mineral content due to decreased patellar tendon stiffness. *Medical hypotheses*, 64(6):1166–9, January 2005.

[43] G R Wohl, R C Shymkiw, J R Matyas, R Kloiber, and R F Zernicke. Periarticular cancellous bone changes following anterior cruciate ligament injury. *Journal of applied physiology*, 91(1):336–42, July 2001.

[44] A M W Chaudhari, P L Briant, S L Bevill, S Koo, and T P Andriacchi. Knee kinematics, cartilage morphology, and osteoarthritis after ACL injury. *Medicine and science in sports and exercise*, 40(2):215–22, February 2008.

[45] T Cervinka, J Hyttinen, and H Sievanen. Enhanced bone structural analysis through pQCT image preprocessing. *Medical engineering & physics*, 32(4):398–406, May 2010.

[46] J D Helterbrand, R E Higgs, P W Iversen, G Tysarczyk-Niemeyer, and M Sato. Application of automatic image segmentation to tibiae and vertebrae from ovariectomized rats. *Bone*, 21(5):401–9, November 1997.

[47] J H Waarsing, J S Day, and H Weinans. An improved segmentation method for in vivo microCT imaging. *Journal of bone and mineral research*, 19(10):1640–50, October 2004.

[48] A J Burghardt, G J Kazakia, and S Majumdar. A local adaptive threshold strategy for high resolution peripheral quantitative computed tomography of trabecular bone. *Annals of biomedical engineering*, 35(10):1678–86, October 2007.

[49] H R Buie, G M Campbell, R J Klinck, J A MacNeil, and S K Boyd. Automatic segmentation of cortical and trabecular compartments based on a dual threshold technique for in vivo micro-CT bone analysis. *Bone*, 41(4):505–15, October 2007.

[50] G Rizzo, D Tresoldi, E Scalco, M Mendez, A M Bianchi, G L Moro, and A Rubinacci. Automatic segmentation of cortical and trabecular components of bone specimens acquired by pQCT. In *Annual International Conference of the IEEE Engineering in Medicine and Biology Society.*, volume 2008, pages 486–9, January 2008.

[51] K A Ward, J E Adams, and T N Hangartner. Recommendations for thresholds for cortical bone geometry and density measurement by peripheral quantitative computed tomography. *Calcified tissue international*, 77(5):275–80, November 2005.

[52] T N Hangartner. Thresholding technique for accurate analysis of density and geometry in QCT, pQCT and microCT images. *Journal of musculoskeletal & neuronal interactions*, 7(1):9–16, 2007.

[53] K A Davis, A J Burghardt, T M Link, and S Majumdar. The effects of geometric and threshold definitions on cortical bone metrics assessed by in vivo high-resolution peripheral quantitative computed tomography. *Calcified tissue international*, 81(5):364–71, November 2007.

[54] ICRU. Report of the Task Group on Reference Man: Integumentary system. *Annals of the ICRP/ICRP Publication*, 23(1):46–85, 1975.

[55] E Klotz, W A Kalender, and T Sandor. Automated definition and evaluation of anatomical ROI's for bone mineral determination by QCT. *IEEE transactions on medical imaging*, 8(4):371–6, January 1989.

[56] X Q Ma and T R Overton. Automated image analysis for bone density measurements using computed tomography. *IEEE transactions on medical imaging*, 10(4):611–5, January 1991.

[57] L Vincent. Current topics in applied morphological image analysis. In W S Kendall, O E Barndorff-Nielsen, and M C van Lieshout, editors, *Current Trends in Stochastic Geometry and Its Applications*. Chapman & Hall, London, 1997.

[58] G Rizzo, E Scalco, D Tresoldi, I Villa, G L Moro, C L Lafortuna, and A Rubinacci. An Automatic Segmentation Method for Regional Analysis of Femoral Neck Images Acquired by pQCT. *Annals of biomedical engineering*, 39(1):1–13, 2011.

[59] L Shi, D Wang, V W Y Hung, B H Y Yeung, J F Griffith, W C W Chu, P A Heng, J C Y Cheng, and L Qin. Fast and accurate 3-D registration of HR-pQCT images. *IEEE transactions on information technology in biomedicine*, 14(5):1291–7, September 2010.

[60] J A Macneil and S K Boyd. Bone strength at the distal radius can be estimated from high-resolution peripheral quantitative computed tomography and the finite element method. *Bone*, 42(6):1203–13, June 2008.

[61] W Li, M Sode, I Saeed, and T Lang. Automated registration of hip and spine for longitudinal QCT studies: integration with 3D densitometric and structural analysis. *Bone*, 38(2):273–9, February 2006.

[62] A Gholipour, N Kehtarnavaz, R Briggs, M Devous, and K Gopinath. Brain functional localization: a survey of image registration techniques. *IEEE transactions on medical imaging*, 26(4):427–51, April 2007.

[63] W Li, I Kezele, D L Collins, A Zijdenbos, J Keyak, J Kornak, A Koyama, I Saeed, A Leblanc, T Harris, Y Lu, and T Lang. Voxel-based modeling and quantification of the proximal femur using inter-subject registration of quantitative CT images. *Bone*, 41(5):888–95, November 2007.

[64] R C Gonzalez and R E Woods. *Digital Image Processing*. Pearson Prentice Hall, New Jersey, third edit edition, 2008.

[65] B Zitova and J Flusser. Image registration methods: a survey. *Image and Vision Computing*, 21(11):977–1000, October 2003.

[66] L G Brown. A survey of image registration techniques. *ACM Computing Surveys*, 24(4):325–376, December 1992.

[67] J B A Maintz and Max A Viergever. A survey of medical image registration. *Medical Image Analysis*, 2(1):1–36, March 1998.

[68] G P Penney, J Weese, J A Little, P Desmedt, D L Hill, and D J Hawkes. A comparison of similarity measures for use in 2-D-3-D medical image registration. *IEEE transactions on medical imaging*, 17(4):586–95, August 1998.

[69] G Demirel, H Yilmaz, N Paker, and S Onel. Osteoporosis after spinal cord injury. *Spinal cord*, 36(12):822–5, December 1998.

[70] S Coupaud, a N McLean, S Lloyd, and D B Allan. Predicting patient-specific rates of bone loss at fracture-prone sites after spinal cord injury. *Disability and rehabilitation*, (August 2011):1–9, May 2012.

[71] P Frey-Rindova, E D de Bruin, E Stüssi, M A Dambacher, and V Dietz. Bone mineral density in upper and lower extremities during 12 months after spinal cord injury measured by peripheral quantitative computed tomography. *Spinal cord*, 38(1):26–32, January 2000.

[72] A Frotzler, M Berger, H Knecht, and P Eser. Bone steady-state is established at reduced bone strength after spinal cord injury: a longitudinal study using peripheral quantitative computed tomography (pQCT). *Bone*, 43(3):549–55, September 2008.

[73] S Takata, A Abbaspour, M Kashihara, S Nakao, and N Yasui. Unilateral chronic insufficiency of anterior cruciate ligament decreases bone mineral content and lean mass of the injured lower extremity. *The Journal of Medical Investigation*, 54(3,4):316–321, 2007.

[74] G Rizzo, P Pasquali, and M Gilardi. Multimodal biomedical image integration: Use of a cross-correlation technique. In *Proceedings IEEE EMBS*, pages 219–220, 1991.

[75] J P W Pluim, J B A Maintz, and M A Viergever. Interpolation Artefacts in Mutual Information-Based Image Registration. *Computer Vision and Image Understanding*, 77(2):211–232, February 2000.

[76] R P Woods. Within-Modality Registration Using Intensity-Based Cost Functions. In *Handbook of Medical Image Processing and Analysis*, pages 605–611. Elsevier Inc., second edi edition, 2008.

[77] J Parker, R V Kenyon, and D E Troxel. Comparison of interpolating methods for image resampling. *IEEE transactions on medical imaging*, 2(1):31–9, January 1983.

[78] J A Kanis, N Burlet, C Cooper, P D Delmas, J-Y Reginster, F Borgstrom, and R Rizzoli. European guidance for the diagnosis and management of osteoporosis in postmenopausal women. *Osteoporosis international*, 19(4):399–428, April 2008.

[79] E Lespessailles, C Gadois, I Kousignian, J P Neveu, P Fardellone, S Kolta, C Roux, J P Do-Huu, and C L Benhamou. Clinical interest of bone texture analysis in osteoporosis: a case control multicenter study. *Osteoporosis international*, 19(7):1019–28, July 2008.

[80] A E Rodríguez-Soto, K D Fritscher, B Schuler, A S Issever, T Roth, F Kamelger, C Kammerlander, M Blauth, R Schubert, and T M Link. Texture analysis, bone mineral density, and cortical thickness of the proximal femur: fracture risk prediction. *Journal of computer assisted tomography*, 34(6):949–57, 2010.

[81] J Bacchetta, S Boutroy, N Vilayphiou, A Fouque-Aubert, P D Delmas, E Lespessailles, D Fouque, and R Chapurlat. Assessment of bone microarchitecture in chronic kidney disease: a comparison of 2D bone texture analysis and high-resolution peripheral quantitative computed tomography at the radius and tibia. *Calcified tissue international*, 87(5):385–91, November 2010.

[82] M Khider, A Taleb-Ahmed, P Dubois, and B Haddad. Classification of trabecular bone texture from MRI and CT scan images by multi resolution analysis. In *Annual International Conference of the IEEE Engineering in Medicine and Biology Society.*, volume 2007, pages 5589–92, January 2007.

[83] I S Boniatis, L I Costaridou, D A Cavouras, E C Panagiotopoulos, and G S Panayiotakis. Quantitative assessment of hip osteoarthritis based on image texture analysis. *The British journal of radiology*, 79(939):232–8, March 2006.

[84] D Chappard, P Guggenbuhl, E Legrand, Michel F Baslé, and M Audran. Texture analysis of X-ray radiographs is correlated with bone histomorphometry. *Journal of bone and mineral metabolism*, 23(1):24–9, January 2005.

[85] S Herlidou, R Grebe, F Grados, N Leuyer, P Fardellone, and M-E Meyer. Influence of age and osteoporosis on calcaneus trabecular bone structure: a preliminary in vivo MRI study by quantitative texture analysis. *Magnetic resonance imaging*, 22(2):237–43, February 2004.

[86] T Cervinka, J Rittweger, J Hyttinen, D Felsenberg, and H Sievänen. Anatomical sector analysis of load-bearing tibial bone structure during 90-day bed rest and 1-year recovery. *Clinical physiology and functional imaging*, 31(4):249–57, July 2011.

[87] K Engelke, T Fuerst, G Dasic, R Y Davies, and H K Genant. Regional distribution of spine and hip QCT BMD responses after one year of once-monthly ibandronate in postmenopausal osteoporosis. *Bone*, 46(6):1626–32, June 2010.

[88] Y M Lai, L Qin, V W Y Hung, and K M Chan. Regional differences in cortical bone mineral density in the weight-bearing long bone shaft–a pQCT study. *Bone*, 36(3):465–71, March 2005.

[89] K Friston. Statistical parametric mapping. In Friston, Ashburner, Kiebel, Nichols, and Penny, editors, *Statistical Parametric Mapping - The Analysis of Functional Brain*

Images, chapter 2, pages 10–31. Elsevier/Academic Press, Amsterdam, 1st ed. edition, 2007.

[90] W Li, J Kornak, T Harris, J Keyak, C Li, Y Lu, X Cheng, and T Lang. Identify fracture-critical regions inside the proximal femur using statistical parametric mapping. *Bone*, 44(4):596–602, April 2009.

[91] Q Zhao, W Li, C Li, P W Chu, J Kornak, T F Lang, J Fang, and Y Lu. A statistical method (cross-validation) for bone loss region detection after spaceflight. *Australasian physical & engineering sciences in medicine*, pages 163–169, July 2010.

[92] N Theera-Umpon and P D Gader. Counting white blood cells using morphological granulometries. *Journal of Electronic Imaging*, 9(2):170, 2000.

[93] G K Matsopoulos and S Marshall. Use of morphological image processing techniques for the measurement of a fetal head from ultrasound images. *Pattern Recognition*, 27(10):1317–1324, 1994.

[94] E R Dougherty, E J Kraus, and J B Pelz. Image Segmentation By Local Morphological Granulometries. In *12th Canadian Symposium on Remote Sensing Geoscience and Remote Sensing Symposium,*, pages 1220–1223. IEEE, 1989.

[95] R M Haralick, S R Sternberg, and X Zhuang. Image Analysis Using Mathematical Morphology. *Pattern Analysis and Machine Intelligence, IEEE Transactions on*, (4):532–550, 1987.

[96] T Sakurai, R Kawamata, S Numayama, T Okada, and I Kashima. Extraction of skeletal patterns from magnetic resonance images using mathematical morphological filters. *Oral Radiology*, 18(1):25–43, June 2002.

[97] Y Chen, E R Dougherty, S M Totterman, and J P Hornak. Classification of trabecular structure in magnetic resonance images based on morphological granulometries. *Magnetic resonance in medicine*, 29(3):358–70, March 1993.

[98] E R Dougherty, J B Pelz, F Sand, and A Lent. Morphological image segmentation by local granulometric size distributions. *Journal of Electronic Imaging*, 1(1):46, 1992.

[99] L W Goldman. Principles of CT and CT technology. *Journal of nuclear medicine technology*, 35(3):115–28; quiz 129–30, September 2007.

[100] R B Paranjape. Fundamental Enhancement Techniques. In Isaac N. Bankman, editor, *Handbook of Medical Imaging*, chapter 1.1, pages 3–18. Elsevier Inc., 2000.

[101] P Ruegsegger and W A Kalender. A phantom for standardization and quality control in peripheral bone measurements by PQCT and DXA. *Physics in Medicine and Biology*, 38:1963, 1993.

[102] J M Bland and D G Altman. Statistical methods for assessing agreement between two methods of clinical measurement. *Lancet*, 1(8476):307–10, February 1986.

[103] M Bland. *An introduction to medical statistics.* Oxford University Press, Oxford New York, 3rd editio edition, 2000.

[104] P Kannus, H Haapasalo, H Sievänen, P Oja, and I Vuori. The site-specific effects of long-term unilateral activity on bone mineral density and content. *Bone*, 15(3):279–84, 1994.

[105] S Coupaud, A N Mclean, S Lloyd, and D B Allan. Predicting patient-specific rates of bone loss at fracture-prone sites after spinal cord injury. *Disability and Rehabilitation*, pages 1–15, 2012.

[106] R P Woods. Spatial Transformation Models. In *Handbook of Medical Image Processing and Analysis*, pages 541–568. Elsevier Inc., second edi edition, 2008.

[107] R D Kortmann, G Becker, J Perelmouter, M Buchgeister, C Meisner, and M Bamberg. Geometric accuracy of field alignment in fractionated stereotactic conformal radiotherapy of brain tumors. *International journal of radiation oncology, biology, physics*, 43(4):921–6, March 1999.

[108] B G Baumert, P Egli, S Studer, C Dehing, and J B Davis. Repositioning accuracy of fractionated stereotactic irradiation: assessment of isocentre alignment for different dental fixations by using sequential CT scanning. *Radiotherapy and oncology*, 74(1):61–6, January 2005.

[109] G Minniti, M Valeriani, E Clarke, M D'Arienzo, M Ciotti, R Montagnoli, F Saporetti, and R M Enrici. Fractionated stereotactic radiotherapy for skull base tumors: analysis of treatment accuracy using a stereotactic mask fixation system. *Radiation oncology*, 5:1, January 2010.

[110] R P Woods. Validation of Registration Accuracy. In *Handbook of Medical Image Processing and Analysis*, pages 569–575. Elsevier Inc., second edi edition, 2008.

[111] S Dudley-Javoroski and R K Shields. Longitudinal changes in femur bone mineral density after spinal cord injury: effects of slice placement and peel method. *Osteoporosis international*, 21(6):985–95, June 2010.

[112] F Faul, E Erdfelder, A Lang, and A Buchner. G*Power 3: a flexible statistical power analysis program for the social, behavioral, and biomedical sciences. *Behavior research methods*, 39(2):175–91, May 2007.

[113] R C Blair and J J Higgins. Comparison of the power of the paired samples t test to that of Wilcoxon's signed-ranks test under various population shapes. *Psychological Bulletin*, 97(1):119–128, 1985.

[114] S Holm. A simple sequentially rejective multiple test procedure. *Scandinavian Journal of Statistics*, 6(2):65–70, 1979.

[115] T V Perneger. What's wrong with Bonferroni adjustments. *British Medical Journal*, 316(7139):1236–1238, April 1998.

[116] K J Friston, C D Frith, P F Liddle, and R S Frackowiak. Comparing functional (PET) images: the assessment of significant change. *Journal of cerebral blood flow and metabolism*, 11(4):690–9, July 1991.

[117] K J Worsley, S Marrett, P Neelin, A C Vandal, K J Friston, and a C Evans. A unified statistical approach for determining significant signals in images of cerebral activation. *Human brain mapping*, 4(1):58–73, January 1996.

[118] A P Holmes, R C Blair, J D Watson, and I Ford. Nonparametric analysis of statistic images from functional mapping experiments. *Journal of cerebral blood flow and metabolism*, 16(1):7–22, January 1996.

[119] T E Nichols and A P Holmes. Nonparametric permutation tests for functional neuroimaging: a primer with examples. *Human Brain Mapping*, 15(1):1–25, 2002.

[120] Y Benjamini and Y Hochberg. Controlling the false discovery rate: a practical and powerful approach to multiple testing. *Journal of the Royal Statistical Society. Series B (Methodological)*, 57(1):289–300, 1995.

[121] C Genovese, N Lazar, and T Nichols. Thresholding of statistical maps in functional neuroimaging using the false discovery rate. *NeuroImage*, 15(4):870–8, April 2002.

[122] C J Miller, C Genovese, R C Nichol, L Wasserman, A Connolly, D Reichart, A Hopkins, J Schneider, and A Moore. Controlling the False-Discovery Rate in Astrophysical Data Analysis. *The Astronomical Journal*, 122(6):3492–3505, December 2001.

[123] T Nichols and S Hayasaka. Controlling the familywise error rate in functional neuroimaging: a comparative review. *Statistical methods in medical research*, 12(5):419–46, October 2003.

[124] J R Chumbley and K J Friston. False discovery rate revisited: FDR and topological inference using Gaussian random fields. *NeuroImage*, 44(1):62–70, January 2009.

[125] C M Bennett, G L Wolford, and M B Miller. The principled control of false positives in neuroimaging. *Social cognitive and affective neuroscience*, 4(4):417–22, December 2009.

[126] Y Benjamini and D Yekutieli. The control of the false discovery rate in multiple testing under dependency. *Annals of statistics*, 29(4):1165–1188, 2001.

[127] G Matheron. *Random sets and integral geometry.* Wiley, New York, 1975.

[128] J Serra. *Image analysis and mathematical morphology.* Academic Press, London, 1982.

[129] H Heijmans. Theoretical aspects of gray-level morphology. *Pattern Analysis and Machine Intelligence,*, 13(6):568–582, 1991.

[130] J Bloem, M Veninga, and J Shepherd. Fully automatic determination of soil bacterium numbers, cell volumes, and frequencies of dividing cells by confocal laser scanning microscopy and image analysis. *Applied and Environmental Microbiology*, 61(3):926–936, 1995.

[131] M Pesaresi and J A Benediktsson. A new approach for the morphological segmentation of high-resolution satellite imagery. *IEEE Transactions on Geoscience and Remote Sensing*, 39(2):309–320, 2001.

[132] J A Benediktsson, M Pesaresi, and K Arnason. Classification and feature extraction for remote sensing images from urban areas based on morphological transformations. *IEEE Transactions on Geoscience and Remote Sensing*, 41(9):1940–1949, September 2003.

[133] F Ortiz, F Torres, E De Juan, and N Cuenca. Colour Mathematical Morphology For Neural Image Analysis. *Real-Time Imaging*, 8(6):455–465, December 2002.

[134] E R Dougherty and R A Lotufo. *Hands-on Morphological Image Processing.* SPIE - The International Society of Optical Engineering, Washington, 2003.

[135] P Soille. Morphological Texture Analysis: An Introduction. In Klaus Mecke and Dietrich Stoyan, editors, *Lecture Notes in Physics Series: Morphology of Condensed Matter*, pages 215–237. Springer Berlin Heidelberg, 2002.

[136] E J Marjanovic, K A Ward, and J E Adams. The impact of accurate positioning on measurements made by peripheral QCT in the distal radius. *Osteoporosis international*, 20(7):1207–14, July 2009.

[137] J Rittweger, K Gerrits, T Altenburg, N Reeves, C N Maganaris, and a de Haan. Bone adaptation to altered loading after spinal cord injury: a study of bone and muscle strength. *Journal of musculoskeletal & neuronal interactions*, 6(3):269–76, 2006.

[138] L Sun, G Beller, and D Felsenberg. Quantification of bone mineral density precision according to repositioning errors in peripheral quantitative computed tomography (pQCT) at the radius and tibia. *Journal of musculoskeletal & neuronal interactions*, 9(1):18–24, 2009.

[139] A Müller, E Rüegsegger, and P Rüegsegger. Peripheral QCT: a low-risk procedure to identify women predisposed to osteoporosis. *Physics in medicine and biology*, 34(6):741–9, June 1989.

[140] E R Dougherty, Y Chen, S Totterman, and J P Hornak. Detection of osteoporosis by morphological granulometries. In *Proceedings of SPIE*, volume 1660, page 666, 1992.

[141] H Sievänen, P Kannus, a Heinonen, P Oja, and I Vuori. Bone mineral density and muscle strength of lower extremities after long-term strength training, subsequent knee ligament injury and rehabilitation: a unique 2-year follow-up of a 26-year-old female student. *Bone*, 15(1):85–90, 1994.

[142] C J Hosie. Measurement of trabecular bone mineral density in the distal radius by two gamma-ray computed tomography scanners. *Physiological measurement*, 14(3):269–76, August 1993.

[143] J M Pritchard, L M Giangregorio, S A Atkinson, K A Beattie, D Inglis, G Ioannidis, Z Punthakee, J D Adachi, and A Papaioannou. Association of larger holes in the trabecular bone at the distal radius in postmenopausal women with type 2 diabetes mellitus compared to controls. *Arthritis care & research*, 64(1):83–91, January 2012.

[144] G J Kazakia, A J Burghardt, T M Link, and S Majumdar. Variations in morphological and biomechanical indices at the distal radius in subjects with identical BMD. *Journal of biomechanics*, 44(2):257–66, January 2011.

[145] X S Liu, A Cohen, E Shane, E Stein, H Rogers, S L Kokolus, P T Yin, D J McMahon, J M Lappe, R R Recker, and X E Guo. Individual trabeculae segmentation (ITS)-based morphological analysis of high-resolution peripheral quantitative computed tomography images detects abnormal trabecular plate and rod microarchitecture in premenopausal women with idiopathic osteoporosis. *Journal of bone and mineral research*, 25(7):1496–505, July 2010.

[146] C. Findlay, SS. Jameson, S. Marshall, B. Walker, C. Walker, RD. Meek, and A. Nicol. Image analysis of bone density following anterior cruciate ligament injury. *Journal of Bone & Joint Surgery, British Volume*, 94-B(SUPP XVIII):31, 2012.